Delft University of Technology

Wake and wind farm aerodynamics of vertical axis wind turbines

Huang, M.

Important note
To cite this publication, please use the final published version (if applicable).
Please check the document version above.

Wake and Wind Farm *Aerodynamics* of Vertical Axis Wind Turbines

Ming Huang 黄明

Propositions

accompanying the dissertation

WAKE AND WIND FARM AERODYNAMICS OF VERTICAL AXIS WIND TURBINES

by

Ming HUANG

1. Vertical axis wind turbines (VAWTs) are the future technology for high-power-density wind farms, given their ability to deform the wake and keep high power extraction when closely placed. (*this thesis*)

2. VAWTs fall into disfavour partly because of their complex aerodynamics, yet the latter guarantees great potential for wake control. Fortunately, simply pitching the blades can achieve complex wake control. (*this thesis*)

3. Unlike planar actuator discs for horizontal axis wind turbines (HAWTs), simplified surrogates for VAWTs should be three-dimensional. (*this thesis*)

4. Controlling the VAWT wake is designing the streamwise vortex system, and the loading distributions over the blade swept area can be regarded as the variables. (*this thesis*)

5. Wind farms sacrifice the performance of a few turbines to extract more energy as a whole. This tells us that to gain, one needs to learn how to lose.

6. Result-oriented research is efficient, but it is the enemy of imagination.

7. Analytical models may seem simple, but they are never easy. The assumptions and justifications for a simplified model usually are much more complex than the model itself.

8. Renewable energy will not completely take over traditional energy because humans need reliable and constant power; However, new technologies exploiting renewable energy will eventually replace outdated ones. This will be true for VAWTs replacing HAWTs.

9. It is not difficult to find the truth, but it takes courage to stick to the truth.

10. The explosion of fragmented information on the Internet threatens systematic learning.

These propositions are regarded as opposable and defendable, and have been approved as such by the promotor prof. dr. ir. C. Simão Ferreira and co-promotor dr. A. Sciacchitano.

Stellingen

behorende bij het proefschrift

WAKE AND WIND FARM AERODYNAMICS OF VERTICAL AXIS WIND TURBINES

door

Ming HUANG

1. Verticale windturbines (VAWTs) zijn de toekomstige technologie voor windparken met een hoge vermogensdichtheid, gezien hun vermogen om het zog te vervormen en een hoog vermogen te behouden wanneer ze dicht bij elkaar staan. (*dit proefschrift*)

2. VAWT's vallen deels in ongenade vanwege hun complexe aerodynamica; toch garandeert de laatste het grote potentieel voor wake controle. Gelukkig kan door simpelweg de bladen te kantelen een complexe wake-control worden bereikt. (*dit proefschrift*)

3. In tegenstelling tot vlakke actuatorschijven voor windturbines met horizontale as (HAWT's), zouden vereenvoudigde surrogaten voor VAWT's driedimensionaal moeten zijn.(*dit proefschrift*)

4. Het beheersen van het VAWT-zog is het ontwerpen van het stroomgewijze vortexsysteem, en de belastingsverdelingen over het door het blad geveegde gebied kunnen als de variabelen worden beschouwd. (*dit proefschrift*)

5. Windparken offeren de prestaties van enkele turbines op om als geheel meer energie te onttrekken. Dit vertelt ons dat om te winnen, men moet leren verliezen.

6. Resultaatgericht onderzoek is efficiënt, maar het is de vijand van de verbeelding.

7. Analytische modellen lijken misschien eenvoudig, maar ze zijn nooit gemakkelijk. De aannames en rechtvaardigingen voor een vereenvoudigd model zijn meestal veel complexer dan het model zelf.

8. Hernieuwbare energie zal traditionele energie niet volledig overnemen omdat mensen betrouwbare en constante stroom nodig hebben; Nieuwe technologieën die gebruik maken van hernieuwbare energie zullen uiteindelijk verouderde technologieën vervangen. Dit geldt voor VAWT's die HAWT's vervangen.

9. Het is niet moeilijk om de waarheid te vinden, maar er is moed voor nodig om je aan de waarheid te houden.

10. De explosie van gefragmenteerde informatie op internet bedreigt systematisch leren.

Deze stellingen worden opponeerbaar en verdedigbaar geacht en zijn als zodanig goedgekeurd door de promotor prof. dr. ir. C. Simão Ferreira en co-promotor dr. A. Sciacchitano.

WAKE AND WIND FARM AERODYNAMICS OF VERTICAL AXIS WIND TURBINES

WAKE AND WIND FARM AERODYNAMICS OF VERTICAL AXIS WIND TURBINES

Proefschrift

ter verkrijging van de graad van doctor
aan de Technische Universiteit Delft,
op gezag van de Rector Magnificus Prof. Dr. Ir. T.H.J.J. van der Hagen,
voorzitter van het College voor Promoties,
in het openbaar te verdedigen op woensdag 15 maart 2023 om 10:00 uur.

door

Ming HUANG

Master of Engineering in Fluid Mechanics,
Northwestern Polytechnical University, China
geboren te Jiangxi, China.

Dit proefschrift is goedgekeurd door de promotoren.

Samenstelling promotiecommissie:

Rector Magnificus,	voorzitter
Prof. Dr. Ir. C.J. Simão Ferreira,	Technische Universiteit Delft, promotor
Dr. A. Sciacchitano,	Technische Universiteit Delft, copromotor

Onafhankelijke leden:

Prof. Dr. P. Chatelain	Université Catholique de Louvain, Belgium
Prof. Dr. F. Porté-agel	École Polytechnique Fédérale de Lausanne, Switzerla
Prof. Dr. Dipl.-Ing. M. Kühn	University of Oldenburg, Germany
Prof. Dr. A.P. Siebesma	Technische Universiteit Delft
Prof. Dr. F. Scarano	Technische Universiteit Delft
Prof. Dr. Ir. L.L.M. Veldhuis	Technische Universiteit Delft, reservelid

An electronic version of this dissertation is available at
http://repository.tudelft.nl/.

SUMMARY

The development of offshore wind energy, especially the steps towards deep water and/or higher density wind farms, revives the prospects of vertical axis wind turbines (VAWTs). Because VAWTs may reduce the cost of floating structures, there is a potential to lower energy costs. However, VAWTs are often assumed to be less efficient and less reliable due to a lack of understanding of their complex aerodynamics.

This research is motivated by the fact that the performance of isolated turbines is no longer the most important factor, but rather performance at the wind farm level. The objective is to comprehend the possible performance of VAWTs in a wind farm.

This dissertation advances the knowledge of wind farm aerodynamics of VAWTs mainly in four aspects: a) It demonstrates the relationship between the rotor loading and wake deflection/deformation, indicating directions for simplified modelling of VAWT wake control; b) It identifies vital characteristics of a VAWT wake, confirming the positive effects of wake deflection on wake recovery and interaction; c) It presents high-fidelity experimental data on the wakes and wake interactions of VAWTs placed upwind and downwind, and validates some cutting-edge models with the data; d) it demonstrates the potential of increased power performance of VAWT arrays by controlling the VAWT flow fields.

In pursuit of these advances, the dissertation identifies and tackles a series of research topics. The first is on the simplified wake models. The state-of-the-art VAWT wake models are mostly transposed from that for HAWTs, based on the planar actuator disc model. However, the effects of the actuator discs' shape, specifically the aspect ratio of rectangular ones (corresponding to VAWTs with various height-to-width ratios), on the wake recovery are not considered. We propose the effective mixing diameter D^* to normalise the shape effects on the wake velocity recovery based on momentum conservation. D^* is validated through particle image velocimetry (PIV) experiments and Reynolds averaged Navier-Stokes (RANS) simulations, and it outperforms the existing scaling lengths in the literature.

The dissertation further questions the validity of planar actuators as surrogates of VAWTs. It compares the three-dimensional wakes of an actuator disc and a lab-scale VAWT using robotic volumetric PIV. The comparison reveals substantial differences in the vortex systems, pointing out the limitations of planar actuators in reproducing VAWT wakes, especially when the wakes are deflected. The results indicate that surrogates for VAWTs should be three-dimensional, coinciding with the swept areas of blades.

Based on the three-dimensional actuator cylinder model and a simplified formulation of the vorticity transport equation, we demonstrate the underlying physics of the generation of the streamwise vortex system, highlighting the effect of different load distributions on the wake convection and mixing. We propose four idealised force distributions resulting in different vortex systems and wake topologies; The proposed model is validated qualitatively with stereoscopic PIV measurements on a lab-scale VAWT. We

quantify the faster wake recovery consequent from the wake deflection using the experimental data.

Furthermore, the wake interaction of two VAWTs placed upwind and downwind is investigated experimentally via PIV and load measurements. The upwind VAWT with positively pitched blades deflects the wake significantly, improving the inflow condition of the downwind VAWT, and thus increasing the overall extraction of the streamwise momentum.

With the high-quality experimental data, we validate the state-of-the-art analytical wake models and simulations for VAWTs and identify their validity ranges. Two analytical wake models (the Jensen model and the Bastankhah-Porté-Agel model), five wake superposition models (four algebraic models and one momentum-conservation-based model) and an unsteady Reynolds averaged Navier-Stokes (URANS) simulation with VAWTs represented by the actuator line model are compared in both isolated and interaction scenarios.

Based on the validated URANS simulation, we explore the wake deflection effects on the enhancement of wind power extraction for two up-scaled VAWTs placed in tandem. The blades of these large H-type VAWTs operate in a high Reynolds number (chord-based, $Re_c \approx 1 \times 10^7$), which ensures a high stall angle; The tip speed ratio is set to a relatively high value (4.5) to avoid severe dynamic stalls. And thus, the simulated VAWTs are optimised for engineering operations and perform better than the lab-scale model introduced earlier. Combinations where each turbine operates in three different fixed pitch angles (-10°, 0°, 10°) resulting in different wake deflections are compared. With wake deflections, the overall power coefficient is increased by up to 45% for a tested configuration, which also depends on the inter-turbine distances. Most interestingly, when the turbine blades are pitched in the same direction, the vorticity system in the wake is enhanced and thus yields a flying formation effect for a VAWT array.

Furthermore, wakes of three inline VAWTs are scrutinised, focusing on the wake interactions, floor effects and momentum recovery. For all the cases the three VAWTs' blades are pitched in the same direction following the so-called flying formation scheme. The vertical flux of momentum is notably enhanced by the VAWT array with positive blade pitches even with the floor present, which is vital to the overall increment of power extraction in a wind farm operating in the atmospheric boundary layer. The overall power extraction is increased by 35% compared to the array with zero blade pitches; More importantly, the downwind VAWTs increase their performances by 113%-154%. The latter indicates the tremendous potential of large wind farms consisting of VAWTs employing blade pitching.

SAMENVATTING

De ontwikkeling van offshore windenergie, met name de stappen naar diep water en/of windparken met een hogere dichtheid, doet de vooruitzichten van windturbines met verticale as (VAWT's) herleven. Omdat VAWT's de kosten van drijvende constructies kunnen verlagen, is er een mogelijkheid om de energiekosten te verminderen. Er wordt echter vaak aangenomen dat VAWT's minder efficiënt en minder betrouwbaar zijn vanwege een gebrek aan begrip van hun complexe aerodynamica.

Dit onderzoek is ingegeven door het feit dat niet langer de prestatie van geïsoleerde turbines de belangrijkste factor is, maar de prestatie van het windpark in zijn geheel. Het doel is om inzicht te krijgen in de mogelijke prestaties van VAWT's in een windpark.

Dit proefschrift bevordert de kennis van de aerodynamica van windmolenparken van VAWT's voornamelijk in vier aspecten: a) Het demonstreert de relatie tussen de rotorbelasting en afbuiging/vervorming van het zog, en geeft aanwijzingen voor vereenvoudigde modellering van VAWT-zogsturing; b) Het identificeert vitale kenmerken van een VAWT-zog, en bevestigt de positieve effecten van zogafbuiging op zogherstel en interactie; c) Het presenteert experimentele gegevens van hoge getrouwheid over de zoggen en zog-interactie van VAWT's die bovenwinds en benedenwinds zijn geplaatst, en valideert enkele geavanceerde modellen met deze gegevens; d) Het demonstreert het potentieel van verhoogde vermogensprestaties van VAWT-paren door de VAWT-stroomvelden te regelen.

In het nastreven van deze vorderingen, identificeert en behandelt het proefschrift een reeks onderzoeksthema's. De eerste is op de vereenvoudigde wake-modellen. De meest recente VAWT-zogmodellen zijn grotendeels overgenomen van die voor HAWT's, gebaseerd op actuator disk theorie. Er wordt echter geen rekening gehouden met de effecten van de vorm van de actuator disk, met name de beeldverhouding van rechthoekige schijven (overeenkomend met VAWT's met verschillende hoogtebreedteverhoudingen), op het herstel van het zog. We stellen de effectieve mengdiameter D^* voor om de vormeffecten op het herstel van de zogsnelheid te normaliseren op basis van behoud van impuls. D^* is gevalideerd door Particle Image Velocimetry (PIV)-experimenten en Reynolds-gemiddelde Navier-Stokes (RANS)-simulaties, en presteert beter dan de bestaande schaallengtes in de literatuur.

Het proefschrift zet verder vraagtekens bij de validiteit van vlakke actuatoren als surrogaten van VAWT's. Het vergelijkt de driedimensionale zoggen van een actuator disk en een VAWT op laboratoriumschaal met behulp van robotvolumetrische PIV. De vergelijking onthult substantiële verschillen in de vortexsystemen, wat wijst op de beperkingen van vlakke actuatoren bij het reproduceren van een VAWT-zog, vooral wanneer het zog wordt afgebogen. De resultaten geven aan dat surrogaten voor VAWT's driedimensionaal moeten zijn, samenvallend met de slag gebieden van de bladen.

Gebaseerd op het driedimensionale actuatorcilindermodel en een vereenvoudigde formulering van de vergelijking voor de evolutie van vorticiteit, demonstreren we de on-

derliggende fysica van het genereren van het stroomsgewijze vortexsysteem, waarbij we het effect van verschillende belastingsverdelingen op de zogconvectie en -menging benadrukken. We stellen vier geïdealiseerde krachtverdelingen voor die resulteren in verschillende vortexsystemen en zogtopologieën; Het voorgestelde model wordt kwalitatief gevalideerd met stereoscopische PIV-metingen op een VAWT op laboratoriumschaal. We kwantificeren het snellere zogherstel als gevolg van de zogafbuiging met behulp van de experimentele gegevens.

Verder wordt de zog-interactie van twee VAWT's die bovenwinds en benedenwinds zijn geplaatst experimenteel onderzocht via PIV- en belastingsmetingen. De bovenwindse VAWT met positieve bladverdraaiing buigt het zog aanzienlijk af, waardoor de instroomconditie van de benedenwindse VAWT wordt verbeterd en de algehele extractie van het stroomsgewijze momentum wordt vergroot.

Met de hoogwaardige experimentele gegevens valideren we de state-of-the-art van analytische zogmodellen en simulaties voor VAWT's en identificeren we hun geldigheidsbereik. Twee analytische zogmodellen (het Jensen-model en het Bastankhah-Porté-Agel-model), vijf zog-superpositiemodellen (vier algebraïsche modellen en één op momentumbehoud gebaseerd model) en een instabiele Reynolds-gemiddelde Navier-Stokes (URANS) simulatie met VAWT's gemodelleerd door het actuatorlijnmodel worden vergeleken in zowel geïsoleerde als interactie scenario's.

Op basis van de gevalideerde URANS-simulatie onderzoeken we de afbuigingseffecten van het zog op de verbetering van windenergie-extractie voor twee opgeschaalde VAWT's die achter elkaar zijn geplaatst. De bladen van deze grote H-type VAWT's werken in een hoog Reynoldsgetal (op basis van de koorde, $Re_c \approx 1 \times 10^7$), wat zorgt voor een hoge overtrekhoek; De verhouding van de tipsnelheid is ingesteld op een relatief hoge waarde (4,5) om ernstig dynamische stall tevoorkomen. Op deze manier zijn de gesimuleerde VAWT's geoptimaliseerd voor operationele condities en presteren ze beter dan het eerder geïntroduceerde model op laboratoriumschaal. Combinaties waarbij elke turbine werkt met drie verschillende vaste bladverdraaiiingingshoeken ($-10°$, $0°$, $10°$) resulterend in verschillende zogafbuigingen worden vergeleken. Met zogafbuigingen wordt de totale vermogenscoëfficiënt met maximaal 45% verhoogd voor een van de geteste configuraties, die ook afhangt van de afstand tussen de turbines. Interessant is ook dat wanneer de bladen in dezelfde richting zijn gedraaid, de vorticiteitin het zog wordt versterkt en dus een vliegend formatie-effect oplevert voor een VAWT-rij.

Verder worden de zoggen van drie VAWT's in een lijn onder de loep genomen, waarbij de nadruk ligt op de zog-interacties, vloereffecten en herstel van impuls. In alle gevallen worden de bladen van de drie VAWT's in dezelfde richting gedraaid volgens het zogenaamde vliegende formatieschema. De verticale flux van impuls wordt met name versterkt door de VAWT-rij met positieve bladhoeken, zelfs als de vloer aanwezig is, wat van vitaal belang is voor de algehele toename van energie opwekking in een windmolenpark dat in de atmosferische grenslaag werkt. De totale energie opwekking wordt met 35% verhoogd in vergelijking met de rij met bladhoeken van nul graden; Wat nog belangrijker is, de benedenwindse VAWT's verhogen hun prestaties met 113%-154%. Dit laatste geeft het enorme potentieel aan van grote windparken bestaande uit VAWT's die gebruik maken van bladverdraaiing.

摘要

海上风能向深水和/或更高密度风电场的发展，重振了垂直轴风力机(VAWT) 的前景。因为垂直轴风力机可以降低浮动结构的成本，进而降低度电成本。然而，由于缺乏对其复杂空气动力学的理解，人们通常认为垂直轴风力机效率较低。

本文研究动机源于业界对风电场设计的认识：最重要的因素不再是风机自身的性能，而是风电场级别的性能。本文旨在深入理解垂直轴风力机在风电场中的巨大潜力。

本文主要从四个方面开展了垂直轴风力机风电场空气动力学研究：a) 论证了转子载荷与尾流偏转/变形之间的关系，为垂直轴风力机尾流控制建模指明了方向；b) 确定了垂直轴风力机尾流的重要特征，确认了尾流偏转对尾流恢复和尾流相互作用的积极影响；c) 提供了垂直轴风力机的尾流和尾流相互作用的高精度实验数据，并用这些数据验证了一些前沿模型；d) 展示了通过控制垂直轴风力机流场来提高垂直轴风力机阵列性能的潜力。

本文确定并解决了一系列研究课题。首先是简化的尾流模型。现存最先进的垂直轴风力机尾流模型大多是从水平轴风力机尾流模型演化而来，后者基于平面致动盘模型。然而，在这些模型中，致动盘的形状，特别是高宽比（对应于具有各种高宽比的垂直轴风力机）对尾流恢复的影响未被考虑。我们基于动量守恒提出了一种有效混合直径，D^*，以归一化形状对尾流速度恢复的影响；并通过粒子图像测速(PIV) 实验和基于雷诺平均的CFD模拟验证了D^*有效性。D^*优于文献中现有的归一化尺度。

本文进一步开展了针对平面致动盘作为垂直轴风力机简化模型的有效性研究。采用了基于机器人的三维体视PIV测量并比较了致动盘和垂直轴风力机模型的三维尾流。揭示了二者尾流中涡流系统的显着差异，指出了平面致动盘在再现垂直轴风力机尾流方面的局限性；当尾流偏转时，二者的差异被进一步放大。该研究结果表明，针对垂直轴风力机的简化模型应该是三维的，正如其叶片的掠过区域为三维圆柱一样。

基于三维致动柱模型和涡量传输方程的简化公式，本文展示了垂直轴风力机尾流中流向涡系统生成的基本物理原理，强调了不同负载分布对尾流对流的影响。提出了四种理想化的力分布，它们能够产生不同的涡流系统和尾流拓扑；对所提出的模型进行了基于三维体视PIV的定性验证，并利用实验数据量化了尾流恢复加快的程度。

此外，本文还通过PIV 和天平测量实验研究了分别位于上游和下游的两个垂直轴风力机的尾流相互作用。具有正桨距角叶片的上游风机能够显着偏转尾流，改善下游风机的来流条件，从而增加垂直轴风力机阵列的整体性能。

基于上述实验数据，本文验证了针对垂直轴风力机的最先进的尾流分析模型和仿真模型，并确定了它们的有效性范围。所验证的模型包括两个尾流分析模型（Jensen 模型和Bastankhah-Porté-Agel 模型）、五个尾流叠加模型（四个代数模型和一个基于动量守恒的模型）和非定常雷诺平均(URANS) 模拟（其中垂直轴风机叶片由致动线模型表示）；验证场景包含独立风机以及风机阵列。

　　基于经过验证的URANS 仿真模拟，本文开展了尾流偏转对两个串联放置的大型垂直轴风力机性能的影响的探索研究。这些大型H 型垂直轴风力机的叶片在高雷诺数（基于弦长，$Re_c \approx 1 \times 10^7$）下运行，确保了较高的失速迎角。桨叶尖速较高（4.5）以避免严重的动态失速。因此，该风机相比前文介绍的实验室尺寸的风机具有更好的性能，更适用于阐释工程场景下的科学问题。本文比较了每个涡轮机以三个不同的固定桨距角（-10°、0°、10°）的组合。不同风机间距下，通过尾流偏转最多可增加45%的总功率系数。最有趣的是，当垂直轴风力机叶片沿同一方向倾斜时，尾流中的涡量系统会增强，从而为VAWT 阵列产生飞行编队效应。此外，论文研究了三个置于流向的垂直轴风力的尾流，重点关注尾流相互作用、地面效应和动量恢复。即使在存在地面的情况下，具有正桨距的垂直轴风力机阵列也显着增强了垂直方向的动量通量，这对于在大气边界层中运行的风电场的整体能量获取增量至关重要。与零桨距阵列相比，整体功率提取提高了35%；而下游风机的性能提高了113%-154%。后者揭示了由具有叶片变桨距的垂直轴风力机组成的大型风电场的潜力。

ACKNOWLEDGEMENTS

Composing the last part of the dissertation, which denotes the last piece of my journey as a PhD candidate at TU Delft, I'm full of emotions. It is undoubtedly one of the most critical periods in my life. Looking back on the journey, I have gained professional skills, happiness, and incredible memories... I was anxious and once felt lost, yet I passed through all those in the end, with support from my supervisors, families and friends. I appreciate everyone that was involved in such a wonderful journey of mine.

First, I would like to express my deepest appreciation to my excellent supervisory team: my promotor, Prof. Dr. Ir. Carlos Simão Ferreira and co-promotor Dr. Andrea Sciacchitano, without them, I could not have undertaken this journey. Carlos has been giving me the greatest freedom in exploring interesting research topics, training me as an independent researcher and only pulling me back when I was far off the track. Most importantly, he always puts faith in me that I can successfully do the job. It gave me a steady stream of motivation. Andrea supported me nearly unconditionally; he was calm and pragmatic forever. Andrea is, as referred to by my experiment buddy Yugandhar and I cannot agree more, the "cool guy with all the solutions".

Words cannot express my gratitude to my advisor, Prof. Dr. Fulvio Scarano. He enlightened me with enthusiasm, dedication and humour. I cannot forget our weekly meetings in the first two years of my PhD. Apart from all those insightful academic discussions, he also taught me to be moderate instead of humble and to set boundaries while still being kind. In the end, some decisions are complicated or even harsh, and some talk I understood or pretended to understand. But I believe I have learned something, not only for academia but also for life.

Further, I would like to acknowledge the jury members. I appreciate their precious time evaluating this dissertation and challenging me in the doctoral defence.

I am also grateful to the supporting staff. Thank you, Sylvia, for handling all the requests and arranging logistics, making my PhD life very much easier. I'd like to acknowledge Dennis Bruikman, Frits Donker Duyvis, Stefan Bernardy, Peter Duyndam and Nico van Beek, for the great technical support and interesting conversations in the workshop and around the coffee corner. Thank you, Colette, for arranging the logistics when I'm in the Aerodynamics group preparing the experiments, and also for letting me keep the desk when I need it in the PhD room.

Thanks should also go to my colleague, friend also co-author, Daan van der Hoek. I still remember the first experiment we did together to get trained for coming experimental campaigns, it was fun. Daan is smart and serious about experiments. It was nice to work with you on the followed up projects, capturing those beautiful wakes. Our cooperation last to this thesis, for Daan carefully translated my summary in Dutch; although this time I will not share a co-authorship. My deep thanks to you again, Daan!

Many thanks to Davide Monni, Yugandhar Vijaykumar Patil and Kodur Venkatesh Nikhilesh for letting me participate in your Master thesis projects. Davide's talent and

NOMENCLATURE

Acronyms

AC	actuator cylinder
AD	actuator disc
AL	actuator line
AP	available power
AR	aspect ratio
BEM	blade element momentum theory
CFD	computational fluid dynamics
CVP	counter-rotating vortex pair
CVV	coaxial volumetric velocimetry
CV	control volume
DDES	delayed detached-eddy simulation
DNS	direct numerical simulation
DSM	dynamic stall model
HAWT	horizontal axis wind turbine
HFSB	helium-filled soap bubbles
IFOV	instantaneous field of view
LBM	Leishman-Beddoes model
LCOE	levelized cost of energy
LES	large eddy simulation
MRV	magnetic resonance velocimetry
PIV	particle image velocimetry
RANS	Reynolds averaged Navier-Stokes
SGS	subgrid-scale

TI	turbulence intensity
TKE	turbulence kinetic energy
VAWT	vertical axis wind turbine

Greek Letters

α	angle of attack
η	inclined angles of pitch axes
λ	tip speed ratio
ω_x	streamwise vorticity
ρ	air density
$\sigma(x)$	Gaussian shape factor as a function of streamwise distance
σ_U	standard deviation of the velocity U
τ	shear stress
θ	azimuth angle over the rotation
φ	blade pitch angles

Latin Letters

f	force vector
$\mathbf{U}_{\text{in}}$	inflow wind speed vector
$\mathbf{U}_{\text{rel}}$	relative velocity vector perceived by the blade element
$\mathbf{U}_{\text{rot}}$	rotational velocity vector
c	chord length
A	frontal area
B	number of blades
C_P	power coefficient
C_T	thrust coefficient
D	rotor diameter
D^*	effective mixing diameter
D_{eq}	equivalent diameter
R	rotor radius

U_∞ freestream velocity

U_c mean wake convection velocity for a wind turbine array

U_i induced velocity

u_t blade linear speed of a H-type VAWT

U_U uncertainty of the time-averaged streamwise velocity

U_w cumulative wake velocity in wind turbine arrays

u_w^i wake of the i-th turbine in stand-alone conditions

W width of the frontal area

x streamwise spatial coordinate

y cross-stream spatial coordinate

z vertical spatial coordinate

CONTENTS

I

PROLOGUE

1

INTRODUCTION

1.1. Background

1.1.1. Modern wind energy industry and the role of VAWT

The modern wind industry has been constantly decreasing its Levelized Cost of Energy (LCOE) on the pathway to energy transition[1] (IRENA, 2021). Especially, it is seeing a boost of offshore wind farms, with continuing growth in the power of individual wind turbines (WindEurope, 2021; GWEC, 2021).

The offshore wind promises a tremendous potential for cost decline in three aspects: First, more favourable wind patterns than onshore wind, e.g., higher wind speed, less turbulence and better consistency (Wang et al., 2015). These properties generally mean more available wind power. Second, it is more suitable to deploy upscaling turbines offshore. By upscaling, a wind turbine will increase the power production by capturing more wind energy at higher altitudes, and thus a wind farm will benefit from an increased capacity factor (Chaviaropoulos et al., 2013, 2014). Third, compared to onshore, the offshore wind farm can be deployed with good access to power-demanding coastal regions while reducing the visual impact or noise pollution onto densely-populated areas (IRENA, 2019; Tigelaar, 2020; Esteban et al., 2011).

However, offshore wind is still facing critical issues hindering the falling of LCOE. The primary problem is the expanse increment in BOP (Balance of plant, including the foundation, electrical cabling, logistics Chaviaropoulos et al., 2014). It is associated with increased distance of the wind farm from the shore and increased water depth. Especially, the upscaling of the conventional horizontal axis wind turbines (HAWTs) requires strong floating constructions to balance the top-heavy structure, which requires significant investments. Hence, to decrease BOP, novel types of wind turbines are needed.

There is also a risk of not harnessing offshore wind significantly via the HAWT-based upscaling because HAWTs may not acclimatize to the floating environment, even though they are technically mature on land/shore. HAWTs have the following pitfalls: In addition to the top-heavy feature that requires high construction cost, they are prone to decrease the energy production due to a higher turbulence intensity (Wharton and Lundquist, 2012)[2]. The severe operating condition on floaters makes it worse, as additional wind speed fluctuations are generated along with the floating motions (Wen et al., 2022).

The wake effect is another issue in offshore wind farms. Wakes produced by upwind turbines feature lower overall wind speed, hampering the energy harvesting of downwind turbines (Howland et al., 2019); The increased turbulence in the wake not only reduces the performance but also aggravates the structural fatigue (Lee et al., 2012), in turn, increases the costs. The wake effect is even more severe offshore than onshore, due to a long-lasting wake region that is a consequence of lower environment turbulence and more giant wind turbines. Let alone the decreasing inter-turbine distances nowadays, leaving stronger wake interactions. To date, practical measures to mitigate the wake effect include a) using staggered layout (Stevens et al., 2014) b) steering the wake via yawing/tilting the rotor disk (Fleming et al., 2019, 2020) c) controlling the tur-

---

[1]E.g., 13% year-on-year fall in the global onshore-LCOE and 9% in the offshore-LCOE were achieved in 2020, even under the impact of the global pandemic caused by COVID-19.

[2]For a wind farm located in western North America, a reduced power production by an average of 15% was observed at a given wind speed with higher amounts of turbulence.

bine blades dynamically (van der Hoek et al., 2022). Except for the first, either option requires additional costs in the yawing/pitching system.

As opposed to HAWTs, VAWTs can have generators and drive trains mounted at the lower part, therefore featuring a lower centre of gravity; The latter means easier access for maintenance and less cost on building foundation. Moreover, VAWTs are less susceptible to flow turbulence, allowing for a more flexible layout to be deployed (Chatelain et al., 2017). Because of these advantages, vertical axis wind turbines are regaining attention as a prospective alternative to HAWTs in floating environments.

Furthermore, VAWTs have a significant potential to achieve a higher power density than their counterparts in a wind farm. It is for the following reasons: a) Faster wake recovery (Rolin and Porté-Agel, 2018), allowing for a closer inter-turbine distance; b) In addition to the conventional aligned or staggered layout, synergistic clusters can be employed for VAWTs to increase farm efficiency (Hezaveh et al., 2018); c) Simpler wake deflection mechanics. Unlike yawed or tilted HAWTs that require the nacelle or tower to move, VAWTs can easily redirect the wake via pitched blades (Jadeja, 2018; Guo and Lei, 2020) or struts connecting the blades (Mendoza and Goude, 2019).

Despite the great potential, VAWTs are confronting massive commercialisation resistance. The pressure first comes from its rival, HAWTs. The latter is prevailing in the wind energy market, making an over 40 years record of success and achieving technical maturity on shore. But as aforementioned, HAWTs also have pitfalls in the future of floating wind farms. Second, VAWTs have to prove their aerodynamic efficiency. VAWTs are usually deemed less efficient due to a lack of understanding of their complex aerodynamics. However, recent studies confirm the possibility of exceeding the performance of HAWTs with a well-designed pitch schedule and achieving higher wind farm power density via deflecting the wake (Dabiri, 2011; LeBlanc and Ferreira, 2021; Huang et al., 2023).

1.1.2. A BRIEF HISTORY OF VAWTS

Vertical axis wind turbines date back to an ancient time: the first recorded ones are Persian vertical axis windmills in the 9th-century (Ackermann and Söder, 2002; De Tavernier, 2021). These windmills glean the wind power via the aerodynamic drag of the device. About a thousand years later, in the 1920s, Sigurd Johannes Savonius invented a fine-tuned drag-type VAWT with self-starting capabilities. Followed by Georges Darrieus, who received a French patent for a lift-type VAWT in 1929 (Owens, 2019); The latter now bears his name.

Most commercial VAWTs nowadays are Darrieus-type. Darrieus VAWTs can be generally classified as Φ-type and H-type, and each finds prototypes constructed in the field. The Φ-type was prevailing in the 1980s, represented by *FloWind* (1987), *Éole* (1987). In the revival of VAWTs today, the H-type and its variants are seen more frequently, e.g., *T1-turbine* (2010), NENUPHAR *VertiWind* (2014) (see Möllerström et al. (2019) for more details about VAWT projects in recent years).

Due to drawbacks like highly complex unsteady three-dimensional aerodynamics, VAWTs have fallen into disfavour for decades. However, the prosperous development of offshore wind, especially the step towards deep water and higher density wind farms, is rejuvenating the prospects of vertical axis wind turbines, provided we can demonstrate their effectiveness in the complex wind farm flow/inflow.

Figure 1.1: Left: Persian vertical axis windmills. Image from https://www.amusingplanet.com/2014/07/the-ancient-windmills-of-nashtifan.html. Center and Right: Modern Φ-type and H-type VAWTs. Photos by Erik Möllerström (Möllerström et al., 2019).

1.2. OBJECTIVES AND RESEARCH QUESTIONS

The dissertation advances the state-of-the-art VAWT technology and analytical, experimental and numerical modelling. Especially in the 3D unsteady rotor-wake and wake-wake interaction, flow and load control, and wake management and modelling. In doing so, we answer the following research questions and sub-questions:

1. How to characterize the wake of VAWTs?
   (a) How does the vorticity system generated by the Actuator Cylinder (VAWT) differ from the Actuator Disk (HAWT)?
   (b) How does the vorticity system generated by an actuator cylinder compare with that generated by an actual VAWT?
   (c) What is the mixing process and energy recovery in the wake of a VAWT?

2. How to control the trajectory and recovery of the wake of a VAWT?
   (a) What load field at the rotor scale leads to wake deflection effectively?
   (b) How does the deflection of the wake affect its recovery?
   (c) How to design the load distribution over the Actuator Cylinder to improve wake recovery?

3. What is the effect of wake-rotor/wake-wake interaction of VAWTs?
   (a) How to experimentally measure the wake interaction of VAWTs?
   (b) How does the wake-wake interaction affect the recovery and deflection of the wake of the downstream turbine?

4. How to model wake-rotor/wake-wake interaction?
   (a) What is the state-of-the-art in the wake modelling/simulating of VAWTs?
   (b) What phenomena are observed experimentally and not accurately modelled?
   (c) How much is the enhancement of power extraction by wake deflection of VAWTs?

Figure 1.2: Upper: Adecon AL-38 turbines in Pincher Creek, Alberta. Photo by Jos Beurskens (Möllerström et al., 2019). Lower: The NENUPHAR concept of floating VAWT with a double 2×5MW rotor concept.

1

1.3. Thesis outline

The dissertation consists of four parts:

Part I: Prologue

This part starts the dissertation with introductions to the research background and reviews of the state-of-the-art methodologies for VAWT wake investigations.

Chapter 1 introduces the background, motivation and objectives of the research.

Chapter 2 Some basic wake aerodynamics and wake models of VAWTs are introduced per the research content presented in the following chapters.

Chapter 3 reviews the state-of-the-art approaches to measuring and simulating VAWT wakes, emphasising the simplified representatives of turbine rotors.

Part II: Wake aerodynamics: Actuator discs vs. VAWTs

This part characterises VAWT wakes and compares them to the wakes of actuator discs.

Chapter 4 experimentally investigated the wake scaling of actuator discs via robotic PIV. The actuator disc model is the simplest representation of a wind turbine and forms the basis of the most up-to-date analytical wake models. This chapter proposes a wake scaling length D^* accounting for the frontal shape effect in the VAWT wake recovery.

Chapter 5 compares the wake of an actuator disc and a lab-scale VAWT, emphasising the significant difference regarding the cross-flow motions; The latter is caused by distinct vortex systems.

Part III: Wind farm aerodynamics

This part presents the advancements in wind farm aerodynamics of VAWTs made by the dissertation, regarding wake steering and interactions. In order to simplify the problem, the experimental measurements and numerical simulations are conducted within the scope of isolated VAWTs and arrays with two or three turbines. The principles revealed in this part are valid for larger wind farms.

Chapter 6 looks into the cross-flow deflection of VAWT wakes using stereoscopic PIV and force balance measurements. The deflection is realised with fixed blade pitches. A qualitative model based on the three-dimensional actuator cylinder concept is proposed to demonstrate the relationship between rotor loading and deflection.

Chapter 7 experimentally investigates the wake interaction in an array of two VAWTs, with the upwind turbine deflecting the wake. The results validate the rapid wake recovery and the efficacy of wake deflection on the power output, which increases the available power in the second rotor.

Chapter 8 validates the simplified numerical and analytical models of VAWT wakes using the experimental data presented in chapter 6 and 7.

Chapter 9 explores the wake deflection effects on the enhancement of wind power extraction for two up-scaled VAWT placed in tandem, with the upwind VAWT deflecting the wake using pitched blades.

PART IV: EPILOGUE
Chapter 10 summarises the dissertation and recommends topics for future investigations.

1

2

STATE OF THE ART: WAKE AERODYNAMICS OF VAWTS

2.1. CHARACTERISTICS OF VAWT WAKES

The wake characteristics of isolated VAWTs have been extensively investigated experimentally, with the majority of studies focusing on the topology (the outline of the shear layer, the vortex structure, etc.), or on the recovery of the wake. Tescione et al. (2014) carried out stereoscopic particle image velocimetry (PIV) measurements in the near wake of a VAWT, emphasising the interaction of tip vorticity generated in the upwind and downwind regions of the blade swept area. Ryan et al. (2016) adopted magnetic resonance velocimetry (MRV) to measure the averaged three-dimensional flow field behind a VAWT, and reported a pair of counter-rotating vortices dominating the wake flow topology. Araya et al. (2017) documented the similarity between the wake of a VAWT and a circular cylinder via planar PIV. Rolin and Porté-Agel (2018) examined the kinetic energy and momentum recovery of a small-scale VAWT in boundary layer flow by means of stereoscopic PIV, confirming that the counter-rotating vortex pairs are responsible for a faster recovery. Very recently, Wei et al. (2021) used 3D particle tracking velocimetry (PTV) to measure the wake of full-scale VAWTs, investigating the effect of blade geometries on the near wake structure. Huang et al. (2023) proposed a qualitative model to describe the relationship between blade loading and wake deflection. The model was verified via stereo-PIV measurements covering the near and far wake regions of isolated VAWTs with different blade pitch angles. Apart from revealing the physics in the wakes of VAWTs, the studies on isolated VAWTs (e.g., Bachant and Wosnik, 2015; Ouro et al., 2019, etc.) contribute to validating numerical simulations and analytical models (Mendoza et al., 2019).

The importance of the vortex system in the wake of VAWTs has been highlighted. As illustrated in figure 2.1, the wake vortex system consists of trailing vortices created around the blade tips and spanwise vortices shed along the span of the blades. The trailing vortices form pairs of streamwise counter-rotating vortices that enhance the advection of momentum and are thus responsible for a faster recovery with respect to the wake of HAWTs; Such vortex pairs are also responsible for the wake deformation and asymmetry (LeBlanc, 2023; Ferreira, 2009; Tescione, 2016); Strengthen these vortices may result in enhanced wake deflection. Additionally, shed vortices usually increase the turbulence intensity (TI) in the near wake, which in turn enhances the turbulent transport of energy.

However, an elaborate physical explanation of the vortex generation and its relation to the turbine loading has not been provided. Some researchers associated it with the rotation of the rotor (Tescione et al., 2014; Wei et al., 2021, etc.). Many of them reported that the rotation of VAWTs creates two branches of horseshoe vortices similar to those of rotating cylinders (e.g., Wei et al., 2021; Craig et al., 2016b), and such vortex systems cause the wake deflection (Rolin and Porté-Agel, 2018; Ryan et al., 2016). In contrast, the results in De Tavernier et al. (2020) proved that a static cylindrical surface with three-dimensional loading could create counter-rotating vortices similar to a VAWT. The loaded cylindrical surface is the so-called three-dimensional actuator cylinder (AC), and is often used as a simplified VAWT. Massie et al. (2019) simulated the wake behind an 3D actuator cylinder that applies the same time-averaged load distribution as a VAWT; the results verified the accuracy of this infinite-blade concept in reproducing vorticity and wake deflection, confirming that the fundamental cause of the deflection is related to the load distribution.
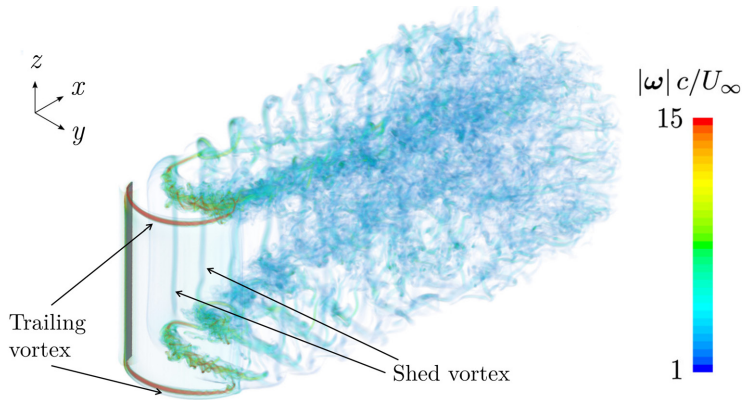
Figure 2.1: Volume rendering of the vorticity magnitude in the wake of a VAWT. Graphic adapted from Boudreau and Dumas (2017).

This dissertation demonstrates the wake development of VAWT by examining blade loading effects on the generation of the vortex system and, in turn, the resulting topology and recovery process of the wake.

2.2. WAKE DEFLECTION

In wind farms, wake deflection is deemed an effective way to reduce the power loss of downwind wind turbines caused by the wake of upwind ones (Porté-Agel et al., 2020). The deflection is often achieved by yawing the rotor discs of HAWTs, using an active control accounting for the variable wind direction (e.g., Fleming et al., 2017, 2019; Park and Law, 2015; Boersma et al., 2017; Bastankhah and Porté-Agel, 2019; Howland et al., 2019). With this technique, the wind farm's total power production is estimated to increase considerably, ranging from 4% to 13%, depending on specific cases. Figure 2.2 illustrates the field experiment of Howland et al. (2019), where a significant power increment (7–13%) was achieved via optimised yaw misalignment.

Numerous investigations have been conducted on the wake deflection of HAWTs by yaw, both experimentally and numerically, highlighting the underlying physics and facilitating the development of analytical models (e.g., Parkin et al., 2001; Medici and Alfredsson, 2006; Bartl et al., 2018; Jiménez et al., 2010; Shapiro et al., 2018; Bastankhah and Porté-Agel, 2016; Zong and Porté-Agel, 2020b). Additionally, a recently proposed deflection technique via vertically tilting the rotor disc has earned attention, intending to increase the downdraft of high-momentum flow (Fleming et al., 2014; Nanos et al., 2020); This approach enhances the vertical flux of kinetic energy, thus increasing the inflow velocity of downwind turbines, and in turn, improving the overall power output (Stevens and Meneveau, 2017; Hamilton et al., 2012). More recently, Bossuyt et al. (2021) experimentally compared the wake deflections that occur in yawed and tilted HAWT, and quantified the evolution of counter-rotating vortices in the wake. With the support of those investigations, several time-efficient and accurate wake models that can retain
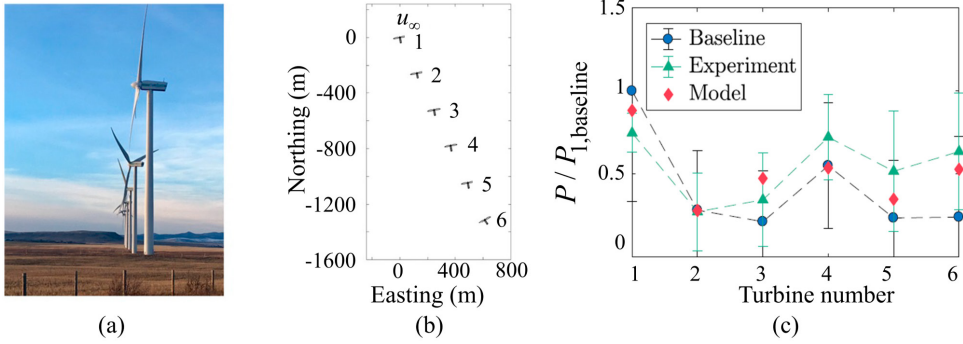
Figure 2.2: Increasing wind power out put via yawing HAWTs. Figure adapted from Howland et al. (2019). (a) A photo of the six Vestas V80 turbines examined in the field test. (b) Top view of the optimised yaw misalignment for the turbines. (c) Power output as a function of turbine numbers: a comparison among the baseline, optimised, and modelled arrays.

the physics of the wake under yaw have been proposed (Zong and Porté-Agel, 2020b; Bastankhah and Porté-Agel, 2016; Bastankhah et al., 2021a). Such models further facilitate the design of wind farms.

The wind farm design community has concluded that, to increase the overall power gain, one needs to focus on the power density of the wind farm as a whole, instead of the efficiency of individual turbines (Campagnolo et al., 2016; Fleming et al., 2017; Howland et al., 2019). Increased power density has been investigated by redirecting/deflecting the wake or by modifying the wind farm layout (e.g., inter-turbine distance: Meyers and Meneveau (2012); Stevens et al. (2016). Placement pattern: Stevens et al. (2014)). As stated by those studies, wind farm power output can benefit from small sacrifices in the power output of upwind turbines that "steer" the wake substantially around downwind turbines.

The ability to deflect wakes within an array of vertical axis wind turbines would be of similar interest. Based on the discussion about the turbine loading effects on the wake topology in section 2.1, it is likely viable to deflect the wake of VAWTs by varying the load distribution. Pitching the blades is the simplest way to modify the load. Ferreira (2009) first proposed that by shifting the pitching axis of a VAWT, the blade load can be shifted upwind or downwind of the swept area of the rotor. Recently, LeBlanc and Ferreira (2021) measured the blade load with an in-house designed VAWT that is able to perform active pitch control continuously, showing that the blade load can be effectively modified with fixed blade pitch. A few studies can also be found in the literature using the pitched blades on the deflection of VAWTs' wake. Jadeja (2018) investigated the wake deflection of a pitched VAWT using the actuator line model (ALM) together with URANS simulation. Guo and Lei (2020) propose to deflect the wake by effectively altering the incline angle of the rotor blade to the flow (which is a close analogue to adjusting the nacelle inclination for a HAWT), and they also use ALM+RANS to verify their design. Figure 2.3-(a) presents a schematic of the mechanical design and 2.3-(b) shows the simulation results of the wake deflection. Mendoza and Goude (2019) propose to achieve a similar outcome by

altering the pitch of the struts connecting the blades to the drive shaft. Both of these are mechanically complex and, potentially difficult to implement even in experiments.
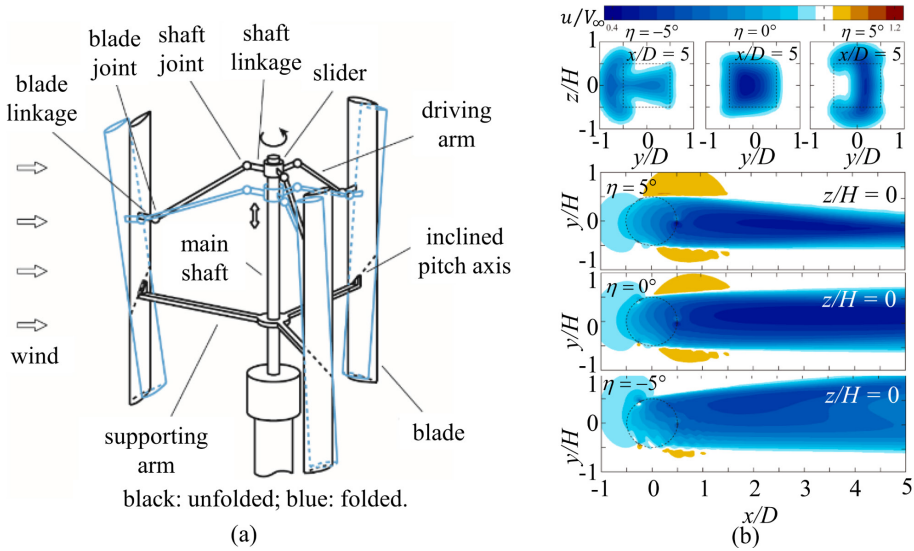
Figure 2.3: VAWT wake deflection using inclined pitch axes. Figure adapted from Guo and Lei (2020). (a) Mechanical design of a VAWT with inclined pitch axes. (b) Wake deflection with different inclined angles ($\eta = -5°, 0°, 5°$).

In the present dissertation, vertical axis wind turbines with continuously variable pitch have been reduced to practice as fixed blade-pitch and show promise to increase power output (chapter 6). We propose a simplified trailing vortex model based on the concept of the 3D actuator cylinder model, accounting for the VAWT wake deflection and deformation under various loading conditions. The proposed vortex system has been verified experimentally, with high-quality stereoscopic particle image velocimetry and force measurements in the Open-Jet Facility of TU Delft.

2.3. WAKE INTERACTION

Wake-rotor interactions and wake-wake interactions are vital in wind farm aerodynamics. Wake-rotor interactions in wind turbine arrays reduce wind turbine performance and increase the risk of structural fatigue; Wake-wake interactions increase the momentum deficit and turbulence intensity, thus affecting the energy production of a wind farm. It has been reported that the wake interference can cause 10 to 40% loss of power production of HAWT farms (Barthelmie et al., 2009; Stevens and Meneveau, 2017). Modelling the wind turbine wake under interactions with the inflow, terrain, other turbines, and their wakes is necessary to inform the wind farm design, which requires a detailed understanding of the complex flow interaction. Numerous investigations have been carried out on the wake interaction of HAWTs (e.g., field tests: Barthelmie et al. (2009); Hasager et al. (2017). Wind tunnel experiments: Rockel et al. (2016); Scott et al. (2020);

Fei et al. (2020); Sun et al. (2020). Numerical simulations: Troldborg et al. (2011); Sarlak et al. (2015); Rezaeiha and Micallef (2021)), filling the knowledge gap and facilitating the development of wake superposition models (e.g., Zong and Porté-Agel, 2020a; Vogel and Willden, 2020a).
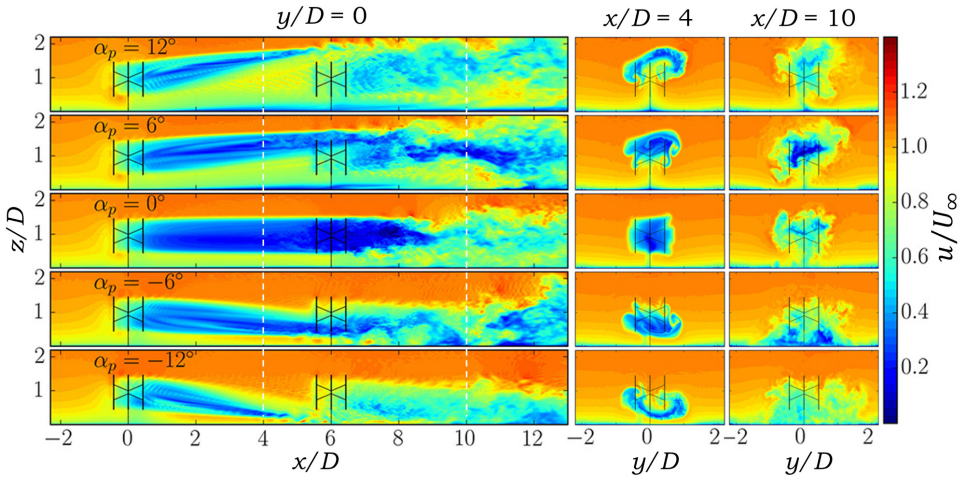
Figure 2.4: Wake interaction between two VAWTs in tandem. Figure adapted from Mendoza and Goude (2019). Wake deflection of the upwind VAWT is based on pitched struts. α_p denotes the pitched angle of the struts.

However, the research on the wake interaction of vertical axis wind turbines is lacking. Of the few experimental studies on the wake of VAWT arrays, most have focused on the synergistic effect of VAWT clusters, a kind of rotor-wake interaction. The synergistic effect occurs when multiple H-type VAWTs are placed close enough; in this condition, the performance of each one can be increased. Brownstein et al. (2019) measured the flow field surrounding a pair of scaled VAWTs with 3D particle tracking velocimetry (PTV), concluding that the increased performance is related to the bluff-body acceleration of the flow velocity around the turbines.

Few studies have been performed on wake-wake interactions of VAWTs, most of which are based on numerical simulations. Among these studies, the wake of VAWTs placed abreast are primarily investigated (Mereu et al., 2017; Posa, 2019; Sahebzadeh et al., 2020). A minority has touched upon the wake interaction between upwind and downwind VAWTs or in tandem (Hezaveh and Bou-Zeid, 2018; Mendoza and Goude, 2019; Silva and Danao, 2021). Likewise, field tests and laboratory experiments on VAWT wake interactions are rare. Kinzel et al. (2015) investigated the wake of a VAWT array under natural wind conditions, finding the similarity to the wake of a plant or urban canopy. Craig et al. (2016a,b) examined the flow characteristics of an array of rotating cylinders via planar-PIV, especially the wake recovery enhanced by the vertical flows, indicating a potential analogy to VAWT arrays.

The wake-wake interaction is a critical consideration for wind farm design. The wakes of upwind wind turbines hit the downwind ones and thus affect the overall mo-

mentum deficit, turbulence intensity fields, energy recovery rate, etc. An illustration on how the wake of the upwind turbine affects the downwind one's is given in figure 2.4. Modelling the wake interactions via superposition models has been a practical technique to estimate multiple wake effects in wind farms (Jensen, 1983; Frandsen et al., 2006; Larsen, 1988). Nevertheless, these models are subject either to oversimplified governing equations such as linear superposition or to the ill-defined superimpose of turbulence fields (Scott et al., 2020; Pierella et al., 2014). Therefore, to improve such models, inspecting the momentum and turbulence distribution under the wake interaction has been of increasing interest for HAWTs (e.g., Zong and Porté-Agel, 2020a; Sun et al., 2020; Vogel and Willden, 2020b); And it would the same case for that of VAWTs, as the wind energy industry is seeing a potential boost of offshore VAWT farms due to their advantages in floating environments (Ennis and Griffith, 2018; Paulsen et al., 2015).

Hence, experimental investigations on the wake interactions of VAWTs located upwind and downwind are desirable. The dissertation presents an experimental study on the wake interaction of a two-VAWT array in tandem, or with lateral offset, with the upwind turbine producing wake deflections, mimicking the wake steering operation in a wind farm (chapter 7).

2.4. WAKE MODELLING

Instead of solving the Navier-Stokes equation numerically, analytical models are formulated based on simplified momentum equations and shape functions describing the self-similarity of turbulent wakes. The instant response and robustness in producing velocity estimation of HAWT wakes have made analytical models prevail during wind farm design optimisation. Extrapolating the models to the VAWT wake is an interesting topic, and some extended models have been proposed in the literature (e.g., Abkar, 2018; Ouro and Lazennec, 2021).

However, these VAWT wake models are still based on the planar actuator disc model introduced for HAWTs without yaw. Therefore, the models are valid only when the wake of VAWTs is similar to that of HAWTs. In other words, the prerequisites of the models include a) The streamwise loading on VAWT is dominant, and the lateral loading is negligible. Because planar actuators merely account for loading perpendicular to its surface; and for the HAWT wake models without yaw, the actuator is perpendicular to the freestream. Usually, VAWTs have to operate in a high tip speed ratio (> 4) to meet this condition (Ferreira, 2009). b) The frontal shape effect is normalised appropriately. Because the actuator disc has to match the frontal shape of VAWTs, and the latter could be square, rectangular, and even egg-beater shaped. Different frontal shapes apparently will result in different wakes.

Craig et al. (2017) compared rectangular porous plates with different solidities to H-type VAWTs. The porous plates mimic actuator discs with different loading (see chapter 4 for a review of porous plates representing actuators in experiments). Significant deviations in the yielded wakes were reported in their work. Thus, the validity of the current extrapolated wake models for VAWTs is questionable.

One of this dissertation's aims is to evaluate the performance and range of validity of the state-of-the-art engineering wake models and wake superposition models. Hence, a review of wind turbine wake models (most are originally defined for HAWTs) and super-

position models is provided as follows.

2.4.1. ANALYTICAL WAKE MODELS

Analytical wind farm models are widely used in the process of engineering design and optimisation of wind farms, siting and economic forecasting, due to their low computational cost. There are two broad categories of analytical wind farm modelling. One is based on the wake structure of wind turbines (bottom-up models); The other is top-down models based on the structure of the atmospheric boundary layer (ABL) (Stevens and Meneveau, 2017). The dissertation focuses on the former.

This section briefly introduces the available analytical wind turbine wake models. Such models are established based on theories that relate to the turbulent wake. Simplifications are adopted for the formulation of the analytical equations. In most scenarios, a wind turbine is considered an actuator disc. All the models below were developed initially for the HAWT wakes, and some have been extrapolated to the VAWT wake modelling. A comparison of the models is depicted in figure 2.5, showing the profile shapes and the accuracy. For details about the governing equations and tuning procedures, check appendix B.
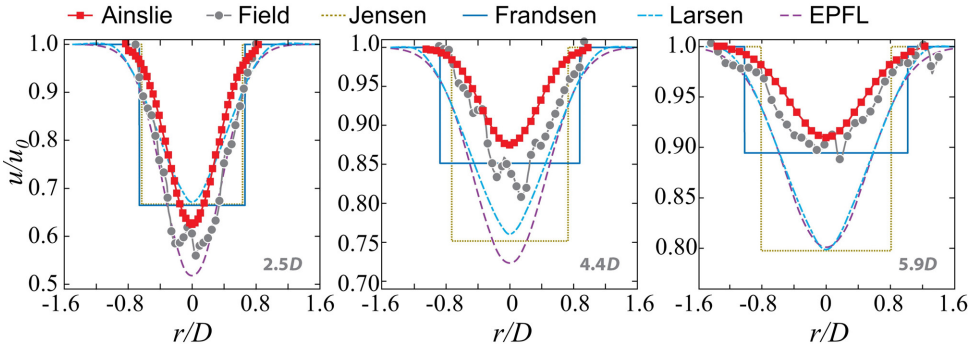
Figure 2.5: Comparison of wake profiles measured in field experiments and the wake models reviewed in this section. The EPFL model is the BPA model with correction for wake expansion rate (Niayifar and Porté-Agel, 2015). Graphic from Stevens and Meneveau (2017); Input parameters: $D = 72.2$ m, $z_h = 57$ m, $I = 11\%$, $C_T = 0.78$, and $k_w = 0.0525$.

JENSEN MODEL

The model proposed by Jensen (1983) and updated by Katić et al. (1987) is probably the earliest wake model developed. It is still widely used due to its simplicity and reasonable estimation accuracy regarding the energy content. The model takes a control volume (CV) right after the rotor, assuming a linearly expanded wake region. Within the wake, top-hat velocity profiles at wake cross-sections are considered. The mass conservation is adopted to obtain the initial velocity deficit, and the velocity recovery is determined with a decay constant k and the downwind location. As stated by the authors, the model gives sufficiently accurate predictions in the far wake (more than 3-4 rotor diameters away from the turbine, see also in Kaldellis et al. (2021)) and only requires a limited amount of input parameters, which is a great advantage during the preliminary design process.

It is worth pointing out the drawbacks of the model. The highly simplified equations bring about high computational efficiency but also low fidelity. There are two main reasons for the latter: 1) The governing equations only account for mass balance, while the momentum exchange is also critical in the wake flow; 2) The assumption of the top-hat shape of the velocity distribution is far from reality, causing large deviations at wake centre and edges. This is problematic, especially when calculating the integrated wind power; The latter is proportional to the cube of the distributed wind velocity.

FRANDSEN MODEL

Frandsen et al. (2006) proposed a wake model based on mass and momentum conservation. A control volume around the wind turbine is considered; It is assumed to be sufficiently large and bounded by the streamlines, such that there is no flow across its lateral surface. The pressure is assumed to be fully recovered downwind, and the shear stress terms are assumed negligible to simplify the momentum equation. Like the Jensen model, top-hat velocity distributions and the mass balance in the CV are considered. Hence, the velocity deficit is obtained right after the pressure recovery using the simplified momentum and mass conservation equations. And velocity at any distance downstream is determined by the initial deficit, a wake decay constant, and a shape constant. The decay and shape constants are obtained by matching the curves of the Jensen model. However, instead of a linear expansion of the wake outline, an exponential expansion proportional to $x^{1/2}$ is adopted, where x denotes the downstream distance.

The Frandsen model has been proved to outperform the Jensen model while keeping low computational cost (Kaldellis et al., 2021). But still, the top-hat-shaped velocity profile entails an inherent error in energy estimation, which is intensified at lower upstream wind speed. Additionally, a crude assumption of the wake expansion and pressure recovery immediately after the rotor is adopted to assure a solution for all thrust coefficient (C_T) values between 0 and 1. Consequently, the model is valid only in the far wake, where the wake expansion due to pressure loss is negligible.

LARSEN MODEL

Larsen (1988) proposed a simple wake calculation procedure in 1988, which was further developed to be a semi-empirical analytical wake model (Larsen, 2009). The model is based on Prandtl's turbulent boundary layer equations because the wake of HAWTs in high Reynolds number is characterised by free shear and turbulence. The modelled wake starts right after the rotor, while the radial growth of the wake is deemed proportional to $x^{1/3}$, which is consistent with that of a classical free turbulent wake (Schlichting and Gersten, 2017). In addition, the model has to take velocities measured right after a full-scale rotor and those at 9.6 D downstream; The velocities are used as the boundary conditions to close the governing equations, whereby the wake deficit and velocity distributions can be calculated.

The model accounts not only for the energy dissipation caused by the Reynolds stresses but also implicitly for the diffusion effect by the atmospheric turbulence. Nonetheless, the model is subject to the uncertainties stemming from a) the measured velocity data as boundary conditions and b) the high Reynolds number assumption. For an arbitrary turbine to be inspected, the empirical coefficients adopted in the model

likely have to be tuned, especially when the flow condition largely deviates from their full-scale experiments.

BASTANKHAH AND PORTÉ-AGEL (BPA) MODEL

Bastankhah and Porté-Agel (2016) proposed an analytical wake model featuring normal-Gaussian shaped velocity distributions. Similar to the Frandsen model, a control volume bounding the wind turbine is selected, where the momentum conservation is applied to obtain the velocity deficit using C_T and the Gaussian shape factor $\sigma(x)$. As for the growth function of wake outlines, instead of an explicit equation of the wake diameter as adopted in both Jensen and Frandsen models, a linear wake growth is given concerning $\sigma(x)$ (see appendix-B).

The model's advantages include a reasonable velocity deficit estimation and continuous velocity profiles, which are more realistic compared to the top-hat shape. The main disadvantage is that the model can only give reasonable predictions in the far wake because the wake similarity assumption for bluff bodies is only valid in the far wake. Since there is no extra calculation process in the near wake, the model occasionally obtains unrealistic recovery rates or even solutions of imaginary numbers in this region.

AINSLIE MODEL

Unlike the other analytical models above, Ainslie (1988) model numerically solves parabolic equation, a simplified RANS equation. The core innovation of the original model is to account for the effects of shear layers, ambient turbulence and wind turbine wakes using a constant. The constant is obtained experimentally.

2.4.2. WAKE SUPERPOSITION MODELS

Wake superposition models are often used with analytical wake models to predict the power production of wind farms. By superimposing wakes calculated from analytical models, one can instantly assess the total velocity deficit in a wind turbine array. The wake superposition process is depicted in figure 2.6. Most models are algebraic methods based on linear summations of velocity deficit or squared velocity deficit (Stevens and Meneveau, 2017; Porté-Agel et al., 2020; Zong and Porté-Agel, 2020a).
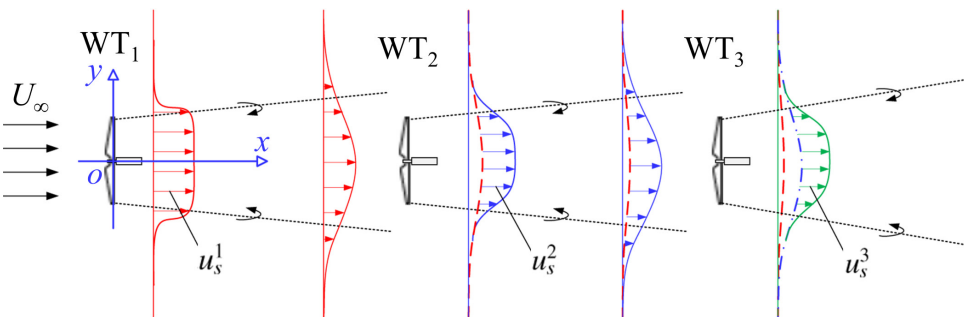
Figure 2.6: Schematic of wake superposition in an array of wind turbines. u_s is the wake velocity deficit imparted by the ith wind turbine. Graphic from Zong and Porté-Agel (2020a).

Lissaman ([1979](#)) propose a model for the cumulative velocity deficit based on the linear superposition of velocity deficits, assuming a fully recovered inflow condition for each wind turbine. The model is formulated as:

$$U_w(x, y, z) = U_\infty - \sum_i \left(U_\infty - u_w^i(x, y, z) \right), \tag{2.1}$$

where U_∞, U_w and u_w^i denote freestream velocity, the cumulative wake behind the turbines, and the wake of the i-th turbine in stand-alone conditions. Katić et al. ([1987](#)) introduced the summation of squared velocity deficit as a superposition strategy. Because squared velocity deficits can make the cumulative deficit reach an equilibrium level quickly in a wind turbine array with several (typically 3-4) rows, matching the experimental results. The model is expressed as:

$$U_w(x, y, z) = U_\infty - \sqrt{\sum_i \left(U_\infty - u_w^i(x, y, z) \right)^2}. \tag{2.2}$$

Later, Voutsinas et al. ([1990](#)) proposed an improved model based on the model of Katić et al. ([1987](#)), using the mean wind speeds perceived by the wind turbines as the inflow velocity to calculate the corresponding velocity deficit, instead of using U_∞, i.e.,

$$U_w(x, y, z) = U_\infty - \sqrt{\sum_i \left(u_0^i - u_w^i(x, y, z) \right)^2}, \tag{2.3}$$

where u_0^i is the mean wind speeds perceived by the i-th wind turbine.

More recently, Niayifar and Porté-Agel ([2015](#)) proposed a new model that incorporates the concept of mean perceived wind speed with Lissaman's model, given by:

$$U_w(x, y, z) = U_\infty - \sum_i \left(u_0^i - u_w^i(x, y, z) \right). \tag{2.4}$$

The models above are simple and robust; however, they are all empirical and lack theoretical justifications. Lately, Zong and Porté-Agel ([2020a](#)) proposed a superposition model based on momentum conservation. In this model, the cumulative wake deficit is given by:

$$U_w(x, y, z) = U_\infty - \sum_i \frac{u_c^i(x)}{U_c(x)} u_s^i(x, y, z), \tag{2.5}$$

where u_c^i and U_c are introduced as mean wake convection velocities for each turbine's wake and the array's combined wake, respectively. u_c^i is calculated separately via:

$$u_c^i(x) = \frac{\iint u_w^i(x, y, z) \cdot u_s^i(x, y, z) \mathrm{d}y \, \mathrm{d}z}{\iint u_s^i(x, y, z) \mathrm{d}y \, \mathrm{d}z}, \tag{2.6}$$

where $u_s^i = u_0^i - u_w^i$. U_c is determined iteratively as follows:

1. Initialise U_c as the maximum value of u_c^i.

2. Substitute U_c into equ. (2.5), update the total velocity deficit U_w.

3. Substitute U_w into equation: $U_c(x) = \dfrac{\iint U_w(x,y,z)\cdot(U_\infty - U_w(x,y,z))\mathrm{d}y\,\mathrm{d}z}{\iint (U_\infty - U_w(x,y,z))\mathrm{d}y\,\mathrm{d}z}$, to update the combined convection velocity. The updated U_c is noted as U_c^*.

4. If $\left| U_c - U_c^* \right| / U_c^* \leqslant 0.001$:

      let $U_c = U_c^*$ and execute step 2 once and get the final U_w;

else:

      let $U_c = U_c^*$, repeat steps 2-4.

3

METHODOLOGY: VAWT WAKE MEASUREMENT AND SIMULATION

3.1. INTRODUCTION

WAKE is the decelerated and highly turbulent flow regions behind a bluff body, a wind turbine, or anything that applies a drag force to the flow. As discussed, knowledge gaps exist regarding the wake characterising of VAWTs, wake interactions, etc. Experiments or models with different fidelity are required depending on specific conditions to fill these gaps. In this chapter, a variety of experimental, numerical and analytical approaches with different fidelity are briefly introduced. These approaches are employed in the following chapters to answer the research questions listed in chapter 1 and are further described in detail.

3.2. PARTICLE IMAGE VELOCIMETRY

Particle image velocimetry is a kind of optical measurement technique which measures the position-in-time of tracer particles that follow the flow motion without disturbing the flow. The velocity in the flow is then obtained via image processing approaches. It is the most widely used approach in lab-scale experiments in the wake of VAWTs. A PIV system typically consists of six subsystems: seeding, illuminating, recording, calibration, evaluation, and post-processing (Raffel et al., 2018), these components are illustrated in figure 3.1.

PIV measurements can be classified according to the dimension of the measurement field and the number of velocity components, such as 2D-2C (planar), 2D-3C (Stereoscopic), and 3D-3C (e.g., tomographic). In the present dissertation, a tomographic PIV setup with a robotic arm measuring the wake of a VAWT and a porous disc is presented in chapter 4 and 5; stereoscopic PIV is used in chapter 6.
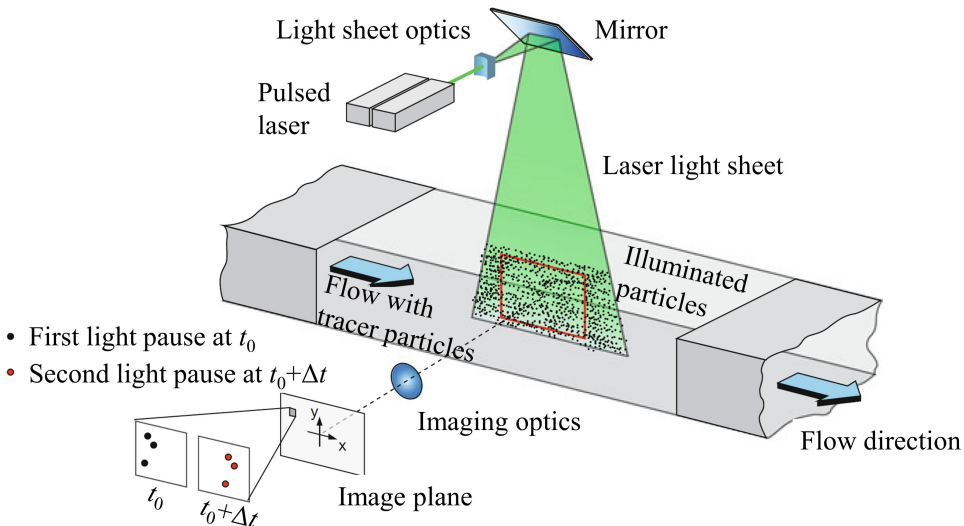
Figure 3.1: Typical setup of a planar (2D-2C) PIV. Graphic from Raffel et al. (2018).

3.2.1. STEREOSCOPIC PIV

A classic planar PIV as depicted in figure 3.1 can only measure the in-plane velocity components, since only one image plane parallel to the laser light sheet is recorded. To capture the out-of-plane velocity component within the light sheet, the stereoscopic PIV (stereo-PIV) is introduced (Raffel et al., 2018). In most stereoscopic setups, two cameras are placed noncollinearly, imaging the same plane. Each camera yields two in-plane components with respect to the measurement plane; With the four measured values and the geometry of the PIV imaging system, the three velocity components in the object plane are obtained (Willert, 1997).

Stereo-PIV is frequently employed measuring the wake of VAWTs to capture the highly three-dimensional flow; for instance, Tescione et al. (2016) used stereo-PIV to measure the vertical centre plane of a VAWT wake and quantify the tip vorticity evolution (figure 3.2-(a) and (b)); Rolin and Porté-Agel (2018) analysed the kinetic energy transportation in the cross-sections of the wake (figure 3.2-(c) and (d)).
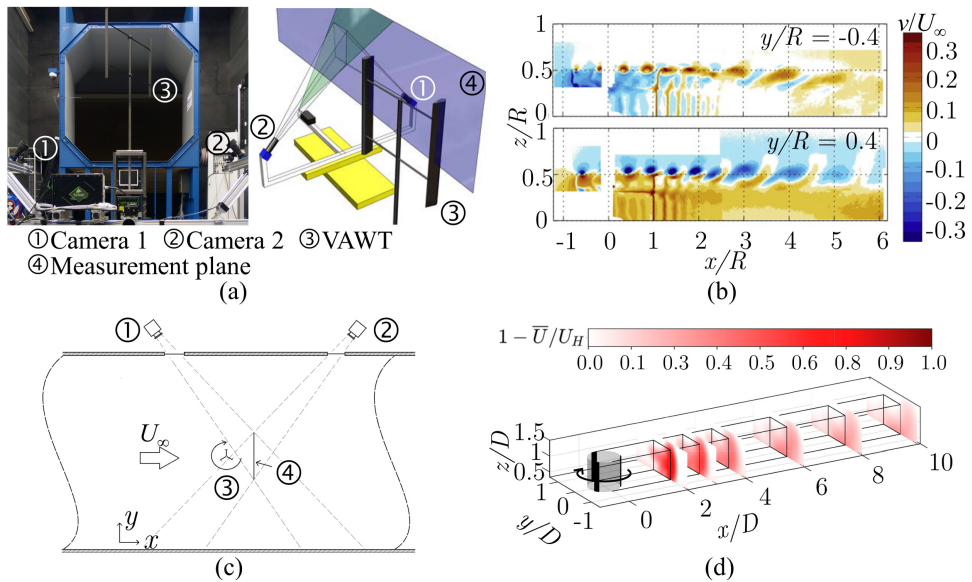
Figure 3.2: Measurements of VAWT wakes using Stereo-PIV. (a) and (b): experimental setup and the out-of-plane velocity contours in the work of Tescione et al. (2016); (c) and (d): experimental setup and the measured velocity deficit. Graphic adapted from Rolin and Porté-Agel (2018).

3.2.2. ROBOTIC VOLUMETRIC PIV

The robotic volumetric PIV proposed by Jux et al. (2018) is a 3D-3C measurement system developed for large-scale complex flow fields. The working principle of the system is to measure the velocity in a small volume with a coaxial volumetric velocimetry (CVV, Schneiders et al., 2018), and precisely move the system using robotics to map the complete field of interest. Since the measuring device is movable to avoid optical obstacles, the robotic PIV has great advantages in measuring the flow surrounding complex ob-

jects.

The CVV system is a combination of tomographic PIV and Lagrangian particle tracking (e.g., Novara and Scarano, 2013; Schanz et al., 2016), with the former featuring coaxial arrangement between the illumination and imaging directions (figure 3.3). A 2D sketch of a CVV system is presented in figure 3.3; For robotic PIV, the Lagrangian particle tracking algorithm used for analysing the particle images is Shake-The-Box (Schanz et al., 2016), an efficient time-resolved method working on the 3D particle positions rather than the intensity distribution for most tomographic reconstruction algorithms.
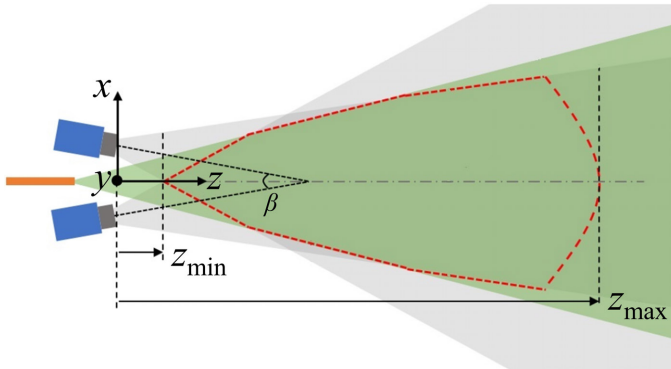
Figure 3.3: A coaxial velocimeter (CVV) setup comprised of the cameras (blue), field of view (grey) and laser illumination (green) provided from an optical fiber (orange). Dashed red: the measurement region; β: tomographic aperture; $z_{\min}$ and $z_{\max}$: the closest and furthest measurement depth. Graphic reproduced from Schneiders et al. (2018).

3.3. VAWT MODELLING

Before introducing the wake calculation methods, VAWT modelling techniques required in these approaches are reviewed. Simplifications made in the VAWT modelling techniques determine the fidelity and computational cost and, in some cases, form the theoretical basis of the calculation.

3.3.1. ACTUATOR DISC MODEL

The actuator disc model (ADM) is probably the simplest model representing a wind turbine. It assumes a wind turbine as a permeable disc with a constant thrust over the disc surface. The idea of replacing a rotor with an actuator disc dates back to more than a hundred years ago in the work of Rankine (1865), yet it was first formulated by Froude (1889) associated with the momentum theory accounting for the axial momentum balance.

Later, Joukowsky (1918) introduced torque applied on an actuator disc on account of angular momentum balance, and he was the first to derive the performance of a static disc representing a rotor. The proposal of Joukowsky's actuator disc is based on his previous work (Joukowsky, 1912) on the vortex model for screw propellers. Almost simultaneously, Betz (1919) published his work on propeller vortex theory. Both Joukowsky's

and Betz's models are proved to converge to Froude's actuator disc in the limit for an in-finite number of blades. More details on the derivation process and historical reviews on the ADM can be appreciated in the book of van Kuik (2018).

For Froude's ADM, a one-dimensional momentum theory is applied within the stream tube bounding the actuator disc and the affected flow. The theory assumes that the velocity at every cross-section is uniformly distributed. An induction factor $a = U_i/U_\infty$ is defined, with U_i being the induced velocity of the actuator disc and U_∞ being the free stream velocity. Capital letters denote a uniform/averaged quantity. At the rotor plane, the velocity is $U_\infty - U_i$. The induction factor a is expressed as a function of the thrust coefficient C_T:

$$a = \left(1 - \sqrt{1 - C_T}\right)/2 \tag{3.1}$$

With the 1D simplification, Froude's ADM-based analytical models feature significantly decreased complexity and computational cost (e.g., Jensen, 1983; Katić et al., 1987). Nevertheless, the uniformly distributed velocity profile in the wake is unrealistic (e.g., White, 2006). To model the continuously distributed velocity profiles, the ADM has been combined with momentum equations in three dimensions. Consider a control volume bounding the actuator disc and the wake that is sufficiently large, such that the pressure and velocity recover to the freestream state around its edges. And in turn, no (turbulent) shear occurs at the edges. Moreover, the radial velocity gradients are negligible compared to the axial gradient. The resulting simplified momentum balance is given by:

$$\rho \int u_w \left(U_\infty - u_w\right) \mathrm{d}A = T \tag{3.2}$$

The equation is well-known as a technique to determine the drag using the far wake velocity information (Anderson Jr, 1985; Tennekes and Lumley, 1972). In the equation, $u_w(y, z)$ is the velocity in a stream tube cross-section that is located at the far wake; A is the cross-sectional area of the stream tube, T is the thrust force applied to the flow by the turbine, which is expressed as:

$$T = \frac{1}{2} C_T \rho A_0 U_\infty^2 \tag{3.3}$$

where A_0 is the frontal area of the turbine.

The ADM has become a prevailing simplified model for HAWTs, and they appear in numerous investigations on HAWTs' wake and wind farm aerodynamics (e.g., Aubrun et al., 2013; Howland et al., 2016; Lignarolo et al., 2016). The model has also been adapted to represent VAWTs, such as the multiple streamtube model (Strickland, 1975) and double multiple streamtube model (Paraschivoiu, 1981). More importantly, the ADM forms the basis of most analytical wake models nowadays developed for HAWTs (Stevens and Meneveau, 2017), and some of those have been extended for VAWTs (Abkar, 2018). However, comparisons of the wake of actuator discs and VAWTs (Huang et al., 2020; Craig et al., 2016a) reveal the limitation of planar actuators, particularly in reproducing the vortex system and the wake deflections. This is further discussed in chapter 5.

3.3.2. ACTUATOR CYLINDER MODEL

The actuator cylinder model (ACM) was initially introduced by Madsen (1982) as an extension of the well-known actuator disc model (ADM), and was dedicated to H-type VAWTs. The model converts the unsteady blade loads to a static, two-dimensional cylinder (a cylinder with infinite height, such that every section is the same and purely 2D). In the work of Madsen (1982), the flow field and wind turbine performance are obtained by solving the governing equations, which are Euler equations without viscous terms in the momentum equation.

Massie et al. (2019) combined the concept of a three-dimensional actuator cylinder with a large eddy simulation, verifying the efficacy of the actuator cylinder model (ACM) in reproducing the time-averaged wake of VAWTs (figure 3.4). In the present dissertation, we adopt the ACM and simplified vorticity transport equation to demonstrate the patterns of vorticity generation and propagation in the wake of VAWTs. The patterns have been validated with PIV measurements; Details are available in chapter 6.
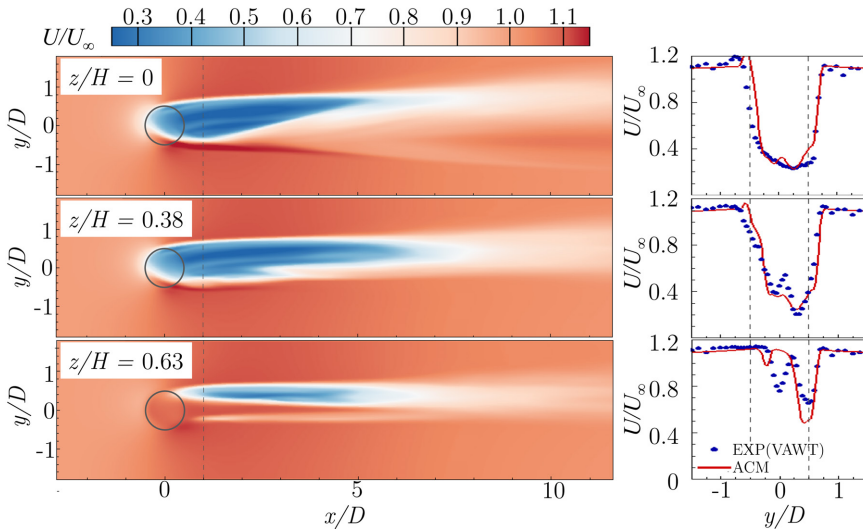
Figure 3.4: The wake of a three-dimensional actuator cylinder (LES results). Left: Mean streamwise velocity contours. Right: comparisons of the simulation results at $x/D = 1$ with experimental data from Bachant and Wosnik (2015). Figure reproduced from Massie et al. (2019).

3.3.3. ACTUATOR LINE MODEL

The actuator line model (ALM) was initially introduced by Sørensen and Shen (2002) to the wind energy community, simulating the wake of HAWTs. It has been applied to investigate wakes of VAWTs, accounting for the unsteady flow phenomena and turbulence fields while precluding small-scale flow structures (e.g., the boundary layer flow around the airfoil) that have minor effects on the macro-behavioural characteristics of the rotor wake.

The model is based on a blade element approach combined with two-dimensional

airfoil characteristics. The blade loading applied to the flow field is determined iteratively via the local angle of attack (AoA) and a lookup table of the airfoil's static force coefficients. The ALM shall be integrated with correction models for the blade loading, accounting for the effects that a static lift-drag polar diagram cannot reveal. For example, dynamic stall models for unsteady behaviour of an airfoil, end effect models for three-dimensional blade tip losses, etc.

In the work of Sørensen and Shen (2002), a Reynolds averaged Navier-Stokes (RANS) solver was adopted to solve the velocity field; Large eddy simulation (LES) is also frequently documented with the ALM in the literature (e.g., Troldborg, 2008; Sarlak et al., 2015). The present dissertation uses the ALM with an unsteady RANS solver (*pimpleFoam* library from OpenFOAM, an open source computational fluid dynamics (CFD) software). The ALM is realised with an open source library *turbinesFoam* (DOI: 10.5281/zenodo.3542301) developed mainly by Bachant et al. (2016). The simulation procedure is illustrated in figure 3.6; The implementation of the ALM and sub-models in *turbinesFoam* is introduced in the following subsections.

BLADE ELEMENT OF A VAWT

As illustrated in figure 3.5, the local angle of attack (α) is determined by the directions of relative velocity ($\mathbf{U}_{\text{rel}}$) and chord-wise. $\mathbf{U}_{\text{rel}}$ is given by:

$$\mathbf{U}_{\text{rel}} = \mathbf{U}_{\text{in}} + \mathbf{U}_{\text{rot}}, \tag{3.4}$$

where $\mathbf{U}_{\text{in}}$ is the inflow wind speed perceived by the blade element, $\mathbf{U}_{\text{in}} = \mathbf{U}_{\infty}$ when undisturbed flow is assumed for a pure geometric calculation of α; As illustrated in figure 3.6, $\mathbf{U}_{\text{in}}$ and α are updated iteratively. $\mathbf{U}_{\text{rot}}$ denotes the rotation speed of the blade, $|\mathbf{U}_{\text{rot}}| = \Omega R$. The AoA is expressed as:

$$\alpha = \phi + \gamma, \tag{3.5}$$

where ϕ is the angle between $\mathbf{U}_{\text{rel}}$ and $\mathbf{U}_{\text{rot}}$, γ is the pitch angle of the blade element. Bold letters stand for vectors.

Figure 3.5: Schematic of velocity and force vectors of a VAWT's blade element. Bold letters denote vectors.

3

Figure 3.6: Flowchart of the actuator line model coupled with RANS simulation.

3

DYNAMIC STALL MODELS

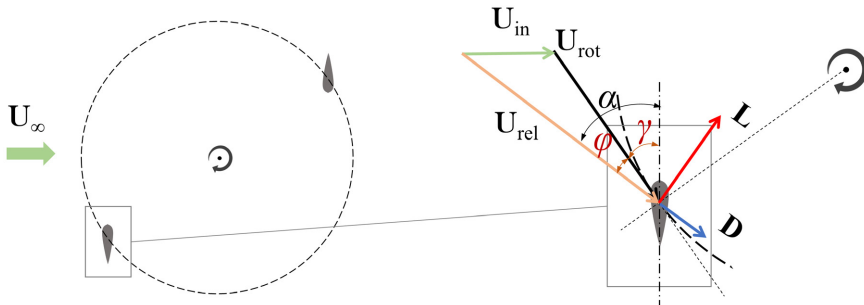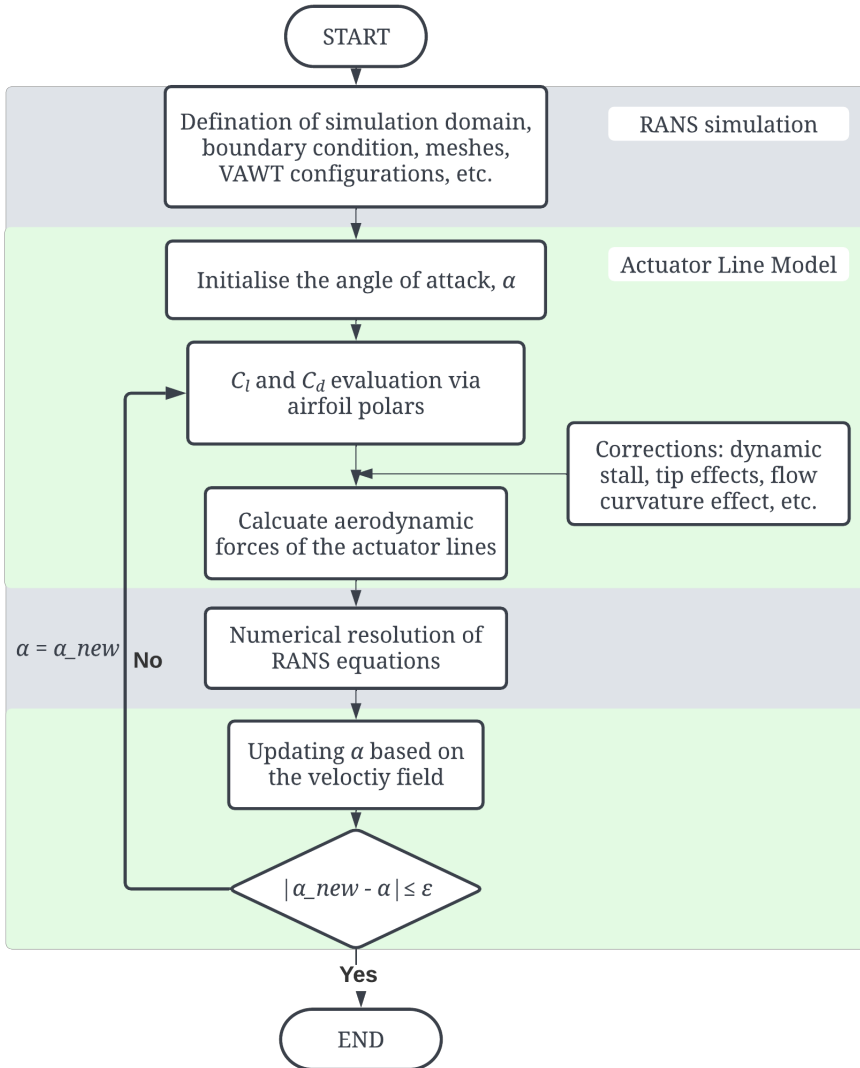Blades of VAWTs encounter various unsteady flow conditions such as time-varying AoA due to rotation, dynamic pitching of the blades, local variations of the inflow velocity, etc. These phenomena lead to dynamic responses on the blade loading, sometimes even triggering dynamic stall (DS). The latter usually occurs under a low tip speed ratio.

Compared to static stalls, airfoils under dynamic stall feature periodic vortex shedding; The shed vortex sweeps over the chord and induces a pressure wave along the airfoil surface. Such variation in the pressure field incurs significant increases in airfoil lift at stall angle. As a consequence, airfoils with periodical motions into dynamic stall exhibit considerable hysteresis in force coefficients (Leishman and Beddoes, 1989; Corke and Thomas, 2015, see visualisations in figure 3.7). The hysteresis, however, is not revealed in a static airfoil polar diagram, and getting dynamic polar for numerous flow conditions is unrealistic. Hence, corrections for dynamic stalls are necessary for approaches based on static airfoil polar, no exception for the ALM for VAWTs.

Early engineering dynamic stall models (DSM), or unsteady flow models, were mostly proposed for helicopter aerodynamics (e.g., Gormont, 1973; Leishman and Beddoes, 1989; McAlister et al., 1984). Therefore, these semi-empirical models are developed specifically for the high wind speed and compressible flow scenario. Among those models, the Leishman-Beddoes model (LBM) is the most popular, due to its incorporation of governing equations reflecting on the physical mechanisms. The model comprises four modules, on account of attached flow, trailing edge separation, leading-edge separation and vortex lift, respectively.

Later, DSMs specially tailored for horizontal axis wind turbines have been introduced, e.g., the model of Snel H., Houwink R., and Bosschers J. (1994), the Risø model (Hansen et al., 2004), and the model of Larsen et al. (2007), to name a few. Except for Snel's model, the other models are based on or similar to the LBM, with simplifications on treatments of compressibility and leading edge separation regime. Sheng et al. (2008) proposed a modified DSM for low Mach numbers based on the LBM, making it more practical for wind turbine aerodynamics. Dyachuk et al. (2014) compared the original LBM and its variants (including Sheng's model and the third generation of LBM) with the Gormont model. They concluded that Sheng's model with calibrated empirical constants suits the operating conditions of VAWT the most and shows better agreement with the experiments. Therefore, Bachant et al. (2016) implemented the Sheng's model in the *turbinesFoam* library, and it has been validated in their follow-up work (Mendoza et al., 2016).

ADDED MASS EFFECT

Added mass or virtual mass effect on VAWTs is attributed to the acceleration of the blade motion. The latter accelerates surrounding air causing extra inertia. It has been implicitly modelled by LBM-based DSM, as part of the non-circulatory or so-called impulsive load. In the *turbinesFoam* library, a correction model for the added mass effect is implemented based on the work of Strickland et al. (1979).

TIP LOSS CORRECTION

Loaded finite blades are subject to tip losses due to the induced tip vortices. The tip vortices cause losses for two reasons. First, the wing-tip vortices contain a large amount

3
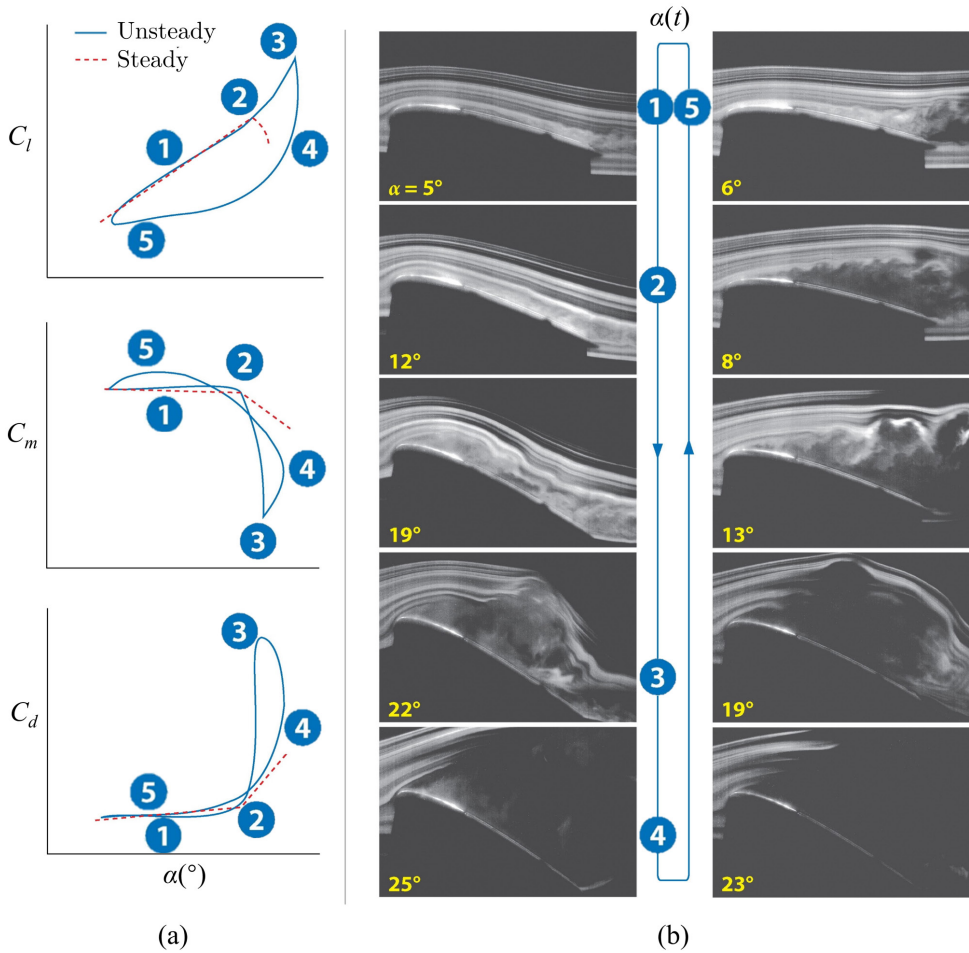
Figure 3.7: Visual presentation of a pitching airfoil undergoing deep dynamic stall. Image from Corke and Thomas (2015). (a) Comparison of static polar and hysteresis loops of the aerodynamic loads, with characteristic stages marked by numbers. (b) Corresponding flow visualisations for the dynamic stall events marked in (a). ① Start of the pitch-up portion of the cycle, where attached flow takes the lead. ② Airfoil exceeds static stall angle, dynamic stall vortex appears. ③ Fully developed DS vortex convects over the airfoil, inducing substantial variation in aerodynamic loading and moment. ④ DS vortex convects off the airfoil and the flow is fully separated. ⑤ Flow begins to reattach.
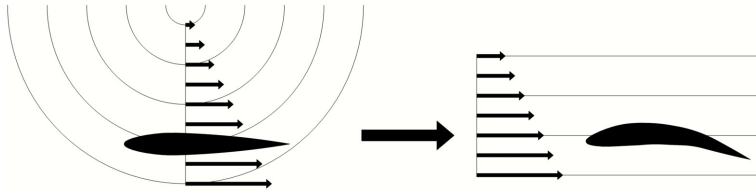
Figure 3.8: Schematic of the flow curvature effect and conformal transformation (virtual airfoil) technique. Graphic from Van Der Horst et al. (2016).

3

of kinetic energy from the incoming wind, which means a loss in the available kinetic energy for the wind turbine. Second, the vortices induce drag and decrease the blade's effective angle of attack, which in turn causes a loss in rotor performance. Glauert (1935) developed a tip-loss model for propellers, which is also prevailing for HAWTs. To account for the tip-loss effect of VAWTs, a more general end-effect model based on Prandtl's lifting line theory (Anderson Jr, 1985) has been implemented in *turbinesFoam*.

FLOW CURVATURE EFFECT
The orbital motion of VAWT blades results in unique radial distances from the rotation axis to every point on chords of blade sections, and therefore causes different inflow velocities and angles of attack along the chord; The latter is the so-called flow curvature effect. A concept of virtual airfoil was introduced by Migliore et al. (1980) to describe such effect, and several models based on the concept have been reviewed in the literature (Van Der Horst et al., 2016). It has been confirmed that for VAWTs with low solidity (less than 0.2), all those models perform similarly. In *turbinesFoam*, a flow curvature model derived in Goude (2012) is available.

3.3.4. BLADE RESOLVED APPROACHES
Blade resolved approaches take the geometry information of blades while solving the flow fields. Therefore, they are adopted when some geometry-related phenomena (e.g., flow curvature, vortex-blade interaction, laminar-turbulent transition on blade surfaces, etc.) must be resolved in detail. Such models can be found in the literature integrated with different flow field solvers, depending on the specific aim, the required fidelity and complexity. For instance, a panel method with vortex cores placed along the outline of a blade airfoil is probably the simplest blade resolved approach; It can resolve the flow curvature effect of VAWTs (De Tavernier, 2021). Blade resolved approaches are more frequently seen with CFD simulations. There are generally two ways of dealing with the blade geometry in CFD simulations: a) generating a surface mesh along the solid wall (i.e., blade surfaces in this case), and applying wall functions or solving the governing equations directly at the boundaries (e.g., Dessoky et al., 2019; Ghasemian et al., 2017). b) specifying an external forcing function to mimic the enforced boundary; in this way, a fixed Cartesian mesh can be used for solving the flow field wherein a VAWT is placed(Balaras, 2004; Posa et al., 2016). Figure 3.9 shows the blade resolved simulation results based on LES from the work of Posa et al. (2016); with this method the near wall vorticity structures are resolved in great detail.
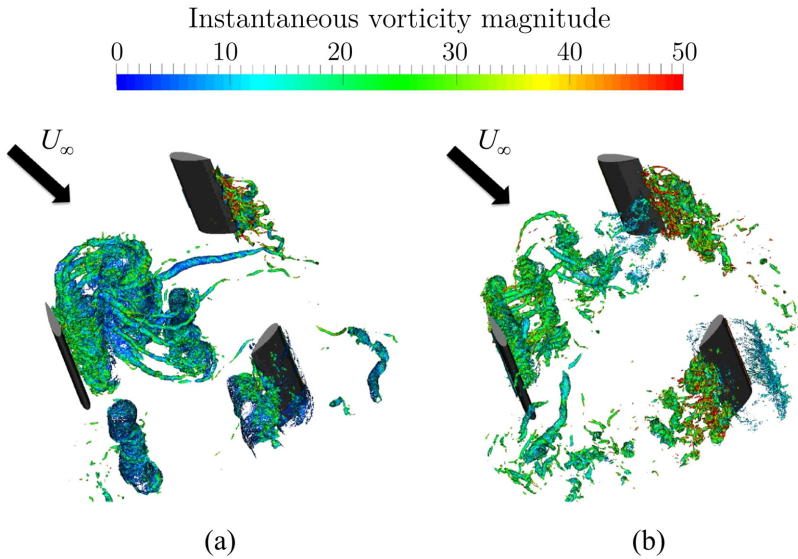
Figure 3.9: Blade resolved simulation results based on LES. Iso-surfaces of pressure coloured by vorticity magnitude. (a) TSR = 1.35; (b) TSR = 2.21. Graphic adapted from Posa et al. (2016).

3.4. WAKE SIMULATIONS

3.4.1. CFD SIMULATIONS

Experimental studies are usually confined to a relatively low Reynolds number, which is inconsistent with the up-scaled scenario on offshore. Although a few field measurements conducted in high Reynolds numbers are seen in the literature (Dabiri, 2011; Kinzel et al., 2013; Wei et al., 2021), such investigations are rare due to the high capital cost, uncertainties in flow conditions, and technical difficulties (Peng et al., 2021). Therefore, CFD simulations have been employed to fill the gap.

CFD simulations solving Navier-Stokes (NS) equations are practical tools accounting for viscous effect, compressibility, and the turbulent nature of fluids. Depending on the turbulent scales resolved, CFD simulations can be generally classified as direct numerical simulation (DNS), large eddy simulation (LES), and Reynolds averaged Navier-Stokes (RANS) simulation. DNS resolves turbulence in all temporal and spatial scales in the flows, providing the highest fidelity yet demanding the most computational resources. Due to the high Reynolds numbers of modern VAWTs and their vigorous wake covering a wide range of turbulence scales, the computational cost of DNS investigations on VAWT wakes is not affordable, and therefore they have not been seen in the literature.

LES resolves large-scale vortices using a subgrid-scale (SGS) model to filter and parameterise vortices with small spatial scales. With the fast development of computers, LES is becoming popular for inspecting large vortices associated with the macro-behavioural phenomena in VAWT wakes. Combining with different rotor representing techniques as discussed in section 3.3, LES with different fidelities have been introduced, e.g., in the work of Posa et al. (2016) (figure 3.9); Shamsoddin and Porté-Age (2016) and

Massie et al. (2019).

For incompressible, Newton fluids, the Navier-Stokes momentum equation is expressed as

$$\frac{\partial u_i}{\partial t} + u_j \frac{\partial u_i}{\partial x_j} = -\frac{1}{\rho}\frac{\partial \rho}{\partial x_i} + \nu \frac{\partial^2 \tilde{u}_i}{\partial x_j \partial x_j}. \tag{3.6}$$

indices i and j denote different flow directions under Einstein notations; u is velocity, ρ is fluid density and ν is the kinematic viscosity.

RANS simulation solves NS equations under Reynolds decomposition (Tennekes and Lumley, 1972). Instantaneous velocities are decomposed as time-averaged and fluctuation velocities:

$$u = \bar{u} + u', \tag{3.7}$$

where the overbar is for time-average while the prime sign marks fluctuation term. The fluctuations become zero upon applying the time average to the flow, and the decomposition of Navier-Stokes momentum equation yields the Reynolds momentum equation:

$$\underbrace{\bar{u}_j \frac{\partial \bar{u}_i}{\partial x_j}}_{\text{advection}} = \frac{1}{\rho}\frac{\partial}{\partial x_j}(\underbrace{-\bar{p}\delta_{ij}}_{\text{pressure}} + \underbrace{2\mu\bar{S}_{ij}}_{\text{viscous}} + \underbrace{\tau_{ij}}_{\text{Reynolds stress}}), \tag{3.8}$$

where δ_{ij} is the Kronecker delta and τ_{ij} is the Reynolds stress tensor. The equation is composed by the advection, pressure, viscous and Reynolds stress terms, and the role of these terms in the momentum recovery of the VAWT wake are discussed in chapter 6. The idea of Reynolds decomposition is to average out the fluctuations; However, there still exist fluctuation terms in the Reynolds stress tensor:

$$\tau_{ij} = -\rho \overline{u_i' u_j'}, \tag{3.9}$$

To numerically solve the RANS equations, the Reynolds stress has to be modelled using the mean velocities. This is known as the closure problem, and turbulence models are the bridges connecting the mean velocity and the fluctuations. To date, most of the turbulence models are based on the eddy viscosity hypothesis first proposed by Boussinesq (1877), where the Reynolds stress is given by:

$$\tau_{ij} = 2\mu_t \bar{S}_{ij} - \frac{2}{3}\rho k \delta_{ij}. \tag{3.10}$$

μ_t is the eddy viscosity, $\bar{S}_{ij}$ stands for the mean rate of strain tensor and k is the turbulent kinetic energy being $\frac{1}{2}\overline{v_i' v_i'}$. Turbulence models based on the Boussinesq hypothesis can be generally classified according to the number of equations used:

- Zero equation (algebraic) models, Prandtl's mixing-length model, etc.

- One equation models, e.g., the Spalart-Allmaras (SA) model (Spalart and Allmaras, 1992), etc.

- Two equation models, e.g., k-ϵ, k-ω, and k-ω SST models (Nallasamy, 1987), etc.
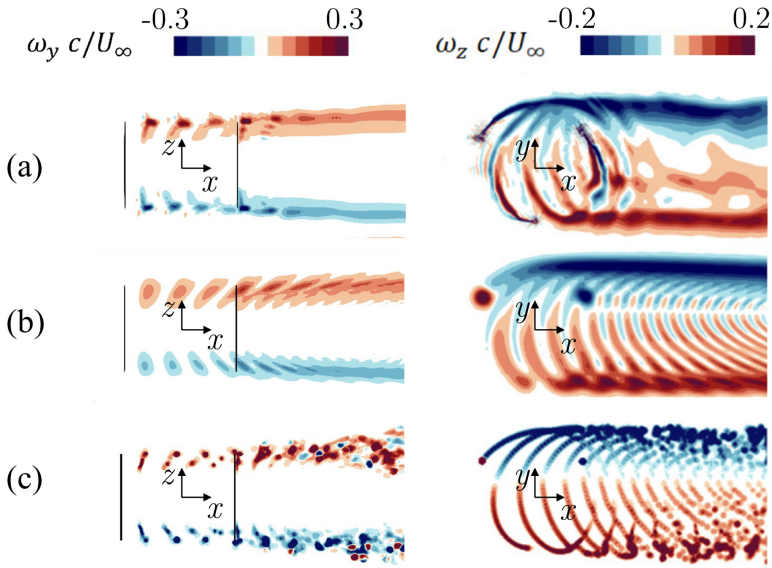
Figure 3.10: Comparison of different numerical methods for VAWT wakes. Left column: lateral vorticity contours; Right: vertical vorticity contours. Row (a): RANS with blade resolved approach. (b) LES with ALM. (c): Free vortex model. Graphic reproduced from Aihara et al. (2022).

In addition, there have been models using more equations in the literature, and they generally achieve higher fidelity while consuming more computing resources. A brief comparison of some popular turbulence models is listed in table 3.1.

RANS simulations can provide a trust-worthy mean flow while their computational cost is dramatically lower than DNS and LES simulations, and therefore they are widely adopted for investigating the wake properties of VAWTs. They can also be combined with rotor simplifications discussed in section 3.3 (e.g., Villeneuve et al., 2021; Bachant et al., 2016; De Tavernier et al., 2020). It is noted that RANS and LES can be combined in blade resolved simulations, in a way that RANS is applied at the near wall region due to its cost efficiency, and LES is adopted for the flow away from the wall to obtain a more detailed vortex and turbulence fields. Such hybrid models including Detached-Eddy simulation (DES) and Delayed Detached-Eddy simulation (DDES), have been applied for VAWT investigations (e.g. Liu et al., 2019; Boudreau and Dumas, 2017).

3.4.2. VORTEX MODELS
In the vortex models for rotor aerodynamics, the blades are usually represented with lifting lines or lifting surfaces, creating tip vortices and shed vortices. One can compute the inducted flow field by those vortices based on the Biot-Savart law.

The initial idea of the lifting line was proposed by Ludwig Prandtl et al. during the period 1911-1918 (Anderson Jr, 1985), based on the Kutta-Joukowski theorem, which states that a bound vortex will experience a force $L' = \rho_\infty U_\infty \Gamma$ (Γ is the bound circulation) such that a loaded blade section can be represented by a bound vortex with a certain strength.

Table 3.1: Comparison of turbulence models.

Models	k-ϵ	k-ω	k-ω SST
Based on	transport equation of k and ϵ	transport equation of k and ω	combination of k-ϵ and k-ω model
Advantages	• robust • accounting for eddy viscosity transport • suitable for fully turbulent flow	• accounting for transports of eddy viscosity • needing no empirical function for viscosity dumping effect • more accurate near wall treatment	• accounting for transports of eddy viscosity and turbulent shear stress • needing no empirical function for viscosity dumping effect • more accurate near wall treatment • more accurate predictions regarding the flow seperations under adverse pressure gradients
Disadvantages	• empirical functions without universal validity • inaccuracy for complex flows involving severe pressure gradient and flow separation	• requires fine mesh resolving the near wall region • high computational cost • v_t and c_f are affected by inflow conditions	• requires fine mesh resolving the near wall region • high computational cost • less suitable for free shear flows

3

And therefore, the lifting line method has to adopt a two-dimensional airfoil polar for load quantification. It is noted that vortex models are under the potential flow assumption, and they follow Helmholtz's and Kelvin's theorems. Due to Helmholtz's theorem, besides a bound vortex placed on the blade, the latter will generate trailing vortices to form a "closed path". According to Kelvin's theorem, the time rate of change of circulation in a closed material (always composed of the same fluid parcels) must be zero; And therefore, shed vortices are generated in the wake to compensate for the strength variations of the bound vortex incurred by the varying blade loading. The first example of the lifting-line-based vortex model for VAWTs might be the work of Strickland et al. (1979).

Additionally, there have been numerous vortex models using other ways of representing VAWT blades, based on the panel method as mentioned in section 3.3.4. For example, using sources and doubles in Shi et al. (2014) or sources and vorticity distributions in Tescione et al. (2016).

II

WAKE AERODYNAMICS: ACTUATOR DISCS VS. VAWTS

4

WAKE SCALING OF ACTUATOR DISCS IN DIFFERENT ASPECT RATIOS

The wake recovery from planar porous actuators that surrogate the effect of wind turbines is investigated, focusing on rectangular shapes for VAWTs. We proposed an effective mixing diameter D^* to scale the streamwise momentum recovery for actuators of arbitrary shape. The length-scale D^* is given by the ratio between frontal area and disc perimeter characterising the wake-freestream interface, whereby the momentum loss and the turbulent exchange of momentum take place. Wind tunnel experiments of planar actuators from porous plates are presented. The three-dimensional development of the wake is surveyed up to six widths/diameters downstream of the actuators making use of robotic particle image velocimetry with helium-filled soap bubbles as flow tracers. The recovery rate analysis is performed using D^* for wake normalisation. The scaled wake data agrees well among actuators in different shapes. And it is significantly improved for rectangular actuators compared with existing scaling lengths. The flow behaviour is confirmed with numerical simulations of VAWT wakes with different aspect ratios, indicating the validity of this scaling concept for wind turbine wake modelling.

4.1. INTRODUCTION

POROUS plates have become prevailing representatives of horizontal axis wind turbines to efficiently simulate wind farm behaviour by experiments (Bossuyt et al., 2017). In this context, a porous plate is often referred to as an actuator disc; The latter has been introduced in chapter 3. As a result, investigations of circular porous plate wake can be found extensively in the literature (Aubrun et al., 2013; Howland et al., 2016). In particular, Lignarolo et al. (2016) shows that these devices reproduce key aerodynamic parameters such as velocity, pressure, and enthalpy fields, provided that the thrust coefficient is matched with that of wind turbines. Very recently, Helvig et al. (2021) compared the near wake of porous plates against a lab-scale HAWT model. They concluded that a porous plate model mimics satisfactorily the mean flow properties, albeit the instantaneous pattern of unsteady vortices is substantially different.

The flow development across a porous plate is characterised by its porosity (Castro, 1971; Steiros and Hultmark, 2018) and shape (Craig et al., 2017; Fail et al., 1957; Medici and Alfredsson, 2005). The former generally determines the drag coefficient, while the latter leads to a distinct flow pattern in its wake. Compared with solid plates, the flow at high porosity features less vortex shedding effect and the wake width is smaller and well approximated by the plate cross-section, so as HAWTs (Lignarolo et al., 2016). These features make porous plates a suitable and significantly simpler surrogate for wind turbines.

The idea to replace a wind turbine with a porous plate stems from the actuator disc theory that forms the basis of most analytical models developed for wind turbine wakes (Stevens and Meneveau, 2017), where the turbine is treated as a stationary, permeable disc. Combined with the assumed self-similar behaviour of HAWT wakes in the far field, the velocity field can be predicted with relatively simple kinematic models (Göçmen et al., 2016; Porté-Agel et al., 2020), despite the complexity of the aerodynamic phenomena involved in the spatial development of the wake. The models from Jensen (1983) and Larsen (1988) are the most popular among the early works, followed by more recent advancements from Bastankhah and Porté-Agel (2014)(BPA).

These models are formulated under different scaling laws, which describe the relation between the wake width δ, the centreline velocity deficit Δu_c and downstream position x (figure 4.1-top). The Jensen model assumes that δ expands linearly with x: $\delta(x)/D \propto x/D$, the normalised streamwise velocity deficit is expressed in terms of an empirical function of the downstream position: $\Delta u_c/U_\infty \propto (x/D)^{-2}$, where D is the wind turbine rotor diameter and U_∞ is the free stream velocity. In contrast, the Larsen model follows the scaling law for a fully developed turbulent wake (Tennekes and Lumley, 1972): $\delta(x)/\theta \propto (x/\theta)^{1/3}$, $\Delta u_c(x)/U_\infty \propto (x/\theta)^{-2/3}$, where θ is the momentum thickness, and is assumed to be equal to the rotor diameter D in the wake model. The BPA model assumes a linear wake expansion as that of the Jensen model: $\delta(x)/D \propto x/D$, while δ is described as a function of the standard deviation σ of the momentum deficit distribution, assumed to be Gaussian.

Despite the different hypotheses adopted, all the above models employ a proper streamwise distance normalisation to determine the velocity deficit evolution. As the circular actuator disc wake is deemed as circular-symmetric, the diameter D naturally becomes the normalisation length, connecting the wake deficit development and the

actuator dimension.
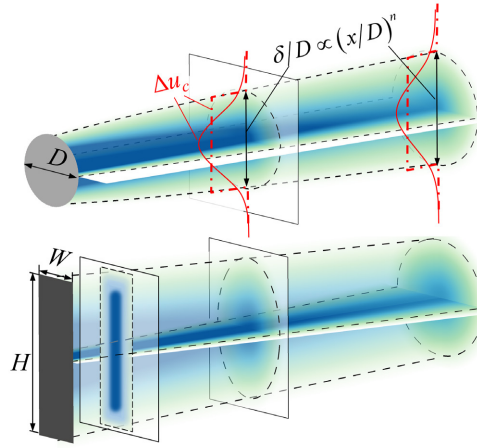
Figure 4.1: Top: schematic representation of the wake of a circular actuator disc modelled with kinematic models, where the velocity distribution can be uniform (Jensen, red dash-dot lines) or continuous (BPA and Larsen, red solid lines). The exponent n denotes different scaling laws adopted($n = 1$: Jensen and BPA, $n = 1/3$: Larsen); Bottom: transition to circular wake of a rectangular plate (Fail et al., 1957). Colour-coded continuous momentum deficit (blue for high values, green for vanishing deficit) and plate type (light grey for permeable plate, dark grey for solid plate).

However, it is less trivial to define the scaling length in the wake of a non-circular-symmetric actuator disc, specifically, a rectangular actuator with a variable aspect ratio (AR), which is the surrogate of vertical axis wind turbine (Craig et al., 2017). In particular, no research is found in the literature comparing the momentum recoveries in the wakes of rectangular and circular porous plates. However, Fail et al. (1957) measured the wake of a solid circular plate and rectangular ones with different ARs, shedding light on the different flow patterns in their wakes (figure 4.1-bottom). As illustrated, a transition from a rectangular to an elliptical and finally to a circular wake is observed. Length scales such as the height (H), the width (W), and the diameter after transition are involved in the wake shape characterisation, indicating that a proper scaling length should be given based on multiple feature lengths to adapt to such transition.

A consistent wake scaling length for rectangular actuators with different ARs is crucial for the formulation of kinematic wake models of VAWTs. Currently, a few rectangular-actuator-based kinematic wake models for VAWTs have been introduced as extrapolations of HAWT wake models (e.g., Abkar, 2018; Abkar and Dabiri, 2017; Lam and Peng, 2017). In these models, the turbine rotor height (H) and diameter (D, corresponding to W of rectangular actuators) are both employed for streamwise distance normalisation, under the assumption that an elliptical wake is imparted by the actuator, which preserves its shape and merely expands by turbulent diffusion. Such assumption preludes an inconsistency in the scaling of a rectangular actuator's wake, because the latter transitions from an elliptical to a circular shape.

A survey in terms of wake scaling lengths for bluff-body/wind turbine with various
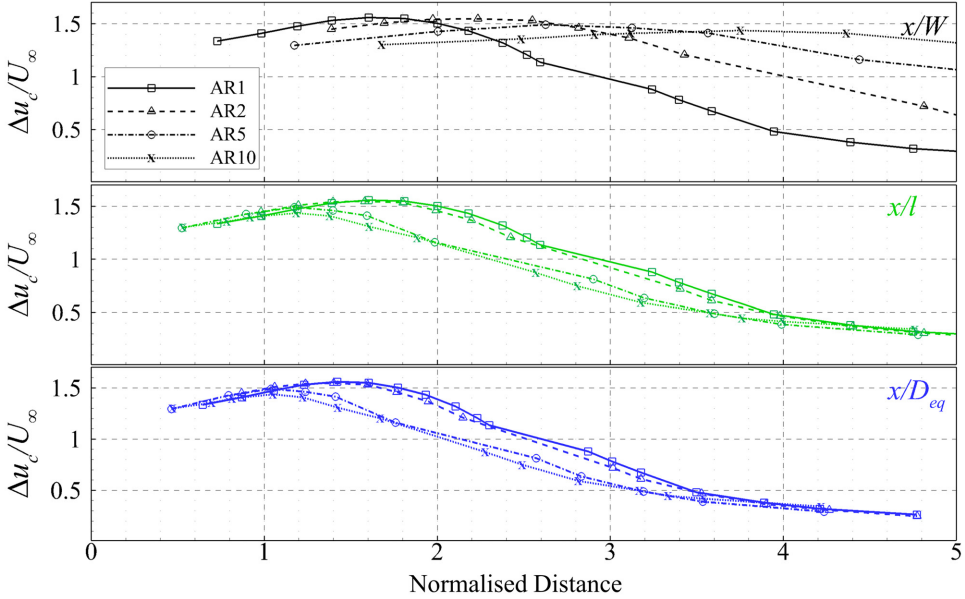
Figure 4.2: Comparison of normalisation lengths (W, l, D_{eq}) for centreline velocity deficits along x-direction. Wake data of rectangular solid plates with AR = {1, 2, 5, 10} are retrieved from Fail et al. (1957).

frontal areas is discussed here. a) The width W (or diameter following the convention of wind turbine wake) is often used in the horizontal and vertical axis wind turbine wake normalisation (Göçmen et al., 2016; Porté-Agel et al., 2020), however, it leads to inconsistency when applied to elongated wake. b) Apart from the width, a characteristic length $l = A^{1/2}$ is widely documented in the literature for the wake normalisation of solid plates with different geometries, including circular, rectangular disc with various ARs, etc. (Fail et al., 1957; Nedić et al., 2015). Here A denotes the frontal area, and l essentially corresponds to the side length of an equivalent square. c) Very recently, Shamsoddin and Porté-Agel (2020) proposed an equivalent diameter $D_{eq} = (4A/\pi)^{1/2}$ for VAWT wake normalisation, based on the assumption that the wake of a VAWT with rectangular frontal area eventually (i.e. at some distance downstream) develops into a circular shape in the far wake (figure 4.1-bottom). D_{eq} is essentially an extrapolation of the momentum thickness concept for planar wakes, where the VAWT's momentum deficit is redistributed to an equivalent circular disc. Their results indicate that the momentum recovery normalised by D_{eq} exhibits a limited degree of match for large values of AR, within the typical inter-turbine separation distances of wind farms (e.g. from 3 to 8 diameters, Stevens and Meneveau, 2017). Due to the same reason, W and l present inconsistencies as scaling lengths. Figure 4.2 depicts a comparison among W, l, and D_{eq} normalisations for rectangular solid plates with various ARs. The centreline velocity deficits are retrieved from Fail et al. (1957). Clearly, although l, and D_{eq} performs better for moderate ARs, large discrepancies show up for AR = {5, 10} at $x/l < 4.5$ and $x/D_{eq} < 4$.

It is argued here that an additional physical constraint needs to be accounted for, which has not been considered in the above works: namely, the region of active mixing for the wake recovery of non-circular-symmetric actuators, which can largely differ from that of the equivalent circular disc. Therefore, the actuator perimeter by the wake, similar to the concept of "wetted perimeter" for flow in ducts of arbitrary cross-sectional shape, is expected to play a role in the rate of kinetic energy exchange and ultimately affect the momentum recovery. In the present work, this concept is first elaborated theoretically and supported by experiments and simulations.

The chapter deals with frontal shape effects on the wake recovery rate, specifically for planar actuator discs with a variable AR adopted in existing kinematic wake models. The scaling of the resulting wake is discussed and an effective mixing length D^* for streamwise normalisation is proposed accounting for the shape effects supported by a theoretical derivation of the concept.

The experimental data is gathered with plates of uniform porosity as actuator discs. Actuators with circular, square and rectangular shapes (AR = 3) are examined. Given the three-dimensional nature of the flow field, the velocity field measurements are conducted with the robotic volumetric particle image velocimetry (PIV) measurement technique Jux et al. (2018). The spatial distribution of the velocity enables the analysis of momentum deficit in the turbulent shear layer and wake recovery. The application scenario of D^* is extended to the wake of a VAWT in a set of numerical simulations based on the URANS equation and the actuator line model. The latter extends the range of AR up to 10 in the attempt to illustrate the asymptotic conditions for wake scaling.

4.2. DERIVATION OF THE EFFECTIVE MIXING DIAMETER, D^*

The momentum recovery and its relation with the shape of the actuator surface are modelled with a control volume (CV) approach. The CV is placed behind the actuator surface; Its cross-section is chosen with the same shape and frontal area as the actuator (figure 4.3-left), the latter has a frontal area A and perimeter P. The definition of the CV is valid at locations where the shape effect is dominant and the expansion of the wake is less notable, usually it is in the near wake yet far enough away from the actuator. The CV also provides a straightforward estimation of the momentum past a hypothetical turbine, and follows the concept widely reported in the literature (Bachant and Wosnik, 2015; Boudreau and Dumas, 2017; Mycek et al., 2014).

For sake of simplicity, the CV is placed sufficiently far from the actuator surface, such that the effect of the static pressure gradient in the equation of momentum conservation can be neglected. A top-hat velocity distribution along cross-sections is assumed, with streamwise velocity equal to U_∞ outside of the CV and to $U(x)$ inside the CV. The upper case letter U denotes uniform streamwise velocity over a surface. Considering a portion of the CV with an infinitesimal streamwise length dx, the flow velocity at the upstream face of the CV is indicated with U, whereas it increases to $U+\mathrm{d}U$ at the downstream face. A cross flow velocity V, solely determined by the streamwise distance x, is presented to guarantee mass conservation (figure 4.3-left):

$$(U + \mathrm{d}U)A - UA - VP\,\mathrm{d}x = 0, \tag{4.1}$$
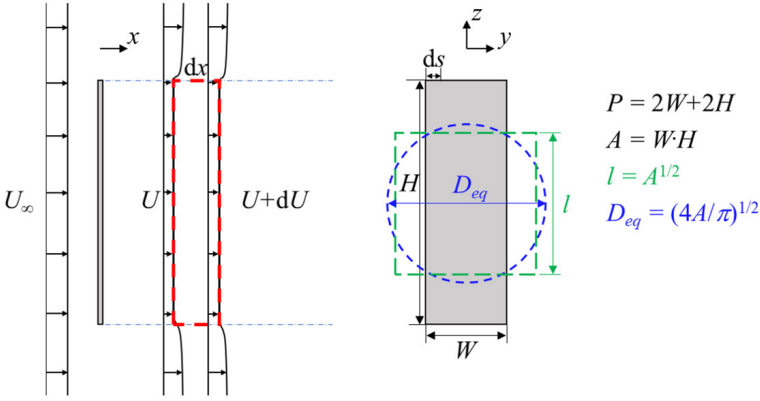
Figure 4.3: Left: sketch of the actuator (grey rectangle) and relative control volume (red dashed rectangle) to formulate the wake momentum development; Right: front view of a rectangular actuator disc, with indicated perimeter P and area A, and illustration of equivalent shapes corresponding to existing normalisation methods (W, l, D_{eq}).

where the sign convention is that a vector pointing out of the CV is positive. And therefore,

$$V = \frac{A}{P} \frac{dU}{dx}. \tag{4.2}$$

The frontal view of the present CV is shown in figure 4.3-right, which is a rectangular actuator (grey rectangle) with a cross-section area $A = WH$. As a comparison, other existing methods to simplify the actuator wake and obtain a normalisation length scale are also illustrated in figure 4.3-right, consisting of a) an equivalent circular area of diameter $D_{eq} = (4A/\pi)^{1/2}$ (represented in blue); b) the square-equivalent actuator, represented in green, with length scale $l = A^{1/2}$. We draw here the attention to the perimeter of the actuator $P = 2W + 2H$ and that of the area-equivalent shapes, namely $P_{eq} = \pi l$ and $P_{sq} = 4l$ for the circular- and square-equivalent cases respectively. In both cases, the latter simplifications underestimate the actual perimeter of the rectangular actuator and in turn that of its wake.

The momentum deficit caused by the actuator is assumed to be uniform over the cross-section, and the shear stress is uniformly distributed along the perimeter of the cross-section of the CV; The latter is assumed to be equal to the actuator perimeter. The recovery of the streamwise velocity (viz. momentum recovery) is treated as a sole function of the streamwise distance past the actuator. The aim of the present analysis is not only to account for the cross-sectional momentum deficit that occurs within the frontal area, but also introduce the momentum transport across the wake interface as the main driver for the process of momentum recovery. By this approach, a normalisation length can be obtained whereby the streamwise development of the momentum in the wake becomes independent of the actuator shape.

Consider the streamwise momentum balance in the CV:

$$\rho(U + dU)^2 A - \rho U^2 A - \rho U_P V P \, dx = \tau P \, dx, \tag{4.3}$$

where U_P is the streamwise velocity along the lateral interface of the free-stream and the wake bounded by the CV. It is assumed that $U < U_P < U_\infty$. The simplifications leading to the formulation in eq. (4.3) are of time-averaged analysis, where time derivatives are neglected. Moreover, body forces are absent and the pressure term is negligible. The shear stress τ is assumed to be uniformly distributed along the perimeter, yet evolving along the developing shear layer; As a result, τ solely depends upon the x-coordinate. Considering the assumptions, and combining with eq. (4.2), eq. (4.3) simplifies to:

$$2\rho U \, \mathrm{d}U A - \rho U_P A \, \mathrm{d}U = \tau P \, \mathrm{d}x, \tag{4.4}$$

where $(\mathrm{d}U)^2$ is neglected compared with $2U\mathrm{d}U$. Thus, the rearranged expression

$$\frac{\mathrm{d}U}{\mathrm{d}x} = \frac{1}{\rho} \frac{P}{A} \frac{\tau}{2U - U_P} \tag{4.5}$$

indicates that the momentum recovery rate depends upon the ratio between cross-sectional area A and the wake perimeter P, in analogy with the concepts of wetted perimeter leading to the hydraulic diameter as originally introduced by Darcy (1857). The effective mixing diameter D^* is defined in the present context that normalises the averaged streamwise velocity recovery:

$$D^* = \frac{4A}{P}. \tag{4.6}$$

Combining eqs. 4.5 and 4.6 one obtains:

$$\frac{\mathrm{d}U}{\mathrm{d}(x/D^*)} = \frac{4}{\rho} \frac{\tau}{2U - U_P}(x) \tag{4.7}$$

Eq. (4.7) indicates that, for an actuator with an arbitrary shape, the wake recovery rate along the streamwise distance normalised by D^* becomes shape independent. Specifically, for a highly elongated actuator, where $H >> W$, $D^* \approx 2W$; for actuators with square cross-section ($H = W$), then $D^* = H = W$.

To verify the adequacy of the effective mixing diameter D^* as a generic scaling length for actuators of different shapes, and assess until where the D^* works or not, a set of wake measurements from circular and rectangular actuator discs are carried out in this work. The experimental data is used to compare the use of D^* with the traditional choices of length scale such as width W and a characteristic length l alongside the recently introduced D_{eq}.

4.3. EXPERIMENTAL SET-UP

4.3.1. WIND TUNNEL AND MODELS

The experiments are conducted in the W-Tunnel of the TU Delft Aerospace Engineering Laboratories, a low-speed open-jet wind tunnel with exit cross-section of 0.6×0.6 m^2. The measurements are carried out at free stream velocity $U_\infty = 5 \, \mathrm{m\,s^{-1}}$ with a turbulence level rated to approximately 1%. The ground is not presented in the measurement.

Circular, square and rectangular porous plates are chosen to realise the actuator discs from perforated metal plates of 2 mm thickness, with uniformly distributed square holes

(figure 4.4). The apertures in the plate are 8 mm wide and the pitch is 12 mm, yielding a porosity of 44%. At the chosen free stream velocity, the Reynolds number based on the model width attains 4×10^4 for circular and square plates, and 2×10^4 for the rectangular plate. The plate is installed at the wind tunnel exit and held by a circular rod of 10 mm diameter (figure 4.5). The properties of the actuators with different geometries are listed in table 4.1.
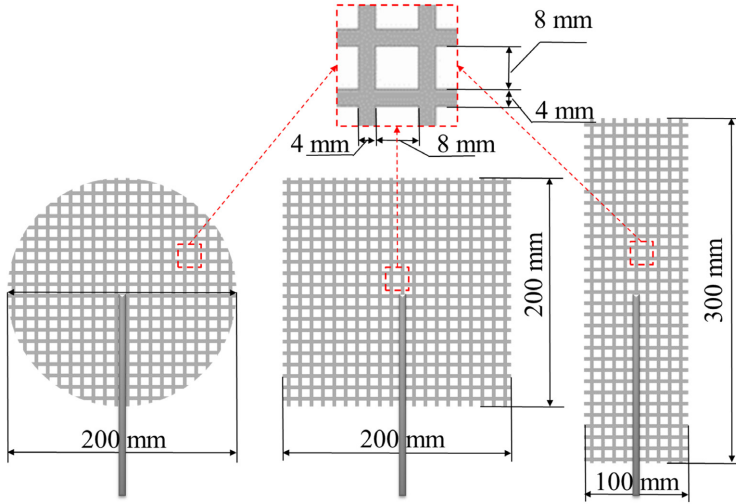
Figure 4.4: Geometrical details of circular, square and rectangular porous plates.

Table 4.1: Geometrical parameters and equivalent length-scales of actuator discs.

Geometry	Area(cm^2)	Perimeter(cm)	$W(D)$ (cm)	D_{eq}(cm)	D^* (cm)
Circle	314.2	62.8	20.0	20.0	20.0
Square	400.0	80.0	20.0	22.6	20.0
Rectangle	300.0	80.0	10.0	19.5	15.0

4.3.2. MEASUREMENT SYSTEMS AND DATA PROCESSING

The aerodynamic drag produced by the plate and its support is measured by a load sensor based on strain gauges (KYOWA, type KFG-5-120-C1-23) applied to an aluminium strut. The strain on the strut is converted into a voltage signal.

The velocity field before and behind the actuator ($-1 < x/W < 6$) is measured by PIV. The overall measurement domain is covered using a robotic PIV system (Jux et al., 2018), based on the principle of coaxial volumetric velocimetry (Schneiders et al., 2018). The measurement system features four CMOS cameras installed in a compact tomographic arrangement (figure 4.5-left). Illumination is provided by a Quantronix $Darwin-Duo$ laser (527 nm wavelength, 2×25 mJ pulse energy at 1 kHz). The light is transported

through an optical fibre and propagates conically from the exit placed between the cameras. The resulting region of measurement has approximately 400×400 mm^2 cross-section at a 400 mm distance from the CVV head. Synchronisation of illumination and imaging is made with a LaVision programmable timing unit (PTU) controlled from a PC with the DaVis 10 software. Helium-filled soap bubbles (HFSB) are used as flow tracers. The HFSB have a mean diameter of 0.4 mm and the neutrally buoyant condition is met within approximately 10% (Faleiros et al., 2019). HFSB are released in the wind tunnel settling chamber at a rate of approximately 5×10^6 bubbles/s yielding a concentration of 2 bubbles/cm^3.
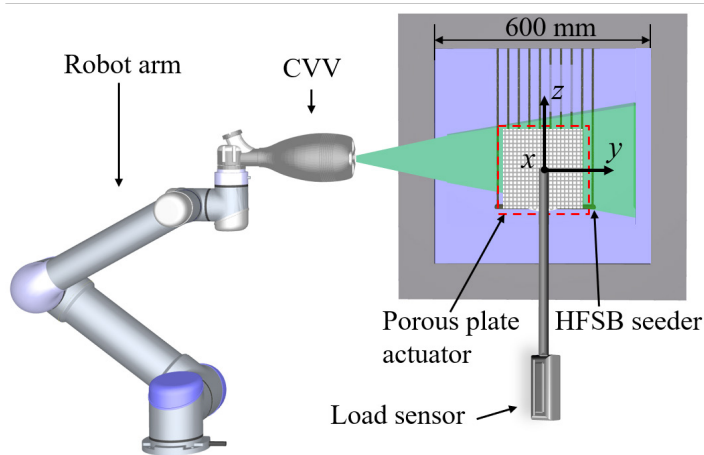
Figure 4.5: Layout of experiments: wind tunnel and square actuator at its exit. Robotic arm and coaxial volumetric velocimeter, with an indication of measurement region.

The measurement views in the horizontal (x-y) and vertical (y-z) planes that compose the domain of interest are shown in figure 4.6. The robotic system points at 16 to 24 positions (instantaneous field of view, IFOV) for the circular/square and rectangular actuators, respectively. At each position, 5000 images are recorded at a rate of 789 Hz (measurement time of 6.3 s). The motion of the CVV system by the robotic arm is controlled using the RoboDK software. Image acquisition and storage require approximately one minute for each measurement position.

Approximately 1200 particle tracks are captured in each recording. The raw images are pre-processed by a temporal high pass filter (see Sciacchitano and Scarano, 2014) that eliminates unwanted background reflections. A sample of raw and pre-processed images is given in figure 4.7. The tracer velocity is obtained via Lagrangian Particle Tracking using the Shake-the-Box algorithm (Schanz et al., 2016). The measured instantaneous velocity vectors are defined at the scattered instantaneous positions of the tracers. The ensemble average velocity is evaluated within cubic cells (or bins) of $20 \times 20 \times 20$ mm^3 volume, yielding the three-dimensional distribution of time-averaged velocity. Adjacent bins overlap by 75%, resulting in a Cartesian grid of velocity vectors with 5 mm pitch. The vorticity vector is evaluated by centred finite-difference of velocity values

from neighbouring grid nodes.
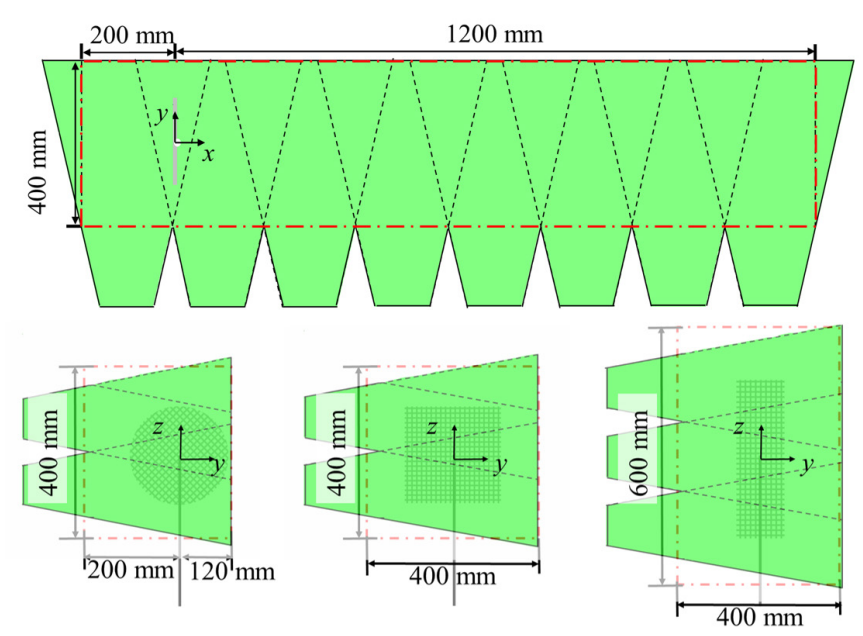
Figure 4.6: Top- (up), and Front- (bottom) view of the porous plate (origin defined at the centre of the plate) and the IFOVs, the overall measurement domain is marked by the red dash-dot line.

Figure 4.7: Raw (left) and pre-processed (right) CVV images of HFSB tracers, with the square actuator surface in view.

4.3.3. Experimental uncertainty

The load sensor was calibrated within the force measurement range 0-1 N. A linear relation between measured voltage and corresponding force was evaluated using least squares regression; the standard uncertainty of the measured load induced by the actuators is 2.3% of the measured value.
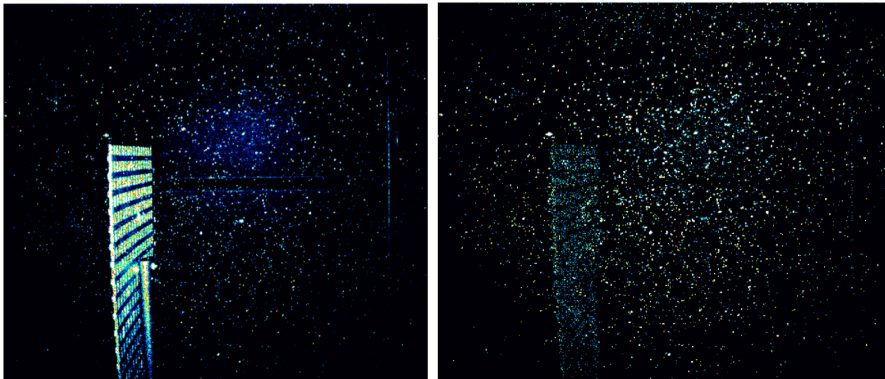
The expanded uncertainty of the time-averaged streamwise velocity estimation u is determined as [1]

$$U_u = \frac{k\sigma_U}{U_\infty \sqrt{N}},\tag{4.8}$$

where σ_U is the standard deviation of instantaneous velocity and $k = 2$ is the coverage factor for 95% confidence level. In the wake of the porous plates, σ_U attains typical values of about $0.2\,\mathrm{m\,s^{-1}}$, corresponding to a turbulence intensity of 4%. The value of the number N of samples is in the order of 1,000 in most of the measurement domain, although it can vary from 50 to 18,000, depending on the distance between the measurement location and the CVV head. The corresponding value of U_U remains below 0.5% in most of the measurement domain. Higher turbulent intensity values (up to 25%) are encountered in the shear layers, leading to an increased uncertainty of the mean velocity, which locally reaches 2% of the free-stream velocity.

4.3.4. Spatial resolution effect

Given the bin size adopted for the robotic PIV measurements ($20 \times 20 \times 20\ \mathrm{mm^3}$), the velocity field reproduces the macroscopic behaviour of the flow around the actuator discs. A high-resolution planar PIV measurement (see appendix A) is employed to verify the applicability of using such PIV technique in measuring the wake of porous plates. Although the detailed behaviour of the flow across the orifices of the porous plates is not captured, the results of robotic PIV are in excellent agreement with the high-resolution planar data upstream of the plate and downstream of it after approximately 6 pore pitches, where the relative error of the velocity is approximately 1.3%.

4.4. Experimental Results and discussion

4.4.1. Actuator thrust coefficient

The thrust coefficient, C_T is one of the inputs for the kinematic wake models examined in this work. C_T is defined as:

$$C_T = \frac{T}{\frac{1}{2}\rho U_\infty^2 A},\tag{4.9}$$

where T is the thrust force induced by the actuator to the fluid, that is the actuator's drag. The effect of the rod is accounted for with the following procedure: firstly, the loads with the actuator attached (T_1) and unattached (T_2) to the supporting rod are measured, respectively; then T is evaluated as $T = T_1 - T_2$. ρ is the air density, U_∞ is the free stream velocity, and A is the frontal area of the actuator. The measured values and resulting relative errors of C_T of the different actuators are listed in table 4.2. The resulting C_T are

---

[1]Lower case letters u, v, w are used for time-averaged velocity components, unless otherwise defined; e.g., $\bar{u}$ in chapter 6 and 7.
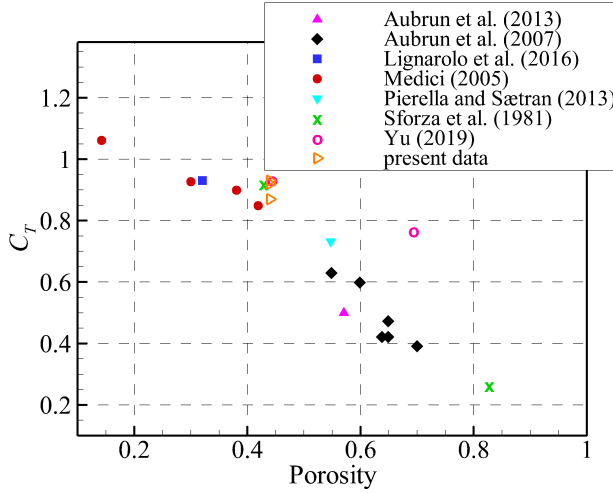
Figure 4.8: Thrust coefficient as a function of porosity; comparison between current results and literature.

approximately the same within the measurement uncertainty, which confirms that C_T is little sensitive to the shape of the actuators. The chosen porosity results in $C_T \approx 0.89$, which is the point of optimal energy extraction according to the actuator disc model and Betz law (Betz, 1919). This value of C_T is similar to that reported in the work of Yu et al. (2019), where the dynamic wake of a plate with the same porosity was investigated. Figure 4.8 compares the relationship between thrust and actuator porosity measured in this work (labelled "present data") with measurements by other authors as reported in the work of Lignarolo et al. (2016) and Yu et al. (2019); the value of C_T measured in this work lies within the cluster of considered data.

Table 4.2: Thrust measurements conditions and results.

	porosity	$U_\infty[\mathrm{ms^{-1}}]$	ρ [kgm^{-3}]	T [N]	C_T	$\mathcal{E}_{C_T}$
Circular	0.44	5.12	1.21	0.460	0.92	4.7%
Square	0.44	5.14	1.19	0.548	0.87	3.7%
Rectangular	0.44	5.15	1.19	0.444	0.93	4.9%

4.4.2. VELOCITY FIELD DISTRIBUTION

The contours of time-averaged streamwise velocity u from PIV measurements are presented in figures 4.9 to 4.13, showing the overall shape of the measurement results. In figures 4.9 and 4.10, the horizontal and vertical planes across the centre of the actuator surfaces are chosen for comparison, respectively. The x-coordinate, which points to the streamwise direction, is normalised by D^*, to examine the validity of normalising the streamwise momentum deficit recovery. Meanwhile, the length scale W, i.e., the diame-

ter of the circular disc and the widths of the square or rectangular disc, is used for length normalisation in both lateral and spanwise directions, as widely adopted in the literature (e.g., Abkar, 2018; Craig et al., 2017; Shamsoddin and Porté-Agel, 2020). This selection is to simply show the cross-sectional wake shape imparted by the actuators.

The velocity contours in the x-y plane (figure 4.9) illustrate the flow deceleration upstream caused by the adverse pressure gradient imposed by the actuator. The rectangle patch in the velocity contour of the circular actuator disc covers a region with relatively high measurement uncertainty, which was due to an accidentally increased background reflection.

The circular and square plates impart a comparable deceleration, whereas the rectangular actuator yields a slightly higher deceleration upstream of the model. The latter is ascribed to the fundamental difference between the 3-dimensional and quasi-2-dimensional condition of adverse pressure gradient associated with the AR of the rectangular actuator, where the scaling of the stagnation region is different from that of a circular-symmetric object.

Figure 4.9: Contours of normalised streamwise velocity (u/U_∞) in the x-y plane at $z/D = 0$. Circular (top), square (middle) and rectangular actuator (bottom). The white contour line represents the location where the wake velocity attains 50% of the free-stream value.

Immediately downstream of the actuator, the most pronounced deficit is associated with the presence of the supporting rod, which also introduces local flow reversal. On the sides (e.g., $y/W = \pm 0.4$) one observes a velocity deficit past the grid of approximately

50%. This result compares favourably with the deficit of 40% reported in the work of Aubrun et al. (2013), where an actuator disc with a porosity of 55% was used.

For the circular actuator, a narrow recirculation region is found at about $x/W = 0.1$, whereas for the square and rectangular surfaces such recirculation region is significantly wider. This may be explained with the support rod blocking a comparatively more perforated area in the cases of square and the rectangular plate, as shown in figure 4.4. The flow evolution along the symmetry axis confirms a smaller effect of the rod for the circular actuator.

In order to assess the topology of the flow induced by the rod, the velocity field in the x-z plane is shown in figure 4.10. The comparison indicates that the effect of the rod is not negligible within $1D^*$, as it causes a flow reversal up to $u/U_\infty = -0.2$ in this region.

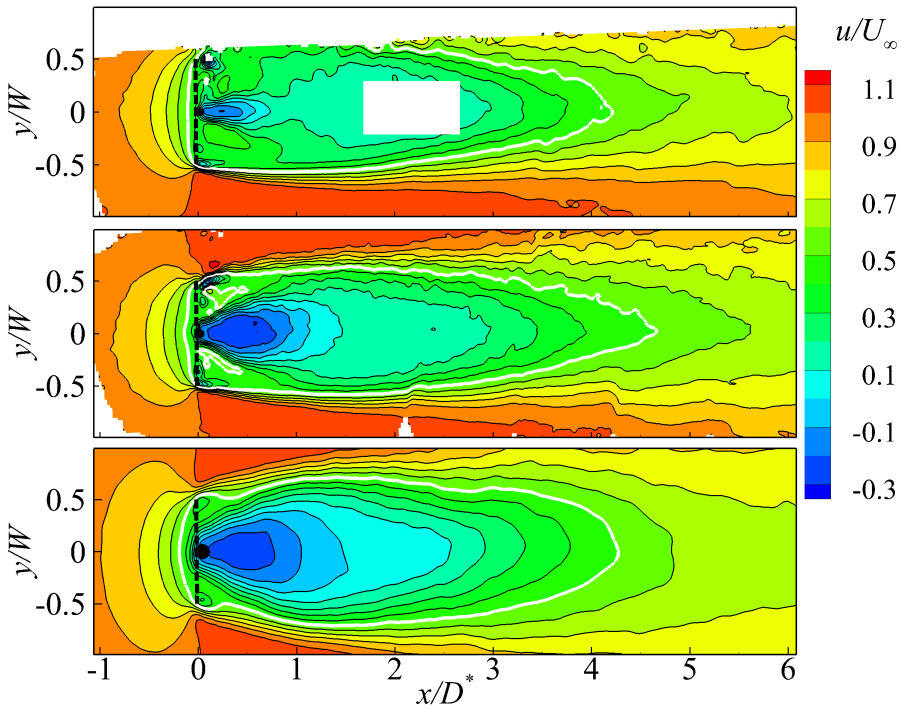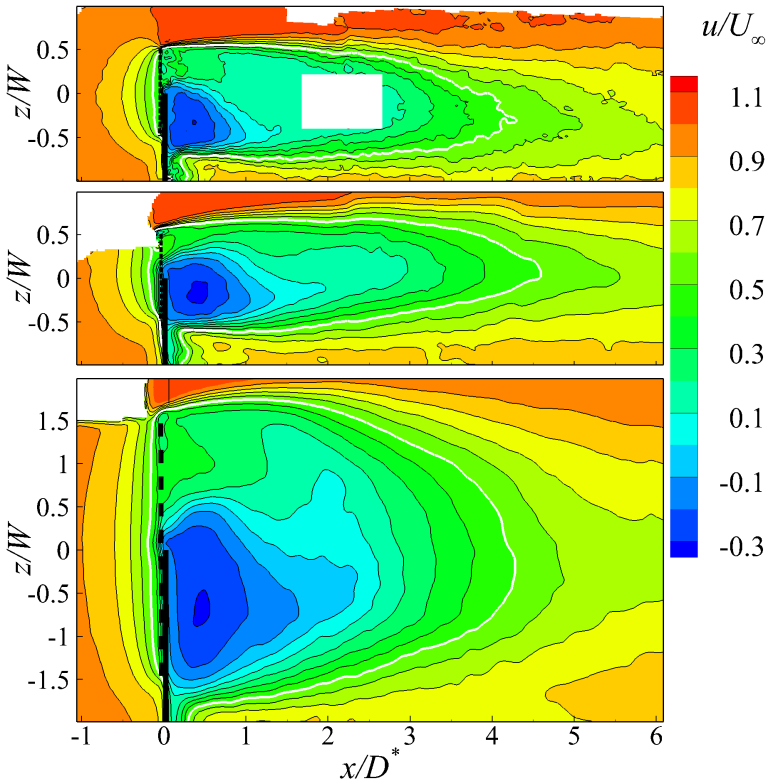Figure 4.10: Contours of normalised streamwise velocity (u/U_∞) in the x-z plane at $y/D = 0$. Circular (top), square (middle) and rectangular actuator (bottom).

The normalisation of the streamwise direction with respect to D^* yields a good agreement among the contour lines in the wakes of the different actuators (see figures 4.9 and 4.10). Take the white contour lines as an example, where the mean streamwise velocity attains 50% of the free-stream value: they extend until around $x = 4.5D^*$ for all the cases. A more quantitative discussion about the validation of D^* for streamwise distance

normalisation is presented in section 4.4.3.

The velocity distribution at different y-z cross-sections in the wakes of the three actuators is depicted in figures 4.11, 4.12 and 4.13, respectively. For the position right after the actuator surfaces, namely when $x/D^* = 0.1$, the wakes feature the same shape as that of the actuator surfaces, but are slightly expanded. Here the localised effect of the supporting rod is clear, inducing reverse flow up to -0.2. As the wakes develop further downstream, their centres slightly shift downwards under the effect of the rod presence, as also reported in the literature (Aubrun et al., 2019; Pierella et al., 2017). The blue contour line indicates the shear layer shape development, which bounds a region with the equivalent actuator frontal area (only the upper half, i.e., $z \geqslant 0$, is considered for area evaluation to avoid including the supporting rod effects).

Figure 4.11: Streamwise velocity contours and in-plane velocity vectors pattern at four cross-sections downstream of the circular actuator. The blue contour line together with the dashed line ($z = 0$) bounds half of the equivalent actuator frontal area and its length correspond to half of the wake cross-section perimeter (eq.(4.6)).

The circular actuator produces a circular-symmetrical development of the deficit region. In contrast, the square actuator exhibits pronounced geometric modifications with the shear layer moving inwards at the corners. The latter is also reported in the work of Nedić et al. (2013) for the wake of a solid square plate. This lower rate of expansion at the corners is ascribed to the onset of streamwise vortex pairs that induce a cross-flow with resultant inward motions at the corners.

As a result, the streamwise velocity contour at $x/D^* = 1$ has already lost the sharp corners and the wake tends towards a cloverleaf shape. At the most downstream observation ($x/D^* = 6$), the region of momentum deficit has almost turned into a diamond shape. The rod effect is similar to that of the circular shape and vanishes by $x/D^* > 3$. Judging from the blue contour lines, the square actuator wake does not evolve into a circular wake within $6D^*$, and the perimeters of the equivalent regions keep close to the actuator perimeter.

The wake of the rectangular actuator features a similar trend to that of the square one, provided that the vertical elongation is taken into account. Judging from the colour map

Figure 4.12: Streamwise velocity contours and in-plane velocity vectors at cross-sections downstream of the square actuator. The blue contour line together with the dashed line ($z = 0$) bounds half of the equivalent actuator frontal area and its length correspond to half of the wake cross-section perimeter (eq.(4.6)).
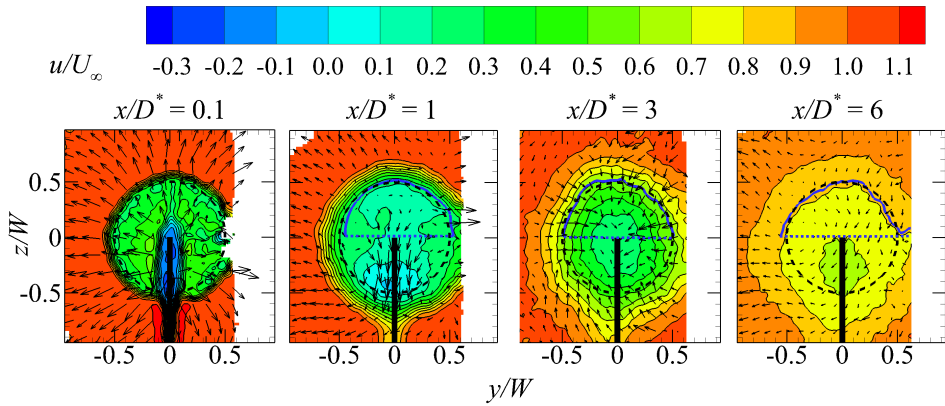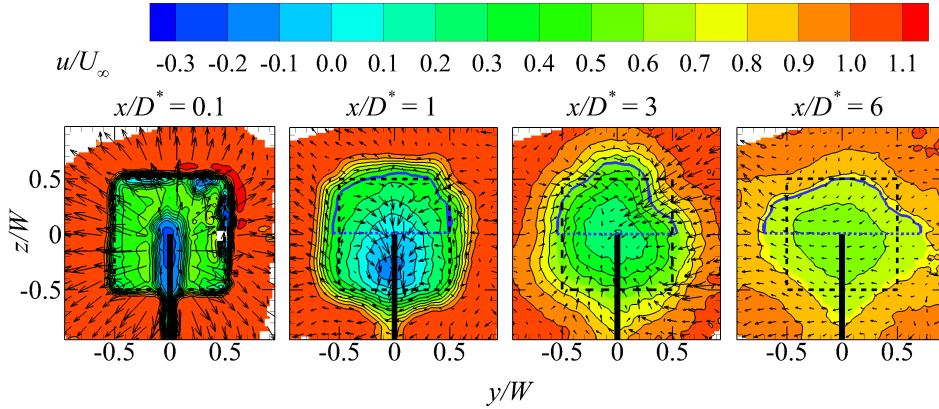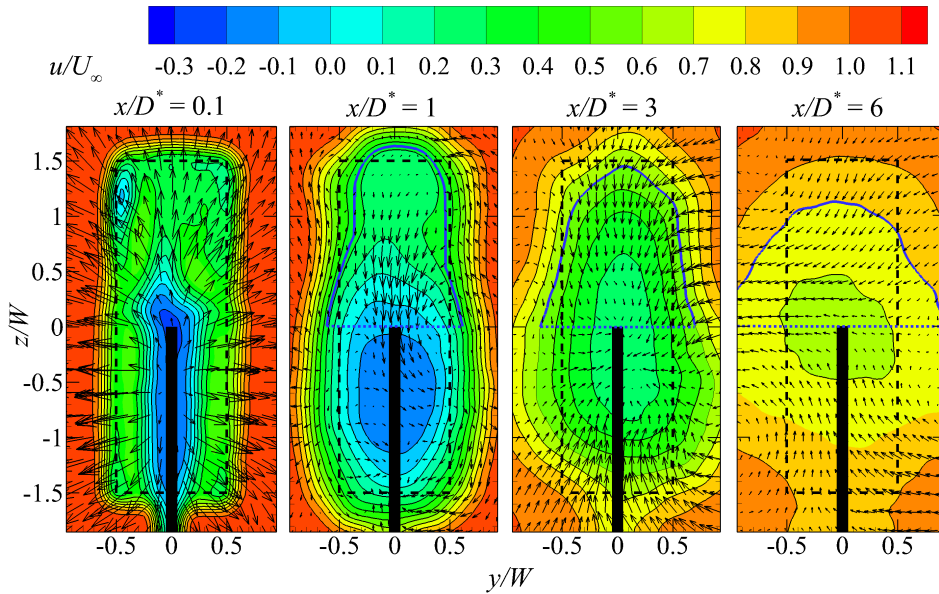

Figure 4.13: Streamwise velocity contours and in-plane velocity vectors at cross-sections downstream of the rectangular actuator. The blue contour line together with the dashed line ($z = 0$) bounds half of the equivalent actuator frontal area and its length correspond to half of the wake cross-section perimeter (eq.(4.6)).

of the contour plots, all the actuators feature a similar momentum deficit at the same number of D^* behind the actuators. The regions with equivalent frontal area, however, do feature an asymptotic development towards a circular wake. Consequently, the AR of the shear layer becomes less at $6D^*$, while constantly decreased perimeters are also observed. A quantitative discussion is available in the next section.

4.4.3. MEAN STREAMWISE VELOCITY DEFICIT NORMALISATION

A comparison of the normalised mean streamwise velocity deficit along the x-coordinate is presented in figure 4.14, where $\Delta U/U_\infty = 1 - U/U_\infty$, to validate the effective mixing diameter D^*. The velocity deficit is averaged within the upper half of the cross-sections, to avoid any effect from the support's wake. Three normalisation lengths in the literature, namely width W (corresponding to rotor diameter D when representing wind turbines), characteristic length $l = A^{1/2}$, and equivalent diameter $D_{eq} = (4WH/\pi)^{1/2}$, together with the concept of the effective mixing diameter D^* proposed in this work, are compared.

When the data are normalised with W, as shown in figure 4.14, the rectangular actuator features the lowest recovery rate. However, the latter can be rather considered as an artefact of the normalisation choice, as the actuator width is also the shortest length among those used in all criteria.

When the data takes into account the overall cross-section (the equivalent diameter scaling, D_{eq}, Shamsoddin and Porté-Agel, 2020, and characteristic length, l), the rectangular actuator features the fastest recovery. Considering the fact that non-circular-symmetric actuators exhibit longer perimeters than circular-symmetric ones, the latter indicates that for a chosen cross-sectional area, the longer the perimeter the higher the momentum recovery rate. Despite a coefficient of $(4/\pi)^{1/2}$, l and D_{eq} are actually based on the same principle. The differences are that the former transforms the wake generator to an equivalent square, whereas the latter transforms it into an equivalent circle.

Including the perimeter of the deficit region in the normalisation (D^*), a more unified behaviour is observed for the three considered cases as the curves of the streamwise velocity deficit development collapse to a better extent.

To examine how the actuator wake shape departs from the circular assumption and how it evolves toward it, the evolution of the wake circularity given by the ratio $D^*(x)/D_{eq}$ is presented in figure 4.15 for the rectangular actuator. $D^*(x)$ is evaluated at each section along x, using the perimeter of the deficit area, which is equivalent to the actuator frontal area. The wake will eventually become circular (Fail et al., 1957), corresponding to the condition $D^*/D_{eq} = 1$. Figure 4.15 indicates such asymptotic behaviour, and the aforementioned normalisation comparison shows that when $D^*/D_{eq} > 0.9$ (corresponding to $x/D^* > 5$), the wake normalisation based on D^* and D_{eq} are equivalent. The latter is also supported in figure 4.14, by a good collapse of the data for D_{eq} at a distance beyond 5 equivalent diameters.

4.5. D^* NORMALISATION FOR VAWT WAKES

In this section, numerical simulations are conducted to assess the validity of the D^* normalisation for the scaling of the wakes of VAWTs with different aspect ratios.
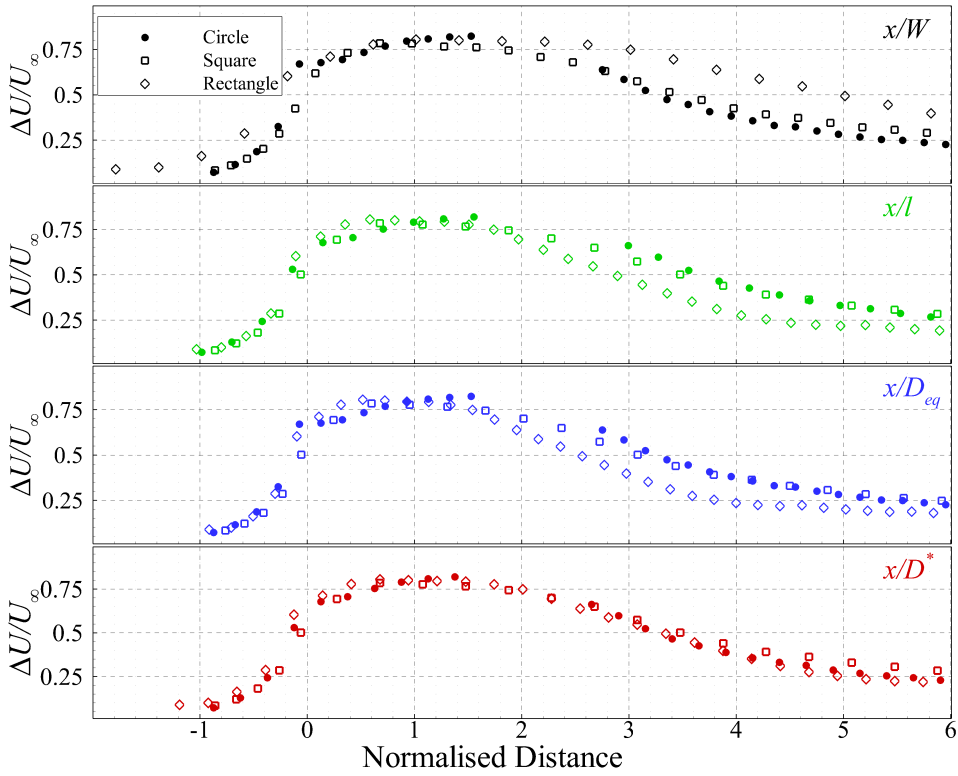
4

Figure 4.14: Comparison of streamwise velocity deficit averaged in the upper half of the projected area along x-direction (downstream distance normalised by W, l, D_{eq}, D^*).
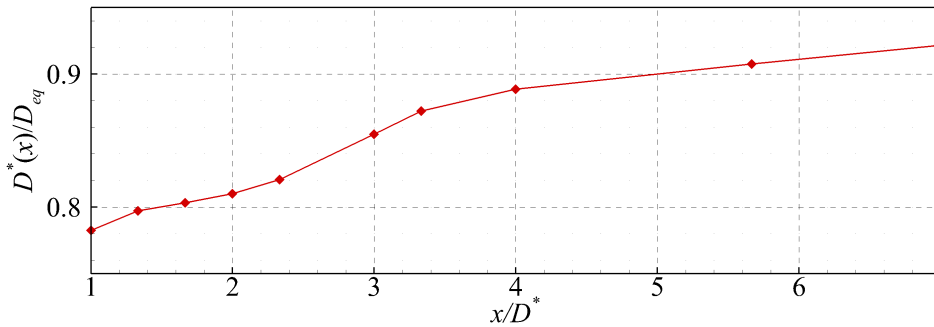

Figure 4.15: Wake circularity ($D^*(x)/D_{eq}$) evolution along x/D^* for the rectangular actuator.

4.5.1. NUMERICAL SIMULATIONS

The simulated VAWTs are based on the geometry investigated and reported by Tescione et al. (2014), with the exception that the struts and the supporting towers are not included, for sake of simplicity. For the purpose of verifying the normalisation based on the D^* concept, a set of simulations covering VAWTs with values of AR varying in the range {1,2,3,10} were carried out. The rotor diameter was kept constant, while the height was varied. All simulations have the same inflow conditions and mesh density/topology. A schematic of the simulation domain is presented in figure 16, where VAWTs with AR of 1 (solid black) and 3 (dashed blue) are illustrated. The dimensions of the computational domain are comparable with those reported by Mendoza et al. (2019). In particular, with varying VAWT heights, the height of the simulation domain is also varied to keep a constant ratio of 7 between the simulation domain and the VAWT heights.
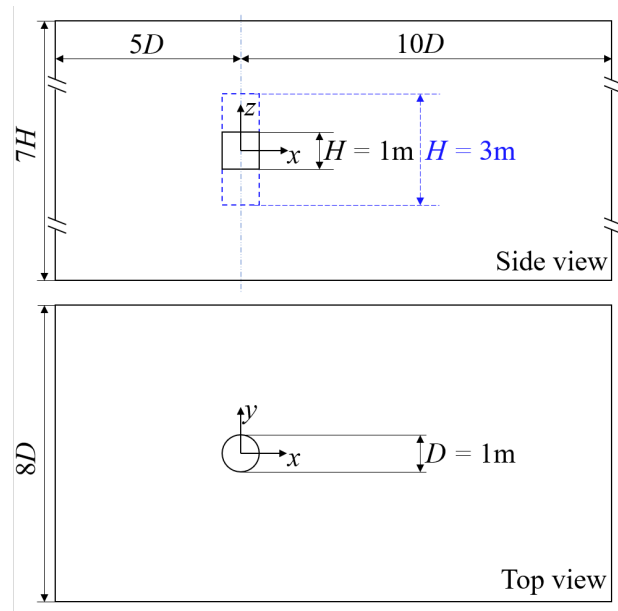
Figure 4.16: Schematic of the numerical simulation domain with variable height. VAWTs with AR = {1, 3} are presented.

Moreover, for the case of AR = 10, the downstream domain is extended to $20D$, so as to enable a comparison with the D_{eq}-based scaling (figures 4.18 and 4.19). All the turbines rotate with the same tip speed ratio of 4.5, similar to the cases of Shamsoddin and Porté-Agel (2020), to achieve the same centre plane C_T (0.92). The tip loss effect causing a decreased overall C_T, especially at small AR is omitted in the comparison. The resulting overall wind turbine thrust coefficients are listed in table 3 for all the cases.

The numerical simulation was carried out with the actuator line model (ALM) coupled with a dynamic stall model (DSM), using the flow velocity from the Navier-Stokes solver and then determining the angle of attack and relative velocity to solve the blade forces. The forces are therefore used as representative of those exerted by the VAWT.

The flow field was simulated with the OpenFOAM, an open-source CFD framework, by solving URANS equations and the k-ϵ turbulence model.

The *turbinesFoam* library developed by Bachant and Wosnik (2015), which consists of the ALM and DSM, was used for the numerical experiment implementation. The library together with the OpenFOAM framework has been extensively validated and reported in the literature. Nevertheless, a case-specific validation, using the same domain topology is presented here, setting flow conditions according to Tescione et al. (2014) and including the struts and shaft. Furthermore, the results are compared to LES simulation data for the same case produced by the same OpenFOAM library Mendoza et al. (2019).

The simulated mean streamwise velocity profiles along horizontal and vertical planes crossing the turbine centre are compared in figure 4.17. The comparison shows that the present URANS simulation reproduces the mean velocity field in agreement with existing experimental and numerical investigations. Local discrepancies are limited within 15% of the free-stream value compared to the experimental data. The comparison of the normalisation methods reported hereafter is based on the cross-sectional average of the velocity, which further decreases the value of such discrepancies to within 8%.
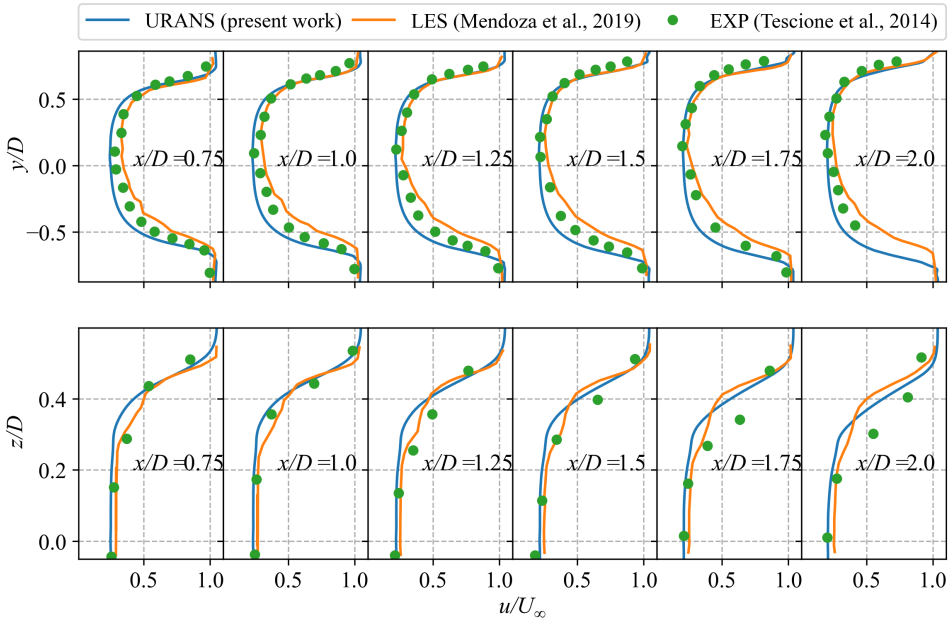
Figure 4.17: Comparison of horizontal (top) and vertical (bottom) profiles of normalised mean streamwise velocity along the x-direction. Blue lines: the URANS simulation results from the present work; Green dots: the experimental data of Tescione et al. (2014); Orange lines: the large eddy simulation (LES) results from Mendoza et al. (2019).
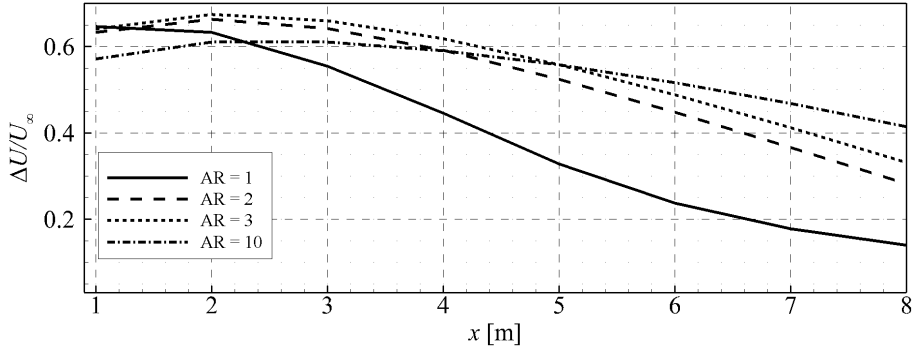
Figure 4.18: Comparison of streamwise velocity deficit (averaged over the projected area) along x-direction in the wake of VAWTs with AR = {1, 2, 3, 10}. The VAWT diameter is $D = 1$ m.

4
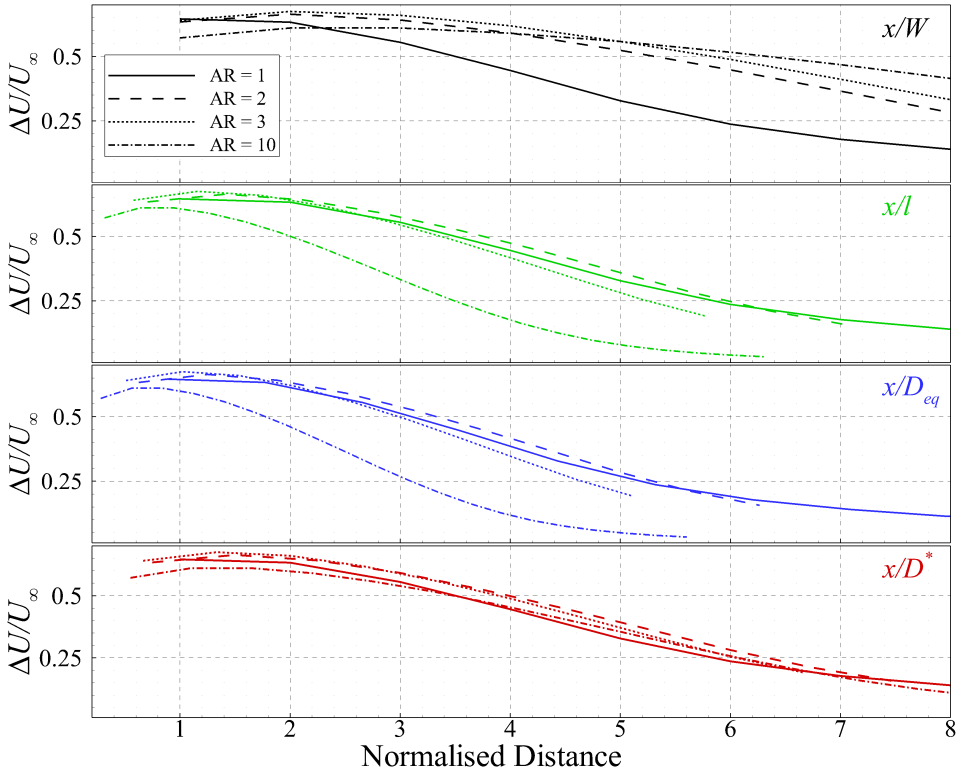
Figure 4.19: Comparison of streamwise velocity deficit (averaged over the projected area) along x-direction. Data are normalised by D, l, D_{eq}, D^* in the wake of VAWTs with AR = {1, 2, 3, 10}.

Table 4.3: Thrust coefficients of the VAWTs with AR = {1, 2, 3, 10}.

AR	1	2	3	10
C_T	0.75	0.81	0.82	0.91

4.5.2. COMPARISON OF WAKE NORMALISATION

The velocity deficit evolution downstream of the turbine locations is presented in figure 18, comparing rotors of different AR. As expected, for a fixed value of the rotor diameter, the larger the AR (cross-sectional area), the longer the wake persists, with a significant increment observed when transitioning from the square cross-section to the turbine with AR = 2.

The velocity deficit evolving along the wake is represented again with the downstream distance normalised by a relevant length scale. A comparison of the velocity deficit considering the aforementioned normalisation lengths (namely D (or W), l, D_{eq}, and D^*) is depicted in figure 19, over the chosen range of AR. It is expected that the normalisation taking into account the relevant driving mechanisms (imparted momentum deficit at the actuator, momentum exchange rate across the wake interface) would yield behaviour of the momentum deficit that is less dependent upon the turbine shape, the AR in the present case.

The wake recovery purely based on D (black lines) does not take into account the increase of cross-sectional area with AR and therefore, the recovery appears to become slower for increasing values of AR. Not surprisingly l (green lines) and D_{eq} (blue lines) scaling yield comparable results, being both based on a symmetric (square or circular respectively) actuator with the equivalent cross-sectional area. In this case, when the turbine cross-sectional shape becomes elongated, the normalising length scale is increased, which results in underpredicting the recovery length. As a result, a significant spreading of the normalised curves is observed in the data.

The normalisation by D^* (red lines) accounts for the equivalent cross-sectional area (initial momentum deficit imparted by the actuator) as well as for the actuator perimeter (momentum exchange rate across the effective wake interfacial area). The normalised wake deficit based on D^* significantly reduces the wake recovery dependency on the AR, indicating the suitability for the general treatment of VAWT wake of arbitrary shape.

4.6. CONCLUSIONS

The effects of actuator shape, specifically the aspect ratio of rectangular ones, on the scaling of the wake recovery have been investigated by means of experiments and simulations. A theoretical derivation of the effective mixing diameter D^*, based on momentum conservation, is provided. The resulting D^* is proportional to the ratio between the actuator's area and its perimeter (in analogy to the hydraulic diameter), and is proposed as a characteristic length to better represent the wake recovery of actuators of different shapes. Three-dimensional data collected in the wake of circular, square and rectangular actuators, obtained from plates of uniform porosity, are used to validate the proposed formulation of D^*, as well as to expand the fundamental knowledge of the frontal shape

effects of actuator surfaces. The results of figures 4.14 and 4.19 confirm that, in spite of the approximation made in the definition of the control volume that accounts for the actuator's perimeter and not for the actual shear layer's perimeter, the use of D^* provides a better agreement among the velocity deficits of different actuator surfaces up to a normalised streamwise distance of 8.

Although the velocity measurements return clear edge effects at the corner of the square and rectangular actuators, thrust measurements with a load sensor indicated that the C_T is not sensitive to the shape of the planar actuator (confirming the independence of streamtube used in BEM theory), and the related edge effects. Nevertheless, the downstream development of the momentum deficit features a significant distortion induced by such edge effects. In particular, a lower rate of expansion at the corners is observed; the latter is caused by streamwise vortex-pairs that induce inward motions.

The proposed normalisation length D^* is compared with the recently proposed equivalent diameter D_{eq} from Shamsoddin and Porté-Agel (2020), a commonly used characteristic length l, and the width W (or diameter D) that is frequently used in kinematic wake models as a scaling parameter. When the latter quantities are used as scaling parameters, the wake recoveries from actuators of different ARs depart considerably from each other. Conversely, when a spatial normalisation by D^* for the streamwise direction is taken, a better agreement is observed between the velocity deficit for different actuator shapes.

Furthermore, D^* is used for the normalisation of VAWT wake as a proof of concept. A good agreement among the wakes of VAWTs with different aspect ratios indicates D^* as a promising normalisation criterion.

5

COMPARISON OF THE WAKES OF A LAB-SCALE VAWT AND ACTUATOR DISCS

Wind tunnel experiments on a scaled VAWT and square porous plate with a porosity of 64% are conducted in the W-tunnel of TU-Delft. The VAWT thrusts in axial and lateral directions are measured with an in-house load cell system based on moment conservation. Wake of the VAWT in tip speed ratio of 1.5 and 2.5 and the porous plate is measured with the robotic particle image velocimetry technique, which enables a three-dimensional velocity measurement in a combined volume encompassing from 1 diameter upstream to 3 diameters downstream. Counter-rotating vortex pairs in VAWT wake and the wake shape deformation and deflection are discussed, which are related to the lateral thrust. A square porous plate inducing a similar axial thrust is compared, which has the same shape as the cross-section of the VAWT. The wake of the porous plate with a yaw angle of 15° is investigated, producing a deflection similar to the VAWT.

5.1. INTRODUCTION

SIMPLIFIED VAWT models producing similar wakes are essential to studying the wake effect in a VAWT farm because they enable more rapid aerodynamic analysis. Specifically, they allow fast estimates of the velocity deficit, turbulence intensity, and wake shape. And it can be practical to study large VAWT arrays with simplified models experimentally. To make reasonable simplifications, the nature of VAWT wakes needs to be fully understood. However, confined to the differences in turbine configuration and operating conditions, previous VAWT wake studies may not show consistent properties, for instance, the structure of the wake that is much related to the solidity and tip speed ratio (TSR, λ) of a specific turbine (Tescione et al., 2014; Rolin and Porté-Agel, 2018). Thus, consistent properties accounting for TSR and solidity need to be found and quantified. An alternative property is the thrust coefficient, C_T, which is one of the most critical parameters for the actuator disc theory. The actuator disc theory is widely used in kinematic wake models for horizontal axis wind turbines (HAWT) (Jensen, 1983; Larsen, 1988; Bastankhah and Porté-Agel, 2014), simplified models for HAWTs based on this theory have been experimentally studied and validated extensively (Aubrun et al., 2013, 2019; Howland et al., 2016; Yu et al., 2019).

In contrast, there are only a few experimental studies on simplified VAWT models. Craig et al. (2017) conducted PIV measurements in the wake of rotating cylinders and rectangular meshes with different porosity to investigate the applicability of low-order physical models for VAWTs. They concluded that the actuator square might produce a similar far wake when VAWTs rotate in a low TSR range (from 1 to 2). However, their experiments conducted at Re = 600 imply laminar or transitional development of the boundary layer along the blade, differing from the regime encountered on wind turbines. Besides, the thrust coefficient is not quantified in their work. Thus, there are still questions about whether a planar actuator can work as a simplified surrogate for a VAWT, and what is the mechanism back or against such simplifications.

In this chapter, experiments are conducted to compare the three-dimensional flow development in the wake of a scaled two-blade VAWT and a planar plate with a porosity of 64%, examining the feasibility of representing a VAWT with a planar actuator. Loads are measured with four load cells mounted on the support structure. The velocity fields from 1 diameter upstream up to 3 diameters downstream of the VAWT and the plate are measured using robotic particle image velocimetry introduced in chapter 3. The velocity and vorticity fields are compared among the different models. Low TSRs (less than 2.5 in this case) are selected to avoid high streamwise thrust coefficients, which can easily exceed 1.0 because of the high solidity of the VAWT. Moreover, it is challenging for models based on the actuator disc to predict the wake of heavily loaded wind turbines (Schmitz and Maniaci, 2017). Thus, to make a fair comparison, TSRs of 1.5 and 2.5 are chosen, similar to that of the previous studies by Craig et al. (2017).

5.2. EXPERIMENTAL SETUP

Experiments are conducted at the W-tunnel of the TU Delft Aerodynamic Laboratories. The W-tunnel is an open-jet wind tunnel with a square 0.6 m × 0.6 m exit. The wake is measured using robotic PIV. The robotic PIV system consists of three major parts: a)

the coaxial volumetric velocimeter, comprised of a compact arrangement of four CMOS cameras (10 bits, 704 × 464 pixels) at a low tomographic aperture and an optical fibre delivering the light emitted by an Nd:YLF Quantronix Darwin Duo Laser (21 mJ pulse energy at 1 kHz, 527 nm wavelength); b) a robotic arm (Universal Robots UR5) that allows the robotic manipulation of the CVV system with six degrees of freedom; c) and the helium-filled soap bubbles (HFSB) seeding generator, which delivers sub-millimetre neutrally buoyant tracer particles. Figure 5.1 shows the overall experimental setup.
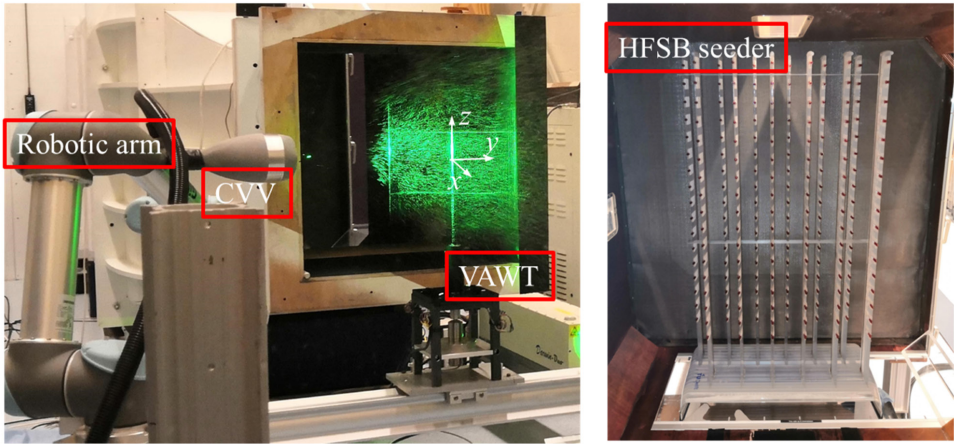
Figure 5.1: Experimental set up: Robotic PIV measuring (left), HFSB seeder inside the settling chamber of W-tunnel (right).

5.2.1. Scaled VAWT model

The VAWT model has two blades with a profile of NACA0012. The length of the blade is 300 mm, and the rotor diameter is 300 mm. A direct current (DC) motor drives the model to reach a TSR from 1 to 5. The detailed design specifications are listed in Table 5.1.

Table 5.1: Design specifications of the VAWT model

Property	Dimension
Number of Blades	2
Blade length	300 mm
Rotor diameter	300 mm
Blade profile	NACA0012
Chord of blades	3 mm
Strut profile	NACA0012
Chord of struts	3 mm
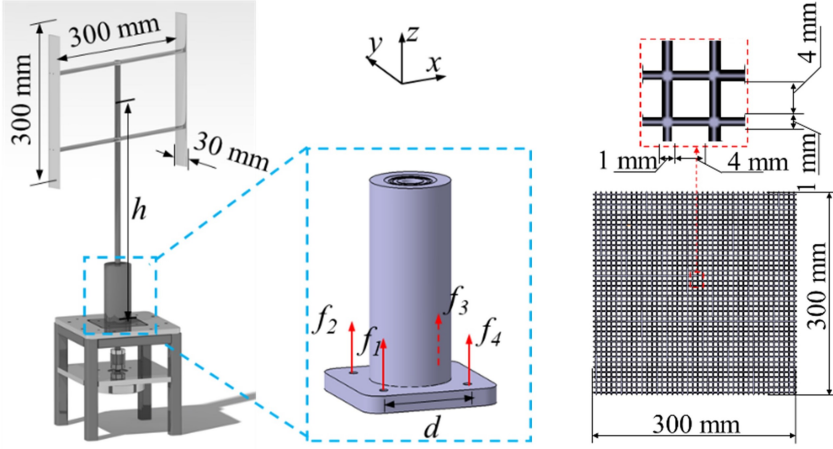
Figure 5.2: Schematic plotting of the models: VAWT model with a thrust measurement system (left) and porous plates (right).

5

5.2.2. Porous plate

A 3D-printed porous plate is adopted as a surrogate for the actuator disc. As illustrated with the sketch in figure 5.2, the aperture of the plate is 4 mm, and the pitch is 5 mm, resulting in a porosity of 64%. The plate thickness is 2 mm. The selection of the porosity is based on a survey of previous results to match the streamwise thrust of the VAWT model. The resulting thrust and the comparison with data from the literature are discussed in section 5.3.1. To make a fair comparison with the VAWT model, the mesh was mounted on the same strut as the VAWT's during the measurement.

5.2.3. Load measurement apparatuses

Loads are measured with four load cells integrated with the supporting structure, which is at the base of the rotor, as shown in figure 5.2. The wind flows towards the positive x-direction, and forces acting at the centre of the rotor are calculated based on moment balance (Leblanc and Ferreira, 2018):

$$F_x = \left[(f_3 + f_4) - (f_1 + f_2) \right] \cdot \frac{d}{2h}$$
$$F_y = \left[(f_2 + f_3) - (f_1 + f_4) \right] \cdot \frac{d}{2h}. \tag{5.1}$$

where d is the distance between the adjacent load cells, h is the distance between the rotor center and the installation plane of the load cells. In this work, $d = 50$ mm, $h = 318$ mm. The thrusts produced by the VAWT model are:

$$T_x = -F_x; T_y = -F_y \tag{5.2}$$

where the negative signs mean that the thrusts are opposite to the forces applied to the rotor centre. Thrust coefficients are calculated as:

$$C_T = \frac{T}{0.5\rho AV^2}.$$

(5.3)

where ρ is the air density, A is the projected rotor area, V is the inflow velocity.

The indirect force measurement using moment balance gives a qualitative trend of the averaged load on the rotor. However, this arrangement of load cells gives rise to uncertainties of absolute values in the following manners: 1) the loaded points on load cells 2-3 and 1-4 must be perfectly aligned with the x-direction. Otherwise, the arm of the forces will vary, and equation 5.1 is no longer valid; 2) the load cell system is contacted with the rotor shaft, and the shaft is attached to a flexible coupling connected with the motor; the latter applies an inevitable force/moment that is not calibrated.

5.2.4. MEASURING AND DATA PROCESSING PROCEDURE OF PIV

The total measurement volume is obtained by combining the individual measurements from different positions of the robotic PIV system. Figure 5.3 shows the measurement views in the vertical cross-section (y-z) and the horizontal (x-y) plane, respectively. In the present study, 48 positions for the instantaneous field of view (IFoV) are chosen. At each place, 5000 images are recorded at 804 images per second (measurement time of 6.3 s). The stitched measurement field covers most of the wake region. However, due to the wake deflection and some technical issues like strong reflections and insufficient seeders, data is unavailable at some places, thus resulting in blanks in the measured field. It is visualised in section 5.3. The motion of the CVV system by the robotic arm is controlled using the *RoboDK* software. Image acquisition and storage require approximately half a minute for each measurement position.

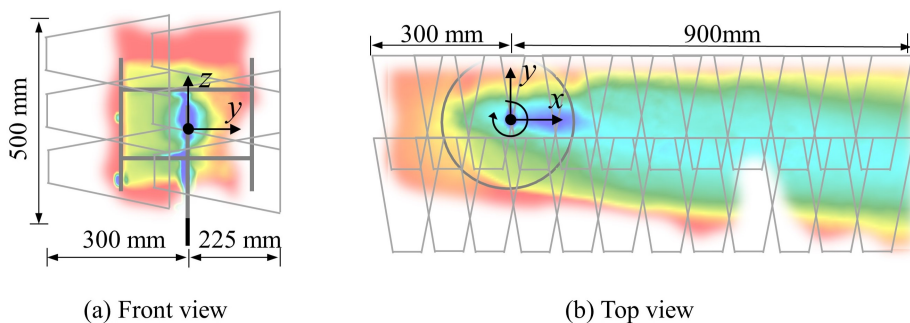(a) Front view   (b) Top view

Figure 5.3: Measurement views in the horizontal (x-y) and vertical (y-z) plane. Grey trapezoids denote the instantaneous field of views. Shaded velocity contours are schematics of measured flow fields.

5.3. Results and Discussion

5.3.1. Thrusts

For the scaled VAWT, the time-averaged thrust coefficients along streamwise and lateral directions versus λ are depicted in figure 5.4-(a). The axial thrust coefficient ($C_{T,x}$) increases as the tip speed ratio increases. In contrast, the lateral thrust coefficient, $C_{T,y}$, decreases at higher tip speed ratios.

Figure 5.4-(b) presents C_T imparted by porous plates versus their porosity. Measured data in this work (marked as 'This work') is compared with data documented in the literature. Compared with the force measurement of the VAWT, C_T of the porous plate is close to that of $\lambda = 1.5$. Therefore, the wake of the porous plate and the VAWT rotating in $\lambda = 1.5$ are compared in the following sections. In addition, the case of $\lambda = 2.5$ is also presented, showing the persisting features of VAWT wakes regardless of the variation of rotation speed.
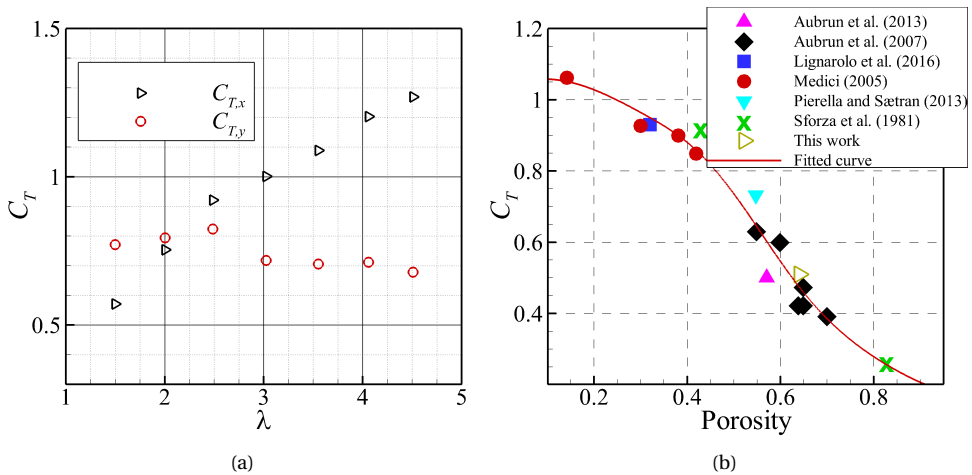
Figure 5.4: Thrusts of the VAWT model and the porous plate. (a) The time-averaged thrust coefficients, both $C_{T,x}$ and $C_{T,y}$, versus λ. (b) Thrust coefficients ($C_{T,x}$) of porous plates as a function of porosity in literature.

5.3.2. Wake of the VAWT

Counter rotating vortex pairs

The velocity fields in y-z planes along streamwise positions are shown in figure 5.5 and figure 5.6, where the velocity developments under $\lambda = 1.5$ and $\lambda = 2.5$ are presented respectively. Solid frames with ticks correspond to the outline of the wind tunnel exit, and dashed squares denote the projected outline of the VAWT rotor.

Counter-rotating vortex pairs (CVP) are observed, resulting in an asymmetric wake shape and a deflection towards the windward region. When $\lambda = 1.5$, the blade force on the advancing blade is considerably higher than the retreating blade. As a result, the maximum deficit and CVP locates in the windward region. Moreover, the CVP stretches

the wake shape into an asymmetric shape, where more vertical expansion presents on the windward side.
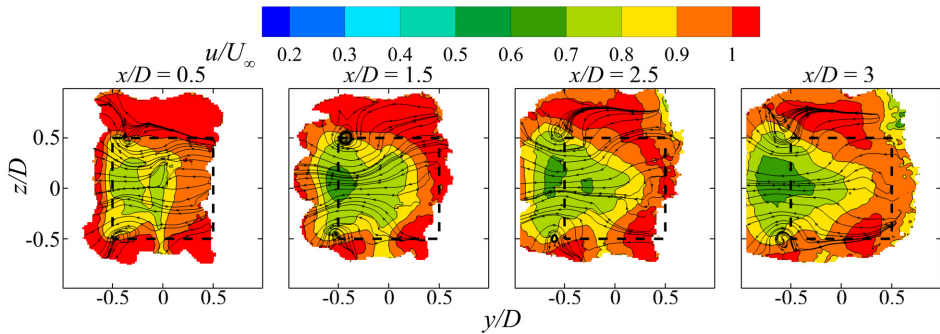
Figure 5.5: Streamwise velocity contours and in-plane streamlines downstream of the VAWT rotating at TSR of 1.5 at $x/D = [0.5, 1.5, 2.5, 3]$.

The VAWT at $\lambda = 2.5$ imparts a more significant streamwise velocity deficit due to a higher streamwise thrust coefficient, which is consistent with the thrust measurement results in figure 5.4-(a). Nonetheless, The wake at $\lambda = 2.5$ manifests features similar to that at $\lambda = 1.5$, particularly the cross-flow motion and the asymmetric wake shape.
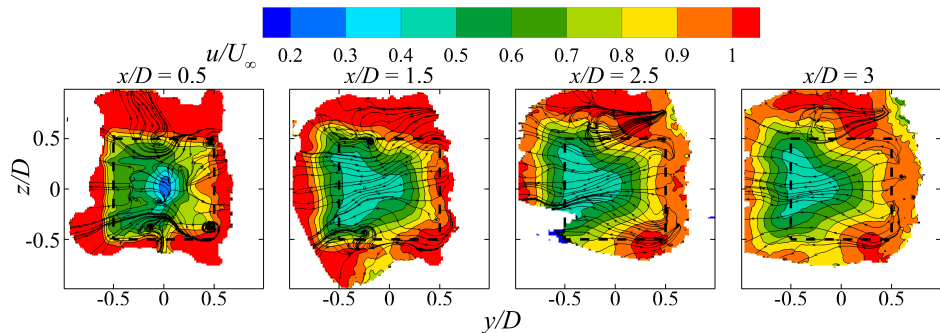
Figure 5.6: Streamwise velocity contours and in-plane streamlines downstream of the VAWT rotating at TSR of 2.5 at $x/D = [0.5, 1.5, 2.5, 3]$.

Similar counter-rotating vortex pairs (CVPs) are reported by Rolin and Porté-Agel (2018). They inspected the transport equation of mean kinetic energy to investigate the wake recovery mechanism of a VAWT model and concluded that CVP accounts for most of the energy entrainment and the wake deflection. In their work, the generation of CVPs is related to the lateral force. The vital role of lateral forces is partly proved in the present work regarding wake deflection, where the velocity fields exihbit a similar wake deflection between the two cases with different λ (figures 5.7 and 5.8), with the measured lateral force being similar. In other words, regardless of the variation in the turbine's operating condition, as long as the lateral force keeps constant, the overall deflection is probably the same. Ryan et al. (2016) also reported the presence of CVPs, claiming that

the tip vortices are responsible for CVP generation. Their conclusion is supported by the present work, where both cases have CVPs around the blade tips.

WAKE DEFLECTION AND EXPANSION

Velocity fields over the xy-plane crossing the rotor centre are shown in figure 5.7 and 5.8 to compare the wake deflection at different λ. The blue contour line denotes where the velocity attains to 90% of inflow velocity. Based on the streamlines and the contour lines, it is clear that the wake is deflected towards the windward region, and the deflection angles of VAWTs at $\lambda = 1.5$ and 2.5 are similar. The similarity in the deflection is likely because the lateral forces discussed in section 5.3.1 have equal strength. For both cases, on the leeward side, the wake outline nearly aligns with the freestream.
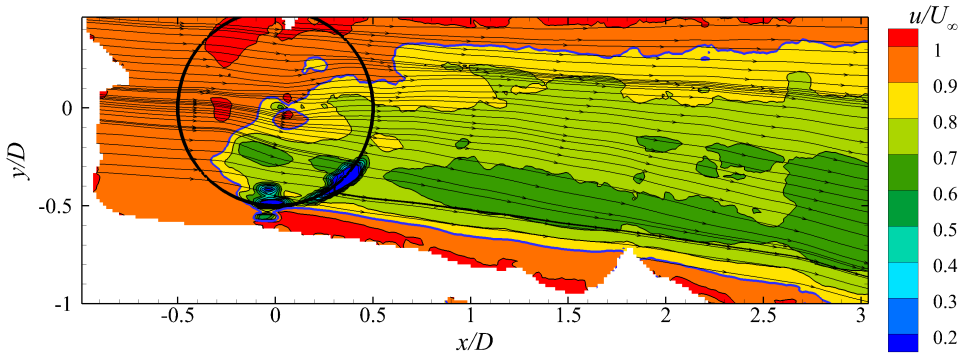
Figure 5.7: Time-averaged and normalized streamwise velocity contour and streamlines in the xy-plane, $z/D = 0$, $\lambda = 1.5$.
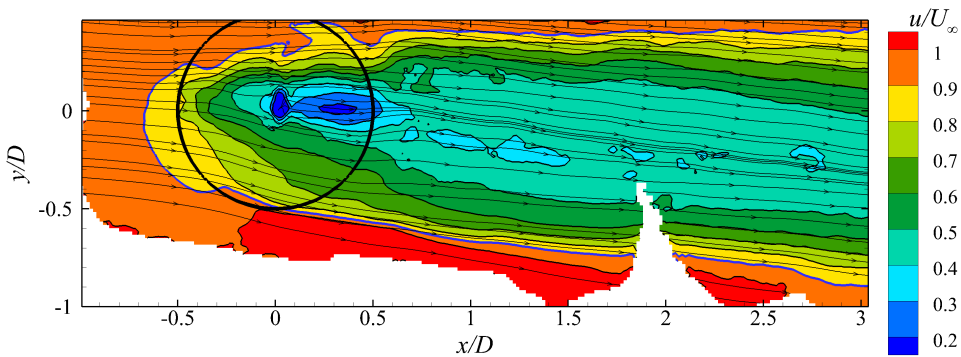
Figure 5.8: Time-averaged and normalized streamwise velocity contour and streamlines in the xy-plane, $z/D = 0$, $\lambda = 2.5$.

5.4. WAKE OF THE POROUS PLATE

The measured axial thrust coefficients without yaw angle is 0.51, which matches the VAWT model operating at $\lambda = 1.5$. Velocity fields in the wake are discussed in the following part of this section.

WAKE SHAPE AND VORTICITY SYSTEM

The normalized streamwise velocity contours and in-plane streamlines at $x/D = 1.5$ are depicted in figure 5.9. When the plate is not yawed, as depicted in figure 5.9-(a), its wake features a symmetric wake shape which is different from that of a VAWT at $x/D = 1.5$ (figure 5.5). The wakes differ in two aspects. First, the outline of the plate's wake is concave at four corners, resulting in a clover-leaf shape; Also, there is no deflection, and the wake expands more. Second, the vortex systems are entirely different. For the VAWT wake, the vortices are generated around the blade tip, associated with the load variation during the blade rotation. In contrast, counter-rotating vortices appear at plate corners due to the plate perimeter's discontinuity in curvature. These vortices induce inward flows around the corners.

As indicated by the work of Rolin and Porté-Agel (2018), a VAWT can remarkably increase the momentum entrainment due to the presence of CVPs. In contrast, less momentum entrainment happens in the wake of a planar actuator disc since strong CVPs are lacking. This explains why the actuator disc wake suffers a higher velocity deficit in the near wake when the induced axial force is similar. Moreover, some outward flows appear at the plate edges because 1.5 diameter downstream is still in the near wake region, where wake expansion is still pronounced.
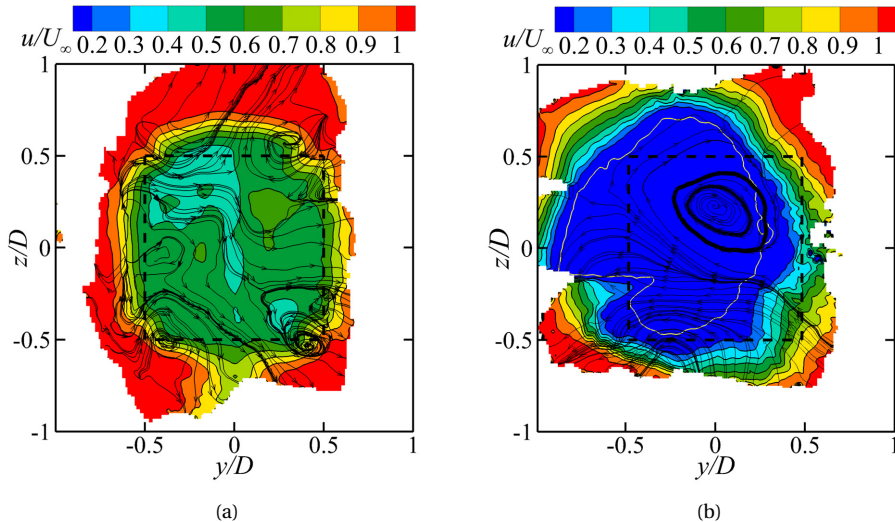
Figure 5.9: Streamwise velocity contour and in-plane streamlines at 1.5 D downstream the porous plate. (a) no yawing (b) with 15° yaw angle. The yellow contour line in (b) indicates where $u/U_\infty = 0$.

Wake deflection by yawing the actuator disc

Craig et al. (2017) has used a yawed rectangular porous mesh producing lateral deflection to mimic VAWT wake, and they concluded that a static actuator could produce a similar wake with VAWTs operating at low TSR (from 1 to 2). To examine the idea of representing a VAWT with a planar actuator disc, the velocity contours of a yawed actuator disc (with 15° yaw angle) are shown in figure 5.9-(b) and figure 5.10.

The cross-sectional streamwise velocity contour and in-plane streamlines at $x/D = 1.5$ is presented in figure 5.9-(b), the yellow contour line denotes where the velocity is zero. Inside the yellow contour line is a reverse flow region, which is quite large and is absent in the VAWT wake. In other words, the wake of yawed plate imparts a much higher velocity deficit and blockage than the VAWT's wake. The expansion is far more substantial, which implies a higher axial thrust exerted on the flow. The higher thrust is because the equivalent porosity is decreased when yawing the mesh, and lower porosity leads to higher blockage and thus more significant thrust.

The outline of the wake cross-section seems like a tilted cloverleaf in relation to the wake of a square actuator that is perpendicular to the inflow. This tilted shape is mainly caused by a strong cross-flow induced by a pair of strong vortices generated around the wake centre.

The wake centre at $x/D = 1.5$ is located around $y/D = -0.25$, similar to that of VAWT operated in $\lambda = 1.5$ and 2.5. In the horizontal ($xy-$) plane, as illustrated in figure 5.10, the time-averaged streamwise velocity and the in-plane streamlines of the yawed plate are depicted. A mask is implemented around the plate position, where a large error arises under the plate's strong reflection. A pronounced vortex is imparted on one side of the recirculation region, pushing the wake to the other side. Thus, the entire wake is deflected, including the "leeward" side ($y/D < 0$, following the convention of the VAWT wake in this work), even though the expansion is strong.
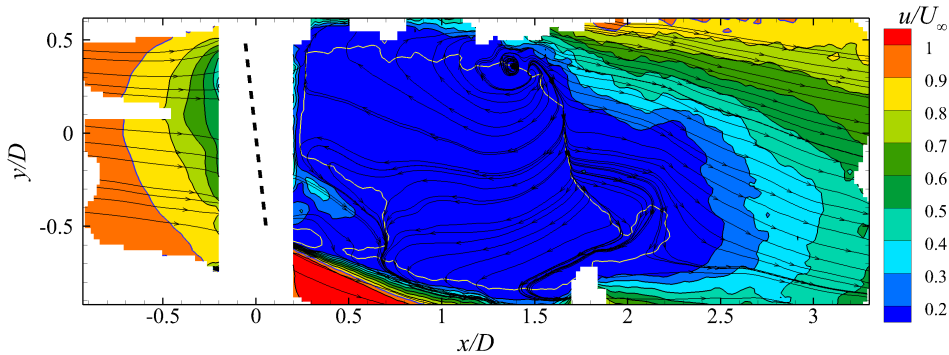

Figure 5.10: Time-averaged and normalized streamwise velocity contour and streamlines in the xy- plane in the wake of the porous plate, $z/D = 0$.

It should be noted that to match the velocity deficit and wake deflection with VAWT using a porous disc is tricky because yawing a mesh will change the projected porosity in the streamwise direction. Therefore, one should use a coarser mesh as a better surrogate. Additionally, the cross-sectional shapes of the wakes of the VAWT and the porous plate

features significant differences, making a planar actuator surface a poor representation of a VAWT.

5.5. CONCLUSIONS

In this study, the thrust coefficients and averaged streamwise velocity fields of a scaled VAWT operating at $\lambda = 1.5$ and $\lambda = 2.5$ are measured. A planar actuator with and without yaw is examined as a simplified surrogate of VAWT. The main findings are as follows:

1. Axial thrust of the VAWT model increases as λ goes higher, on the contrary, lateral thrust keeps nearly constant in lower λ (1 to 2.5) but decreases with higher λ (2.5 to 4.5).

2. Counter-rotating vortex pairs found in the VAWT wake are related to the lateral force, which induces a cross flow and results in asymmetric wake shape and deflection.

3. The VAWT wake is deflected towards the windward side. On the leeward side, wake expansion compensates for deflection, and streamlines around the leeward are almost aligned with the inflow.

4. Planar actuator disc imparting a similar streamwise thrust with a VAWT can cause a higher deficit in the wake. CVPs are present around the corners, and no lateral forces are induced when the porous plate is not yawed.

5. For yawed actuator disc, CVPs are present around the plate center; while for the VAWT, two strong CVPs are located at the blade tip.

6. Yawed actuator disc features a stronger velocity deficit and expansion in the wake, indicating an increased streamwise thrust.

III

WIND FARM AERODYNAMICS

6

ON THE WAKE DEFLECTION OF VERTICAL AXIS WIND TURBINES BY PITCHED BLADES

Wake losses are a critical consideration in wind farm design. The ability to steer and deform wakes can result in increased wind farm power density and reduced energy costs and can be used to optimise wind farm designs. This study investigates the wake deflection of a VAWT experimentally, emphasising the effect of different load distributions on the wake convection and mixing. A trailing vortex system responsible for the wake topology is hypothesised based on a simplified vorticity equation that describes the relationship between load distribution and its vortex generation; The proposed vorticity system and the resulting wake topology are experimentally validated in the wind tunnel via stereoscopic particle image velocimetry measurements of the flow field at several wake cross-sections. Variations in load distribution are accomplished by a set of fixed blade pitches. The experimental results not only validate the predicted vorticity system, but also highlight the critical role of the streamwise vorticity component in the deflection and deformation of the wake, thus affecting the momentum and energy recoveries. The evaluation of the various loading cases demonstrates the significant effect of the wake deflection on the wind power available to a downwind turbine, even when the distance between the two turbines is only three diameters.

6.1. INTRODUCTION

WAKE deflection is of practical interest to increase the power yield from wind farms of horizontal axis wind turbines. Compared to HAWTs, VAWTs have a significant potential to achieve a higher power density in a wind farm, as discussed in chapter 1. Hence, the ability to deflect wakes within an array of VAWTs would be of similar interest. The wake of VAWTs, however, is significantly more complex, and the physics underlying its deflection is still not fully understood.

This chapter examines the wake deflection of VAWTs by pitched blades, emphasising the 3D loading effect. The load of the VAWT is modelled via the 3D actuator cylinder model; The load distribution generates a vortex system responsible for the wake deflection. As proof of concept, we performed stereoscopic particle image velocimetry measurements in the wake of a lab-scale VAWT with different fixed-blade-pitch angles. The measurements were taken between one and ten diameters behind the turbine, encompassing both the near and far wake regions. The results confirm that the streamwise vortex system is responsible for most of the macro-behavioural characteristics of a VAWT's wake, including the deflection and deformation of the wake's shear layer. We analyse the vortex system and the recovery of the VAWT's wake under various pitch conditions, demonstrating that the vortex system can be effectively manipulated by varying the fixed-blade-pitch angles of the blades. Additionally, the physics revealed in this work sheds light on the VAWT array's wake control strategy.

The remainder of the chapter is structured as follows. In section 6.2, a theoretical analysis of the vortex system resulting from a 3D actuator cylinder is provided, explaining the underlying physics that is responsible for the wake deflection of VAWT; The theoretical analysis is followed by the descriptions of the experimental setup and the data analysis procedures. Section 6.3 and 6.4 present the results and key findings regarding the wake properties and the impact on VAWT arrays, respectively; Section 6.5 summarises the main findings of this chapter.

6.2. METHODOLOGY

6.2.1. RELATION BETWEEN THE VAWT LOADING AND THE WAKE TOPOLOGY

The wake topology and its development is a direct consequence of the force field generated by a wind turbine, as expressed by the vorticity equation (see appendix D); Different wake topologies will result in different wake deflections. Therefore, by understanding the relationship between the force field created by a VAWT and the wake topology it generates, we can interpret how force fields affect wake deflections. In this section, we use the 3D actuator cylinder model as an idealisation of a VAWT and apply the vorticity transport equation to understand the relation between the force field of a VAWT and the resulting wake topology. We discuss how certain load distributions generate trailing vortices, and how these vortices affect the wake topology and deflection, under the induced velocity concept (Anderson Jr, 1985).
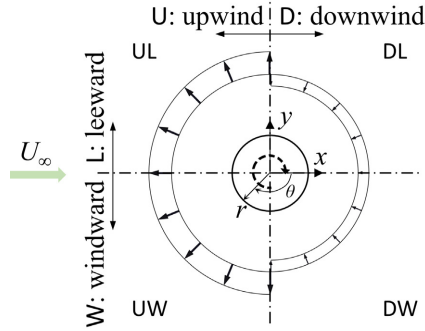
Figure 6.1: Top-view of a simplified three-dimensional actuator cylinder, the AC is divided into four regions following the convention of a clockwise rotating VAWT, with capital letters denoting corresponding quadrants (e.g., UW: upwind-windward).

THREE-DIMENSIONAL ACTUATOR CYLINDER

Here we introduce the idealisation of a VAWT based on the three-dimensional actuator cylinder model, which has been verified as a good representation of an H-type VAWT (Massie et al., 2019). The AC has a height-to-diameter ratio of one, the same as the VAWTs investigated in the literature (Tescione et al., 2014; LeBlanc and Ferreira, 2021, and etc.). For simplicity, assume the load is uniformly distributed in the upwind and downwind locations, respectively, with the upwind half loaded more heavily (figure 6.1). The latter is also the case for most H-type VAWTs with zero blade pitch in the literature (e.g., Madsen et al., 2014; Massie et al., 2019, and etc.); All the force vectors are perpendicular to the cylindrical surface, based on the previous observation that normal loading accounts for most of the total turbine loading (Leblanc and Ferreira, 2020). Moreover, the force vectors point to upwind, assuming that the loading from each region consumes/extracts streamwise kinetic energy of the inflow. The AC is divided into four quadrants as illustrated in figure 6.1, marked with UL, DL, DW, UW, respectively. The division follows the convention of a VAWT rotating clockwise. It is noted that the AC is static, and such division is only for the ease of discussion hereafter.

VORTICITY GENERATION BY THE ACTUATOR CYLINDER

We introduce here the principle of vorticity generation of actuator cylinders. The simplified vorticity equation for incompressible and inviscid flow is given by:

$$\rho \frac{D\boldsymbol{\omega}}{Dt} = \nabla \times \mathbf{f}, \tag{6.1}$$

where ρ is the air density, $\boldsymbol{\omega}$ and $\mathbf{f}$ are vorticity vector and body force vector, respectively. The equation holds for a VAWT for two reasons: a) due to the low Mach number, a flow field wherein a wind turbine is placed can be regarded as incompressible; b) the viscous terms can be neglected due to a sufficiently large diameter-based Reynolds number. However, this equation is only valid for the vorticity generation; if the vortex evolution needs to be resolved, the vortex stretching terms should be retained. More details about the derivation of equation 6.1 is provided in appendix D.
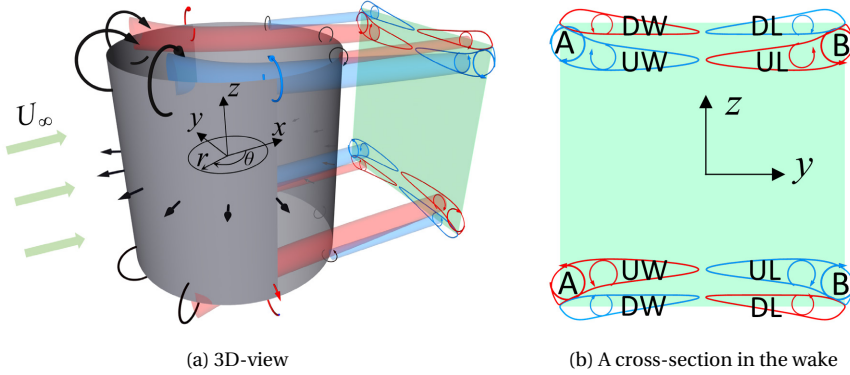
(a) 3D-view (b) A cross-section in the wake

Figure 6.2: Schematic of the trailing vortex system generated by an actuator cylinder. (a): 3D view. Curled arrows in black: trailing vortices; arrows in red and blue: streamwise components of the trailing vortices with positive and negative values, respectively. Tubular shade in red and blue: propagation paths of some of the streamwise vorticity. (b): A cross-section in the wake. A and B: two pairs of counter-rotating vortices with the largest streamwise vorticity on the windward and leeward side, respectively. Closed red and blue curves: regions with non-zero vorticity; Capital letters ("UW" and so on): the generation region of the vorticity; corresponding to the division in figure 6.1. Green square: the frontal area of the AC.

Now we apply the principle to the three-dimensional AC. Rewriting equation 6.1 in cylindrical coordinates, and eliminating the terms with zero value ($f_\theta = f_z = 0$), one obtains:

$$\rho \frac{D\omega}{Dt} = \nabla \times \mathbf{f}$$

$$= \frac{1}{r} \begin{vmatrix} \hat{e}_r & r\hat{e}_\theta & \hat{e}_z \\ \frac{\partial}{\partial r} & \frac{\partial}{\partial \theta} & \frac{\partial}{\partial z} \\ f_r & r f_\theta & f_z \end{vmatrix}$$

$$= \frac{1}{r} \left[\left(\frac{\partial f_z}{\partial \theta} - \frac{\partial (r f_\theta)}{\partial z} \right) \quad \left(-\frac{\partial f_z}{\partial r} + \frac{\partial f_r}{\partial z} \right) \quad \left(\frac{\partial (r f_\theta)}{\partial r} - \frac{\partial f_r}{\partial \theta} \right) \right] \begin{bmatrix} \hat{e}_r \\ r\hat{e}_\theta \\ \hat{e}_z \end{bmatrix} \quad (6.2)$$

$$= \begin{cases} \frac{\partial f_r}{\partial z} \hat{e}_\theta, \text{ when } r = \frac{D}{2}, z = \pm \frac{H}{2} \\ \frac{\partial f_r}{\partial z} \hat{e}_\theta - \frac{1}{r} \frac{\partial f_r}{\partial \theta} \hat{e}_z, \text{ when } r = \frac{D}{2}, |z| \leq \pm \frac{H}{2}, \text{ and } \theta = 90° \text{ or } 270° \end{cases}$$

where $\hat{e}_r, r\hat{e}_\theta, \hat{e}_z$ are the unit vectors for the r-,θ-, and z-axes, respectively.

Equation 6.2 reveals that the vorticity is mostly generated along the top and bottom edges of the AC, except for the spanwise vorticity generated along the connections of the upwind and downwind half of the AC. An overview of resulting trailing vortex system is illustrated schematically in figure 6.2-(a), with the black curled vectors denoting the trailing vortices, red and blue vectors are the streamwise vorticity components pointing to the positive and negative x-axis, respectively. The spanwise vorticity is not presented. The propagation paths of some of the streamwise vorticity are shaded.

For the upwind half of the AC, vortices along the periphery of the cylinder induce an inboard velocity component on the top and bottom lids of the cylinder. On the contrary, the downwind part produces the opposite, with the vortices creating an outboard velocity component. Therefore, the upwind trailing vortices are transported more to the centre plane ($z/D = 0$) compared to downwind ones, as illustrated with the shaded paths in figure 6.2-(a). In figure 6.2-(b), a cross-section in the near wake is presented, where only streamwise vortices are presented. This is because the streamwise vorticity is deemed to be the most important factor related to the wake deflection and deformation (e.g., Rolin and Porté-Agel, 2018; Bastankhah et al., 2021b). In the cross-section, the green square is the frontal area of the AC. The vortices marked with A and B are the strongest streamwise counter-rotating vortex pairs (CVPs) appear in the windward and leeward of the wake, respectively. Closed curves that are marked with capital letters represent the region with non-zero streamwise vorticity: red for the positive and blue for negative. The capital letters are for different quadrants shown in figure 6.1, denoting the generation region of the vorticity. Such streamwise vortex system is verified in section 6.3.4.

WAKE DEFLECTION INCURRED BY THE STREAMWISE VORTICITY
To understand the pattern of wake deflections, we further simplify the hypothesised streamwise vorticity system proposed in section 6.2.1, based on the previous simulation results on the wake topology of actuator cylinders (De Tavernier et al., 2020). The simplification is illustrated in figure 6.3. The strongest vortex pairs A and B at windward and leeward side are illustrated as they are deemed the primary reason for the wake deflection and deformation. In contrast, double-layer vorticity regions (closed curves in figure 6.2-(b)) are neglected, under the assumption that vortices at those regions will eventually merge with the stronger vortices A and B in the far wake. Four ideal force fields are presented in figure 6.3 to demonstrate the concept. The initial wake shape is assumed to be a square that is the same as the frontal area of the AC. The wake is deformed under the velocity induced by the streamwise vorticity; The wake shapes after deformation is depicted with the closed black curves.

When the resulting lateral force is null (figure 6.3-(a) and figure 6.3-(b)), the wake deforms but does not experience a lateral deflection. With the upwind half loaded more, the wake expands more horizontally. In contrast, when the downwind half is loaded more, the wake is stretched vertically. On the other hand, wake deflections occur when the resulting lateral force is not null. For example, applying more load in the UW region, as depicted in figure 6.3-(c), will increase the strength of the CVP-A, resulting in a wake deflection towards the windward side. On the leeward side, the vorticity generated from upwind and downwind has the same magnitude and the opposite direction; thus, in the first approximation, the generated streamwise vortices cancel out. Conversely, when the DW region is loaded more than the other regions, the wake deflects towards the leeward side, as illustrated in figure 6.3-(d).

In all, the wake deflection of an AC (a simplified VAWT) is due to an overall lateral force, and is accompanied by a deformation which is closely related to the dominating CVPs appearing in the wake. It is worth mentioning that the four cases in figure 6.3 are extremely simplified; For a VAWT under more realistic working conditions (e.g., dynamic inflow, dynamic stall, etc.), the wake topology will be more complicated, with the location and strength of CVP A and B varying. Nonetheless, those complex configurations

can be described with combinations of the four cases above, and this is verified with the experimental results presented in section 6.3.4.
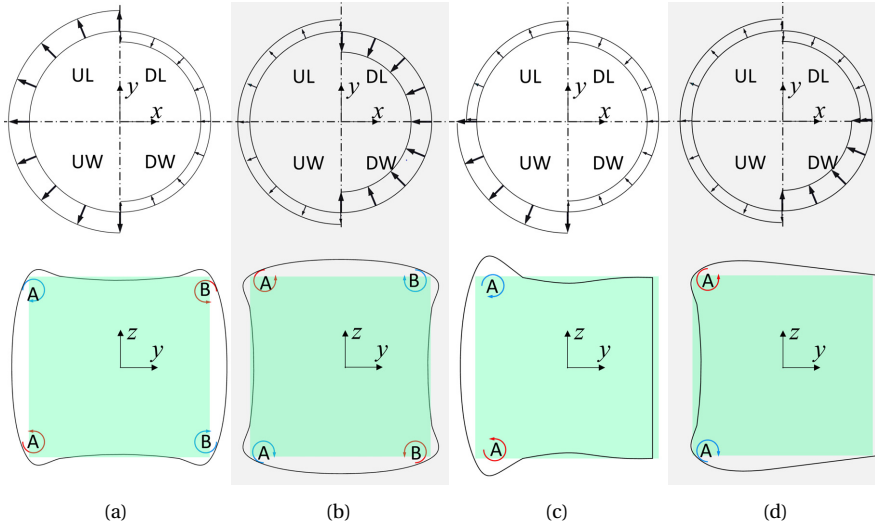

Figure 6.3: Schematic of wake deflections caused by 3D actuator cylinders with different force fields. The first row shows the force fields and the second row consists of the resuting wake topologies. The incoming flow direction and the coordinate system follows those in figure (a). (a) and (b): the ACs are loaded equally windward and leeward, but loaded more heavily upwind or downwind, respectively; (c) and (d): the ACs are loaded more at UW and DW regions, respectively.

6.2.2. EXPERIMENTAL SETUP

WIND TUNNEL FACILITY AND VAWT MODEL

The experiments are conducted in the Open-Jet Facility (OJF) of the TU Delft Aerospace Engineering Laboratories. The OJF features an open exit of 2.85×2.85 m^2, and a turbulence intensity lower then 2% within the test region at the free-stream velocity of $U_\infty = 5\,\text{m s}^{-1}$ (see Lignarolo et al., 2015). The uniform-flow region reduces to 2×2 m^2 at 6 m ($20D$) from the jet exit, which covers the entire area of interest even for the case with significant wake deflection (P10 as introduced in section 6.2.2).

The tested VAWT is an H-type, with a rotor size of 30×30cm (Huang et al., 2020). The resulting Reynolds number based on the diameter is about 1.0×10^5. The tip speed ratio $\lambda = u_t/U_\infty$ is fixed to 2.5 to keep a moderate thrust coefficient and a comparable working condition for all the cases studied, where u_t denotes the linear speed of the blades. The pitch conditions are illustrated in figure 6.4. The attributes of the VAWT are listed in table 6.1, while a sketch of the device can be seen in figure 6.4. It is noted that no ground effect is considered in the experiment.

LOAD MEASUREMENT

A three-component balance that is in-house designed and constructed is employed for the load measurement, enabling quantification of both the drag (equals to the VAWT's
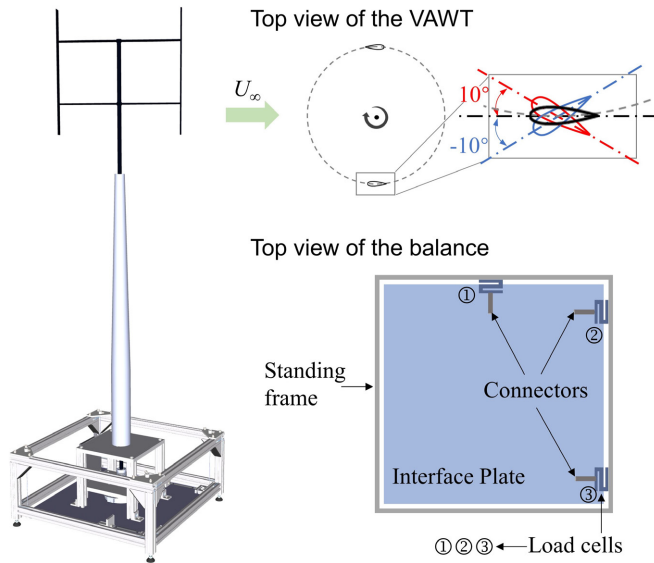
Figure 6.4: Schematic of the tested VAWT model mounted on the in-house designed balance.

Table 6.1: Attributes of the VAWT model

Symbol	Parameter	Value
N_s	number of struts	4
B	number of blades	2
D	rotor diameter (m)	0.3
c	chord length (m)	0.03
D_t	tower diameter (m)	0.01

thrust) and the lateral force.

The balance consists of three S-shape load cells (type: KD40s, max range ±50N, max error ≤ 0.1%), with two of them measuring the streamwise force (drag/thrust) while the other one measuring the lateral force. These load cells are mounted on the bottom part of the same standing frame that is stiff enough to avoid severe vibration and deformation. The other ends of the load cells are connected to the interface plate, on which the VAWT is mounted, using specially designed connectors. Those special connectors are flexural rods that transmit forces only along their spanwise, delivering no moment. They make sure the load cells measure only the tensile or compressive forces (no shear forces are applied). The interface plate is lifted with four steel strings; together with the load cells, they allow for minor structural deformation in the directions of the flexural rods while preventing rotations caused by the torque (figure 6.4). When the flexural rods are aligned with streamwise and lateral forces respectively, the overall uncertainty of the force measurement is of the same level as the load cells.

Compared with the previous balance system proposed in Huang et al. (2020), the

current design forms a cantilever system so that all the horizontal forces applied to the VAWT will be balanced and thus measured by the load cells, yielding more accurate measurements.

Stereoscopic particle image velocimetry

A stereoscopic particle image velocimetry (PIV) setup is used to measure the velocity fields in cross-sections of the VAWT's wake. A SAFEX smoke generator releases water-glycol seeding particles of average 1 μm diameter. A Quantel *Evergreen* double-pulsed Nd:YAG laser produces pulses with 200 mJ energy at a wavelength of 532 nm within a laser sheet of approximately 3 mm thickness. The seeding particles are imaged by two LaVision's Imager sCMOS cameras in successive cross-sections of the wake. In doing so, a traversing system is employed whereby the stereo-PIV setup is mounted on, enabling navigation from 1 to 10 diameters (D) downstream with a step of 1D. An overview of the experimental setup is shown in figure 6.5; With the illustrated setup, a field of view (FoV) of approximate 80 × 55 cm is achieved. More technical specifications are listed in table 6.2.

Table 6.2: Technical specifications of the stereo-PIV setup.

	Tracer particle	Water-glycol particles
Seeding	Particle size	1 μm
	Particle density	10^3 kg m^{-3}
Illumination	Pulse energy	2 × 200 mJ
	Wavelength	532 nm
	FoV	approx 800 × 550 mm^2
	Active sensor	2560 px × 2160 px
Imaging	Pixel pitch	6.5 μm
	Acquisition frequency	15 Hz
	Δt	230 μs
Optics	Focal length	50 mm
	Numerical aperture	4
	Interrogation window size	32 px×32 px (8.22 × 8.22 mm^2)
Data processing	Overlap factor	75%
	Vector pitch	2.055 mm

Uncertainty of the flow field measurement

Following the work of Sciacchitano and Wieneke (2016), we introduce the uncertainties of relevant quantities here. This work deals with the time-averaged velocity, of which the standard uncertainty can be calculated as:

$$U_{\bar{U}} = \frac{\sigma_U}{\sqrt{N}}, \tag{6.3}$$

where σ_U is the standard deviation of the velocity U, which has three components u, v, w, respectively. For its streamwise component (the out-of-plane velocity), σ_u

①camera 1 ②camera 2 ③VAWT ④force balance ⑤laser sheet ⑥stereo-FoV
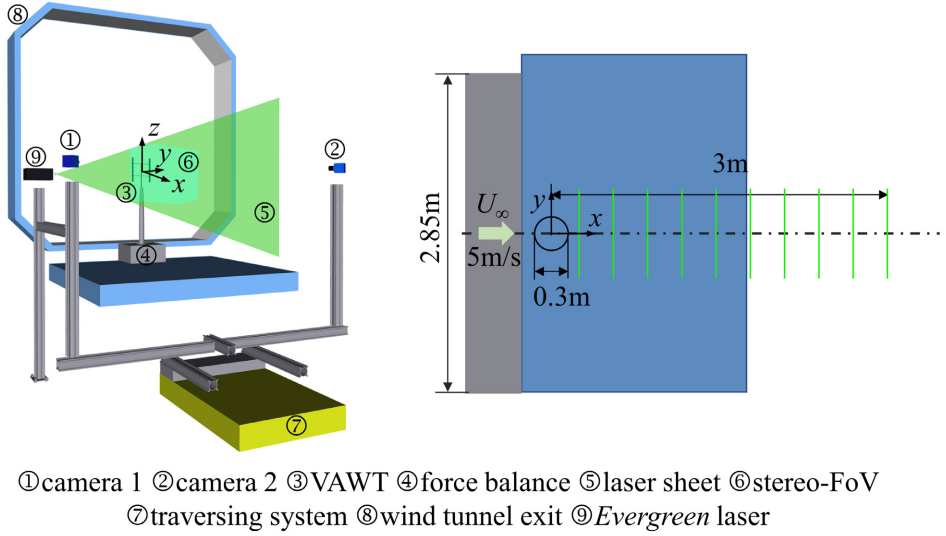⑦traversing system ⑧wind tunnel exit ⑨*Evergreen* laser

Figure 6.5: Left: Schematic of the experimental setup with the equipment labelled. The origin of the coordinate system is placed at the centre of the rotor. Right: a sketch of the top view presenting the size of the setup and the PIV acquisition locations.

reaches its highest value typically at the shear layer, not exceeding $0.6\,\mathrm{m\,s^{-1}}$. The effective number of samples N is around 400, resulting in uncertainty values below $0.03\,\mathrm{m\,s^{-1}}$ (less than 1% of local velocity) in the shear layer. For the in-plane velocity components (v and w), smaller standard deviations in the shear layer around $0.4\,\mathrm{m\,s^{-1}}$ are obtained. Following equation 6.3, the maximum value of $U_{\bar{v}}$ or $U_{\bar{w}}$ is $0.02\,\mathrm{m\,s^{-1}}$.

The uncertainty of the time-averaged out-of-plane (i.e., streamwise) vorticity is formulated as:

$$U_{\bar{\omega}_x} = \frac{U_{\bar{v}\,\text{or}\,\bar{w}}}{d}\sqrt{1 - \rho(2d)}. \tag{6.4}$$

where $U_{\bar{v}\,\text{or}\,\bar{w}}$ is the uncertainty of time averaged in-plane velocity vectors. d and $\rho(2d)$ denote grid spacing of the interrogation window and cross-correlation coefficient of spatially correlated velocities, respectively. As listed in table 2, $d = 8.22$ mm. For the interrogation window size and overlap factor adopted in the present work (see table 2), $\rho(2d) \cong 0.45$ Sciacchitano and Wieneke (2016). Hence, the value of $U_{\bar{\omega}_x}$ is lower than $1.81\ \mathrm{s^{-1}}$.

The uncertainty of the Reynolds normal stress is given by:

$$U_{R_{uu}} = \sigma_u^2\sqrt{\frac{2}{N-1}} \leqslant 0.025\ \mathrm{m^2\,s^{-2}}. \tag{6.5}$$

Similarly,

$$U_{R_{vv}} = U_{R_{ww}} \leqslant 0.006\ \mathrm{m^2\,s^{-2}}. \tag{6.6}$$

Furthermore, the uncertainty of the turbulence kinetic energy (TKE) is expressed as:

$$U_{\text{TKE}} = \frac{1}{2}\sqrt{U_{R_{u\omega}}^2 + U_{R_{vv}}^2 + U_{R_{ww}}^2} \leqslant 0.014\,\text{m}^2\,\text{s}^{-2}, \tag{6.7}$$

where TKE $= \frac{1}{2}\overline{u_i'u_i'} = \frac{1}{2}(R_{uu} + R_{vv} + R_{ww})$.

CASES DESCRIPTION

In order to modify the load distribution of the VAWT, and investigate the effect of fixed blade pitch on the wake development, three cases with $-10°$, 0, and $10°$ pitch angles are selected. The convention of the sign of the pitch angles is indicated in figure 6.4, with the blade pitching towards the rotating axis as positive. For simplicity, the cases are numbered in table 6.3. It is worth noting that these extreme pitch angles were chosen to emphasize the pitched blade's significant effect on wake deflection. The effect of these pitch angles on dynamic stall is beyond the scope of this work. However, here we qualitatively discuss where dynamic stall occurs in different pitch cases and how it yields different loading over the swept area of VAWT blades. In doing so, we calculate the blade's angle of attack (α) while rotation using the 2D AC model proposed by Madsen (1983). For simplicity, the lift-drag polar of a flat plate is adopted, without dynamic stall correction. The results, as illustrated in figure 6.6, indicate the dynamic stall regions, where exceedingly high $|\alpha|$ is perceived. For instance, for P10 case, the blades operate above the static stall angle within the upwind half of the rotor, while the most severe flow separation and aerodynamic force drop likely occur in the windward-leeward region ($\theta \approx 100°$). On the contrary, the P-10 would feature dynamic stall at the downwind rotor.

Table 6.3: Configurations

Case	Description
P-10	With pitched blades, - 10 degree
P0	Zero pitch angle
P10	With pitched blades, + 10 degree

6.2.3. WAKE ANALYSIS PROCEDURES

WAKE CENTRE

To compare the deflections quantitatively, the wake centre is calculated with a "centre of mass" method with respect to the velocity deficit; this method is widely accepted in characterising the wake topology of wind turbines (Howland et al., 2016; Wei et al., 2021):

$$y_c(x) = \frac{\iint y\Delta\bar{u}(x,y,z)\text{d}y\text{d}z}{\iint \Delta\bar{u}(x,y,z)\text{d}y\text{d}z}, \tag{6.8}$$

where $\Delta\bar{u}(x,y,z) = U_\infty - u(x,y,z)$. The integrals are computed over cross-sectional planes, perpendicular to the streamwise velocity. Only the horizontal coordinate of the wake centre is discussed in this article, since the pitched blades mainly yield lateral deflection of the wake.
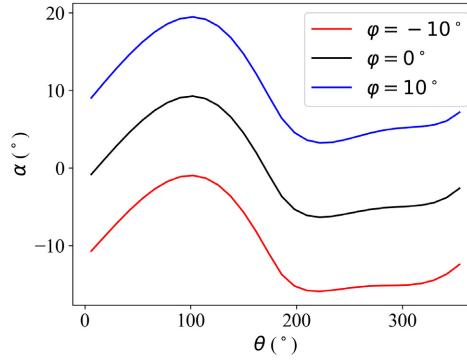
Figure 6.6: A schematic of blade pitch effect on the angle of attack variation. φ: the angle of fixed blade pitch.

STREAMWISE MOMENTUM BUDGETS

The Reynolds averaged Navier-Stokes equation is rearranged as equation 6.9 to inspect the budget of streamwise momentum. This process is widely adopted to identify the main contributors to the momentum recovery (e.g., Boudreau and Dumas, 2017; Bossuyt et al., 2021), the latter is critical in a wind farm. In equation 6.9, the viscous terms are neglected due to the sufficiently high Reynolds number in the wake (1×10^5, based on the rotor diameter):

$$\underbrace{\bar{u}\frac{\partial \bar{u}}{\partial x}}_{} = \underbrace{-\bar{v}\frac{\partial \bar{u}}{\partial y} - \bar{w}\frac{\partial \bar{u}}{\partial z}}_{\text{advection}} \underbrace{-\frac{1}{\rho}\frac{\partial \bar{p}}{\partial x}}_{\text{pressure}} \underbrace{-\frac{\partial \overline{u'u'}}{\partial x} - \frac{\partial \overline{u'v'}}{\partial y} - \frac{\partial \overline{u'w'}}{\partial z}}_{\text{Reynolds stress}}, \tag{6.9}$$

where u, v, w represents streamwise (x-), transverse (y-) and vertical (z-) velocities, respectively, p is pressure, and ρ is density. Overlines stand for time-averaging, and primes for fluctuations.

The equation is constituted by 3 parts, i.e., the advection terms, the pressure term, and the Reynolds stress terms. Except for the streamwise advection term $\bar{u}(\partial \bar{u}/\partial x)$, the remaining terms are written to the right-hand side (RHS) to examine their contributions to the streamwise momentum recovery.

AVAILABLE POWER

Different momentum recovery will cause different available power distribuion in the wake. To visualise the impact of the wake deflection on the available wind power (AP) distribution under different pitched blade conditions, and identify the best location for a downwind wind turbine in array configurations, a moving average of the coefficient of available streamwise wind power ($\bar{u}^3/U_\infty^3$) within the frontal area of a hypothetical downwind VAWT is presented in section 6.4.3. The calculation procedure is presented as follows. The calculation is formulated as:

$$\begin{cases} f_{AP}\left(x_0, y_0, z_0\right) = \iint_S \bar{u}^3\left(x_0, y, z\right)/U_\infty^3 \, \mathrm{d}z \, \mathrm{d}y/(DH) \\ S: \left|y - y_0\right| \leqslant 0.5D, |z| \leqslant 0.5H \end{cases}, \tag{6.10}$$

where f_{AP} represents the coefficient of available power. (x_0, y_0, z_0) is the coordinate of the centre of the hypothetical downwind VAWT. D and H are the diameter and the height of the VAWT. The hypothetical VAWT has the same dimension as the pitched (upwind) VAWT. The integration and average is performed within a translating square with the same area as that of the VAWT. A schematic of the integration window and its coordinate system is depicted in figure 6.7: At a given cross-section ($x = x_0$) downstream of the upwind VAWT, the solid blue box is the current integration window, while the dashed one is the projection of the upstream turbine. The coordinate system, specifically the horizontal axis y for figure 6.7, is defined as follows: the origin is the centre of the dashed box, y is positive towards the right. The contour in the background represents the integrated quantity, in this case is the normalised streamwise wind power, $\bar{u}^3/U_\infty^3$.
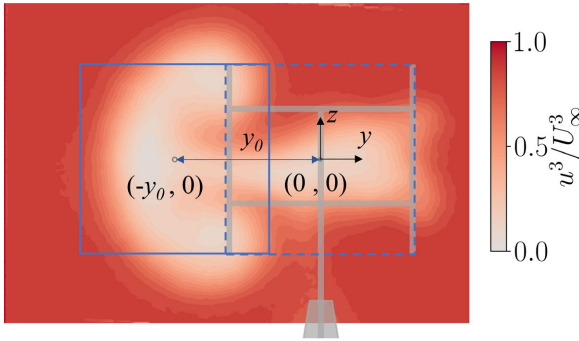

Figure 6.7: Schematic of the integration window for AP estimation. Square with solid blue line: integration window moving transversely; Dashed square: frontal area of the VAWT; Background contour: the normalised streamwise wind power, $\bar{u}^3/U_\infty^3$.

A theoretical comparison of f_{AP} based on the classical actuator disc (AD) theory is provided as well. The AD model is extremely simplified in that only considers the streamwise momentum conservation, whereas no recovery and no deflection is accounted for in the model. The AD model is well accepted for estimating the maximum velocity deficit and minimum f_{AP} in the near wake of a wind turbine. It has been adopted in the most advanced engineering wake models (Stevens and Meneveau, 2017; Porté-Agel et al., 2020). The model takes the streamwise thrust coefficient $C_{T,x}$ as input, calculating the induction factor $a = (1 - \sqrt{1 - C_{T,x}})/2$, and further the minimum wake velocity $u_w = (1 - 2a)U_\infty$. In this way, the minimum coefficient of AP for a hypothetical downwind wind turbine that is inline with the upwind one can be estimated as:

$$f_{AP|AD} = \bar{u}_w^3/U_\infty^3 = (1 - C_{T,x})^{3/2} \tag{6.11}$$

6.3. RESULTS AND DISCUSSION

6.3.1. THRUST AND LATERAL FORCE

The streamwise and lateral thrusts ($C_{T,x}$ and $C_{T,y}$) are given by:

$$C_T = \frac{T}{0.5\rho U_\infty^2 A}, \tag{6.12}$$

where T is the measured thrust, equivalent to the force perceived by the turbine. $A = DH$ is the frontal area of the turbine. As it can be seen in the results of table 6.4, the negative pitched angle slightly decreases the thrust and the lateral force, compared to the zero-pitch case. This is caused by two factors: a) the blades work in a decreased angle of attack during the upwind pass; b) deep stall occurs on the downwind pass. These factors result in a decreased blade loading along the revolution passage, and therefore an overall decreased thrust and lateral force. Such phenomenon has been confirmed by both load and flow field measurements performed on the blades of a larger H-type VAWT (LeBlanc and Ferreira, 2021). In contrast, positive pitch increases both streamwise and lateral force by 25% and 180%, respectively. Besides that, LeBlanc and Ferreira (2021) reported significantly increased blade load in the upwind-windward region, and a sudden drop in the upwind-leeward region. The same happens in the current measurement, which can be justified by the averaged velocity deficit fields presented in section 6.4.1. That is, P10 features a deeper momentum deficit on the windward side compared with P0, while less deficit on the leeward side.

Table 6.4: Measured $C_{T,x}$ and $C_{T,y}$.

Case	$C_{T,x}$	$C_{T,y}$
P-10	0.60	0.09
P0	0.65	0.14
P10	0.81	0.39

6.3.2. Velocity fields

The measured time-averaged streamwise velocity contour and in-plane velocity vectors are presented in figure 6.8. The velocities are normalised with the free stream velocity U_∞. The wake of P-10 features a minimum streamwise velocity around 0.3 U_∞. The outline of the wake cross-section in the near wake region ($x/D = 1$) is a square that is elongated along its vertical symmetric axis. The elongation lasts to the far wake.

The case with zero pitch, P0, features a similar maximum velocity deficit and a slightly larger wake deflection compared to P-10 based on the visual comparison of the contour colour. The similarity between the two wakes is attributed to the similar streamwise and lateral thrust exerted by the turbine, which can be justified by the load measurement results listed in table 6.4. However, large discrepancies in terms of the cross-sectional shapes of the wake between these two cases are observed. The outline of P0's wake cross-section is formed into a trapezoid at $x/D = 1$ instead of the stretched square for P-10. The difference of the wake outlines is attributed to distinct streamwise vorticity distributions, which are further discussed in section 6.3.3.

In contrast, the wake of P10 presents a remarkable lateral deflection towards windward and a cross-sectional deformation as predicted in figure 6.3-(c). Guo and Lei (2020) reported similar cross-sectional shapes using RANS simulation integrated with the actuator line model (Bachant et al., 2016). Besides, P10 features a larger wake region and a deeper velocity deficit in the proximity of the turbine, which are ascribed to stronger lift produced by the advancing blades at windward side, resulting in a larger side force in-
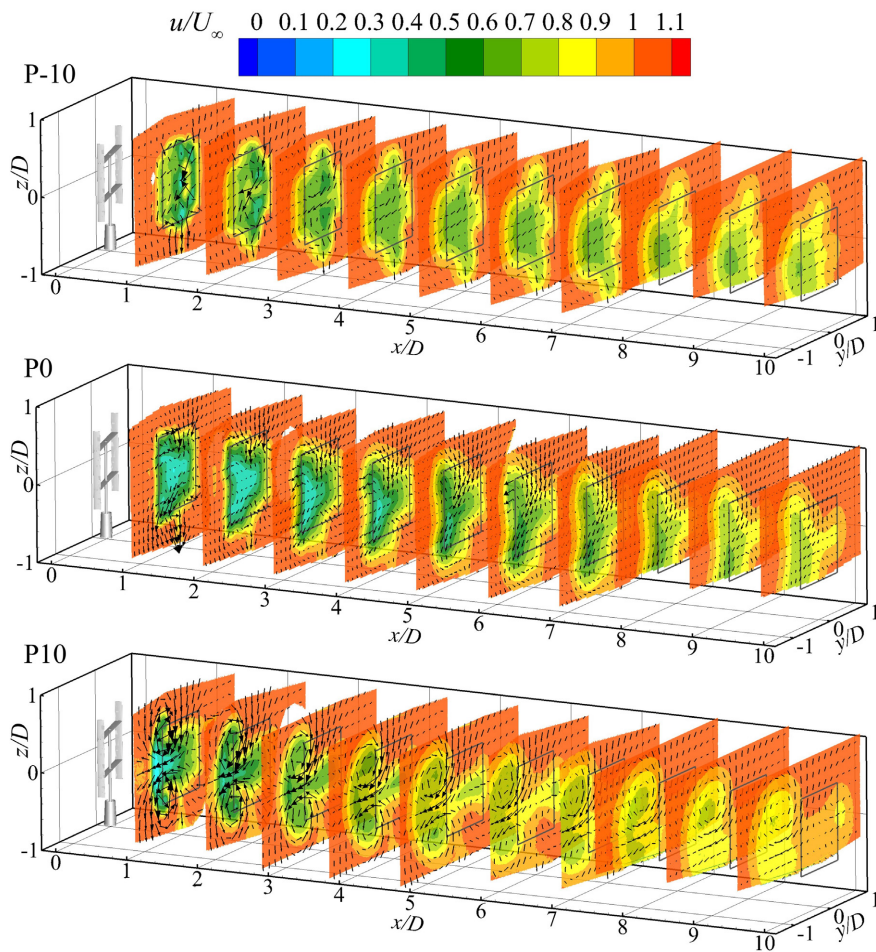
Figure 6.8: Contours of normalised stream-wise velocity with in-plane velocity vectors from 1 to 10 *D* after the VAWT. The VAWT rotates clockwise when looking from the top. The grey box denotes the projected frontal area of the VAWT.

ducing lateral velocities. A similar phenomenon has been documented in the literature (see Rolin and Porté-Agel, 2018; Ryan et al., 2016; Huang et al., 2020).
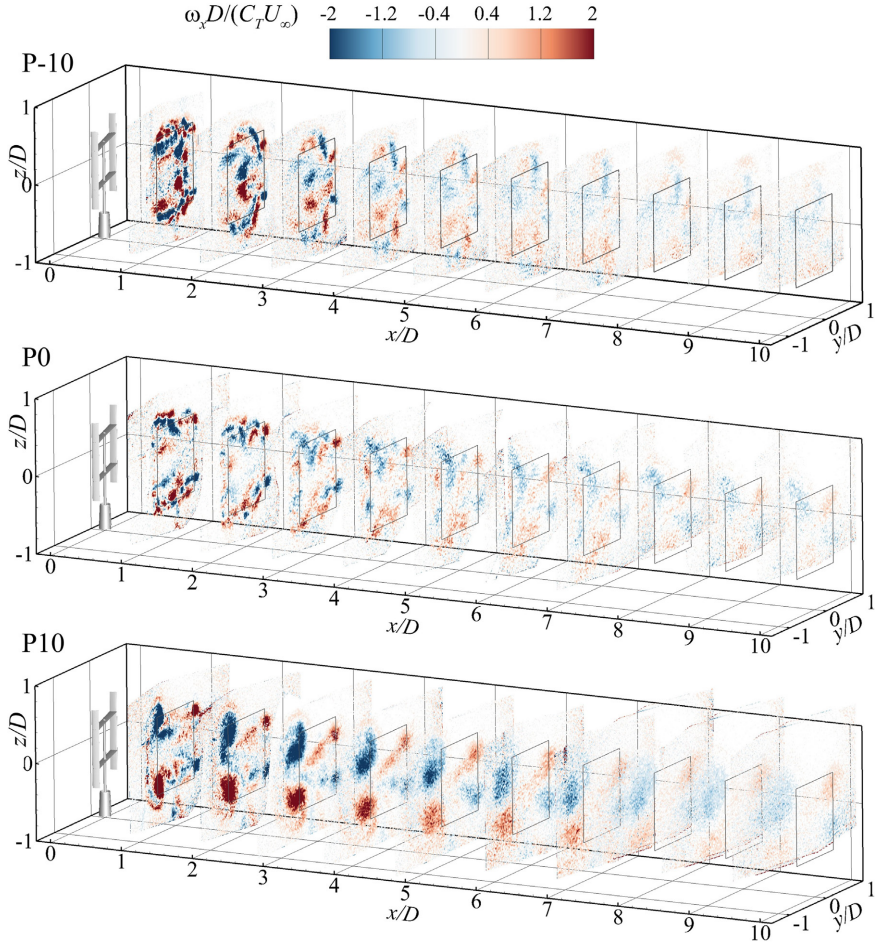
Figure 6.9: Contours of normalised streamwise vorticity. The centre of the rotor is placed at the origin; grey squares in the successive cross-sections denote the projection of the frontal areal of the VAWT.

6.3.3. STREAMWISE VORTICITY

An overview of the normalised streamwise vorticity fields is presented in figure 6.9. The streamwise vorticity plays a key role in forming the wake shape until at least $5D$ downstream of the VAWT model, and is still noticeable at $x/D = 10$. The vorticity is normalised with $C_{T,x}U_\infty/D$. While normalisation for vorticity using U_∞/D is well accepted in the literature (Wei et al., 2021; Rolin and Porté-Agel, 2018), the values of $C_{T,x}$ are also used in the current study to compensate the effect of different loading level. The use of the thrust

coefficient in the normalisation of the vorticity is chosen because the wake deflection is analysed in relation to the deflection of thrust vectors, and the vorticity generated remains proportional to both the crossflow component and the balance between upwind and downwind loading. For vectors with different magnitudes, the overall lateral force can be the same, so as the wake deflection. However, the local vorticity magnitude will be completely different. To avoid such deviation and make the vorticity magnitude consistent with the deflection, the force magnitude should be taken into account for normalisation. And we select the the main component, the streamwise thrust coefficient, for simplicity.

The streamwise vorticity is mainly produced by the trailing vortices that are generated at the blade tips according to Helmholtz's theorem (Ryan et al., 2016; Wei et al., 2021). By pitching the blade, the blade load along its rotation passage is modified, and so is the vortex system. As discussed in section 6.3.2, P-10 and P0 feature largely different wake shapes as they possess different blade loads, although the integrated thrusts are similar. P10 features two pairs of strong counter-rotating vortices at windward and leeward, respectively.

6.3.4. VERIFICATION OF THE HYPOTHESISED VORTICITY SYSTEM

We compare the measurement results with the vorticity system proposed in section 6.2.1 by identifying the components illustrated in figure 6.2-(b). The normalised streamwise vorticity fields at $x/D = 1, 3, 5$ are presented in contour plots in figure 6.10, together with the in-plane streamlines that are helpful in locating the strong counter-rotating vortex pairs. The green contour lines are plotted where $\bar{u}/U_\infty = 1$, representing the shape of the wake. The first row of figure 6.10 depicts the initial topology of the streamwise vortical system in correspondence to the hypothesis, the second and the third rows show the development of the streamwise vorticity at $x/D = 3$ and 5, and the CVPs in the wake.

Due to the absence of the ground, the vorticity field is almost symmetrical with respect to $z/D = 0$, and the symmetry is slightly broken when the wake of the tower starts to interact with the wake of the rotor, after $x/D = 5$. Based on the symmetry, only the upper halves of the wakes are marked in relation to the hypothesised vortical system. For all the cases, the hypothesised double-layer vorticity structures are clearly present initially at $x/D = 1$. The upper layers are generated in the downwind region of the rotor, while the lower layers are generated upwind. It is worth mentioning that there exists strong vorticity near $y/D = 0 \sim 0.5$ and $z/D = -0.25 \sim 0.25$, in the wake of P-10 at $x/D = 1$, as illustrated in figure 6.10. This is due to a concentration of vorticity on the blades causing vortex roll-up. Apart from that, the propagating and merging of the vorticity field still follow the proposed model. However, further investigations are required if details such as vortex rolling-up and stretching need to be modelled.

The strong counter-rotating vortices are identified based on the in-plane streamlines. The cross-sections at $x/D = 3$ and 5 provide a cleaner view of the CVPs because the merging of the vortices occurs and only strong CVPs are left. The merging process is as follows: the smaller vortices will change their directions of rotation under the effect of the stronger vortex, and then merge with the latter into a larger region with a weaker vorticity. For all the cases, the double-layer structure starts to break at $x/D = 3$ and disappears at $x/D = 5$.
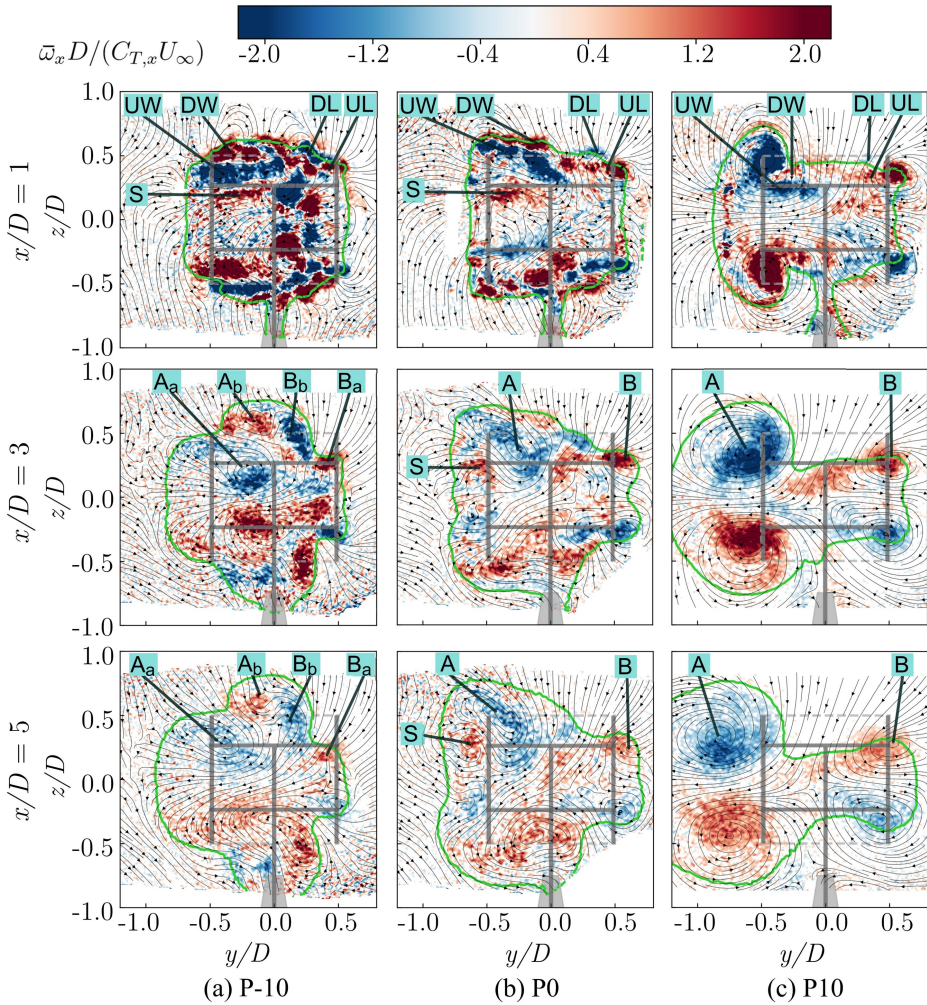
Figure 6.10: Contours of streamwise vorticity with in-plane streamlines for P-10, P0 and P10 at $x/D = 1, 3, 5$. The generation regions of the vorticity are marked corresponding to those in figure 6.2. Green contour lines: $u/U_\infty = 1$; A and B: the strong vortices on the windward side and leeward side; S: the vorticity generated due to the presence of the struts.

P-10 features four pairs of CVPs in the wake, and its vorticity system is a combination of the pattern (a) and (b) in figure 6.3. The CVP-A_a is slightly stronger than the CVP-B_a, resulting in a slight deflection to negative y. The CVP-A_b and CVP-B_b are responsible for the vertical expansion of the wake.

The vorticity system of P0 and P10 can be described with an asymmetrical version of pattern (a). In both cases, the CVP-A induces a larger transverse velocity to the windward side, and thus results in a wake deflection. The distinct differences are: 1) the location of the CVP-A: In the wake of P0, the CVP-A is located around the centreline of the rotor

($y/D = 0$), whereas the one in P10 is located around the edge of the wake at the windward side; 2) The strengths of the CVPs: in P10, the CVPs are so strong that merging of streamwise vortices occurs significantly. The CVPs entrain other streamwise vortices and merges them into larger regions much faster than P-10 and P0: At $x/D = 3$ the trace of weaker vortices is almost gone in the wake of P10. These differences are responsible for the distinctions in the wake deflection and deformation.

Additionally, the vorticity generated due to the presence of the struts is marked with capital S. This vorticity has a small effect on the wake deformation, which can be appreciated in the wake of P0 at $x/D = 5$.

6.3.5. TURBULENCE INTENSITY

The turbulence intensity magnitude $I_{|U|} = \sqrt{\overline{u'u'} + \overline{v'v'} + \overline{w'w'}}/U_\infty$, is illustrated in figure 6.11. For all the cases, $I_{|U|}$ is mostly concentrated at the interface between the freestream and the wake, i.e., the perimetre of the wake cross-section. As indicated in the previous study by the authors (Huang et al., 2020), the longer the perimeter, the faster momentum recovery due to the turbulent diffusion and shear is expected, provided that the overall streamwise thrust is the same.

The turbulence intensity fields correlate well with the vorticity fields, with high $I_{|U|}$ in regions of strong vorticity. In P-10, the maximum turbulence intensity concentrates around the centre right of the wake, which is also the region of the standing out CVPs discussed in section 6.3.4. P0 and P10 feature the same pattern, with the maximum $I_{|U|}$ at the spots of the CVPs. Besides that, the $I_{|U|}$ contours depict the shape of the wake perimeter.

6.4. THE IMPACT OF PITCHED BLADES ON VAWT ARRAYS

6.4.1. VELOCITY DEFICIT AND WAKE CENTRE DEVELOPMENT

The distributions of streamwise velocity deficits (($\bar{u} - U_\infty)/U_\infty$) for all the cases are compared in figure 6.12, where the cross-sections at $x/D = 1, 3, 5$ are presented. From left to right are case P-10, P0, and P10, which generate deficit areas that feature shapes of octagon, trapezoid, and left-arrow at $x/D = 1$, respectively. The maximum deficit of P-10 is shifted slightly to the right compared to P0; P10 shifts to the left largely, which is clearly attributed to the larger side force generated by the VAWT at positive pitch, and hence to the strong counter-rotating vortices in the wake.

The in-plane velocity vectors disclose the trace of at least two pairs of streamwise CVPs, as discussed in section 6.3.4. With the effects of these CVPs, the wake shapes are quickly deformed along the streamwise directions: those of P0 and P10 become thinner vertically at $y/D = 0$, whereas the wake of P-10 expands remarkably along the spanwise direction z.

The wake centre developments are compared in figure 6.13. As expected, the positive pitch produces the largest deflection towards the windward side (negative y), which is nearly twice that of the P0 case; instead, the wake deflections of the P0 and P-10 cases are very similar, with the negative pitch yielding slightly larger deflection after $x/D = 5$. All the cases feature approximately linear wake deflections within near wake ($5D$), which is also observed in the wake of HAWTs with a constant yaw angle Howland et al. (2016). It
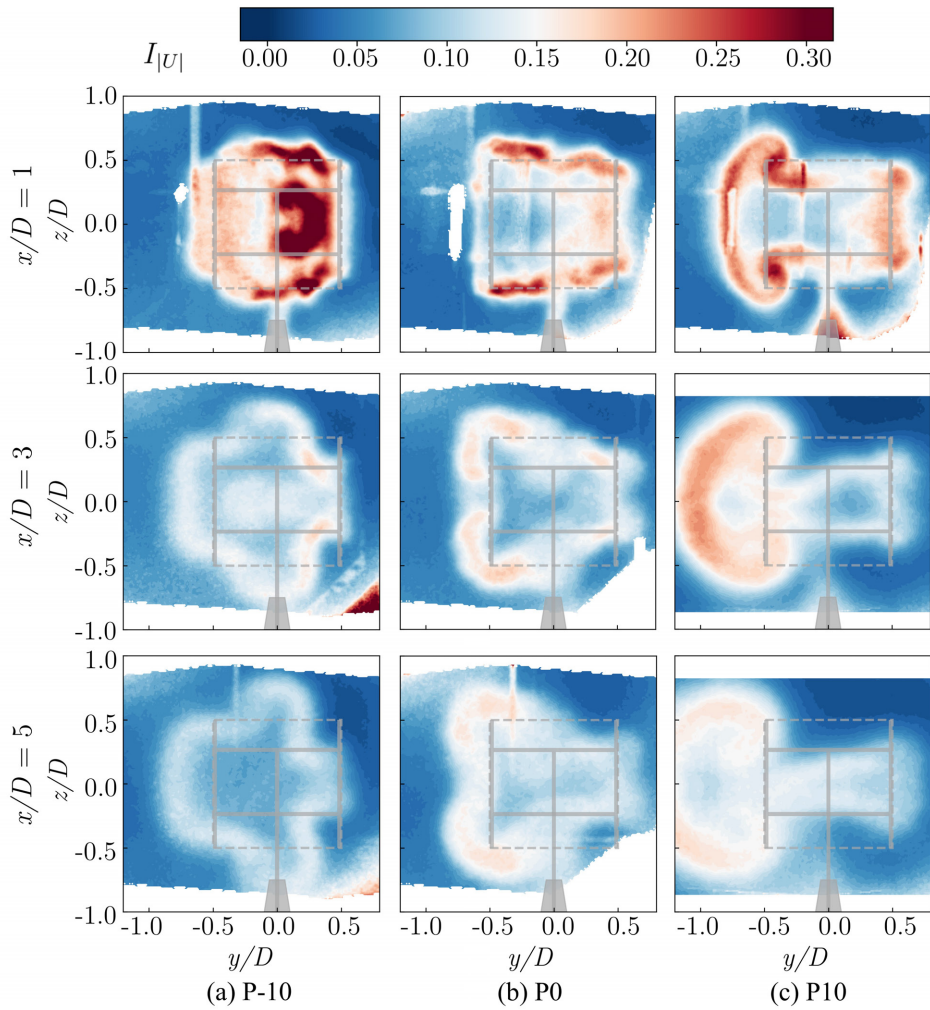
Figure 6.11: Contours of turbulence intensity magnitudes, $I_{|U|}$, for P-10, P0 and P10 at $x/D = 1, 3, 5$.
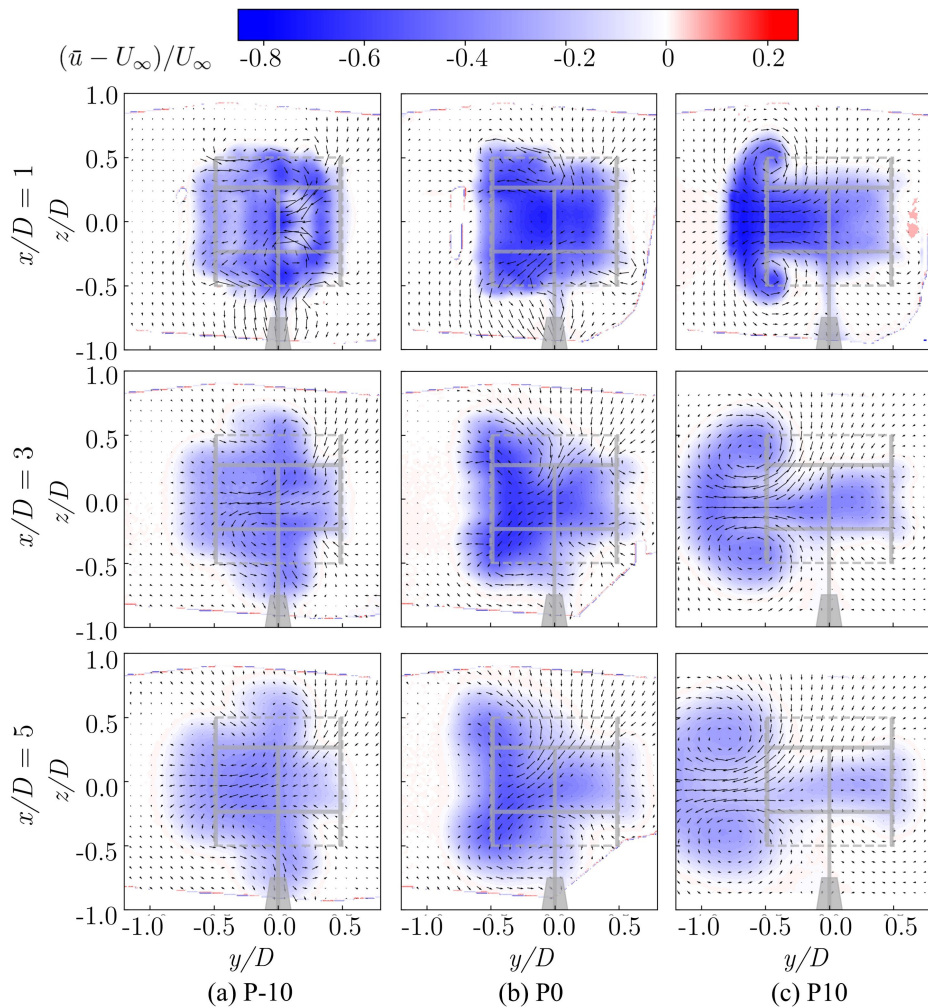
Figure 6.12: Contours of velocity deficit with in-plane velocity vectors for case P-10, P0 and P10, at $x/D = 1, 3, 5$. Schematics for the VAWT with tower are marked in grey.

is noted that the wake shapes of VAWTs are complex and the calculation of wake centre may not be the optimal approach to quantify the wake deflection. In the far wake, the deflection should eventually reach an asymptotic value.
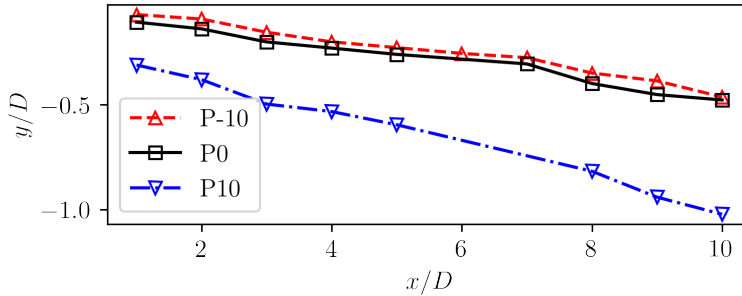

Figure 6.13: Comparison of the lateral deflections of the wake centre for varying streamwise distance from the turbine.

6.4.2. STREAMWISE MOMENTUM RECOVERY

The available terms of equation 6.9 are calculated at $x/D = 3$ and depicted in contour plots in figure 6.14. The pressure term is not measured, therefore is omitted in the comparison. The in-plane spatial derivative $\partial/\partial y$ and $\partial/\partial z$ are calculated with second order central difference within the measured cross-sections. Due to the relatively large separation between the cross-flow planes, it is not possible to accurately evaluate the streamwise derivatives $\partial/\partial x$, and therefore the related terms ($\bar{u}(\partial\bar{u}/\partial x)$ and $\overline{\partial u'u'}/\partial x$) are not presented. However, $\partial\bar{u}/\partial x$ is calculated using second order polynomial regression with the data at $x/D = 2$ and 4, to get an evaluation of the maximum value of $\bar{u}(\partial\bar{u}/\partial x)$ for each case, as the normalisation values for the presented terms in figure 6.14, following the work of Bossuyt et al. (2021). In this way, one can identify the main contributors to the redistribution of the streamwise momentum in the wake, based on a relative comparison of the momentum budget.

In figure 6.14, positive values contribute to the momentum recovery positively, and vice versa. The first row presents the horizontal advection of streamwise momentum. All three cases feature negative regions on the windward edges of the wakes due to substantial horizontal expansions that transport low momentum flow from the centre of the wake to the edges.

The vertical advection of streamwise momentum is illustrated at the second row. It is clear that for all these cases, the vertical advection contributes positively on the leeward side, where the heights of the wakes are shrinking due to the vorticity system discussed in section 6.3.4. Such motion entrains high momentum flow into the wake. On the contrary, the vertical advection contributes negatively where the vertical expansion of the wake occurs; The latter transport low momentum flow from the wake centre to the edges. For P-10, such expansion regions locate along the centre and the windward side of the wake, while P0 and P10 expand majorly at their windward edges.

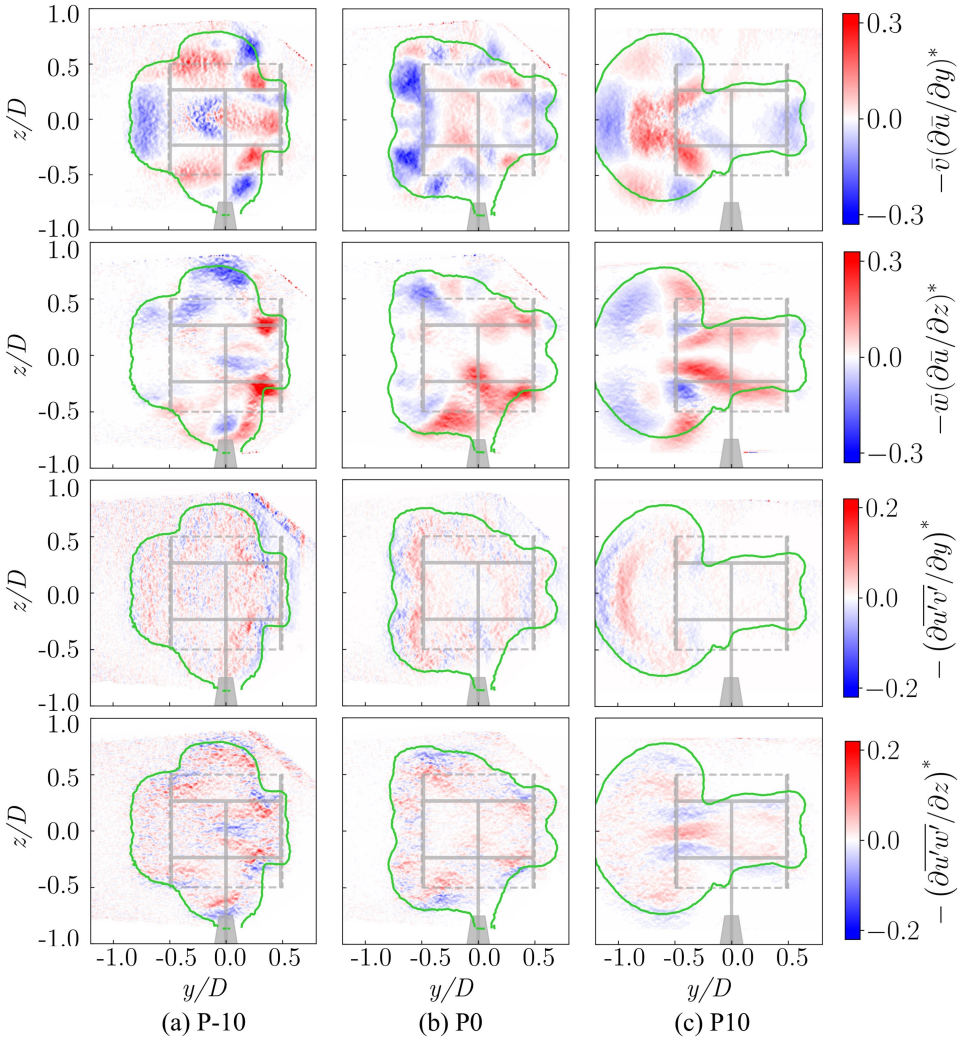Based on the visual comparisons between the two top rows and the two bottom rows

Figure 6.14: Measured terms of the RANS equation in the streamwise direction. For each case the terms are normalised by the maximum value of $\bar{u}(\partial\bar{u}/\partial x)$, as denoted by *.

of figure 6.14, the advection of momentum plays a more critical role in redistributing the streamwise momentum than the Reynolds stress terms. This is attributed to the in-plane velocity vectors being relatively strong at $x/D = 3$.

Another important observation is that the distributions of transport of momentum both by the mean flow and the turbulence are affected by the wake shape, viz., the recovery concentrates along the perimeter of the cross-section of the wake. In comparison, P10 creates a more extended wake perimeter than P0, whilst P-10 makes a shorter one. To better understand the effect of the deformed wake on the wake recovery, the averaged budgets of the wake recovery rate are compared in figure 6.15. The process follows the work of Boudreau and Dumas (2017), with equation 6.9 being rearranged as:

$$\frac{\partial \bar{u}}{\partial x} = \frac{1}{\bar{u}}(-\bar{v}\frac{\partial \bar{u}}{\partial y} - \bar{w}\frac{\partial \bar{u}}{\partial z} - \frac{1}{\rho}\frac{\partial \bar{p}}{\partial x} - \frac{\partial \overline{u'u'}}{\partial x} - \frac{\partial \overline{u'v'}}{\partial y} - \frac{\partial \overline{u'w'}}{\partial z}). \tag{6.13}$$

As aforementioned, only the in-plane advection and Reynolds stress terms are examined, and they are normalised with U_∞/D. It has to be clarified that, compared to the previous work of Boudreau and Dumas (2017), the terms presented here are averaged within the wake region that is determined by the contour line of $\bar{u}/U_\infty = 1$, instead of a square region that is identical to the frontal area of the turbine, to account for the deformed cross-sectional shape of the wake.
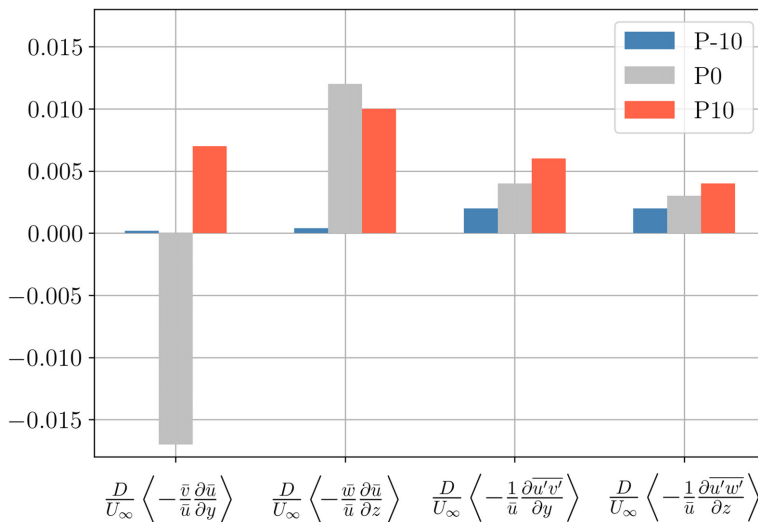
Figure 6.15: Budgets of the wake recovery rate for all three cases at $x/D = 3$. Each term has been averaged within the corresponding wake region that is determined by the contour line of $u/U_\infty = 1$ (as illustrated with green contour lines in figure 6.14). Angle brackets denote the spatial average within the wake region.

With figure 6.15, one can identify each term's net contribution to the momentum recovery within the wake. The horizontal advection (the first term) has minimal effect on the total momentum recovery for P-10; On the contrary, it costs quite a portion of

momentum to redistribute the wake in P0 (so that it has a negative value), and entrains momentum for P10. On the other hand, the vertical advection (the second term) still has a small effect on the wake of P-10; while it contributes positively to the wake of P0 and P10. For all the three cases, the Reynolds stress terms always have a positive contribution to the momentum recovery, and they are positively related to the turbulence intensity that concentrates along the wake perimeter, as shown in figure 6.11.

Based on the above discussion, it can be concluded that, by pitching the blades, the resulting vortex system deflects and deforms the wake. The deflections are effective in redistributing the momentum in the wake, while the deformations are essential in modifying the wake perimeter, thus affecting the momentum recovery.

6.4.3. AVAILABLE POWER FOR HYPOTHETICAL DOWNWIND TURBINES

The integration of available power (AP) is carried out at $x/D = 1,3,5,9$. As shown in figure 6.16, the cases P-10 and P0 feature an overall similar wake effect in terms of the AP distribution. In contrast, the P10 case is much more effective in shifting the low-power flow to the windward side, negative y in this case. In the proximity of the upstream turbine ($1D$), the AP for all the cases is similar, due to an onset stage of the wake where the largely deformed wake structure has not been fully developed. For the P10 case, the wake deflects quickly: the minimum available power is located at $y/D = 0.5$ already at a downstream distance $x/D = 3$.

At $x/D = 3$ and $y/D = 0$, the AP in the wake of P10 reaches 0.61 of that in the free stream, compared to 0.41 and 0.32 for P-10 and P0, respectively. At $x/D = 5$, the AP of P10 increases to 0.74 at inline location; further downstream, the available power increases at a lower rate, reaching 0.77 at $x/D = 8$. The slow-down of the increase of the available power occurs because the wake recovery at this location is no longer dominated by the advection of momentum, but by the turbulence transport and expansion, similarly to classical shear dominated turbulent wakes. Moreover, the transverse location of the minimum AP is constantly deflected to the windward side of the VAWT, yielding a shift exceeding $1\,D$ at $x/D = 8$.

A comparison of the measured AP coefficient with the estimated value from the actuator disc model is provided in table 6.5. The measured data is selected close to the VAWT model ($x/D = 1$) where the wake deficit has not recovered much. The measured minimum AP indicates the effect of the fixed blade pitch on the recovery of the wake. The baseline P0 features a great match with the theory, showing that the streamwise momentum conservation is valid for a regular VAWT; P-10 also shows a good agreement, with a slightly increase of the f_{AP} due to the recovery of the wake; conversely, the available power in the P10 case features a clear mismatch with the actuator disc theory, because the latter cannot reproduce the wake deflection caused by the pitched the blades. The f_{AP} is increased by nearly 300% compared to the prediction, which is due to the enhancement of the momentum advection that follows the large streamwise vortical structure introduced in section 6.3.3 and discussed in more details in section 6.3.4. On the other hand, the comparison of f_{AP} at inline location ($x/D = 1, y/D = 0$) proves the effectiveness of P10: Even with a higher $C_{T,x}$ of the upwind turbine, the available power increases by nearly 100% compared to the P0 case. Conversely, P-10 has little improvement considering the less loaded rotor; in other terms, the increase of AP for P-10 is
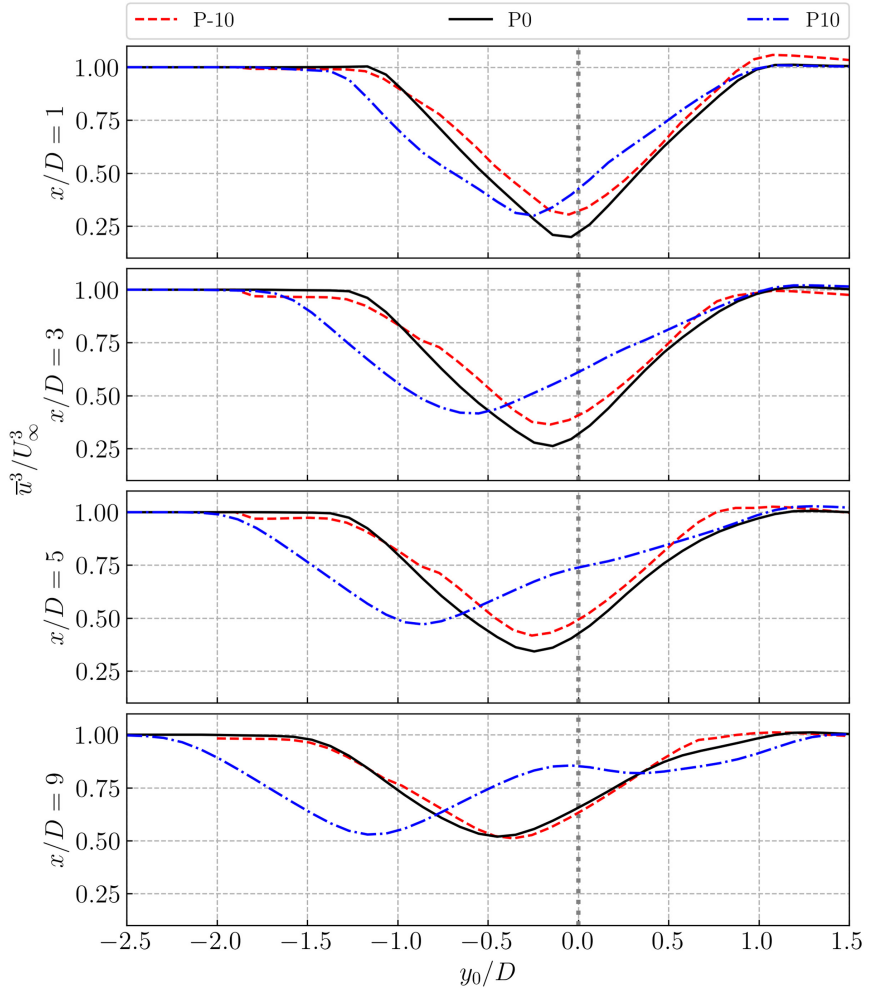
Figure 6.16: Available power distribution along transverse locations at $x/D = 1, 3, 5, 9$.

mostly the effect of a lower $C_{T,x}$.

Table 6.5: Comparison of estimated AP using AD model, measured minimum AP, and AP at $x/D = 1$ inline with the turbine.

Case	$C_{T,x}$	$f_{AP|AD}$	$f_{AP|min,EXP}$	$f_{AP|inline,EXP}$			
				$x/D = 1$	$x/D = 3$	$x/D = 5$	$x/D = 8$
P-10	0.60	0.25	0.30	0.32	0.41	0.49	0.65
P0	0.65	0.21	0.19	0.22	0.32	0.43	0.63
P10	0.81	0.08	0.30	0.43	0.61	0.74	0.85

6.5. CONCLUSIONS

The effect of VAWTs' load distribution on its wake deflection is theoretically investigated using the actuator cylinder model with an infinite blade assumption. The proposed vortical structure is further validated using stereoscopic PIV measurements of the wake deflection caused by changing the fixed blade-pitch of a VAWT. The measured velocity, vorticity, and turbulence fields are used to illustrate the pitched blade effect and to explain the physics of wake structure formation.

This work emphasises the importance of the streamwise vortical system. The streamwise vortices in the wake, generated at the top and bottom of the rotor as a consequence of the VAWT loading, are the main driver of the wake deflection and deformation.

The distribution of turbulence intensity follows the wake's topology, with the majority of $I_{|U|}$ concentrated along the wake's perimeter. By examining the streamwise momentum budgets in the RANS equation, it is found that the momentum recovery within the VAWT wake is primarily due to the momentum advection along the wake perimeter, whereas the turbulence transport plays a less relevant role.

The VAWT with positively pitched blades (case P10) exhibits the greatest wake deflection, resulting in the highest available power for a hypothetical downwind turbine aligned with the upwind turbine. While P0 and P-10 (0 and -10 degrees pitch) exhibit wake deflections that are comparable between them, and significantly lower than the P10 case.

7

EXPERIMENTAL STUDY OF THE WAKE INTERACTION BETWEEN TWO VAWTS

Wakes and wake interactions in wind turbine arrays diminish energy output and raise the risk of structural fatigue; hence, comprehending the features of rotor-wake interactions is of practical relevance. Previous studies suggest that VAWTs can facilitate a quicker wake recovery. This study experimentally investigates the rotor-wake and wake-wake interaction of VAWTs; different pitch angles of the blades of the upwind VAWT are considered to assess the interactions for different wake deflections. With stereoscopic particle image velocimetry, the wake interactions of two vertical-axis wind turbines (VAWTs) are analysed in nine distinct wake deflection and rotor location configurations. The time-average velocity fields at several planes upwind and downwind from the rotors are measured. Additionally, time-average loads on the VAWTs are measured via force balances. The results validate the rapid wake recovery and the efficacy of wake deflection, which increases the available power in the second rotor.

7.1. Introduction

THE interaction between wind turbine wakes and downwind rotors is one of the most crucial issues resulting in power losses in a wind farm. Downwind turbines operating in the wakes of upwind ones suffer from a decelerated and highly turbulent inflow, thus extracting less kinetic energy and enduring more severe fatigue loads. To alleviate the wake interaction effects, ample inter-turbine space and wake steering techniques are required for a wind farm of horizontal axis wind turbines (Fleming et al., 2017, 2019). However, the limitation of site resources and the increasing demand for power production often leads to a smaller inter-turbine distance of (3 to 8 diameters, Stevens et al., 2016), in turn intensifying the wake interaction in a wind farm.

In contrast, vertical axis wind turbines are less susceptible to the inflow direction and turbulence (Chatelain et al., 2017), allowing for closer deployments without significantly deteriorating the performance of individual turbines. Additionally, reduced inter-turbine spacing of VAWTs has been identified promising in increasing the wind farm power density. That is attributed to a faster wake recovery rate (Dabiri, 2011), which has been confirmed both experimentally (Rolin and Porté-Agel, 2018) and numerically (Boudreau and Dumas, 2017). In fact, to further increase the power density of an array of VAWTs, the wake steering concept has been adapted from HAWTs. Instead of using yawing mechanics of HAWTs to steer the wake, pitching the blades of VAWTs can easily deflect and deform their wakes (Huang et al., 2023). The simplified mechanics means lower construction cost, which is beneficial to reducing the cost of power generation.

We have demonstrated in chapter 6 that, isolated VAWTs can significantly redistribute the available wind power in the wake, and manifest a quicker wake recovery rate via pitched blades. However, the effect of the wake deflection and deformation on downwind wind turbines was only hinted at and not assessed.

Hence, in this chapter, we investigate the wake interactions of VAWTs placed inline and with offset employing stereo-PIV, focusing on whether the wake deflection of VAWT gives more energy to an array configuration. In doing so, the upwind VAWT is set to vary the constant pitch angle of the blades to deflect its wake. Additionally, an in-house designed force balance system is adopted to quantify the averaged thrusts on the VAWTs, thus assessing the turbines' ability to extract momentum from the wind.

The remainder of the chapter is organised as follows. The methodology, the experiment apparatus and the cases examined are introduced in section 7.2. Then, a section of results and discussion follows (section 7.3), where an overview of the wake produced by the upwind VAWT with different fixed blade-pitch-angles is provided first as the control group. Second, the time-averaged thrust performance and wake properties of the interaction groups, together with a discussion on the available power behind the downwind VAWT, are presented. Finally, the key findings of this work are summarised in section 7.4.

7.2. Experimental Methodology

7.2.1. Wind tunnel facility

The experiments are undertaken in the Open-Jet Facility (OJF) of the TU Delft Aerodynamics Laboratories. The OJF features a contraction ratio of 3:1 and an open exit of 2.85×2.85 m^2. The stable free-stream, which is not affected by the development of the

jet shear layer (Lignarolo et al., 2014), contracts with a 4.75° semi-angle, resulting in an effective test area around 2.35 × 2.35 m at 3 m behind the exit. The test wind speed is $U_\infty = 5\,\mathrm{m\,s^{-1}}$, with a free-stream turbulence intensity lower then 2% within the test region (see Lignarolo et al., 2015).

7.2.2. THE VAWT MODEL

The scaled VAWT model is in-house designed, H-type, with a rotor size of 30x30 cm (Huang et al., 2020). The two straight blades are made of aluminium, and the airfoil of the blades is NACA0012, with a chord length of 0.03 m. The solidity of the model is 0.2. The blades are connected to the tower with a pair of dedicated struts, the cross-section profile of the latter on the blade side is NACA0012 and transits to an ellipse with a thickness of 12% on the tower side, to reduce the drag and flow separation. The blades and the struts are connected with two pairs of bolts, allowing for a quick release and adjusting the fixed pitching angle; A pair of 3D printed adaptors are used to adjust the pitch angle (see figure 7.2-(a)). The pitch convention is presented in figure 7.2-(b), with pitching towards the tower as positive, and vice versa. The rotor is driven by a brushless motor: *MAXON* EC 90 flat, and the motor is controlled by a *ESCON* 50/5 control module. A flexible coupling is used to filter out small vibrations in consideration of the misalignment due to machining accuracy. The locators at four feet are used to mount the entire VAWT model onto the balance system.

(a)   (b)
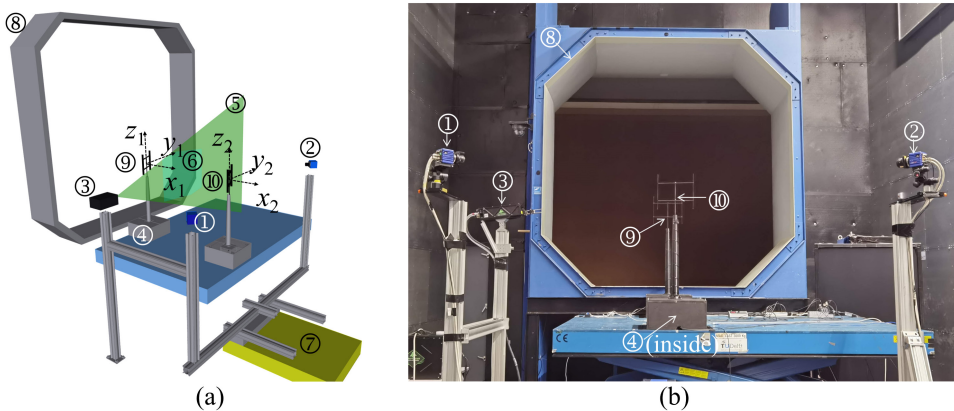
①camera 1 ②camera 2 ③*Evergreen* laser ④force balance ⑤laser sheet
⑥stereo-FoV ⑦traversing system ⑧wind tunnel exit ⑨VAWT1 ⑩VAWT2

Figure 7.1: (a): schematic of the experimental setup; (b): a snapshot of the setup.

7.2.3. THE THREE-COMPONENT FORCE BALANCE

An in-house designed and constructed three-component balance is employed for the load measurement. The balance is able to measure the streamwise and lateral forces, and the moment around the z-axis. It consists of three load cells (type: KD40s, max range ±50N, max error: ⩽ 0.1%), with two of them measuring the streamwise force (drag/thrust) while the other one measuring the lateral force. The overall uncertainty of
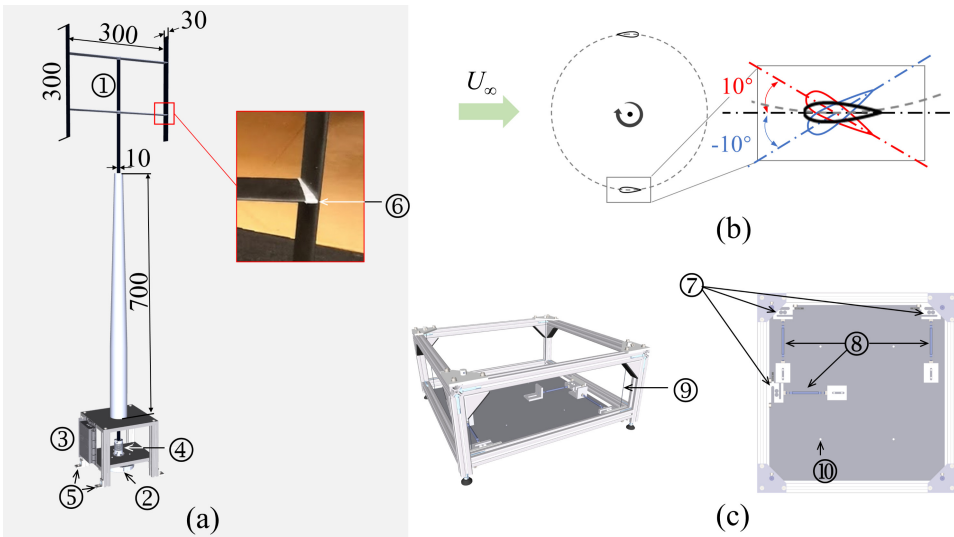
①VAWT rotor ②brushless motor ③motor controller ④flexible coupling ⑤locators
⑥pitch adapter ⑦Load cells ⑧connectors ⑨steel string ⑩positioning hole

Figure 7.2: (a): schematic of the VAWT model, dimensions in mm; (b): convention of the blade pitch; (c): an in-house designed three component balance system.

the force measurement is of the same level as the load cells, provided that the flexural rods are aligned with the lift and the drag. As illustrated in figure 7.2-(c), the load cells have one side attached to a stable aluminium frame directly and the other side to a platform via a dedicated flexural rod. The platform is suspended with four steel strings connected to the aluminium frame. The combination of the strings and the load cells prevents rotation caused by torque. The flexural rods are designed to solely transmit forces along its span-wise to prevent transmitting a moment and thus improve the measurement accuracy. The assembly was designed to tolerance levels of ±0.05 to ±0.15 mm. Additionally, four positioning holes are used to precisely centre the VAWT on the platform.

7.2.4. STEREOSCOPIC PARTICLE IMAGE VELOCIMETRY

The velocity fields in the wake of the VAWTs were obtained with stereoscopic PIV, which measures three velocity components within two-dimensional planes. A Quantel *Evergreen* double-pulsed Nd:YAG laser produced pulses with 200 mJ energy at a wavelength of 532 nm within a laser sheet of approximately 3 mm width. A *SAFEX* smoke generator released water-glycol seeding particles of average 1 μm diameter. The seeding particles were imaged by two LaVision's Imager sCMOS cameras in successive cross-sections of the wake. The cameras have an image resolution of 2560 px × 2160 px, a pixel pitch of 6.5 μm/px; they were coupled with 50 mm lenses with a numerical aperture of 4. We placed the cameras about 2.2 m away from the centre of the laser sheet with a stereoscopic an-

gle of 90°, resulting in a camera Field of View (FoV) about 80 × 55 cm, a magnification factor of 0.026, and a digital image resolution of 3.9 px mm.

To translate the PIV system precisely, a traversing system is employed whereby the stereo-PIV setup is mounted on, enabling navigation from 0.3 m to 3 m behind the wind tunnel exit with a step of 0.3 m. An overview of the experimental setup is shown in figure 7.1. As illustrated, there is no ground effect accounted for in the measurement.

7.2.5. CASES DESCRIPTION

Measurements of the isolated VAWT at three different pitch angles (-10°, 0°, and 10°) compose the control group. As illustrated in figure 7.3, measurements take place at 10 planes behind the turbine with $1D$ spacing, being $D = 30$ cm the VAWT diameter. These measurements are used as the control group to evaluate the free wake in absence of the downwind turbine. The wake deflection mechanism of the isolated VAWTs and some velocity fields have already been presented in the work of Huang et al. (2023), but are presented also here for sake of completeness.

Six wake interaction cases with two turbines aligned along the streamwise direction and with $1D$ lateral offset are investigated. The blade pitch of the upwind VAWT, indicated with VAWT1, varies as aforementioned to yield different wake deflections; conversely, the downwind VAWT, indicated with VAWT2, operates at a constant zero pitch. The streamwise distance between the rotor centres is 5 rotor diameters (D). The VAWTs rotate at a speed of 800 rpm, resulting in a tip speed ratio (λ) of 2.5 relative to U_∞.

In addition, two coordinate systems are adopted: one has the origin at the rotor centre of VAWT1, the other at that of VAWT2. The selection of the coordinate systems is for the ease of discussion on the wake deflection relative to each VAWT. The relationship between the coordinates is given by the following equations:

$$x_1 = x_2 + 5D, y_1 = \begin{cases} y_2, \text{inline cases} \\ y_2 - 1D, \text{offset cases} \end{cases} \tag{7.1}$$

Table 7.1: Description of the measured configurations.

|	case	Description
	P-10	Isolated VAWT with pitched blades, - 10°
Control group	P0	Isolated VAWT with zero pitch
	P10	Isolated VAWT with pitched blades, + 10°
	P-10_0D	VAWT1 with -10° pitch, VAWT2 with zero transverse offset
Inline group	P0_0D	VAWT1 with zero pitch, VAWT2 with zero transverse offset
	P10_0D	VAWT1 with 10° pitch, VAWT2 with zero transverse offset
	P-10_1D	VAWT1 with -10° pitch, VAWT2 with 1 D transverse offset
Offset group	P0_1D	VAWT1 with zero pitch, VAWT2 with 1 D transverse offset
	P10_1D	VAWT1 with 10° pitch, VAWT2 with 1 D transverse offset
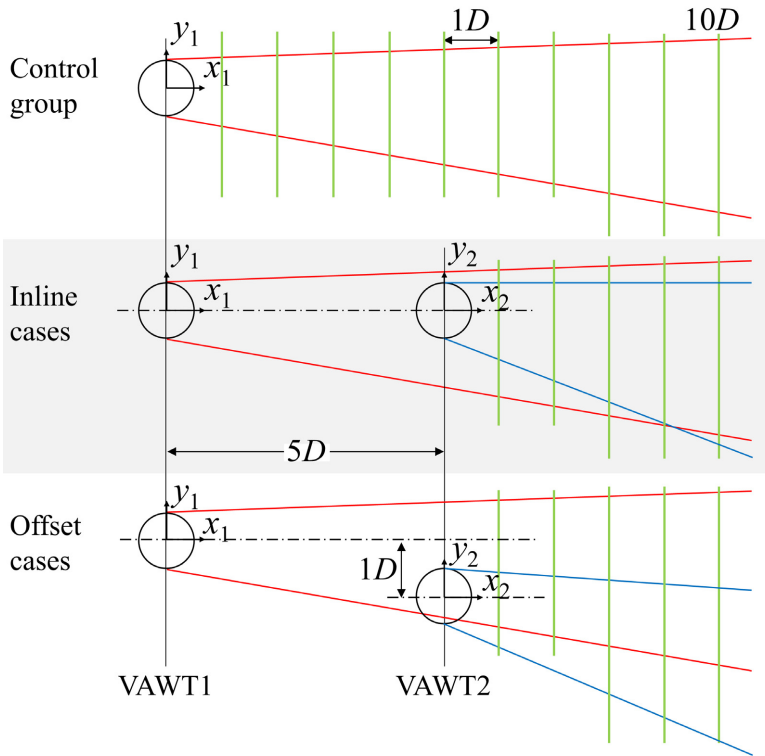
Figure 7.3: Schematic of the coordinate systems for the cases measured.

7.2.6. DATA ACQUISITION AND EXPERIMENT PROCEDURES

For the control group, the PIV measurement planes range from $1D$ to $10D$ behind the VAWT; For the interaction cases, the PIV measurements are performed $2D$ upstream and $1D$ to $5D$ downstream of VAWT2. At each acquisition plane, 300 image pairs are taken at a frequency of 15 Hz to perform an ensemble average over a period of 20 s (266.7 rotations).

The time-averaged thrust forces of the control group are measured at free-stream velocities ranging from 3 to 7 m s^{-1}, corresponding to λ from 1.8 to 4.2. Curves of thrust coefficient versus λ are obtained (figure 7.4). The thrusts ($C_{T,x}$ and $C_{T,y}$) are expressed as:

$$C_T = \frac{T}{0.5\rho U_\infty^2 A},\tag{7.2}$$

where T is the streamwise or lateral force exerted on the flow, which is equal and opposite to the measured force applied to the VAWT. U_∞ is the free-stream velocity and A is the frontal area of the VAWT, 0.09 m^2.

7.3. RESULTS AND DISCUSSION

7.3.1. THE CONTROL GROUP

Because the presence of an upwind turbine affects the inflow conditions of downwind turbines, in this section, we assess the performances and the wake development of an isolated turbine (corresponding to VAWT1 in the interaction cases) with and without blade pitch.

FORCE BALANCE MEASUREMENT RESULTS

The variation of the streamwise thrust coefficient ($C_{T,x}$) with the tip speed ratio λ in the control group is depicted in figure 7.4 (left). With λ increasing, $C_{T,x}$ increases almost linearly. Similar trends within these tip speed ratios have been reported in the literature (Rezaeiha et al., 2018a,b). Take case P0 as the baseline; it is noticed that a positive pitch shifts the curve upwards, thus leading to a higher thrust coefficient at the same λ. Vice versa, a negative pitch shifts the curve downwards, resulting in a lower thrust coefficient at the same λ. The shifting of $C_{T,x}$ via blade pitching is consistent with that documented in Ferreira (2009), where a VAWT with different pitch axes, rotating in constant tip speed ratio, was simulated.

The lateral force coefficient ($C_{T,y}$) - λ curves are presented in figure 7.4 (right). The curves of P-10 and P10 cases feature monotonically increasing trends. However, the increase is much steeper for the P10 case. In contrast, the lateral force of P0 decreases slightly with increasing λ. Similar trends have been reported by Huang et al. (2020), where the forces of the same VAWT rotor were measured with a different balance system. Also, P10 features much stronger lateral forces causing significant wake deflection as shown in section 7.3.1; whereas for the P0 and P-10 cases, $C_{T,y}$ remain below 0.2.
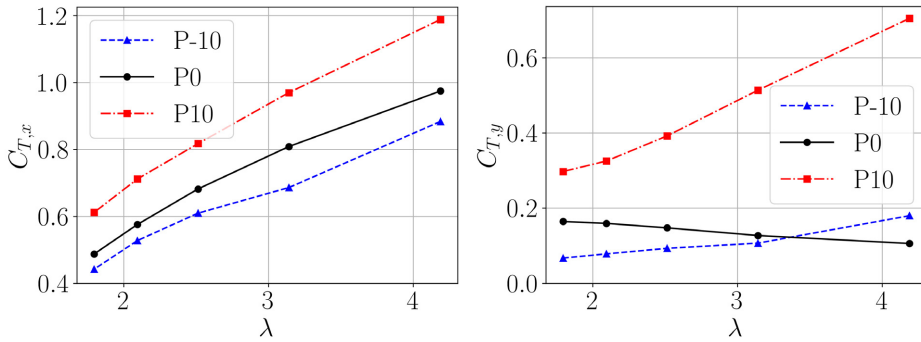
Figure 7.4: $C_{T,x}$-λ (left) and $C_{T,y}$-λ (right) curves of isolated P-10, P0, and P10.

PIV MEASUREMENT RESULTS

To evaluate the impact of the upwind turbines on the inflow of the downwind ones, the velocity, vorticity and turbulence fields in the wake of isolated VAWTs with different pitch angles are measured with PIV and illustrated in figure 7.5. Data at $x_1/D = 5$ is selected in accordance with the locations of downwind VAWTs' rotor centre. Data at different downwind locations has been presented in chapter 6 and is presented in the appendix E.

All the contours are almost symmetric with respect to $z/D = 0$, because of the absence of the ground, except for the region in proximity to the wake of the tower. P-10 features the minimum lateral wake deflection among the three cases. There is elongation along the span-wise direction around the centre of the wake. The wake of P0 features a trapezoidal shape with concave sidelines, and is slightly deflected towards negative y. In contrast, the wake of P10 has a significant deflection to the left, and a faster velocity recovery around $y/D = 0$. The streamwise vorticity fields, illustrated in the second line of figure 7.5, are characterised by a set of counter-rotating vortex pairs (CVPs) (Rolin and Porté-Agel, 2018; Ryan et al., 2016; Huang et al., 2020). The wakes of P-10 and P0 feature more than two pairs of counter-rotating vortices, whereas in the wake of P10 only two strong CVPs are present. The turbulence intensity contours, depicted in the third line of figure 7.5, clearly show that the highest turbulence intensity is concentrated along the perimeters of the wakes.

The isolated VAWTs with different blade-pitch angles feature different cross-flow thrusts and thus produce different wake deflections. The relation between the rotor loading and the wake deflection has been reported by Huang et al. (2023), while the amount of deflection is discussed with a wake centre technique in section 7.3.2. Additionally, the variation in blade pitches results in completely different structures of streamwise vorticity, as well as different levels of turbulence intensity (TI), and hence, different wake recovery rates. In particular, the case P10 (with positive 10° pitch) manifests the strongest counter-rotating vortex pair and the highest TI level, resulting in the fastest wake recovery even though its initial momentum deficit is the highest.
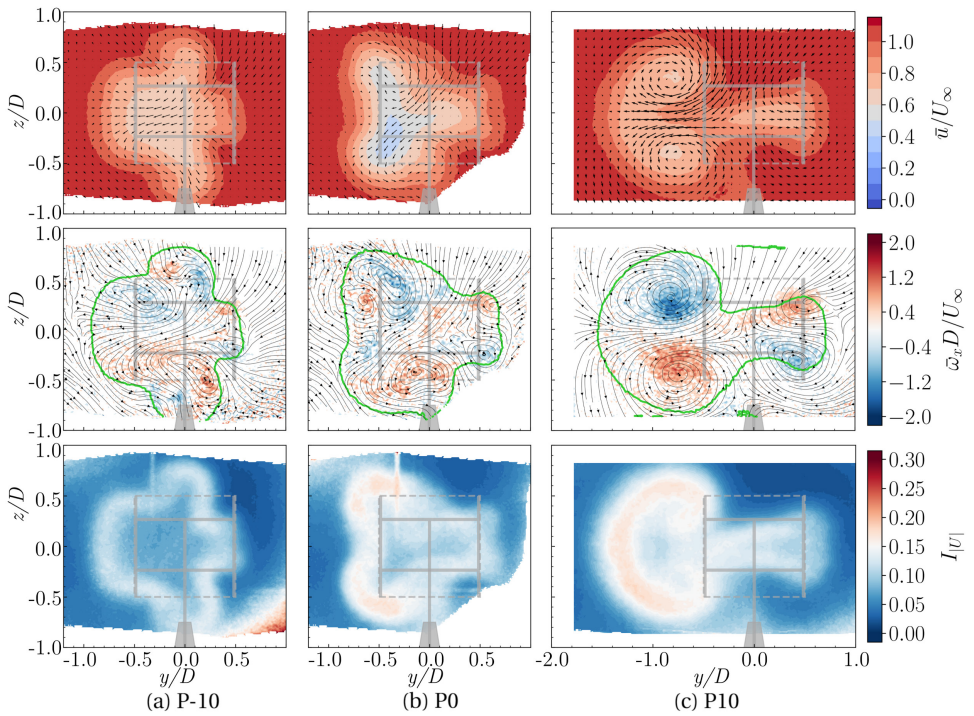
Figure 7.5: Contours of streamwise velocity with in-plane velocity vectors, vorticity with in-plane streamlines, and turbulence intensity for the isolated VAWT P-10, P0 and P10 at $x_1/D = 5$. Green contour lines are where $\bar{u}/U_\infty = 1$, showing the outline of the wake; Grey schematics denote the transverse location and frontal area of VAWT1.

7.3.2. Wake interactions with the presence of downwind turbines

Thrusts and lateral forces

The measured forces T_x and T_y of the downwind VAWT are listed in table 7.2. The estimation of available power (AP, $< U_0^3/U_\infty^3 >$) introduced in the previous work (Huang et al., 2023) for a hypothetical downwind turbine is adopted here to discuss the wake effect on the performance of the downwind rotor (VAWT2). U_0 is the hypothesised inflow velocity for the VAWT2, being the streamwise velocity in the wake of isolated VAWTs at $x_1/D = 5$. It is assumed that the VAWT2's effect on the inflow can be omitted, and the cross-flow components in the wake of isolated VAWTs are negligible. The angle bracket denotes a spatial average within the frontal area of VAWT2, which is a square region located aligned with the upwind turbine (VAWT1) or with $1D$ offset, at $x_1/D = 5$. In comparison with the measured forces, available momentum (AM, $< U_0^2/U_\infty^2 >$) estimations are also listed in table 7.2.

For the inline cases, when the upwind turbine has 10° pitch, AM increases the most, +55% compared to P0_0D and +39% to P-10_0D. This is due to the wake deflection and faster wake recovery produced by VAWT1. AP follows the same trend as AM. In contrast, when VAWT2 is translated $1D$ laterally, the inflow momentum increases in cases P-10_1D and P0_1D, while it decreases in P10_1D. This is due to the largely deflected wake towards the VAWT2 in the latter case. Moreover, P-10_1D features a higher AM increment than P0_1D, because P-10's wake is deflected slightly away from VAWT2 compared to that of P0. The wake deflection can be appreciated in section 7.3.2.

The measured thrusts confirm that the estimation of AM and AP in the wake of isolated VAWT is in accordance with the performance of the downwind turbine. P0_0D features the least AM and AP and thus T_x of VAWT2 in this case is the minimum among all the cases. P10_0D has the highest AM and AP among the inline cases, proving that the wake deflection due to a positive pitch can be beneficial to the downwind wind turbines. The AM and AP in the $1D$ offset cases show that translating the VAWT2 away from the wake centre of VAWT1 will mitigate the wake effect and gain more power for downwind turbines. The wake centre is discussed in section 7.3.2.

Table 7.2: Measured forces of the isolated pitched turbines or downwind turbines with zero pitch, with available momentum ($< U_0^2/U_\infty^2 >$) and available power ($< U_0^3/U_\infty^3 >$) calculated from the velocity field of the isolated pitched turbines.

	Case	$< U_0^2/U_\infty^2 >$	$< U_0^3/U_\infty^3 >$	T_x [N]	T_y [N]
	P-10	1	1	0.80	0.12
Isolated turbines	P0	1	1	0.88	0.19
	P10	1	1	1.09	0.52
	P-10_0D	0.62 (+9.7%)	0.50 (+13.6%)	0.64 (+4.9%)	0.12
	P0_0D	0.56	0.44	0.61	0.14
	P10_0D	0.81 (+44.6%)	0.74 (+68.2%)	0.69 (+13.1%)	0.12
Downwind turbines	P-10_1D	0.85 (+51.8%)	0.82 (+86.4%)	—	—
	P0_1D	0.83 (+48.2%)	0.80 (+81.8%)	0.73 (+19.7%)	0.14
	P10_1D	0.62 (+10.7%)	0.50 (+13.6%)	—	—

VELOCITY FIELDS

An overview of the placement of the VAWTs and corresponding measurement planes is given in figure 7.6, where the centre of VAWT1 is selected as the origin of the global coordinate system. The velocity contour $2D$ ahead of the VAWT2 is very much similar to that measured in the isolated turbine cases at the same location ($3D$ behind VAWT1, see appendix E). This confirms the assumption made in 7.3.2 that the VAWT2's effect on the inflow is negligible.

Figure 7.7 illustrates comparisons of the streamwise velocity contours behind VAWT2, where the origin of the coordinate system is the centre of VAWT2. The black outline of VAWT1 denotes its frontal area and the transverse location, which is the same as that of VAWT1 in this case. For all the three inline cases, the wake of VAWT2 is embedded into the background wake of VAWT1, and thus the wake deformation is significantly affected by the inflow velocity field.
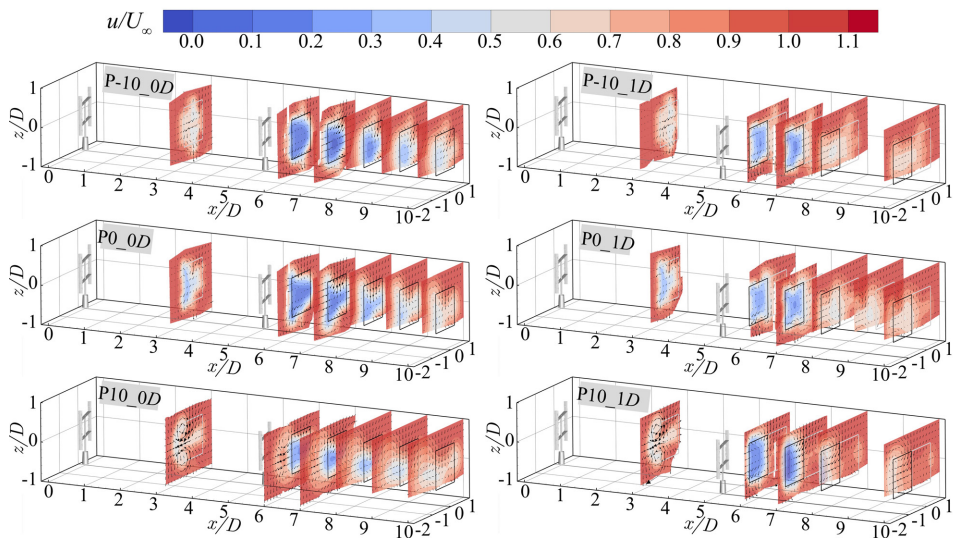

Figure 7.6: Overview of the placement of the turbine and measured streamwise velocity contours. Grey squares denote the frontal area of the upwind turbine while black squares for the downwind turbine.

Compared to the control group (see also appendix E), the wakes of the inline cases remain similar to that of the isolated VAWTs, but the velocity deficits in the wake centre are increased due to the presence of the downwind VAWT. P-10_0D features a deeper velocity deficit than P0_0D, because the former exerts a higher thrust against the free-stream while the lateral forces of the two are similar. In contrast, P10_0D exerts the highest T_x and T_y, but the lowest velocity deficit. This is due to two reasons: first, a large portion of the extracted streamwise momentum is transferred to the horizontal deflection, and that explains the largest wake deflection compared with the other two cases; Second, its significant wake deformation yields a faster recovery, by enhancing the entrainment of momentum via the advection and the increased wake-free-stream interface (Huang
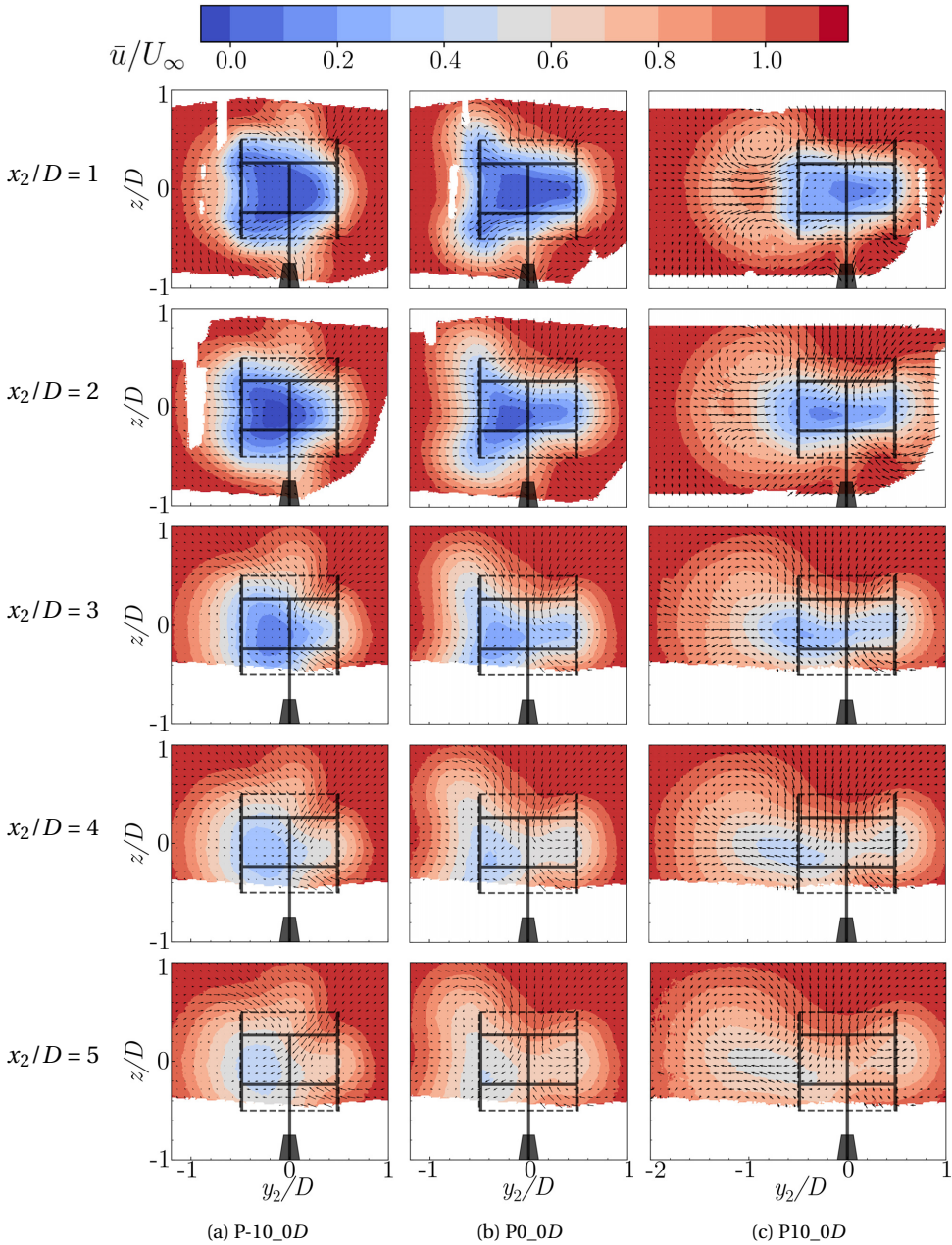
et al., 2023).

Figure 7.7: Contours of streamwise velocity with in-plane vectors with upwind turbine as P-10, P0 and P10, at the near wake of VAWT2 ($x_2/D = 1,2,3,4,5$). Black schematics represent VAWT2.

The velocity fields in the wake of P-10_1D, P0_1D, and P10_1D are illustrated in figure 7.8. The black outline represents VAWT2 while the grey outline is for VAWT1. The origin of the coordinate system in the graphics is the centre of the VAWT2. In the near wake re-
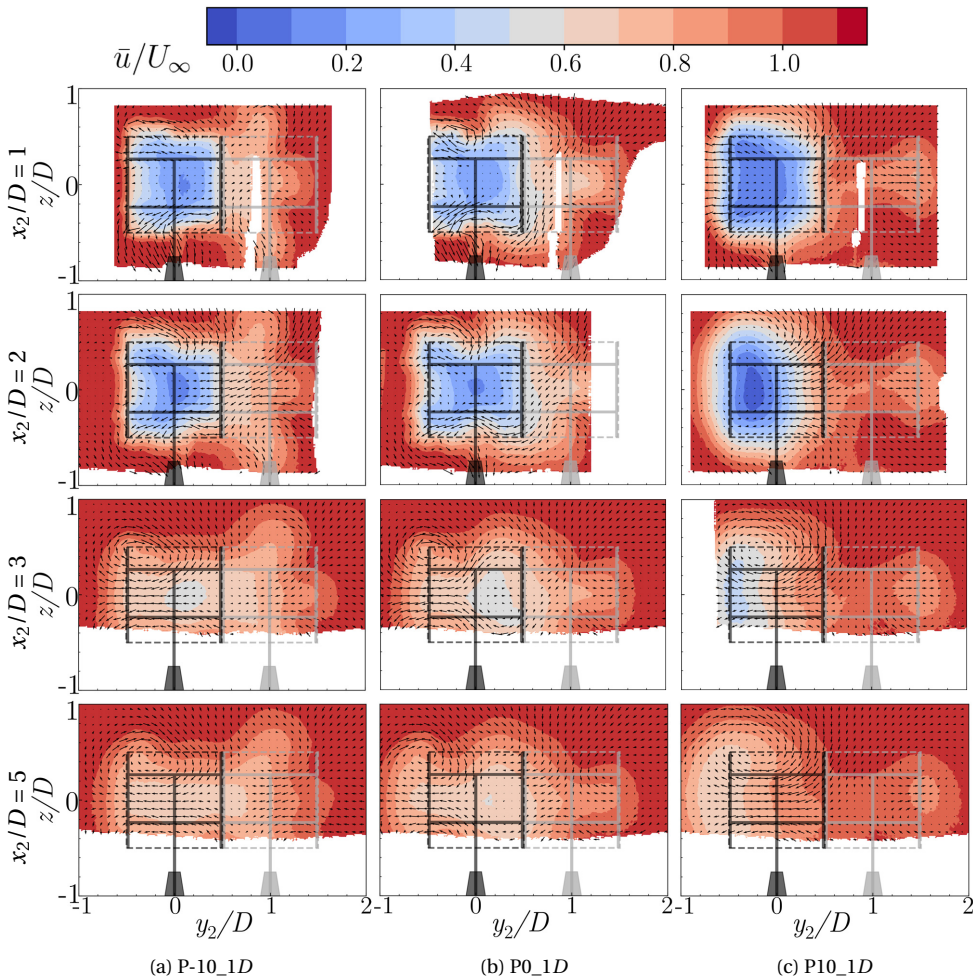

Figure 7.8: Contours of streamwise velocity with in-plane vectors with upwind turbine as P-10, P0 and P10, at $x/D = 1, 3, 5$ of the downwind turbine. Grey and Black schematics represent VAWT1 and VAWT2, respectively.

gion ($x_2/D = 1$), the outlines of the wakes of VAWT2 are similar among the three different configurations. The wake interaction in P-10_1D and P0_1D occurs at regions where the right edge of VAWT2's wake overlapped with the left of VAWT1's wake; whereas in P10_1D, the wake of VAWT2 is bounded by the wake of VAWT1 entirely. The wakes of P-10_1D and P0_1D look like the superposition of two isolated wakes, where the right and the left parts are the wakes of VAWTs with and without pitched blades, respectively.

However, the wake outline of P10_1D is similar to the wake of isolated P10, except for a deeper velocity deficit.

WAKE CENTRE

The wake centre is calculated by evaluating the centre of mass of the velocity deficit (Howland et al., 2016; Wei et al., 2021):

$$y_c(x) = \frac{\iint y \Delta u(x, y, z) \mathrm{d}y\mathrm{d}z}{\iint \Delta u(x, y, z) \mathrm{d}y\mathrm{d}z}, \tag{7.3}$$

where $\Delta u(x, y, z) = U_\infty - u(x, y, z)$. The integrals are computed over cross-sectional planes, perpendicular to the streamwise velocity. The coordinate system is based on the isolated VAWT. Only the lateral (horizontal) coordinate of the wake centre is discussed in this article for sake of simplicity.

As shown in figure 7.9, the 10° positive blade-pitch of the isolated VAWT more than doubles the wake deflection, while the negative pitch slightly decreases the deflection. The rate of VAWT2's wake deflection features a similar trend, with positively pitched VAWT1 increasing the deflection, and vice versa. In contrast, when the VAWT2 is translated horizontally (0D cases vs 1D cases), the translation has little effect on the slope of wake deflection curves; however, it could shift the wake centre significantly. In other words, blade pitching of the upwind turbine effectively varies the wake centre slope of the downwind turbine, while translating the downwind turbine is effective in shifting the downwind wake centre whilst keeping the slope.
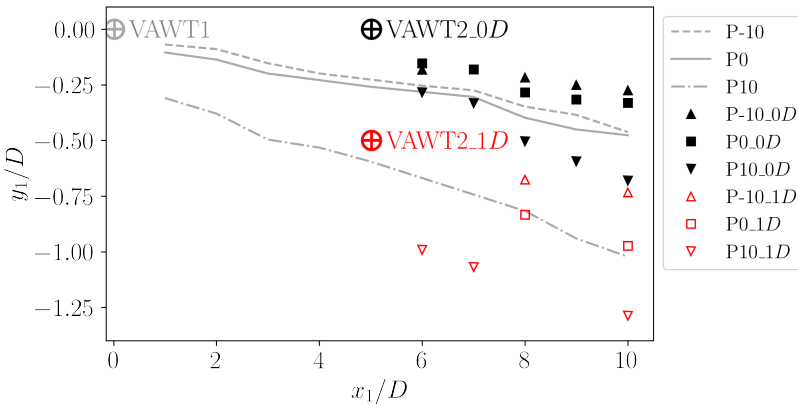

Figure 7.9: Wake centre development of all the cases. Missing points for the 1D offset cases are due to a) measurement planes at $x_1/D = 9$ are not available for these cases; b) unrealistic estimations due to object reflection in the PIV measurements.

STREAMWISE VORTICITY

The streamwise vorticity of the inline and 1D-offset cases are shown in figure 7.10 and 7.11, respectively. For the inline cases P-10_0D, P0_0D, and P10_0D, the vortex generated by VAWT2 interacts directly with that generated by VAWT1. They are eventually merged

together and keep the same macroscopic behaviour as that of the corresponding isolated VAWT. In the wake of P10_0D, the vorticity of VAWT2 is not interacting with the CVPs of P10 initially at $x_2/D = 1$, because their locations are relatively far apart. However, the CVPs of P10 are strong enough to merge with those of the VAWT2 as the wake develops further downstream.

A similar phenomenon occurs when the downwind VAWT2 is translated out of the centre of the upwind VAWT1's wake, such that its vorticity does not directly interact with that of VAWT1, and thus a double-layer structure remains at its near wake ($x_2/D = 1$, P-10_1D and P0_1D)(Huang et al., 2023). However, in these two cases, the background vorticity is not strong enough to merge the vorticity of VAWT2, resulting a structure with spread multi-CVPs. On the contrary, in the wake of P10_1D, the vorticity of VAWT2 firstly interacts directly with the strongest counter-rotating vortex pair of VAWT1, and is completely merged with it at $x_2/D = 5$. This leads to an almost unchanged wake outline compared to that of P10.

TURBULENCE INTENSITY

The measured turbulence intensity magnitudes are presented in figures E.5 (isolated turbines) and 7.12 -7.13 (wakes interactions). The turbulence intensity in the control group depicts the footprint of the wake, with the turbulence concentrating along the wake perimeter.

The presence of the downwind VAWT increases the turbulence in the wake. In figure 7.12, the increased turbulence intensity initially distributes along the wake outline of VAWT2 at $x_2/D = 1$, as in a simple overlap with the background turbulence. Merging of the turbulence occurs vigorously, and the turbulence intensity is smeared almost uniformly within the wake region at $x_2/D = 5$.

When the wake of VAWT2 is shifted out of the wake centre of VAWT1, the interaction of the turbulence becomes less vigorous, as illustrated in figure 7.13. That is because the counter-rotating vortex pairs are shifted away from each other, as discussed in section 7.3.2. For example, in cases P-10_1D and P0_1D, the turbulence is increased at $-0.5 < y_2/D < 0.5$, concentrating on the wake perimeter of VAWT2. At $x_2/D = 3$ and 5, a merged wake and a new outline are generated, and thus the turbulence is distributed along the new edges. On the contrary, in P10_1D, the turbulence intensity around VAWT2 increases dramatically since $x_2/D = 1$, due to a direct interaction of the CVPs. As reported in the literature (Abkar and Porté-Agel, 2014; VerHulst and Meneveau, 2014; Bachant and Wosnik, 2016), higher TI is beneficial to faster wake recovery. The vortical structure presented in the section indicates an acceleration of wake recovery via enhancing the TI.

AVAILABLE POWER BEHIND VAWT2

The normalised available power distribution behind the VAWT2 at $x_2/D = 3$ and 5 is depicted in figure 7.14. The procedure for the AP calculation has been breifly introduced in section 6.1, and more details can be found in the work of Huang et al. (2023). In figure 7.14, the vertical axis denotes the averaged wind power within the frontal area of a hypothetical VAWT (a third VAWT, VAWT3) placed downwind of VAWT2, the lateral location of its rotor centre is presented relative to VAWT1, i.e. y_1/D, for the sake of clarity.
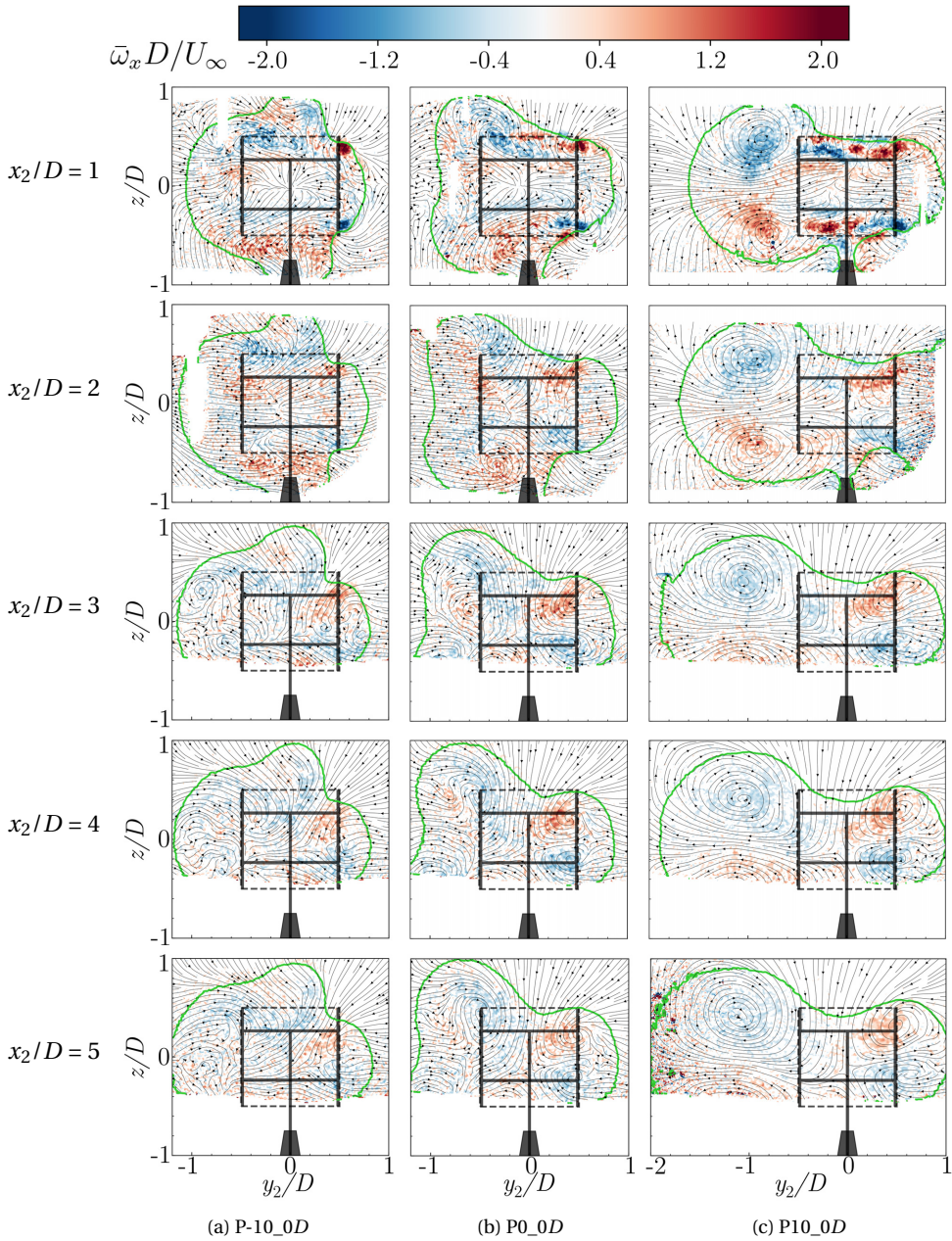
Figure 7.10: Streamwise vorticity contours with in-plane streamlines for inline cases, at the near wake of VAWT2 ($x_2/D = 1, 2, 3, 4, 5$). Green contour lines indicate $u/U_\infty = 1$. Black schematics represent VAWT2.
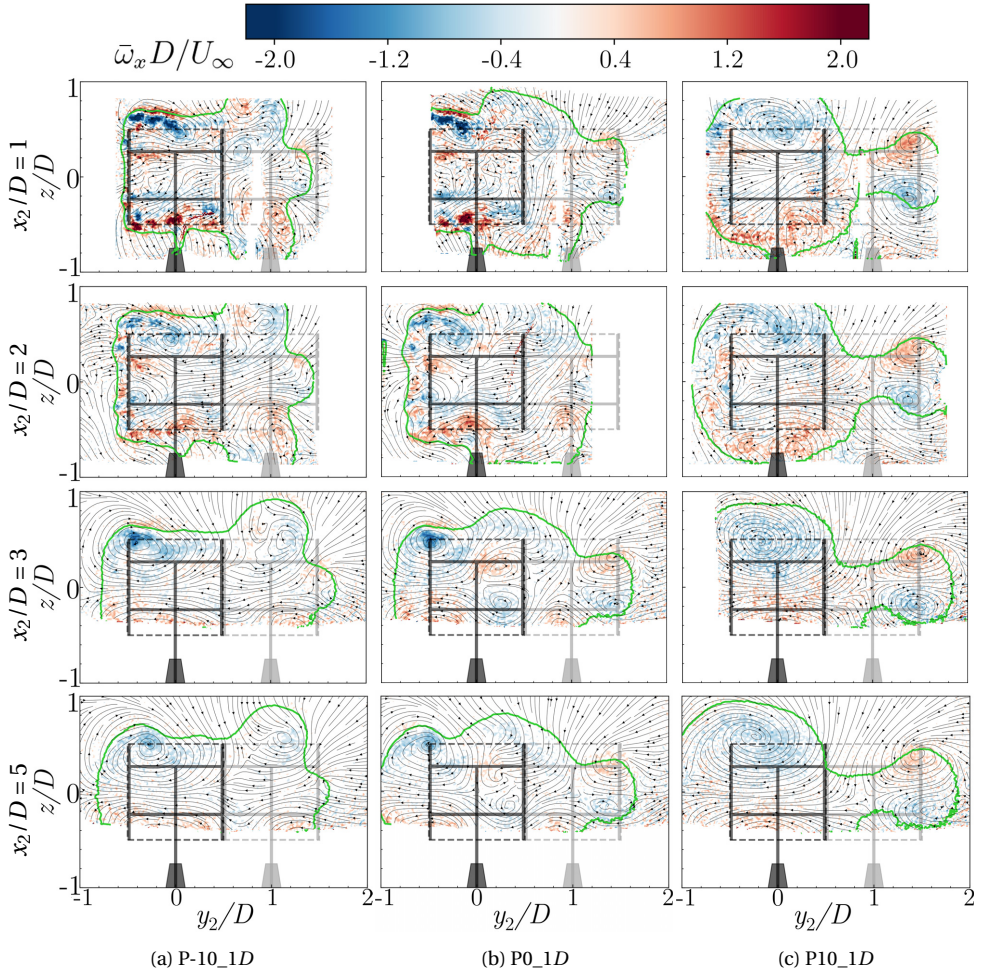
Figure 7.11: Streamwise vorticity contours with in-plane streamlines for offset cases, at the near wake of VAWT2 ($x_2/D = 1, 2, 3, 5$). Green contour lines indicate $u/U_\infty = 1$. Grey and Black schematics represent VAWT1 and VAWT2, respectively.
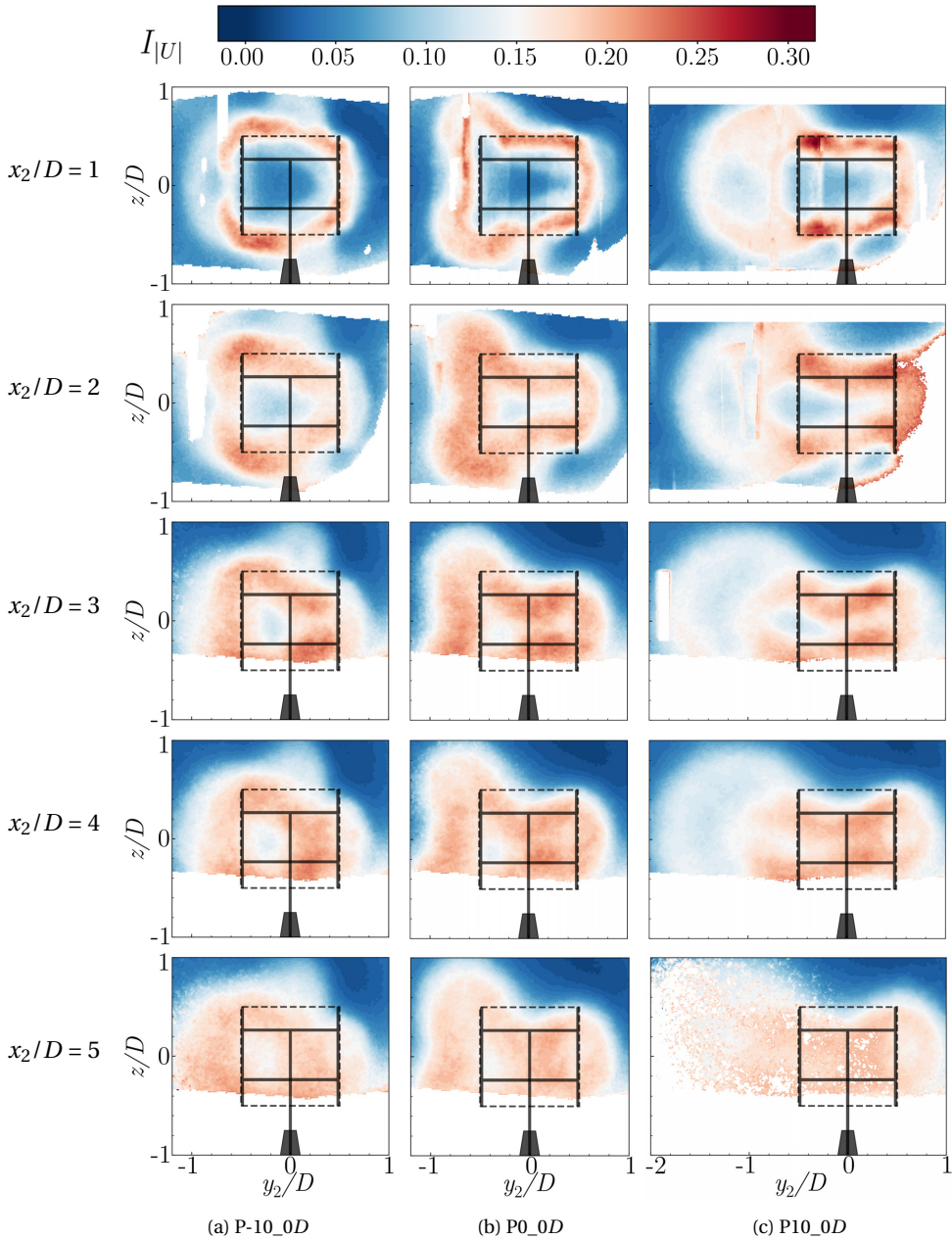
Figure 7.12: Contours of turbulence intensity magnitude for inline cases, at the near wake of VAWT2 ($x_2/D = 1, 2, 3, 4, 5$). Black schematics represent VAWT2.
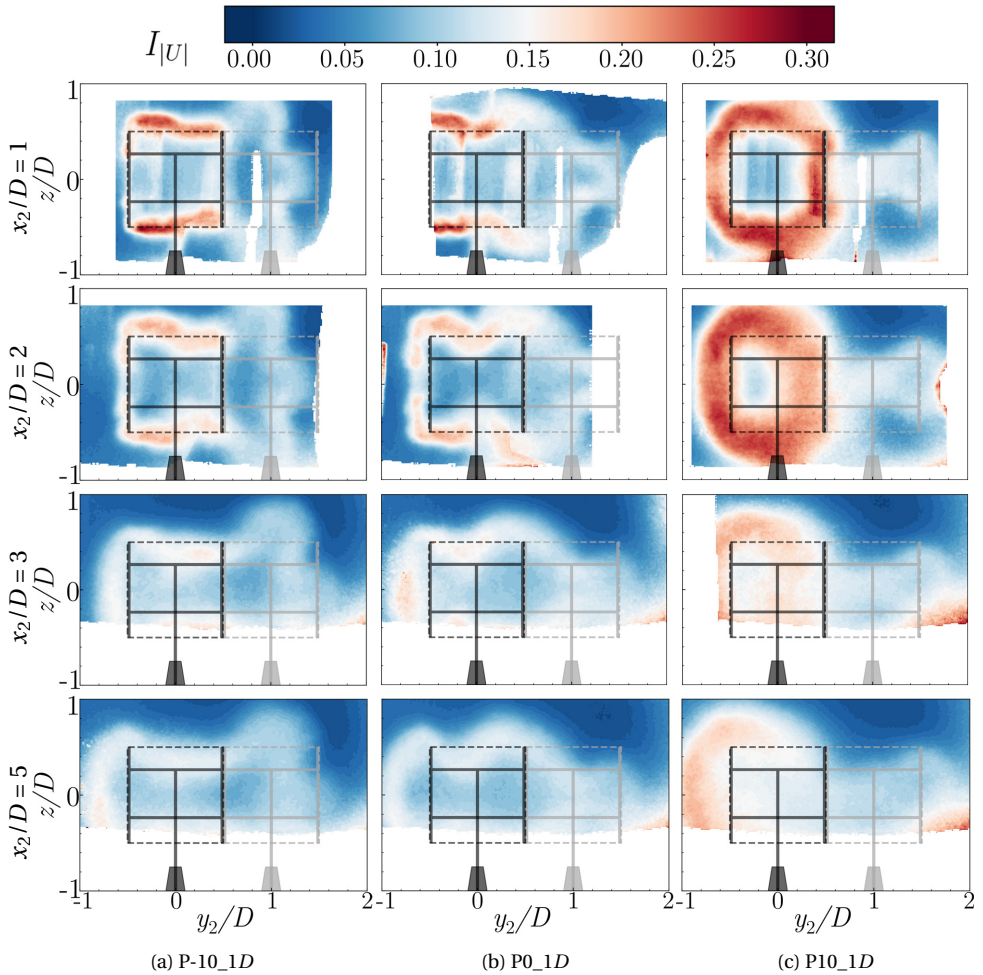
Figure 7.13: Contours of turbulence intensity magnitude for offset cases, at the near wake of VAWT2 ($x_2/D = 1, 2, 3, 5$). Grey and black schematics represent VAWT1 and VAWT2, respectively.

Generally, one would extract more wind energy by placing the VAWT3 out of the valley of AP curves. Inline cases P-10_0D and P0_0D, offset case P10_1D exhibit narrower distributions of low AP than the others, because VAWT2 mainly operates in the wake of VAWT1 in these cases. The narrower distribution means more abundant AP along transverse locations for the hypothetical VAWT. Among the three cases, P10_1D has the narrowest AP distribution, showing the efficacy of wake deflection.

However, in these three cases, VAWT2 mainly operates in the wake of VAWT1; the former has to extract energy in a decelerated and highly turbulent inflow. The wake effect as such will reduce the power extraction of VAWT2. Therefore, VAWT2 are moved out of VAWT1's wake in the other cases, i.e., offset cases P-10_1D and P0_1D, and the inline case P10_0D. The AP curves feature wider valleys for these cases, indicating more wind power extracted by VAWT1 and VAWT2 than in cases where the upwind turbine's wake entirely bounds the downwind turbine. The trade-off is, however, the narrowed high AP region for VAWT3.
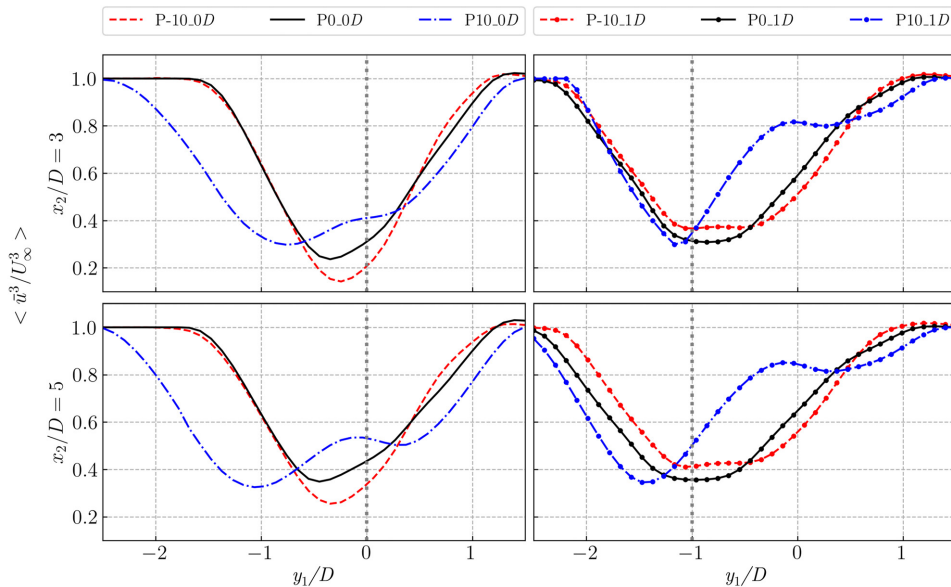

Figure 7.14: Available power distribution for VAWT3 along transverse locations (y_1/D) at $x_2/D = 3$ and 5. Grey dotted lines denote the rotor centre of VAWT2.

7.4. Conclusions

The wake interaction of two VAWTs placed upwind and downwind has been investigated experimentally via PIV and load measurements. The distance between the two turbines in the flow direction is 5D, and flow measurements cover a region 10D downstream of the first turbine (5D downstream of the second turbine).

The VAWT blade pitches are effective in modifying the rotor loading and deflecting the wake. With a positive 10° pitch, the VAWT increases the lateral force and deflects

the wake centre more than twice compared to the zero-pitch case. The deflected wake changes the inflow condition of the downwind VAWT inline with the upwind turbine (an increment of 44.6% available momentum at $5D$ downstream the rotor than P0), and thus increases the overall extraction of streamwise momentum ($C_{T,x}$ of VAWT2 increased 13.1%).

The study also covers in detail the case in which the wake is deflected towards the second turbine, to explore the more complex and undesirable situation. The wake of the upwind VAWT has a dominant effect on the wake topology and recovery of the downwind VAWT, provided that the latter is fully immersed by the wake of the upwind one. The vorticity system plays an important role in the interaction. When the counter-rotating vortices generated by the VAWTs are placed close enough, they lead to vigorous interaction and merging, thus increasing the turbulence intensity and in turn the wake recovery rate. On the contrary, if they are placed far enough but not separated completely, the merging of the wakes' shear layers takes the lead while the counter-rotating vortices are more effective in deforming the wake instead of increasing turbulence.

Deflecting the upwind turbine's wake and shifting the downwind rotor can both mitigate the wake effect, although wake deflection via blade pitch is apparently more flexible and easier to control in an array configuration. The wake deflection and the modified streamwise vortical system retain till the far wake, deflecting the downwind turbine's wake and enhancing the momentum recovery.

The results demonstrate the potential of VAWTs for enhanced wake recovery and provide a database for model validation. Additionally, they raise questions for future research on the maximum potential of energy recovery and how it can be achieved.

7

8

ON THE SIMULATING AND MODELING OF VAWT WAKES

This chapter examines the state-of-the-art analytical models and the Reynolds averaged Navier-Stokes simulation integrated with the actuator line model via comparison against high-fidelity experimental data. The analytical wake models and superposition models match the experiment well when the VAWT wake is barely deflected. However, when the wake deflection is significant, the analytical models yield substantial deviation.

8.1. INTRODUCTION

As mentioned in chapter 2 and 3, to capture the flow surrounding VAWTs and therefore investigate their characteristics, a great number of experimental and numerical studies have been carried out. However, experimental studies are usually confined to a relatively low Reynolds number, which is inconsistent with the up-scaled scenario offshore. Hence, computational fluid dynamics simulations have been employed to fill the gap.

Various simplifications of turbine representations have been introduced to yield accurate simulation results with less computational cost based on CFD. The actuator line model is prevailing due to its computational cost-efficiency and ability to reproduce unsteady wake dynamics. Analytical models are even more simplified and faster tools for wake velocity prediction. They are helpful in the engineering design optimisation of wind farms, where the instant response of the models is critical. Analytical models for wake and wake superposition are often employed to estimate the wind farm power output.

This chapter is composed of four aspects: 1) Verifying RANS+ALM simulation and analytical models of VAWT wakes introduced in chapter 3, using high-fidelity experimental data presented in chapter 6. 2) Validating RANS+ALM under significant lateral wake deflection. 3) Comparing the existing wake superposition models and the RANS+ALM simulation. 4) Reflecting on improvement approaches.

We answer the following research questions:

1. What is the range of validity of the cutting-edge models for the VAWT wake?
2. How to improve the current simulations/models?

8.2. METHODOLOGY

8.2.1. VALIDATION CASES

The available analytical models do not account for wake deflection. Hence, for a fair comparison, we choose a baseline case without operations for wake deflection to verify the models, i.e., the zero-pitch case (P0) in chapter 6 (Page 92). Then, case P10 is selected to validate the RANS+ALM model under significant wake deflection, considering P10's effectiveness in deflecting the wake and enhancing the power output. Finally, the P0_0D in chapter 7 is used to verify the wake superposition models and the RANS+ALM simulation.

8.2.2. ANALYTICAL WAKE MODELS

Two analytical wake models based on 1D and 2D actuator disc models are selected for comparison. The models are the Jensen model and the Gaussian-similarity-based models proposed by Bastankhah and Porté-Agel (2014) (BPA model). Both models have an extrapolated version from the wake of HAWTs to that of VAWTs (Abkar, 2018).

A short review of the models' governing equations is provided in appendix B. It has been pointed out that calibrating the wake growth rate is a prerequisite for the models reviewed. As indicated in the appendix, the model has been tuned for engineering purposes, which often feature high Reynolds numbers (e.g., Frandsen, 1992; Niayifar and Porté-Agel, 2015; Penã et al., 2016). However, the expression of expansion rate for the low Re scheme is not found in the literature, and using the ones for high Re is question-

able. Therefore, this section presents the calibration procedure using the experimental data for the small VAWT without pitch, and the resulting wake growth/expansion rate are used in the models for comparison.

The standard normal Gaussian shape is used for the calibration of the wake expansion. At each downstream location of the wake, the velocity profile at horizontal line crossing the centre of the rotor is fitted with normal Gaussian shape function. The normalised standard deviations σ/D from the Gaussian function versus the downstream location x/D are depicted in figure 8.1. The normalised standard deviations are fitted with a first-order polynomial, based on assuming the wake expands linearly. The slope k^* is the expansion rate adopted in the model. The figure shows that the calibrated wake expansion factor is $k^* = 0.020$. This value is adopted in the Jensen model for simplicity.
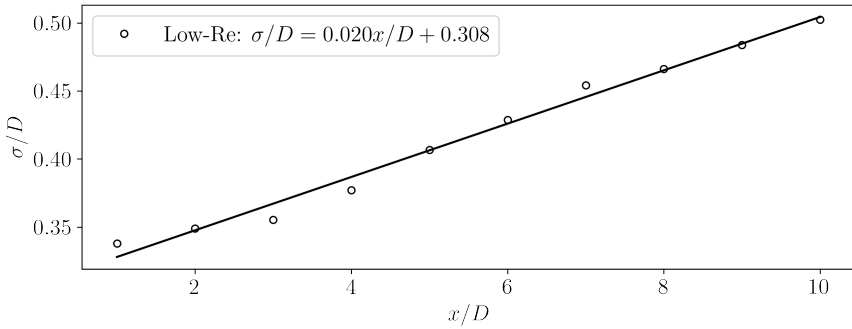

Figure 8.1: The normalised standard deviations of the velocity deficit profiles along streamwise locations.

8.2.3. WAKE SUPERPOSITION MODELS
The existing superposition models in the literature have been reviewed in chapter 3. Here below are their formulations.

$$\text{Method A:} \, U_w(x, y, z) = U_\infty - \sum_i \left(U_\infty - u_w^i(x, y, z) \right) \tag{8.1}$$

$$\text{Method B: } U_w(x, y, z) = U_\infty - \sqrt{\sum_i \left(U_\infty - u_w^i(x, y, z) \right)^2} \tag{8.2}$$

$$\text{Method C : } U_w(x, y, z) = U_\infty - \sum_i \left(u_0^i - u_w^i(x, y, z) \right) \tag{8.3}$$

$$\text{Method D: } U_w(x, y, z) = U_\infty - \sqrt{\sum_i \left(u_0^i - u_w^i(x, y, z) \right)^2} \tag{8.4}$$

$$\text{Method E: } U_w(x, y, z) = U_\infty - \sum_i \frac{u_c^i(x)}{U_c(x)} u_s^i(x, y, z) \tag{8.5}$$

The present work uses the ALM with an unsteady RANS solver (*pimpleFoam* library from
OpenFOAM, an open source CFD software). The simulation procedure is illustrated in
figure 3.6. Comparisons and convergence studies for meshes and time steps have been
reported in the Master theses of Monni (2021), Patil (2021), and Nikhilesh (2021).

8.3. Validation results

8.3.1. Case P0: models comparison under moderate wake deflections

Velocity contours
The measured and modelled streamwise velocity contours are compared in figure 8.2.
The Jensen model is the simplest and gives a uniform wake velocity within a square re-
gion. In comparison, the BPA model yields a continuous velocity field. Both the analyti-
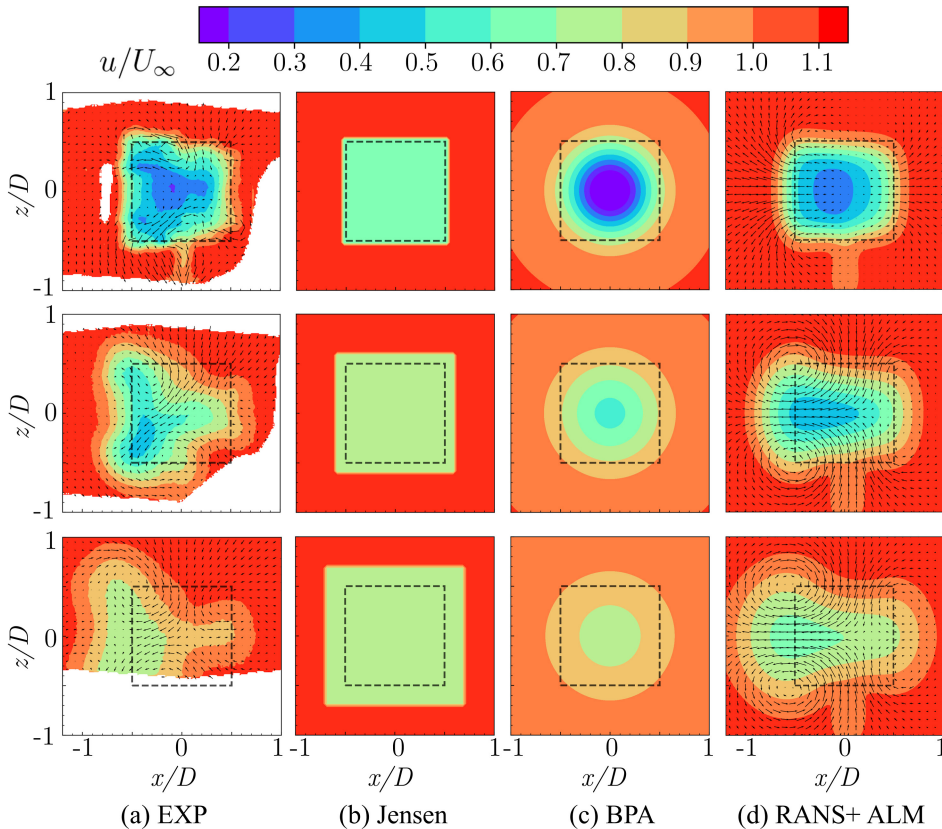cal models

Figure 8.2: Cross-sectional streamwise velocity contour and in-plane vectors, the latter is not ap-
plicable for the analytical models BPA and Jensen model. Each row from top to bottom stands for
$x/D = 1,5,10$, respectively. Black dashed square denotes the VAWT's frontal area.

cannot predict the in-plane velocities, and they can only produce axis-symmetric wakes, given that no yaw/deflection correction is integrated. As expected, the RANS+ALM yields the highest fidelity among the models. Besides a comparable velocity deficit that is discussed further in section 8.3.1, the ALM-based simulation reveals in-plane motions that are identified as crucial in deflecting and deforming the wake (Huang et al., 2023). Moreover, the wake of the tower is also simulated. However, the in-plane velocities have different directions and strengths compared to the PIV results. In chapter 6, we have shown that the in-plane velocity is closely related to the tip vortices, and the latter is generated due to the variation of blade loading. This implies that the airfoil lift and drag coefficients are not accurately evaluated with the simulation, probably because 1) the static polar of the airfoil needs correction, 2) dynamic stall correction fails at such a low Reynolds number that causes the occurrence of deep stall.

VELOCITY DEFICIT PROFILES
The profiles of velocity deficit are compared in figure 8.3 to examine the performance of the models in predicting wake recovery. The Jensen and the BPA model only predict valid maximum velocity deficit in the far wake (approx. $x/D \geqslant 5$ for the Jensen and $x/D \geqslant 3$ for the BPA model). In the near wake, the Jensen model underestimates the deficit, whereas the BPA model overestimates it. The measured wake is slightly deflected horizontally; however, the location of maximum deficit in the analytical models is always in the centre of the projected rotor. In contrast, the RANS+ALM predicts comparable velocity deficit and wake deflection.
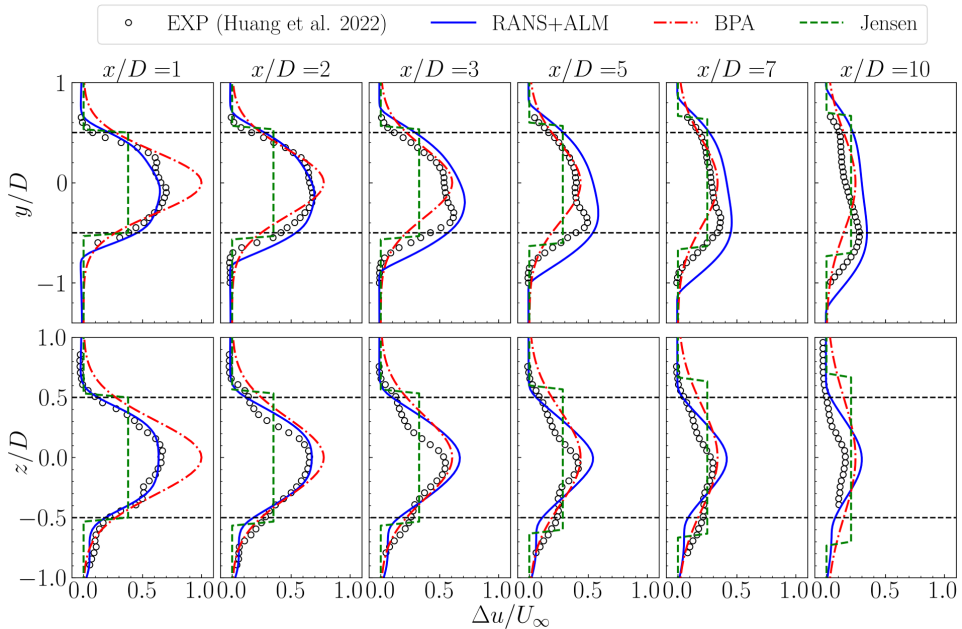

Figure 8.3: Centreline velocity deficit profiles of P0 (both horizontal and vertical) from the measurements or models in different fidelity.

8.3.2. CASE P10: VALIDATION OF RANS+ALM UNDER SIGNIFICANT WAKE DEFLECTIONS

We have shown that only RANS+ALM accounts for the wake deflection among the wake models inspected in this work. Thus, in this section, we further verify its performance in a significant wake deflection by comparing the simulation with the experiment.

VELOCITY CONTOURS

The cross-sections at both near and far regions in the wake ($x/D = 1,5,10$) are compared in figure 8.4. The simulation matches the experiment very well; It resolves the wake deflection and deformation, the in-plane motions and the vortex locations. The simulation performs excellently in the far wake ($x/D = 5,10$), substantially giving velocity fields that resemble the experimental data. In the near wake, it underestimates the maximum deficit around the windward (also the advancing) side of the VAWT.
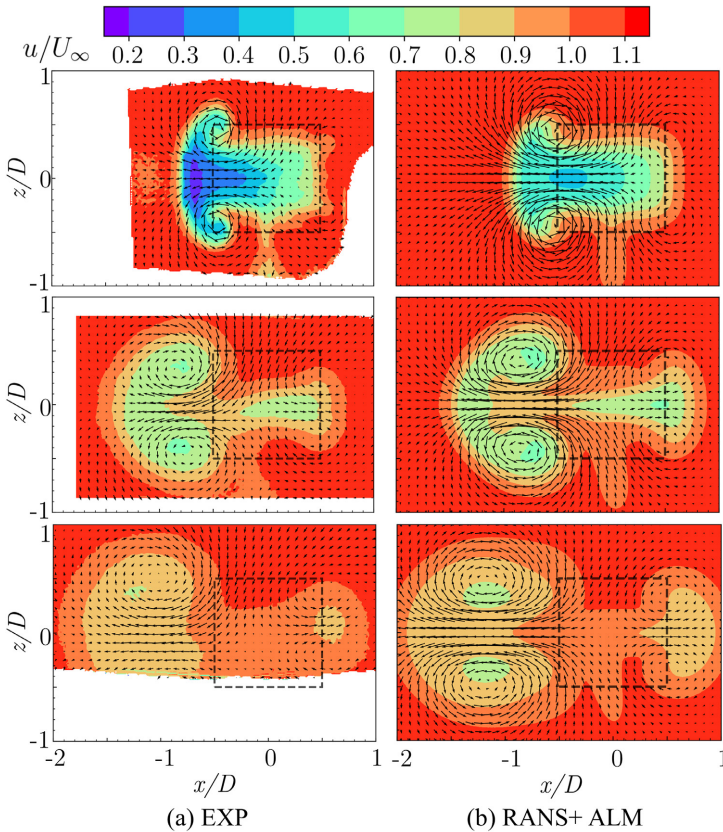
Figure 8.4: Cross-sectional streamwise velocity contour and in-plane vectors. Black squares denote the frontal area of the VAWT. Each row from top to bottom are extracted at $x/D = 1,5,10$, respectively.

VELOCITY PROFILES

We extract the velocity deficit profiles in the cross-sections along the horizontal and vertical planes crossing the turbine centre, showing them in figure 8.5. As illustrated, the curves of the simulation and the experiment collapse since $x/D = 2$. The slight difference at $x/D = 1$ could be attributed to the dynamic stall correction adopted in the simulation, which underestimates the lift coefficient at an extremely large angle of attack and low Reynolds number.
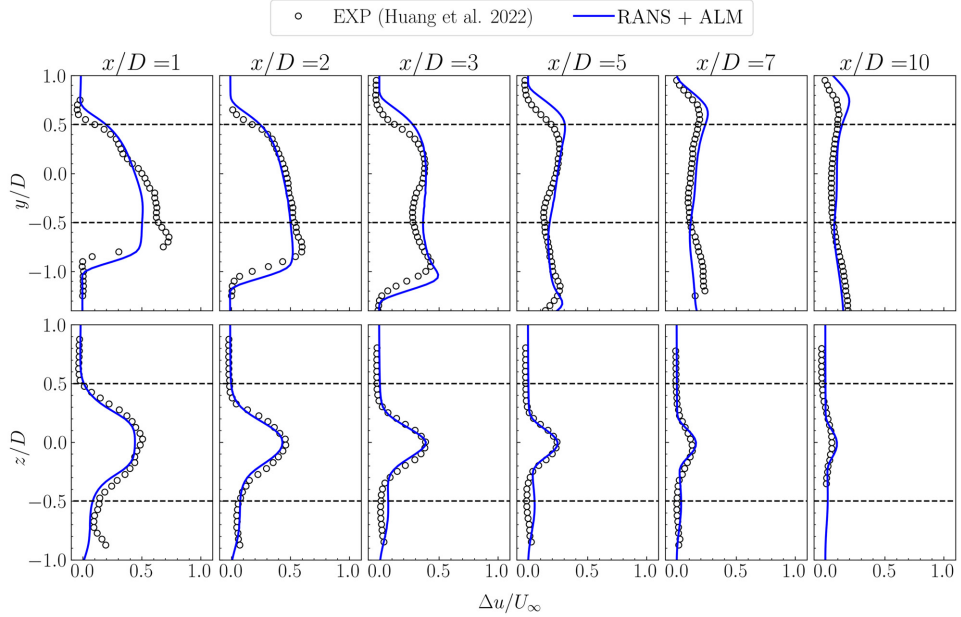

Figure 8.5: Centreline velocity deficit profiles of P10 (both horizontal and vertical) from the measurements or models in different fidelity.

NORMAL FORCE VECTORS AND RESULTING WAKE OUTLINES

Based on the actuator cylinder model and vorticity transport equation, we presented simplified normal force fields and resulting patterns of wake deflections and deformations in chapter 6 (figure 6.3), yet the force field distribution along the blade swept area was not measured in the experiment. With numerical simulations examined in this section, the normal force distribution on the swept area is extracted from the blade loading using the following expression:

$$f_n = \frac{B}{2\pi R}(L \cdot \cos(\alpha - \varphi) + D \cdot \sin(\alpha - \varphi)) \quad . \tag{8.6}$$

where B is the number of blades, L and D are the averaged lift and drag over the blade at a certain azimuth, α is the angle of attack, φ is the blade pitch angle.

The normal force fields of cases P0 and P10 are illustrated in figure 8.6. Figure 8.6-(a) is similar to the case shown in 6.3-(a) with slightly higher lateral forces towards negative

y, while 8.6-(b) corresponds to 6.3-(c). The wake outlines and vorticity systems are consistent with the model proposed in chapter 6. It is observed that P10 has a stronger lateral force yielding more significant lateral wake deflection; This confirms that the wake deflection of VAWTs is ascribed to the overall lateral forces over the swept area. The lateral force induces counter-rotating vortices modifying the wake topology.
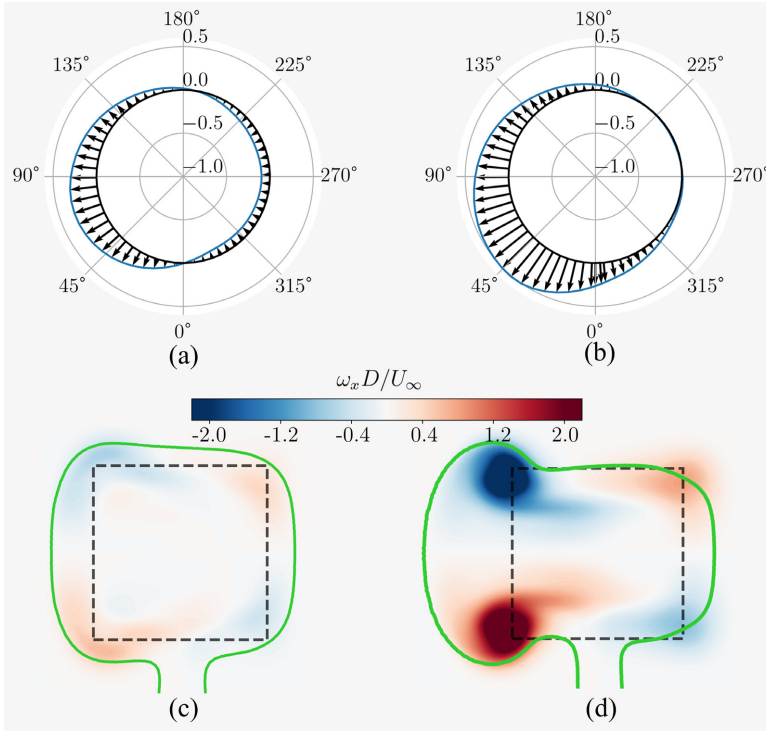

Figure 8.6: Normal force (C_N) vectors and resulting wake outlines of P0 (left) and P10 (right). (a) and (b): normal force vectors distributed along the actuator cylinder. The freestream flows from $90°$ to $270°$. (c) and (d): resulting streamwise vorticity field and wake outline at $x/D = 1$. Green contour lines are where $u/U_\infty = 1$.

8.3.3. VALIDATION OF WAKE SUPERPOSITION MODELS

The velocity contours at cross-sections from the experiment, wake superposition models, and the RANS+ALM model are compared in figures 8.7 and 8.8. Figure 8.7 corresponds to the P0_0D case in chapter 7, illustrating the wake superposition in a slight deflection by the upwind turbine. Based on the visual comparison, model A overestimates the velocity deficit whereas model D underestimates it; Models B, C and E produce similar velocity deficit and deflection compared with the experiment at $x_2/D = 3, 4, 5$, which are in the far wake region of the downwind VAWT (indicated as VAWT2). Nonetheless, models C and E exhibit larger deviations with the experiment at $x_2/D = 1, 2$. In contrast, the RANS+ALM model performs robustly in both near and far wake, yielding velocity and

wake deflection in good matches with the experiment. However, considering the simulation's much heavier computational cost compared to the analytical models, we believe it is fair to conclude here for the wake superposition with very small wake deflection, model B outperforms the other models.
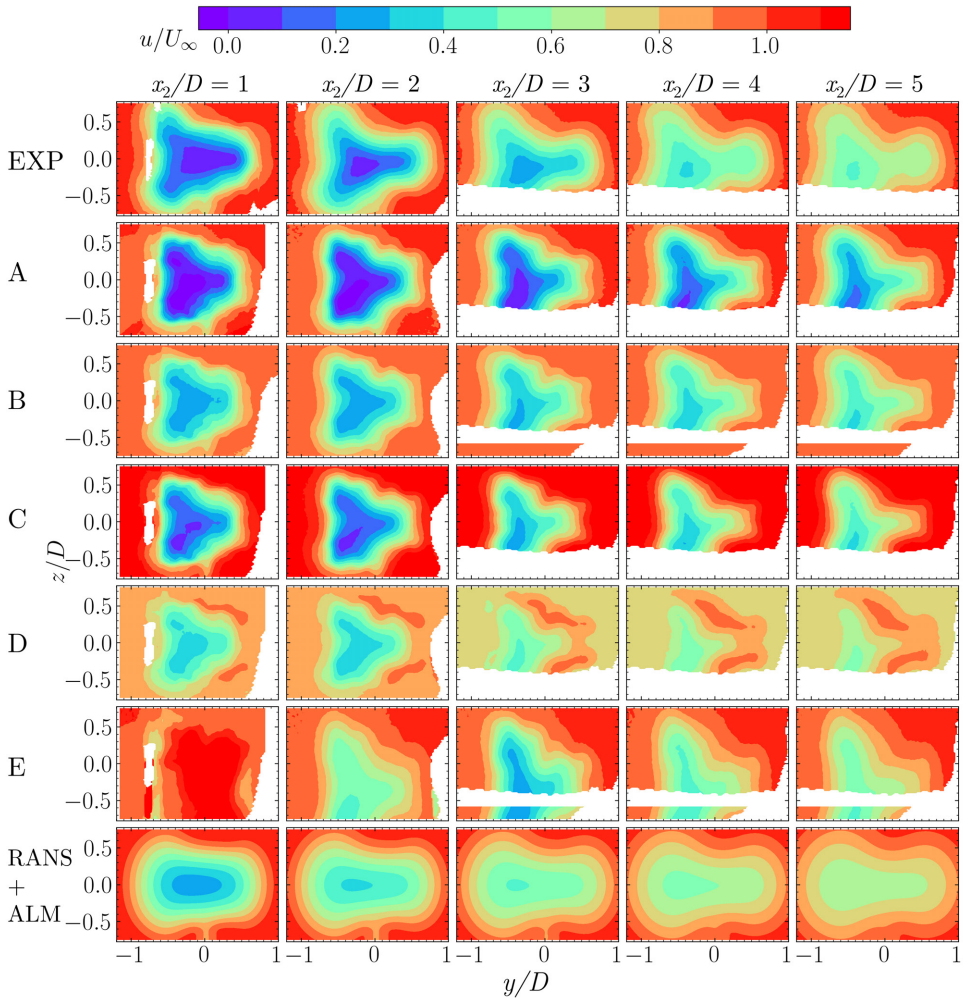

Figure 8.7: P0_0D: Comparison of the normalised streamwise velocities from the experiment and the examined models. Rows from top to bottom: experimental data, method A-E predictions and simulation data; Columns from left to right: x_2/D(distance behind the second turbine) = {1,2,3,4,5}.

The wake superposition in a significant wake deflection is shown in figure 8.8, where the wake in P10_0D (see chapter 7) is examined. All the analytical superposition models yield significant deviation from the experimental result. The models simply overlap two

separate wakes without considering the diffusion process during the wake interaction. Instead, the simulation produces rather smooth velocity contours, resolving comparable velocity deficit, wake outline, and the wake merging process.
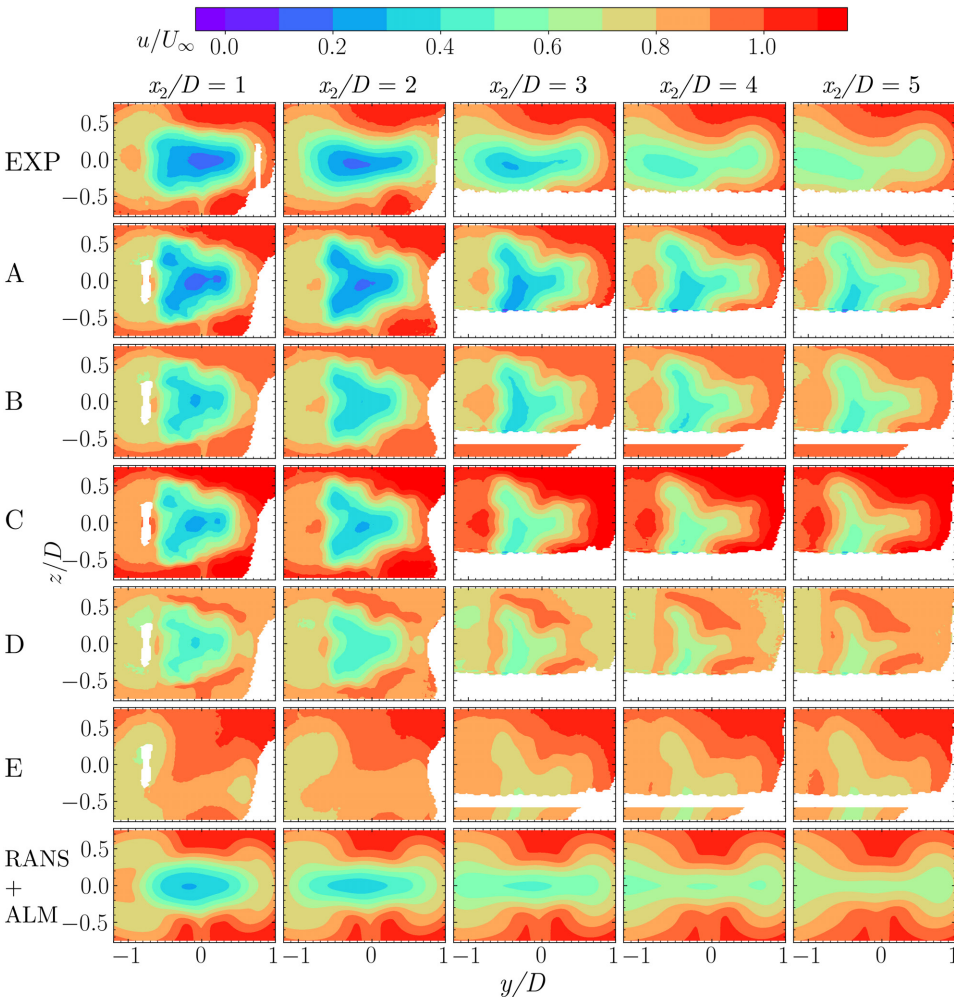
Figure 8.8: P10_0D: Comparison of the normalised streamwise velocities from the experiment and the examined models. Rows from top to bottom: experimental data, method A-E predictions and simulation data; Columns from left to right: x_2/D (distance behind the second turbine) = {1,2,3,4,5}.

8.3.4. DISCUSSION ON POSSIBLE WAYS OF IMPROVEMENT
The comparison above has revealed the limitations of the state-of-the-art analytical models for isolated VAWT's wake and superposition of multiple wakes, especially when

there is a notable wake deflection. The latter is deemed as an effective way to increase the wind farm power output (Huang et al., 2023), and modelling wake deflections of VAWTs is beneficial for the wind farm design. Hence, in this section, we discuss the reasoning and shed light on possible ways of improvement for these models to characterise and match VAWT wakes with large deflections.

WAKE SELF-SIMILARITY ON ACCOUNT OF DEFLECTION

Existing techniques of the analytical models to match the velocity profiles are all based on the self-similarity of the wake. Here we scrutinise the similarity in the wake of P0, using the high fidelity experimental data aquired in chapter 6 instead of the simulation data, as depicted in figure 8.9. The velocity deficit profiles at different downwind locations (x/D) on the plane crossing the mid span ($z/D = 0$) are compared following the classical normalisation method documented in Pope (2001), the method has been proved effective for turbulent wakes without lateral actuations. The comparison is illustrated in figure 8.9-left, where the ordinate is $u(x, y)/\Delta u_{\max}(x)$, and the abscissa is $y/\delta_w(x)$. $\Delta u_{\max}(x)$ is the maximum streamwise velocity deficit at a specific x, while $\delta_w(x)$ is the local characterised wake width. δ_w is determined at each x as follows:

$$\begin{cases} \Delta u \left(y = \delta_{w,1} \text{ or } \delta_{w,2} \right) = \dfrac{1}{2} \Delta u_{\max} \\ \delta_w = |\delta_{w,1} - \delta_{w,2}| \end{cases} \tag{8.7}$$

In other words, the characterised wake width selected for normalisation denotes a region where the velocity deficit is larger than half of the maximum deficit.
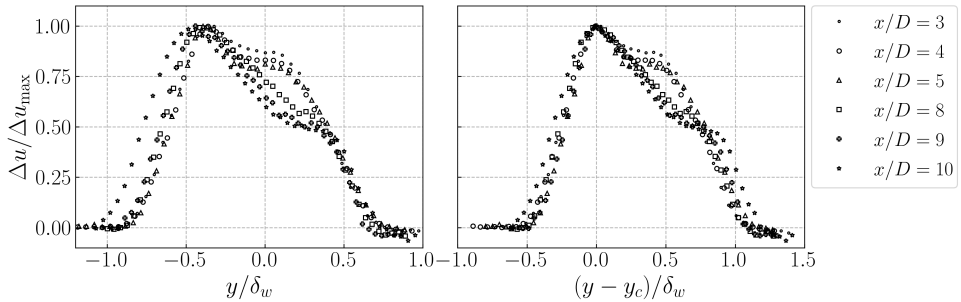

Figure 8.9: The self-similar velocity deficit profiles of P0 (experimental data from chapter 6). Left: without subtracting wake centres; Right: subtracting wake centres.

The velocity profiles collapse well on the leeward side ($y>0$ in this case); However, they feature a shift on the windward side. The latter is ascribed to the wake deflection. Such a shift has not been taken into account in the currently available analytical wake models for VAWT, and therefore, these models fail to depict a deflected wake. This has been discussed in section 8.3.1. Abkar and Dabiri (2017) proposed an approach to eliminate the deflection effect and seek the similarity, by subtracting the wake centre:

$$\eta_y = \left(y - y_c \right) / \delta_w. \tag{8.8}$$

where y_c is the y-coordinate of the wake centre that is defined as the location where the maximum velocity deficit occurs.

The resulting velocity profiles are presented in figure 8.9-right. It is obvious that a better similarity is achieved after sufficient distances downwind from the turbine ($x/D \geqslant$ 3), by subtracting the deflection of the wake centre. The distribution of wake centres is illustrated in figure 8.10.
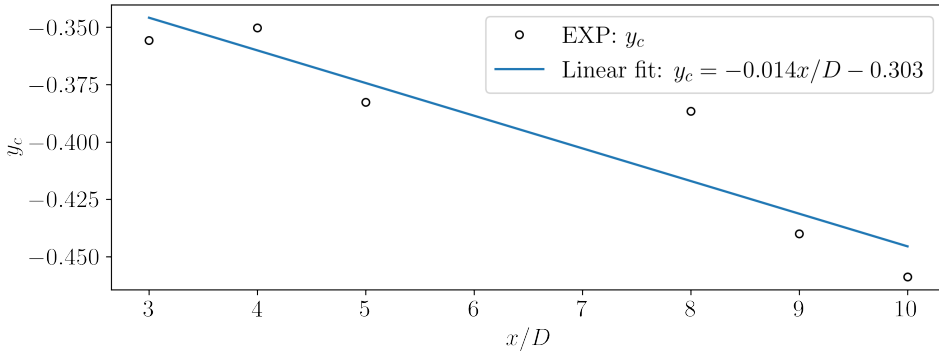

Figure 8.10: Wake centre locations development of case P0.

It is observed that the similarity manifest in the wake of P0 is different from that in the HAWT wakes. The similarity in a HAWT wake is characterised by a normal Gaussian distribution and has been widely adopted in HAWT wake models (see appendix A). Hence, those VAWT wake models simply transposed from models for HAWTs have an inherent error due to the misinterpretation of the wake similarity. And such error is intensified when significant wake deflections and the asymmetry of velocity profiles are present.

There have been some efforts paid to investigate different similarity shapes to improve the models, such as super-Gaussian in the work of Ouro and Lazennec (2021) to account for the height-to-width ratio of VAWTs, double-Gaussian in the work of Schreiber et al. (2020) and Keane et al. (2016) to improve the near wake accuracy of HAWT wake models. Curve-fitting for the velocity profiles of P10's wake, based on the normal Gaussian, the skew Gaussian and the double Gaussian are carried out, as illustrated in figure 8.11. Double Gaussian and skew Gaussian curves match with the velocity better than the normal Gaussian in terms of reproducing the wake deflection. The double Gaussian has more fitting variables than the others and thus features the best match. In all, using proper shape functions is likely helpful in improving the analytical models for VAWT wakes.

MOMENTUM CONSERVING IN CROSS-FLOW DIRECTION

We have shown that the wake models and superposition models yield substantial errors when the VAWT wake is significantly deflected. This is ascribed to a lack of consideration of the cross-flow actuation and could be accounted for by the momentum conservation in the cross-flow direction. Bastankhah and Porté-Agel (2016) discussed the generation of counter-rotating vortex pairs by the cross-flow steering in yawed HAWT's
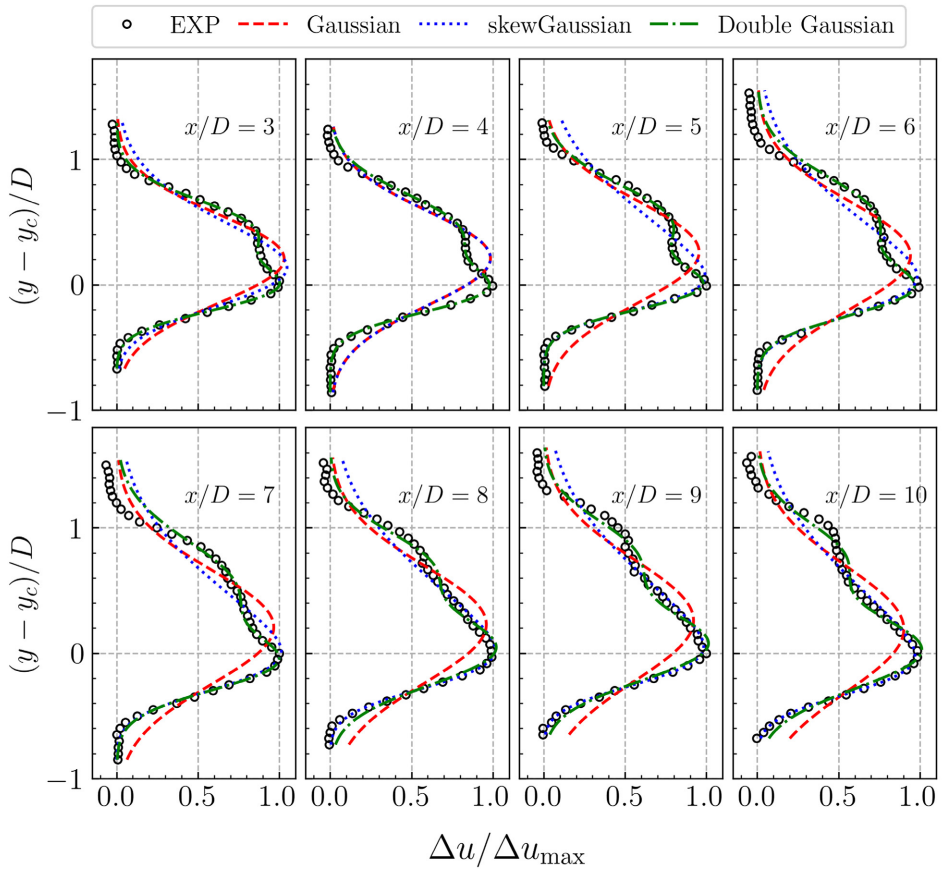
Figure 8.11: The self-similar velocity deficit profiles of P0 (experimental data from chapter 6). Data fitted with Gaussian, skew Gaussian and Double Gaussian shapes.

wake, based on the mass conservation. They pointed out that the lateral force is related to such an in-plane motion, and further proposed an analytical wake model for yawed HAWTs, treating the wake centre deflection analogous to a coflowing jet; The lateral velocity induction is determined empirically using the model proposed by Coleman et al. (1945), which is derived based on the induced-velocity field of an idealized helicopter rotor. However, as indicated in chapter 5, the wake of helicopter rotors with a planar-disc-shaped swept area is likely to deviate from that of a VAWT. And thus, extrapolating existing wake models for yawed HAWT to account for the wake deflection of VAWT is probably not viable. A physics-based justification of the lateral motion is necessary for a VAWT wake model, and the author recommends using the coflowing jet analogy with the momentum conservation, the latter relates the velocity and forces.

8.4. Conclusions

The state-of-the-art analytical models for stand-alone VAWT wake (the Jensen model and the BPA model) and wake superpositions (algebraic models and a momentum-conservation-based model), and a RANS simulation integrated with the ALM model are validated using the high-fidelity PIV data. The main findings in this chapter are as follows:

- The analytical wake models need to be tuned regarding the wake expansion rates. The tuned models show satisfactory agreements on the maximum velocity deficits along x. However, both models fail to predict the wake deflection. In contrast, the RANS+ALM yields velocity fields matching well with the experimental data.

- All the superposition models examined are only valid when the wake deflection is negligible. The model of Zong and Porté-Agel (2020a) shows better agreement with the experiment in the far wake of the downwind turbine, while it yields unrealistic results at $x_2/D = 1$. This is caused by a non-negligible pressure gradient in the proximity of VAWT2, thus the governing equation of the model is not applicable here.

- The RANS+ALM simulation features higher fidelity than the analytical models. It resolves the cross-flow motions actuating the wake deflection and the interaction process in multiple wakes. The disadvantages compared with the analytical models are a) more expansive computational cost; b) higher complexity in setting up an evaluation; c) it needs correct airfoil lift-drag polar which is not always available for arbitrary Reynolds numbers.

9

EVALUATION OF THE POWER ENHANCEMENT: A SIMULATION STUDY

9.1. INTRODUCTION

BASED on the validated RANS model, we explore the wake deflection effects on the power performance of a full-scale VAWT. The upscaling results in a chord-based Reynolds number at 1×10^7. The blade airfoil features a high stall angle in such a high Reynolds number. This allows for an extensive operation range for the blade pitching without hampering the performance. Contrary to the experimental cases reported in chapter 6 and 7, the tip speed ratio of the upscaled simulation is set to a relatively high value (4.5), avoiding severe dynamic stalls of the rotating blades. For the sake of simplicity, struts, tower, and floor are not present in the simulation unless otherwise specified, and the freestream is uniform.

9.1.1. CASES DESCRIPTION

Four groups of cases are analysed, covering the isolated VAWTs and array configurations with two or three VAWTs. First, the wakes of isolated VAWTs are simulated, with different fixed blade pitches (-10°, 0° and 10°) to deflect the wake. The convention of pitching has been introduced in chapter 6, with the positive pitching towards the rotating shaft and vice versa. The attributes of the VAWT and the freestream are listed in table 9.1. It is noted that the rotation speed of all the turbines is kept the same unless otherwise stated, resulting in a tip speed ratio of 4.5 with respect to the freestream. The mesh topology for calculation is kept the same as that for the lab-scale VAWT (chapter 8), except that the entire simulation domain has been scaled. The $k - \epsilon$ turbulence model has been tuned for such a turbulence intensity level and Reynolds number, as documented in the Master thesis of Monni (2021).

Table 9.1: Attributes of the simulated up-scaled VAWT and the freestream.

Symbol	Parameter	Value
U_∞	Freestream velocity	$10\,\mathrm{m\,s^{-1}}$
I	Turbulence intensity	8%
AR	Aspect ratio, H/D	1
Re_D	Diameter-based Reynolds number	1.1×10^8
B	Number of blades	3
c/R	Normalised chord length	0.025
λ	Tip speed ratio	4.5
φ	Pitch angles	$-10°, 0°, 10°$
	Blade profile	NACA0025
	Rotation direction	Counterclockwise

Then, the inter-turbine distance effects on the wake interaction are studied with array configurations, wherein two VAWTs are considered. The upwind VAWT is denoted as VAWT1 and the downwind is VAWT2, as illustrated in figure 9.1. VAWT1 deflects the wake via different blade pitch angles while VAWT2 operates with zero pitch angle. The inter-turbine distance varies between 3, 4 and 5 rotor diameters.

To explore the wake interactions of two pitched VAWTs and shed light on optimum blade pitch patterns in a wind farm, the third group of simulations has been conducted

where VAWT1 and VAWT2 are both pitched to deflect their wakes; The inter-turbine distance is kept as four diameters.

The fourth group simulates three-VAWTs arrays with and without floor. Except for examining the floor effect, the sustainability of the enhancement on the power extraction is investigated via examining the vertical advection of mean kinetic energy (MKE) of pitching combinations selected based on the third group.
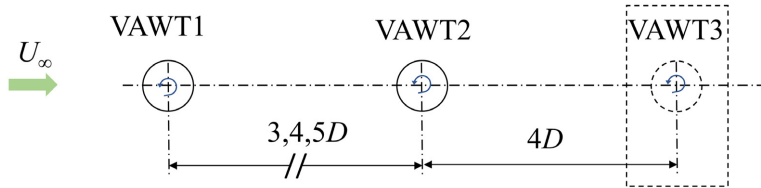

Figure 9.1: A schematic top view of array configurations. VAWT3 presents in some cases.

9.2. RESULTS AND DISCUSSION

This section first presents the simulation results of the isolated turbines, assessing their performance and wake features. The vortex system is emphasised and validates the simplified patterns proposed in chapter 6. Then, the enhancement of power extraction in array configurations is discussed. The effects of inter-turbine distance, blade pitching combination and floor are analysed.

ISOLATED VAWTS

9.2.1. TURBINE PERFORMANCES

The performances of isolated turbines with different pitch angles are listed in table 9.2. With pitch angles of $-10°$ and $10°$, the rotor produces significant lateral forces to deflect the wake while sacrifices the rotor performance slightly.

Table 9.2: Performance of isolated VAWTs.

cases	C_P	$C_{T,x}$	$C_{T,y}$
P-10	0.46 (-8%)	0.69	-0.37
P0	0.50	0.68	0.02
P10	0.44 (-12%)	0.64	0.34

The time-averaged normal loading over the swept area is calculated based on the AC model (equation 8.6). The loading distributions on the AC are depicted in figure 9.2. It is reminded here that the coordinate system presented in figure 9.2 follows the convention of a VAWT rotating counterclockwise; Therefore, the coordinates seem flipped compared to that in figure 6.1. However, the coordinate systems are essentially the same in that θ starts on the advancing side and increases along the blade rotation direction.
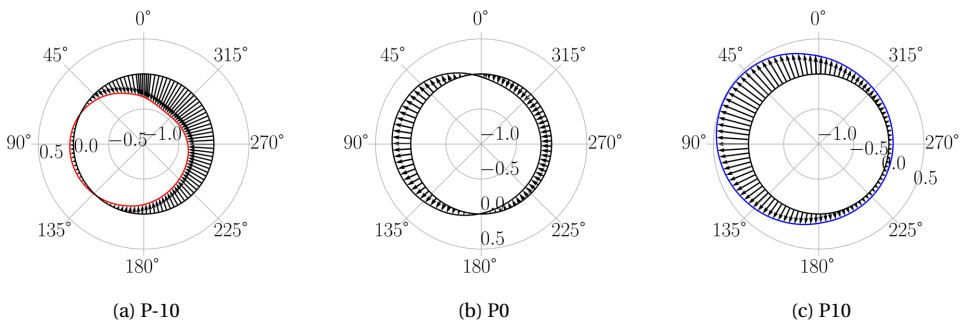
Figure 9.2: Normal force coefficient ($C_{\mathbf{f},n}$) distributions for different blade pitches.

Compared to P0, when the VAWT is with negative blade pitch (P-10), the loading is shifted to the downwind part, and vice versa. P-10 and P10 feature notable overall lateral forces on opposite sides. The distributions of torque coefficients are presented in figure 9.3. Clearly, torque coefficients shift corresponding to the loading. The resulting velocity and vorticity fields are presented in the following sections.
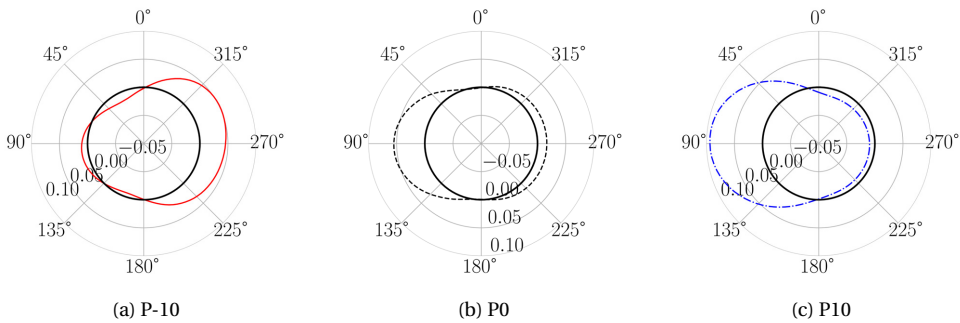

Figure 9.3: Torque coefficient ($C_{q,t}$) distributions for different blade pitches.

9.2.2. STREAMWISE VELOCITY AND VORTICITY FIELDS

The streamwise velocity and vorticity fields in the near wake ($x/D = 1, 3, 5$) of the isolated VAWTs with different blade pitches are presented in figure 9.4 and 9.5, respectively. The positive blade pitch deflects the wake towards the windward of the swept area and the negative pitch towards leeward (following the division of the swept area in figure 6.1).

The relationships between the wake outlines and the normal force distributions are successfully predicted in figure 6.3. With the loading shifted upwind or downwind, the wake features horizontal or vertical stretching, as depicted in 6.3-(a) and 6.3-(b). The overall lateral forces cause the deflection. Both the stretching and the deflection contribute to a higher streamwise velocity in the projected area, giving more available power for downwind turbines. The increased power output in an array due to the wake deflection is reported in section 9.2.5.
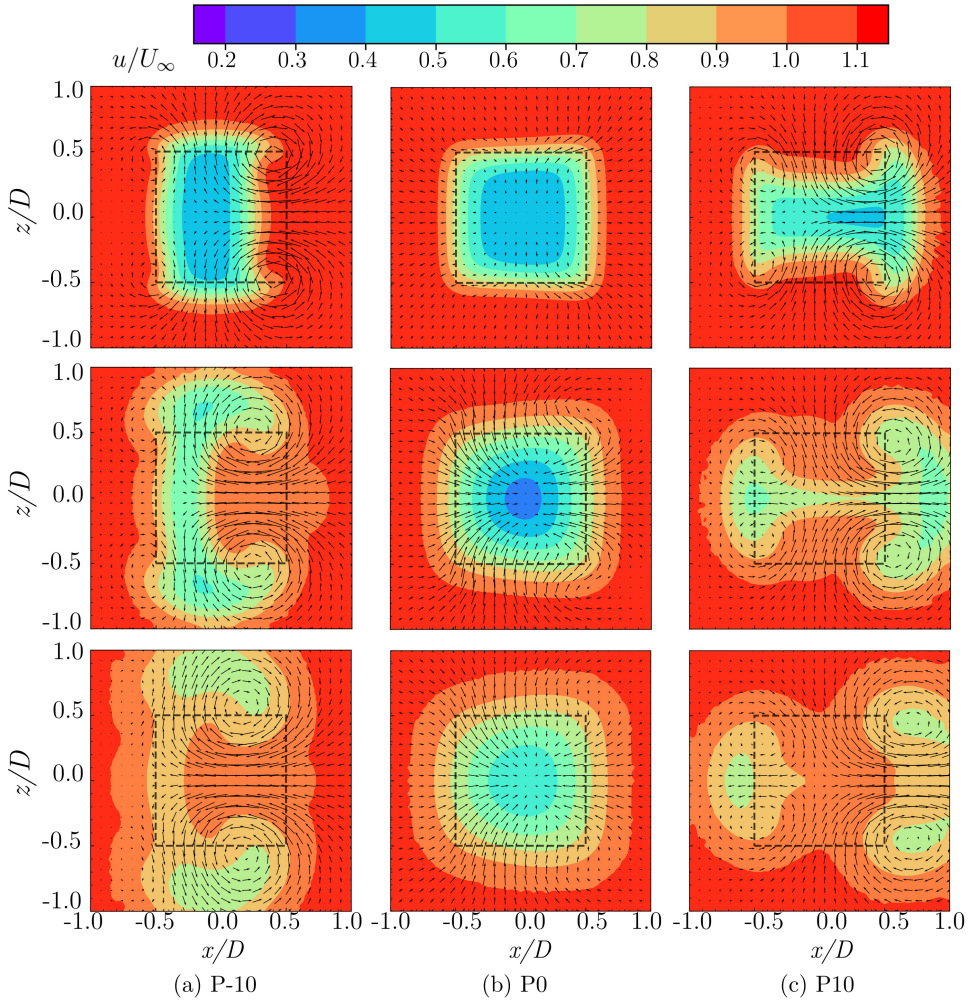
Figure 9.4: Cross-sectional streamwise velocity contours and in-plane vectors for cases P-10, P0 and P10. Each row from top to bottom stands for $x/D = 1, 3, 5$, respectively. Black dashed squares denote the VAWT's frontal area.
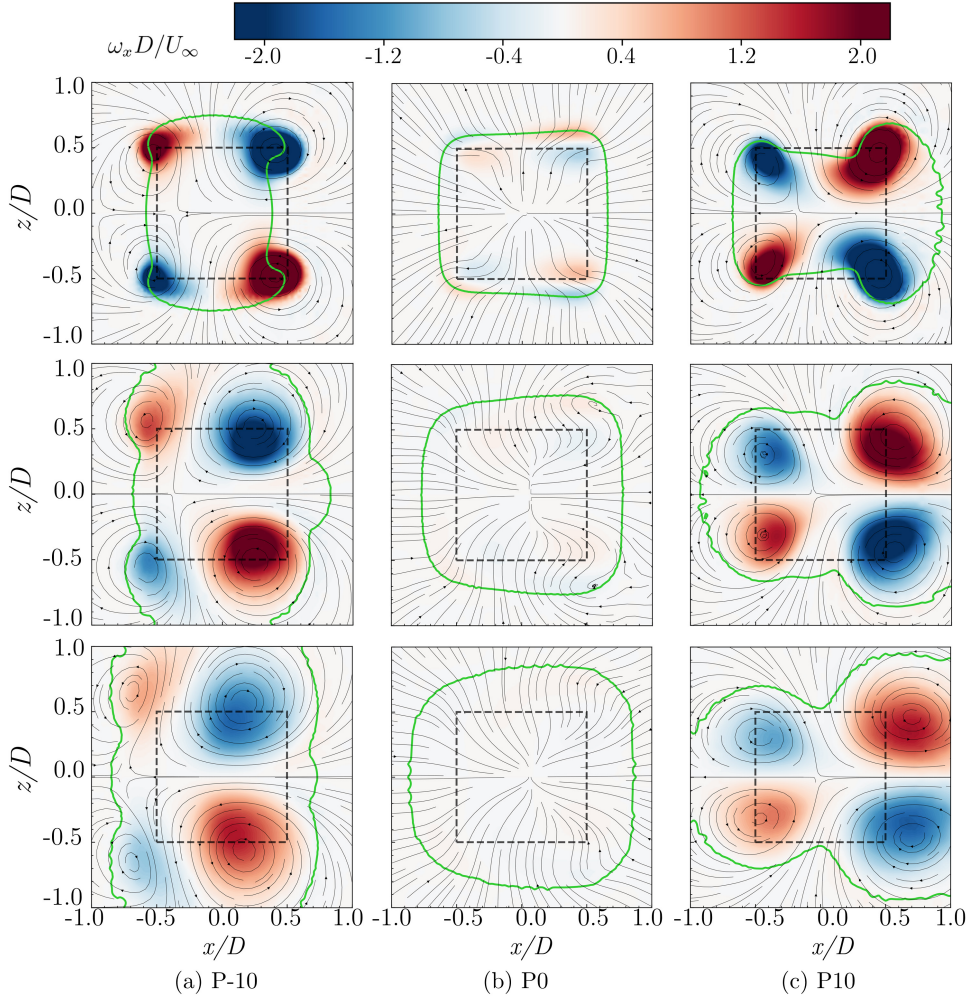
Figure 9.5: Cross-sectional streamwise vorticity contours and in-plane streamlines for cases P-10, P0 and P10. Each row from top to bottom stands for $x/D = 1, 3, 5$, respectively. Black dashed squares denote the VAWT's frontal area. Green contour lines indicate where $u/U_{\text{inf}} = 1$.

9.2.3. AVAILABLE POWER

The available wind power in the wakes of the isolated VAWTs is calculated based on the approach introduced in section 6.2.3, and is illustrated in figure 9.6. P-10 and P10 increase the AP remarkably compare to P0, e.g., at $x/D = 5$, AP of the former recovers to more than 0.75 while the AP of P0 only reaches 0.34. On the other hand, the minimum AP of P-10 and P0 remains around $y_0/D = 0$; whereas P10 deflect the minimum AP horizontally, and it reaches $y_0/D = 1.2$ at $x/D = 9$. It is observed that the wake of P-10 features the highest AP off the inline position, which indicates closer deployment spaces abreast.
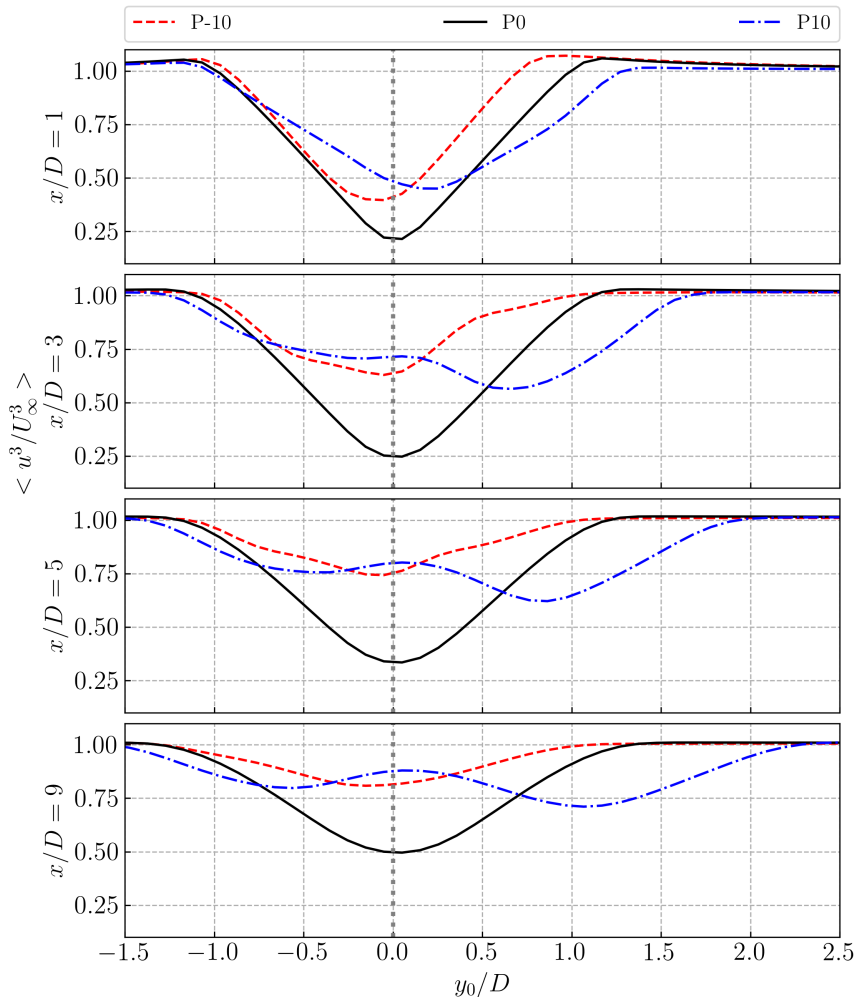

Figure 9.6: Available power behind the isolated VAWTs.

9.2.4. 3D EVOLUTION OF THE INSTANTANEOUS VORTEX SYSTEM

To visualise the vortex structure in the different deflection cases, the iso-surfaces of Q-criterion coloured by the streamwise vorticity are presented from figure 9.7 to 9.9. The iso-surfaces of Q-criterion indicate regions with high enough vorticity magnitude, while the streamwise vorticity is selected to colour the surfaces because they are the main contributor to the wake deflection and deformation. As illustrated in these graphics, vortices are generated along the blade, and the streamwise vorticity concentrates at the blade tips. Figure 9.7 shows that the tip vortices are generated mostly in the downwind portion of the rotor in P-10, with two pairs of counter rotating vortices concentrated at the windward and leeward regions. With zero blade-pitch in P0, the tip vortices appear also at the upwind portion of the rotor. As opposed to P-10, P10 generates tip vortices mainly at the upwind region, and the strong vortex pairs in the wake have the opposite sign compared to those in P-10. It is noted that the upwind tip vortex moves inward to the wake while the downwind tip vortex moves up, which confirms the validity of the assumption adopted in the simplified model in chapter 6.
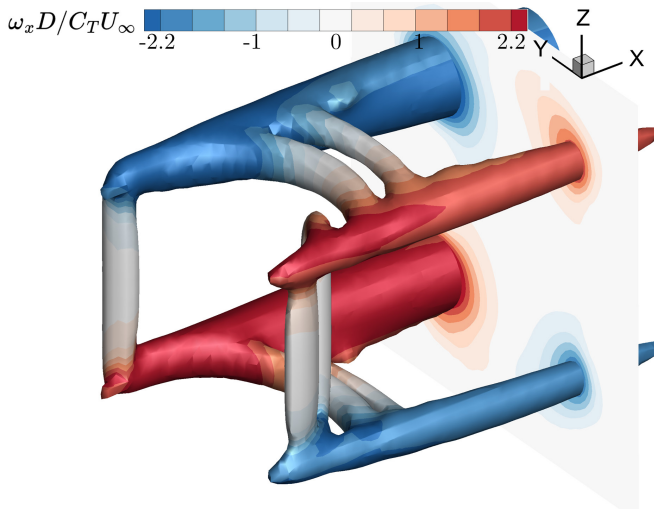
Figure 9.7: P-10: Instantaneous vortex system in 3D. Q-criterion coloured by streamwise vorticity.

VAWT ARRAYS

9.2.5. TURBINE PERFORMANCES

The performances of the VAWT arrays are listed in table 9.3 and illustrated in the bar chart in figure 9.10. The coefficients are calculated based on the freestream velocity instead of the inflow velocity of each turbine, for the sake of a direct comparison on the absolute value of the power extraction.

The wake deflection significantly increases the overall power extraction of the VAWT array by 32% to 41% compared to the cases without deflection, which proves the prediction in Huang et al. (2023). The overall power coefficient reaches 0.82 with an inter-
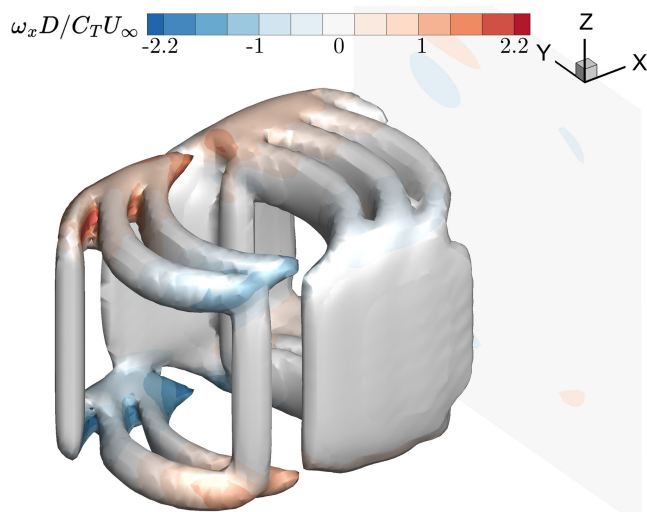
Figure 9.8: P0: Instantaneous vortex system in 3D. Q-criterion coloured by streamwise vorticity.
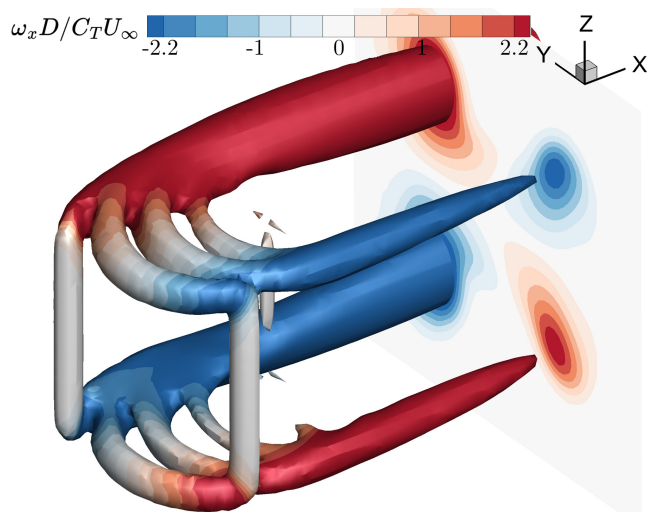

Figure 9.9: P10: Instantaneous vortex system in 3D. Q-criterion coloured by streamwise vorticity.

turbine distance of $3D$ with the first turbine's blade positively pitched. As the inter-turbine distance increases, the performance of VAWT2 first increases notably and then converges to a constant. It is because the wake recovery rate in the far wake is slowed compared to that in the near wake. Thus, once VAWT2 is placed in the far wake of VAWT1, available power increment by increasing inter-turbine distance is not as effective as in the near wake. As demonstrated in Huang et al. (2023), the momentum recovers faster in the near wake of VAWTs due to streamwise vorticity that enhances the advection. While in the far wake, the turbulent transport of momentum takes the lead, which is less effective than the advection.

Table 9.3: Performances of two VAWTs placed aligned, with an inter-turbine distance of 3,4 and $5D$. VAWT1 is pitched with different angles, while VAWT2 has zero blade pitch angle. Coefficients calculated based on U_∞. Differences compared to P0_3,4,5D are marked in red.

Case	C_{P1}	$C_{T,x1}$	$C_{T,y1}$	C_{P2}	$C_{T,x2}$	$C_{T,y2}$	$C_{P,\text{total}}$
P-10_3D	0.45	0.69	-0.37	0.35 (+289%)	0.55	0.07	0.80 (+38%)
P0_3D	0.49	0.67	0.02	0.09	0.32	0.00	0.58
P10_3D	0.44	0.64	0.34	0.38 (+322%)	0.59	-0.06	0.82 (+41%)
P-10_4D	0.46	0.69	-0.37	0.40 (+167%)	0.61	0.08	0.86 (+32%)
P0_4D	0.50	0.68	0.02	0.15	0.39	0.00	0.65
P10_4D	0.44	0.64	0.34	0.41 (+173%)	0.61	-0.04	0.85 (+30%)
P-10_5D	0.46	0.69	-0.37	0.43 (+169%)	0.63	0.08	0.89 (+35%)
P0_5D	0.50	0.68	0.02	0.16	0.41	0.00	0.66
P10_5D	0.44	0.64	0.34	0.43 (+169%)	0.63	-0.03	0.87 (+32%)

It is worth pointing out that when the two VAWTs are placed close ($3D$), the power coefficient of the upwind turbine drops slightly; while increasing the inter-turbine distances, the downwind turbine does not affect the upwind one anymore.

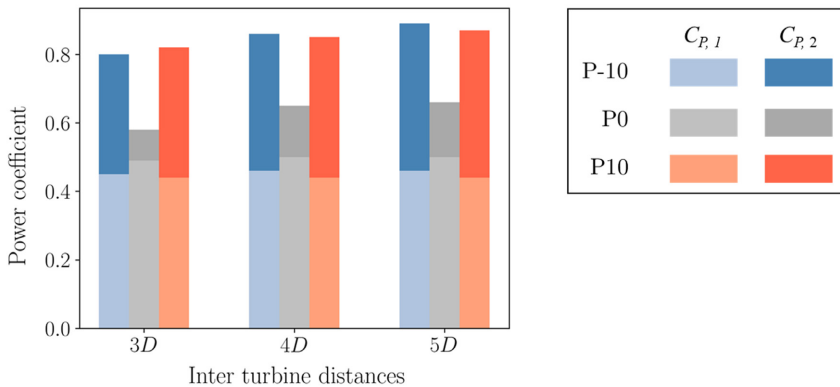

Figure 9.10: Visual illustration of the values in table 9.3. VAWT1 is pitched with different angles, while VAWT2 has zero blade pitch angle. C_{P1} in light colors and C_{P2} in dark colors; the total length denotes the $C_{P,\text{total}}$.

On the other hand, when the inter-turbine distance is kept constant, and both turbines are pitched to deflect the wake (table 9.4), the overall power output still mainly depends on the performance of VAWT2. Among these cases, P-10_P10 yields the highest $C_{P\text{total}}$ while leaving the most substantial velocity deficit region within the projected area, which is discussed in the following section (figure 9.16). The notable wake deficit area will reduce the performance of downwind VAWTs in line with VAWT2. In contrast, the combination of two P-10 (i.e. P-10_P-10) might be a better balance, of which the wake further downstream is effectively deflected while the overall performance is increased by +20%.

Table 9.4: Performance of two pitched VAWTs placed aligned, with an inter-turbine distance of $4D$. Coefficients calculated based on U_{∞}. Differences compared to P0_4D are marked in red.

Case	C_{P1}	$C_{T,x1}$	$C_{T,y1}$	C_{P2}	$C_{T,x2}$	$C_{T,y2}$	$C_{P\text{total}}$
P0_P0(P0_4D)	0.50	0.68	0.02	0.15	0.39	0.00	0.65
P0_P-10	0.50	0.68	0.02	0.11 (-27%)	0.4	-0.27	0.61 (-6%)
P0_P10	0.49	0.68	0.02	0.06 (-60%)	0.35	0.19	0.55 (-15%)
P-10_P-10	0.45	0.69	-0.37	0.33 (+120%)	0.67	-0.27	0.78 (+20%)
P-10_P10	0.46	0.69	-0.37	0.35 (+133%)	0.51	0.35	0.81 (+25%)
P10_P-10	0.44	0.64	0.34	0.31 (+107%)	0.62	0.23	0.75(+15%)
P10_P10	0.44	0.64	0.34	0.31 (+107%)	0.62	0.23	0.75 (+15%)

9.2.6. VELOCITY AND VORTICITY FIELDS

The time-averaged streamwise velocity and instantaneous vorticity magnitudes of the configurations with two VAWTs and without floor, are illustrated in figures 9.11-9.19. When the upwind turbine is not pitched (i.e. cases P0_P0, P0_P-10 and P0_P10, figure 9.11-9.13), the wake of VAWT1 is barely deflected, and VAWT2 almost operates in the wake centre of VAWT1. This results in a low available power for VAWT2, dramatically reducing its performance. Among these cases, the one with both VAWTs not pitched (i.e., case P0_P0), features the most substantial velocity deficit behind VAWT2 in its projected square at $x/D = 5$ and 7, as illustrated in figure 9.11. In contrast, the strong wake deflection of VAWT1 in the other cases (cases with VAWT1 being P-10 and P10, figure 9.14-9.19) significantly improves the incoming flow of VAWT2, increasing its performance, which is consistent with the data listed in table 9.3 and 9.4.

When both VAWT1 and VAWT2 are pitched, the deflected wake of VAWT2 interacts with that of VAWT1 in the following manner. Suppose VAWT1 and VAWT2 are pitched both positively or negatively (P-10_P-10, figure 9.15; P10_P10, figure 9.19), the wake behind VAWT2 features the same topology with the corresponding isolated VAWT pitched in the same sign. For example, for P-10_P-10, the wake at $3D$ behind VAWT2 (corresponding to $x/D = 7$ in the global coordinates) highly resemble the wake of P-10 at $x/D = 3$ (figure 9.4); The same phenomenon holds for cases P10_P10 and P10. The array configurations P-10_P-10 and P10_P10 feature even higher velocity at $x/D = 7$ than $x/D = 3$ within the turbine projected area. This is analogous to the flying formation of migratory birds, of which downwind birds benefit from the wake of upwind ones flying at

the same height and speed yet costing less energy. Downwind VAWTs with pitch angles in the same sign in an array could deflect the wake more effectively. Considering that the overall performance and the available momentum for the downstream turbine are improved, the configurations with the same pitching direction are promising in increasing the power density in VAWT farms.

In contrast, when blade pitches of VAWT1 and VAWT2 are in the opposite direction, the opposite wake deflections tend to cancel each other out, and the resulting wake behind VAWT2 is like the merge of two deflected wakes. Take P-10_P10 as an example (figure 9.16); The wake at $x/D = 5$ is like a superposition of the wake of P-10 at $x/D = 3$ and P10 at $x/D = 1$ (figure 9.4). At further downstream ($x/D = 7$), the wake is stretched both vertically and horizontally due to the presence of strong counter-rotating vortices from both turbines. Judging by the in-plane velocity vectors at the cross-sections along x, as illustrated in figure 9.16 and 9.18, the interactions of the vortex systems follow the same pattern introduced in chapter 6 and 7. That is, the strong counter-rotating vortex pairs are crucial. The stronger CVPs will merge with the weaker ones if they are located closer. If they are far apart, the CVPs will remain and deform the wake locally. Further investigations into the vortex interactions are recommended to interpret the complex wake interactions occurring in these cases.

9

Figure 9.11: P0_P0: (a): volume rendering of the instantaneous vorticity magnitude; (b): Streamwise velocity contours in different planes.

Figure 9.12: P0_P-10: (a): volume rendering of the instantaneous vorticity magnitude; (b): Streamwise velocity contours in different planes.
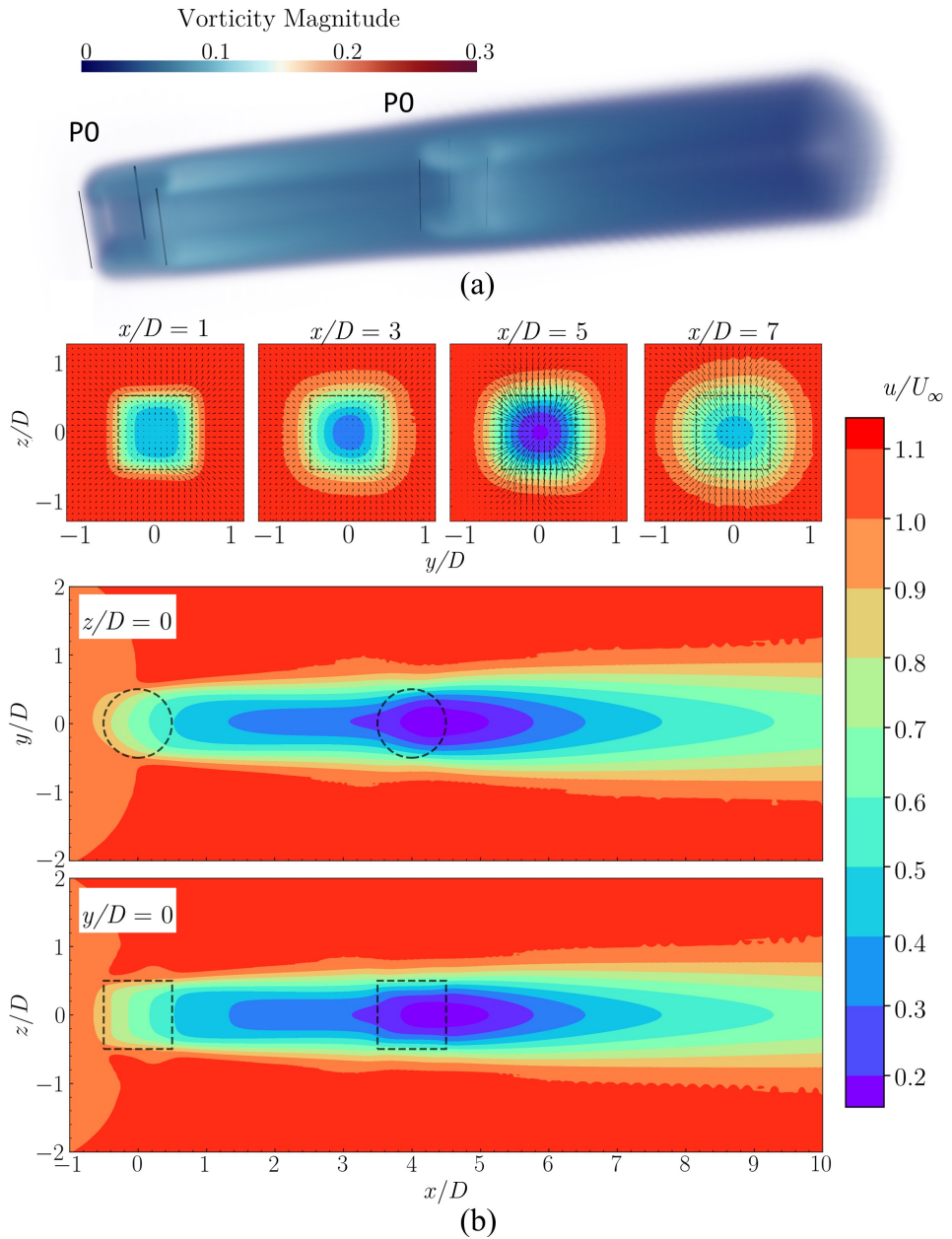
Figure 9.13: P0_P10: (a): volume rendering of the instantaneous vorticity magnitude; (b): Streamwise velocity contours in different planes.
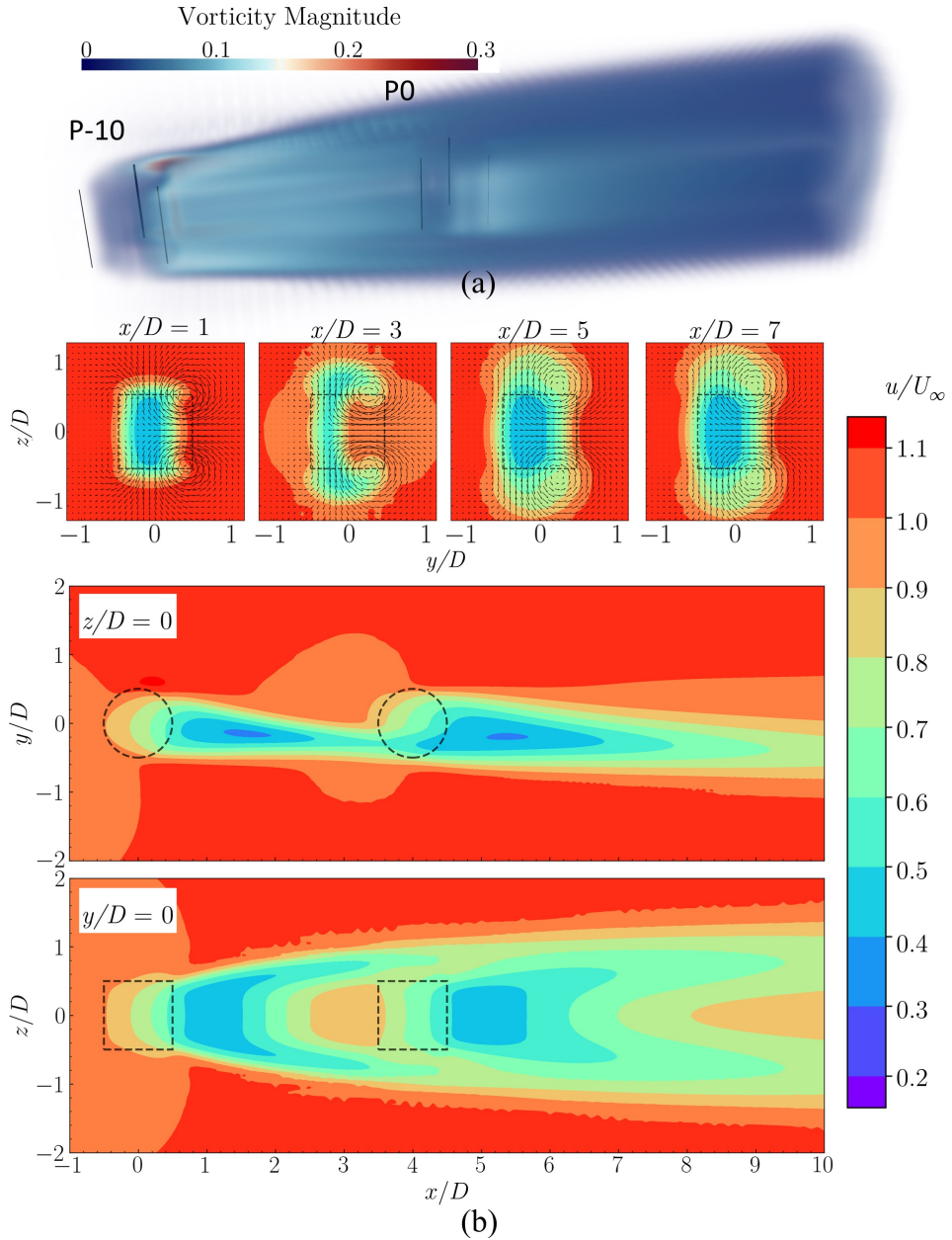
Figure 9.14: P-10_P0: (a): volume rendering of the instantaneous vorticity magnitude; (b): Streamwise velocity contours in different planes.
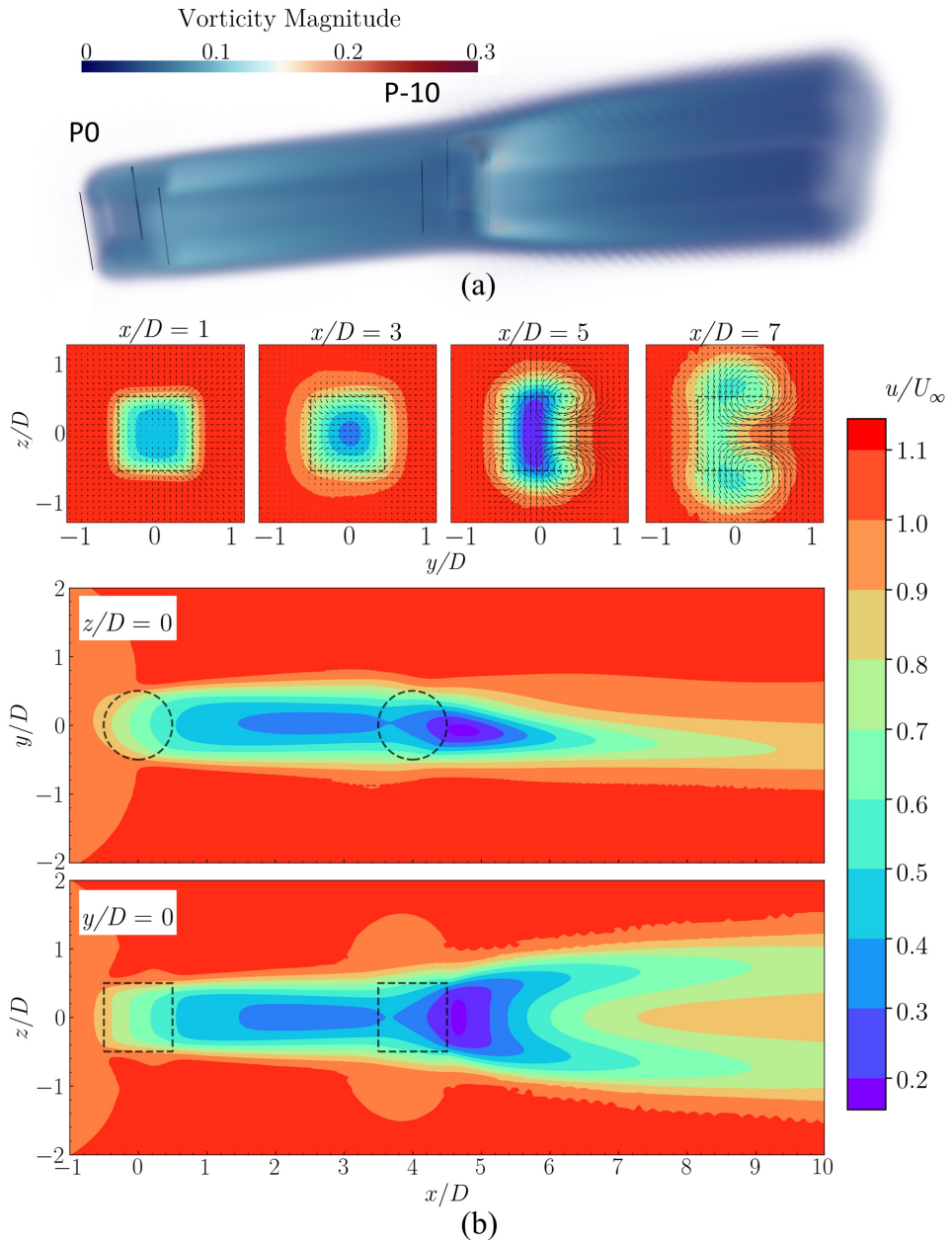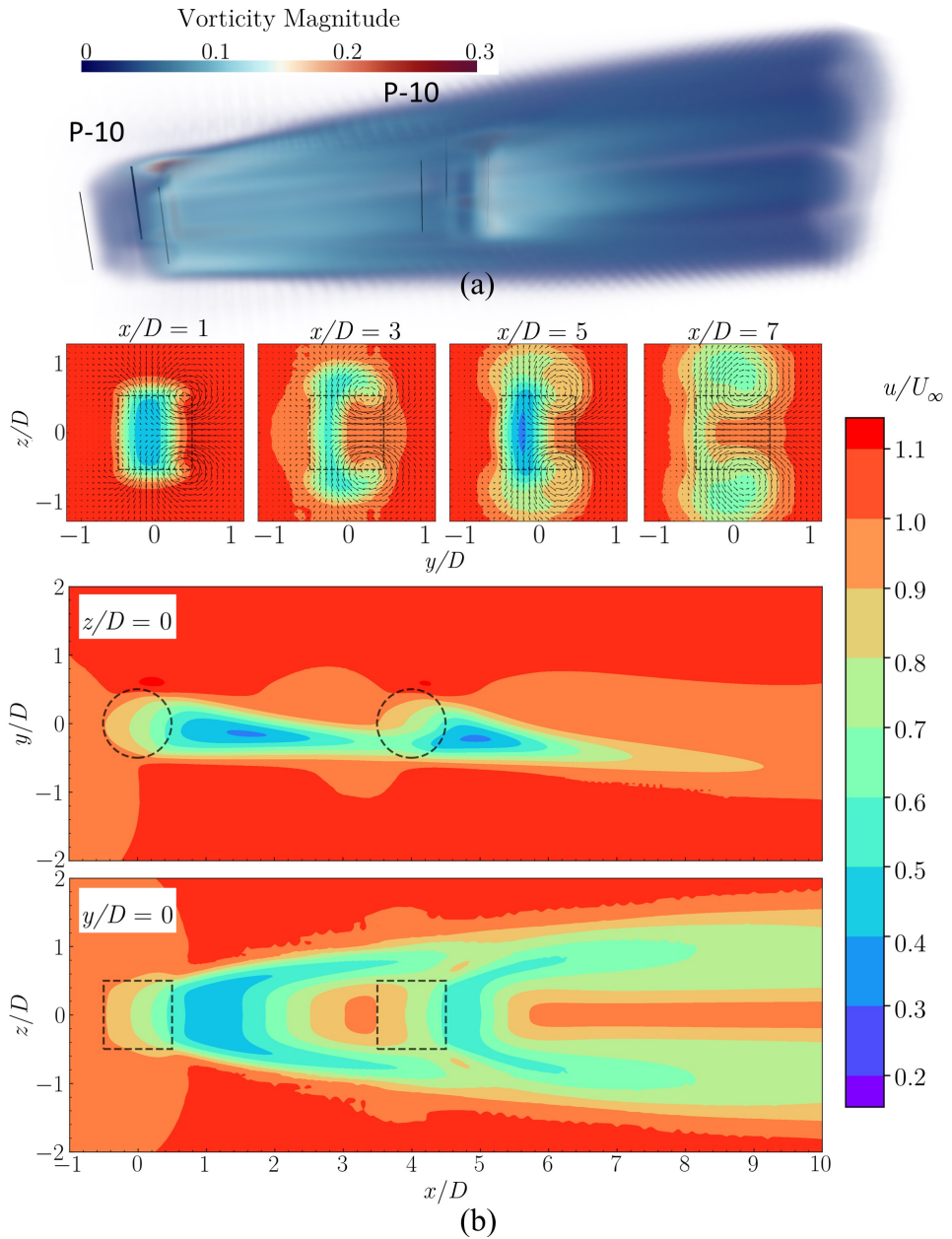
Figure 9.15: P-10_P-10: (a): volume rendering of the instantaneous vorticity magnitude; (b): Streamwise velocity contours in different planes.

Figure 9.16: P-10_P10: (a): volume rendering of the instantaneous vorticity magnitude; (b): Streamwise velocity contours in different planes.
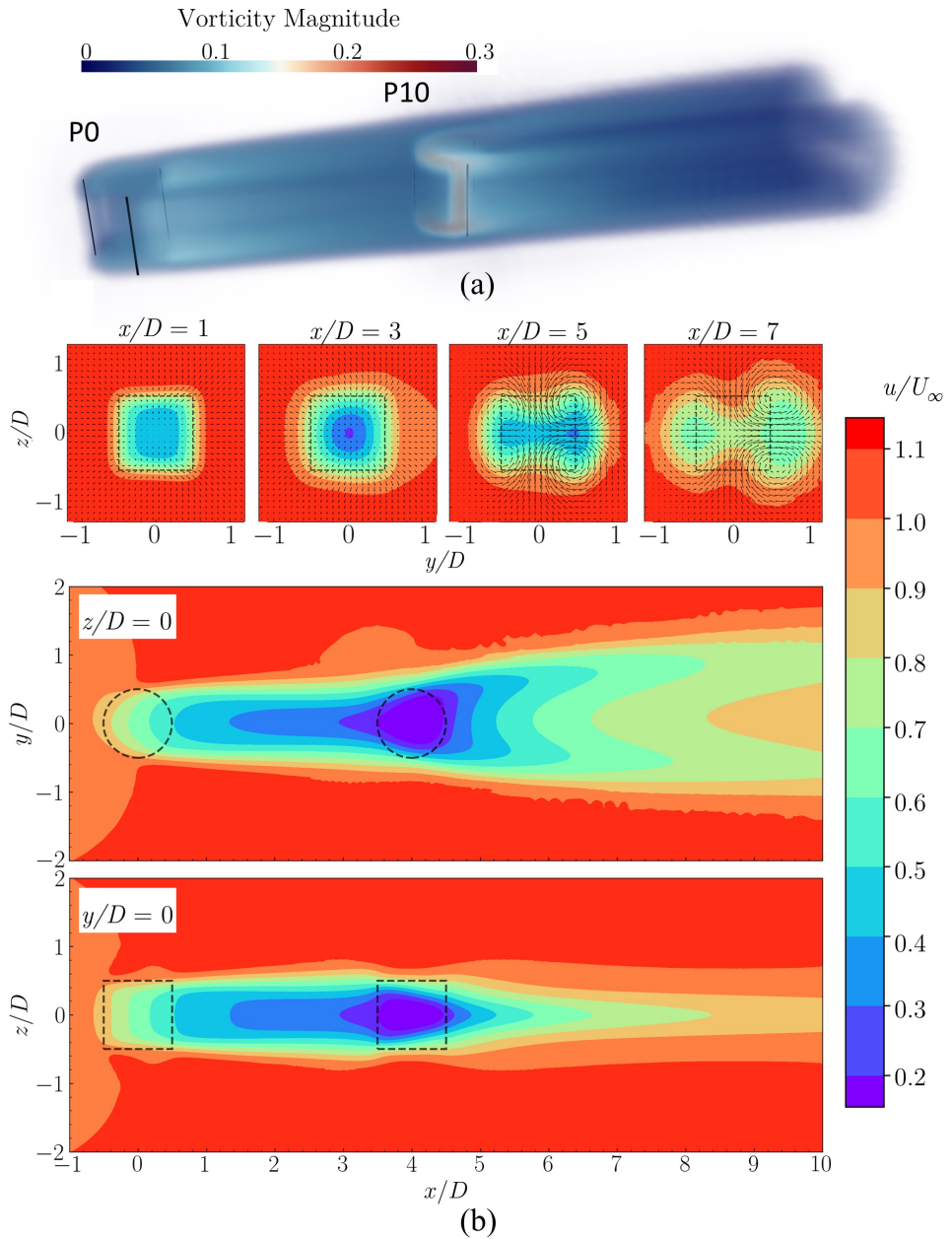
Figure 9.17: P10_P0: (a): volume rendering of the instantaneous vorticity magnitude; (b): Streamwise velocity contours in different planes.

Figure 9.18: P10_P-10: (a): volume rendering of the instantaneous vorticity magnitude; (b): Streamwise velocity contours in different planes.

Figure 9.19: P10_P10: (a): volume rendering of the instantaneous vorticity magnitude; (b): Streamwise velocity contours in different planes.
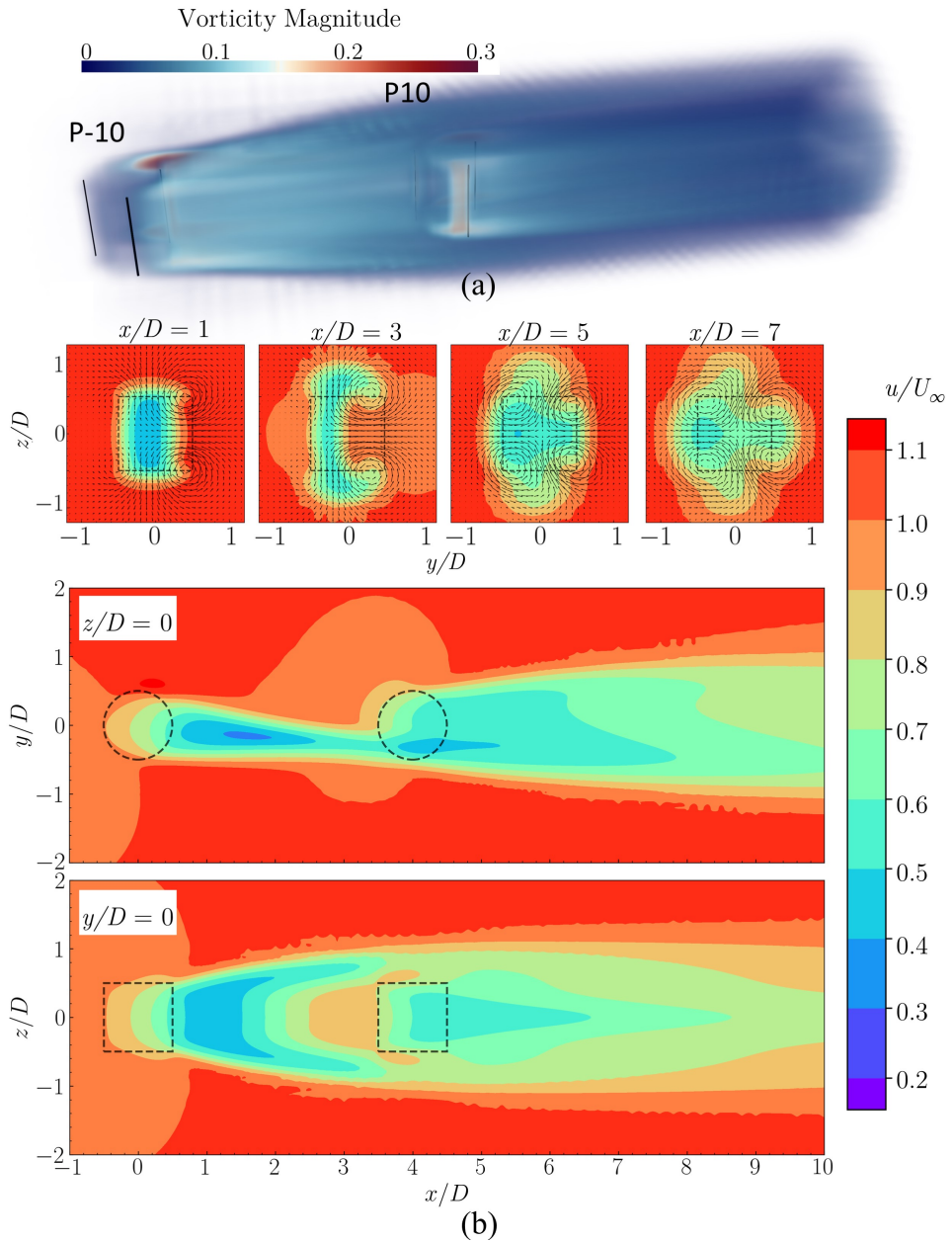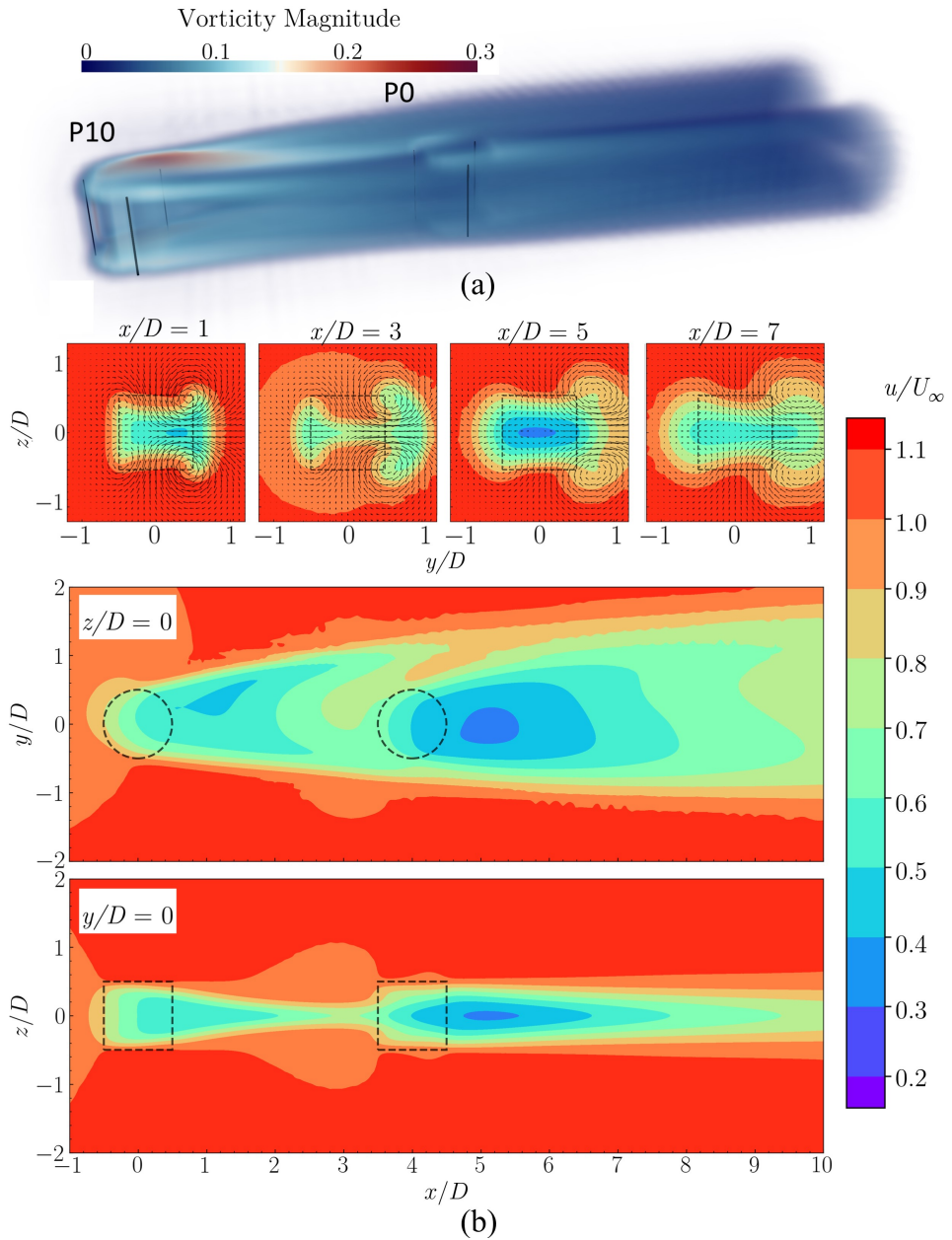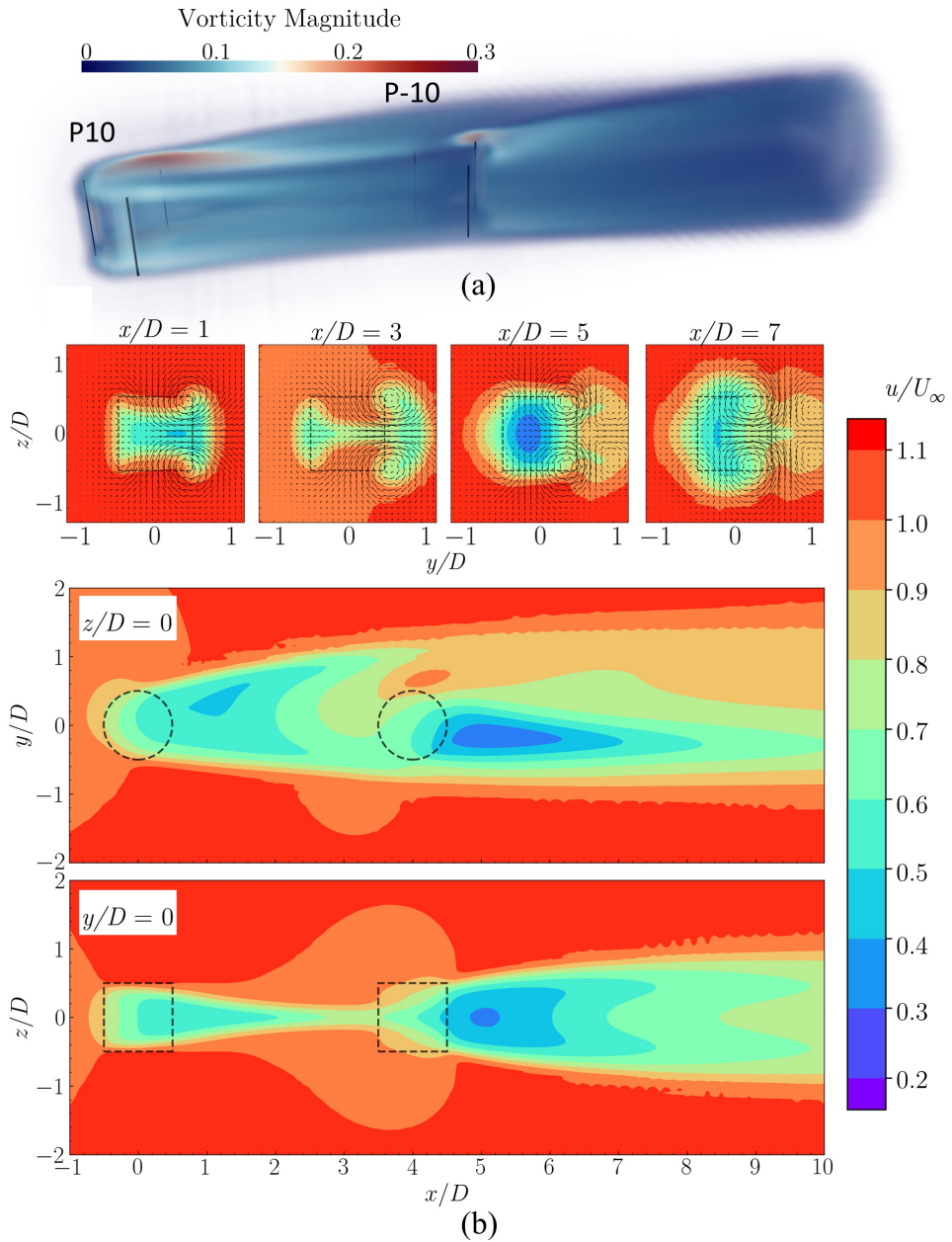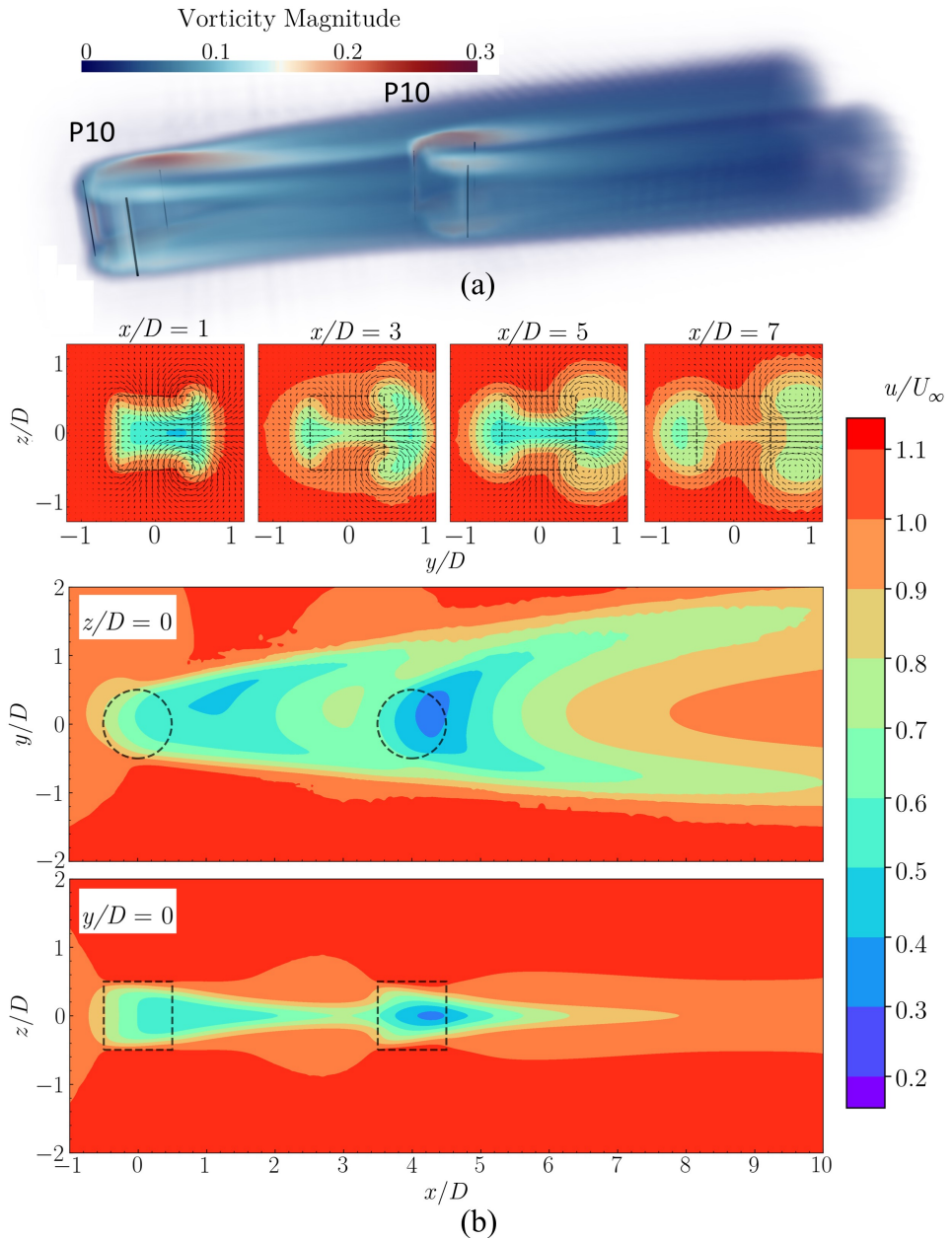
9.3. SUSTAINABILITY OF THE POWER ENHANCEMENT

We have demonstrated the efficacy of fixed blade pitches in the wake deflection and power extraction enhancement in arrays with two VAWTs. However, it is yet to be explored whether such enhancement is sustainable in wind farms with more turbine rows; In this scenario, the floor effect on the wake deflection and further the available power has to be accounted for; Because as the streamwise distance increases, the expanded wakes will inevitably interact with floors and thus affecting their available power.

Therefore, in this section, we simulate the wake development of three VAWTs in a line, pitching in the so-called flying formation of VAWTs, which has been proven to be efficient in section 9.2.6. In other words, the turbines are pitched in the same direction. For simplicity, we use constant blade pitches, i.e. -10 or 10 degrees, for all the turbines. The inter-turbine distance is $4D$. Cases with and without floor are used to study the floor effect. The floor is $0.7D$ below the rotor centre. The inflow conditions and the turbine attributes are kept the same.

9.3.1. TURBINE PERFORMANCES

The performances of each VAWT are presented in table 9.5. As expected, VAWT1 in all the cases gets the highest power coefficient because it confronts the undisturbed inflow featuring the highest streamwise velocity. VAWT2 and VAWT3 extract less wind power than VAWT1; However, they feature similar power coefficients. This indicates the performances of downwind turbines could already reach an asymptotic state, which means downwind turbines (VAWT4,5,...) will feature similar C_P. In the following sections 9.3.2 and 9.3.3, we validate this hypothesis via comparing the wakes behind VAWT2 and VAWT3.

The floor has a minor effect to the array with P0s (P0×3_F). This is because the wake moderately expands and starts to interact with the floor right in front of VAWT3; Hence, only the performance of VAWT3 drops slightly. The wakes are appreciated in the following sections. In contrast, P-10×3_F suffers from the strongest C_P decreasing (from 1.13 to 1.08) due to the floor. However, its overall performance is still the highest among the with-floor cases.

9

Table 9.5: Performance of three pitched VAWTs placed aligned, with an inter-turbine distance of $4D$. '×3' denotes that all the three turbines are at the same pitch anlge. With (denoted by _F) and without floor. Coefficients are calculated based on U_∞.

Case	C_{P1}	$C_{T,x1}$	$C_{T,y1}$	C_{P2}	$C_{T,x2}$	$C_{T,y2}$	C_{P3}	$C_{T,x3}$	$C_{T,y3}$	$C_{P,total}$
P0×3	0.5	0.68	0.02	0.13	0.37	0	0.15	0.4	0	0.78
P0×3_F	0.5	0.68	0.01	0.13	0.37	0	0.14(-7%)	0.38	0	0.77(-1%)
P-10×3	0.45	0.69	-0.37	0.33 (154%)	0.67	-0.27	0.35 (133%)	0.69	-0.24	1.13(45%)
P-10×3_F	0.46	0.68	-0.37	0.30 (131%)	0.63	-0.28	0.32 (113%)	0.66	-0.24	1.08(38%)
P10×3	0.44	0.64	0.34	0.31 (138%)	0.62	0.23	0.32 (113%)	0.62	0.26	1.07(37%)
P10×3_F	0.45	0.65	0.35	0.32(146%)	0.62	0.24	0.28(87%)	0.6	0.24	1.05(35%)

9.3.2. VELOCITY FIELDS

The velocity fields at 1 ($x/D = 1,5,9$) and 3 diameters ($x/D = 3,7,11$) behind the three turbines are compared in figures 9.20 - 9.25. When the blades are not pitched, strong deficits are imparted around the centre of each turbine and stay within the projected area; as illustrated in figures 9.20 and 9.21. Since the rotors rotate in the same constant speed, the downwind turbines feature much higher tip speed ratio with respect to their inflow velocity. Therefore, VAWT2 and VAWT3 are heavily loaded and produce significant velocity deficits. As shown in figure 9.21, the floor has a minor effect on this case because the wake expands slowly and starts to affect the velocity field within the frontal area around $x/D = 7$. It is consistent with the performances listed in table 9.5.

For both P-10s and P10s, it is observed that the wake topologies in the projected square region behind the VAWT2 and VAWT3, including the in-plane motions and the streamwise velocity deficits, are similar, indicating the sustainability of the inflow conditions for downwind turbines when the VAWTs are pitched in the same direction. With the similar inflow, performances of downwind turbines with the same blade pitching will also be similar. Furthermore, the floor has a greater impact on the wake for these two cases. $C_{P\text{total}}$ of P-10×3_F decreases by 0.05 while P10×3_F by 0.02.

9.3.3. VORTICITY FIELDS

The streamwise velocity contours and in-plane velocity vectors are depicted from figures 9.26 to 9.31. The P0 cases feature weaker vorticity magnitudes at all locations compared to the other cases. There are double layer structures barely visible right behind VAWT1, at $x/D = 1$. The floor has minor effect on their vorticity fields because the latter is not strong enough. The in-board streamlines at $1D$ behind VAWT2 and VAWT3 are due to the flow reversal presented in figures 9.20 and 9.21.

In contrast, cases with P-10s or P10s present two pairs of strong CVPs leading the stretching of the wake outlines. For each case, the vorticity fields at the downwind of VAWT2 and VAWT3 are very similar, which proves that the vorticity system reaches an asymptotic state. The floor has a notable impact on the vorticity development. The vorticity regions are squeezed by the floor, thus affecting the induced velocity field and in turn the wake outline. For P10×3_F, the vortices at bottom are pushed closer, resulting in a stronger interaction. As these vortices are in the opposite direction, they decline the strength of each other.

Addition to the velocity and vorticity cross-sections, the instantaneous vorticity magnitude in 3D and velocity contours in y- and z- planes for the three turbine cases are presented from figure 9.33 to 9.37, illustrating an overview of the wake developments.

Figure 9.20: P0×3: Streamwise velocity contours at $1D$ ($x/D = \{1, 5, 9\}$) and $3D$ ($x/D = \{3, 7, 11\}$) behind each turbine.
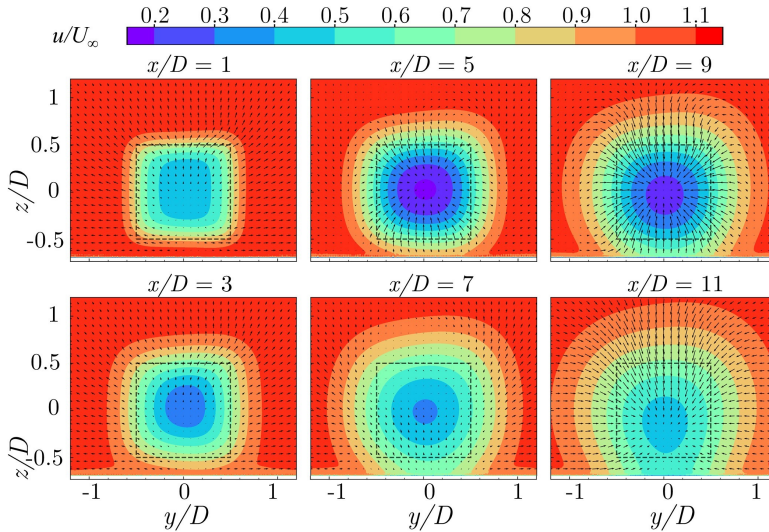
Figure 9.21: P0×3_F: Streamwise velocity contours at $1D$ and $3D$ behind each turbine. Floor presents at $z/D = -0.7$.

Figure 9.22: P-10×3: Comparison of streamwise velocity contours at $1D$ ($x/D = \{1, 5, 9\}$) and $3D$ ($x/D = \{3, 7, 11\}$) behind each turbine.

Figure 9.23: P-10×3_F: Streamwise velocity contours at $1D$ ($x/D = \{1, 5, 9\}$) and $3D$ ($x/D = \{3, 7, 11\}$) behind each turbine. Floor presents at $z/D = -0.7$.
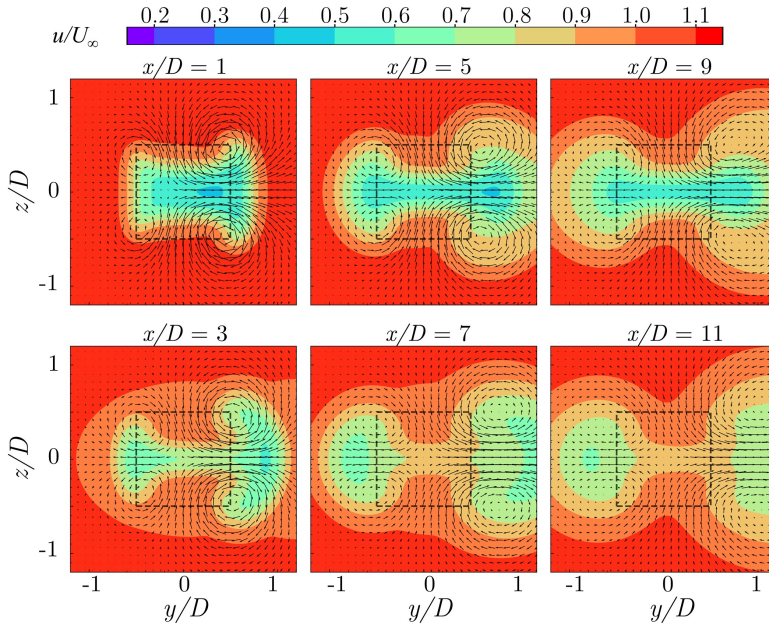
Figure 9.24: P10×3: Streamwise velocity contours at $1D$ and $3D$ behind each turbine.
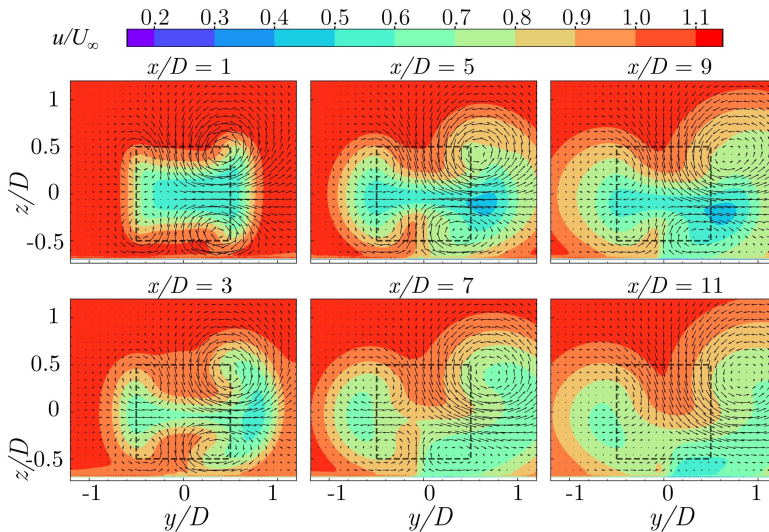
Figure 9.25: P10×3_F: Comparison of streamwise velocity contours at $1D$ ($x/D = \{1, 5, 9\}$) and $3D$ ($x/D = \{3, 7, 11\}$) behind each turbine. Floor presents at $z/D = -0.7$.
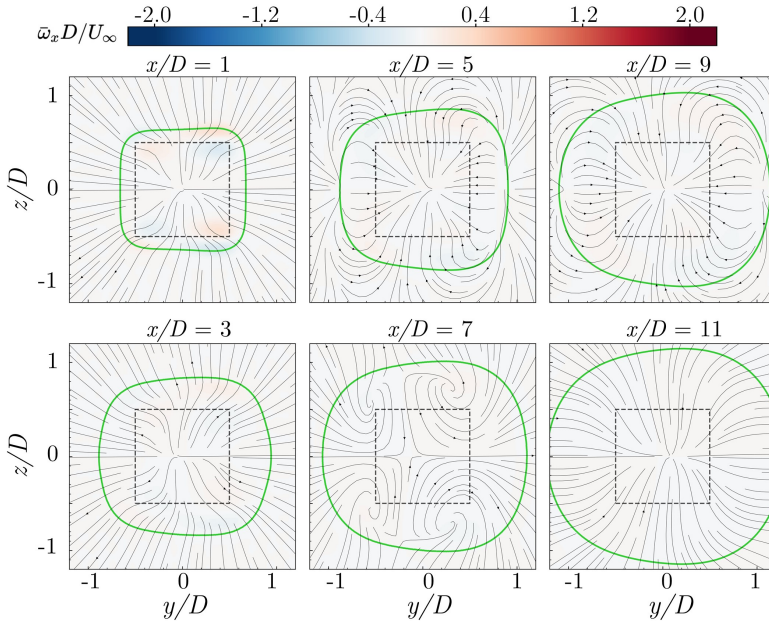
Figure 9.26: P0×3: Comparison of streamwise vorticity contours at $1D$ ($x/D = \{1, 5, 9\}$) and $3D$ ($x/D = \{3, 7, 11\}$) behind each turbine.
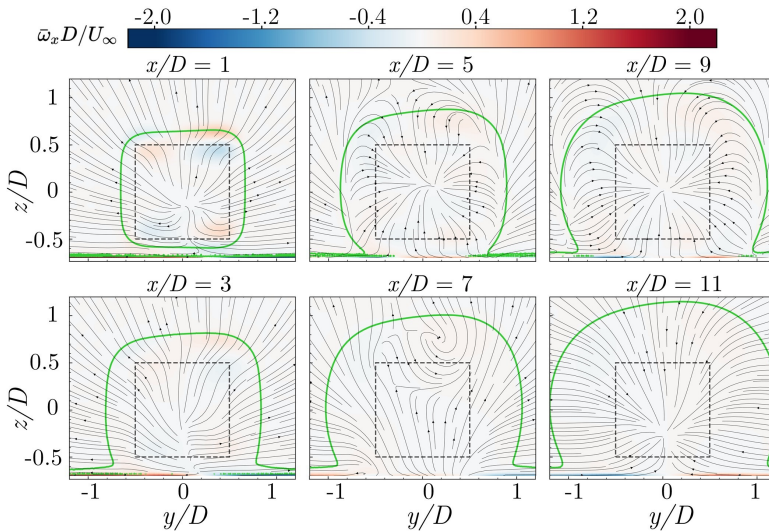
Figure 9.27: P0×3_F: Comparison of streamwise vorticity contours at $1D$ ($x/D = \{1, 5, 9\}$) and $3D$ ($x/D = \{3, 7, 11\}$) behind each turbine. Floor presents at $z/D = -0.7$.
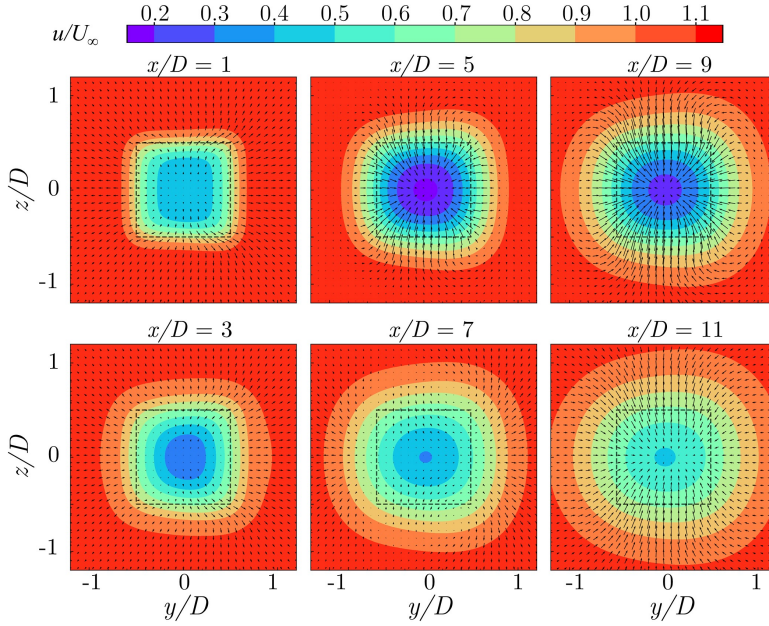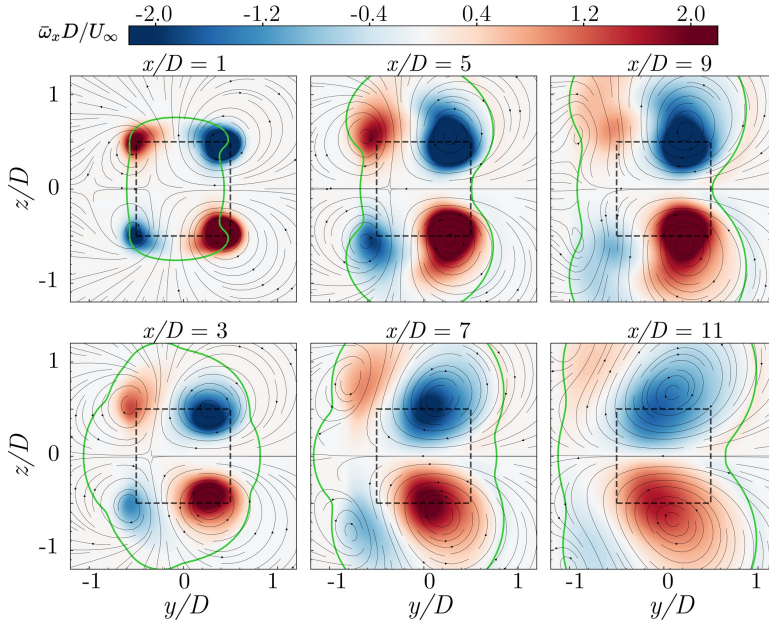
Figure 9.28: P-10×3: Comparison of streamwise vorticity contours at $1D$ ($x/D = \{1, 5, 9\}$) and $3D$ ($x/D = \{3, 7, 11\}$) behind each turbine.
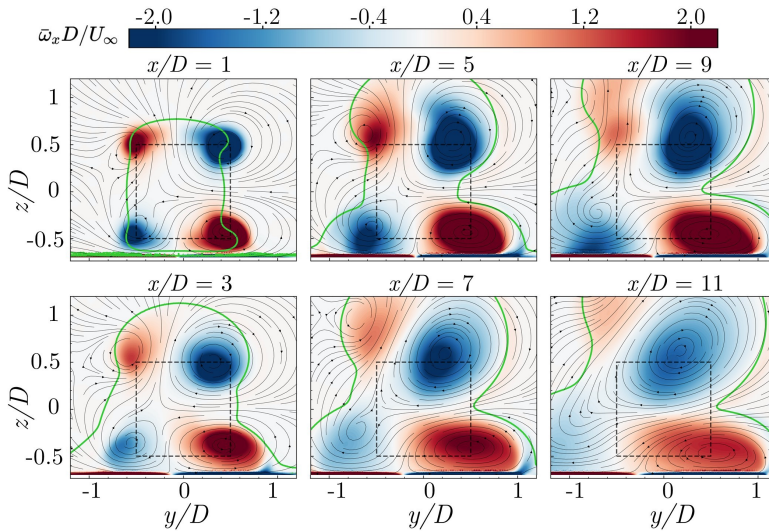
Figure 9.29: P-10×3_F: Comparison of streamwise vorticity contours at $1D$ ($x/D = \{1, 5, 9\}$) and $3D$ ($x/D = \{3, 7, 11\}$) behind each turbine. Floor presents at $z/D = -0.7$.
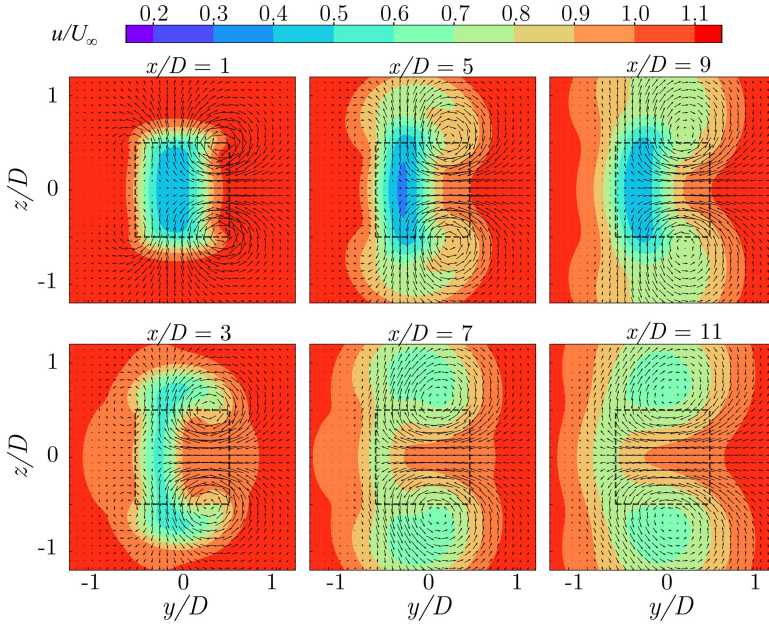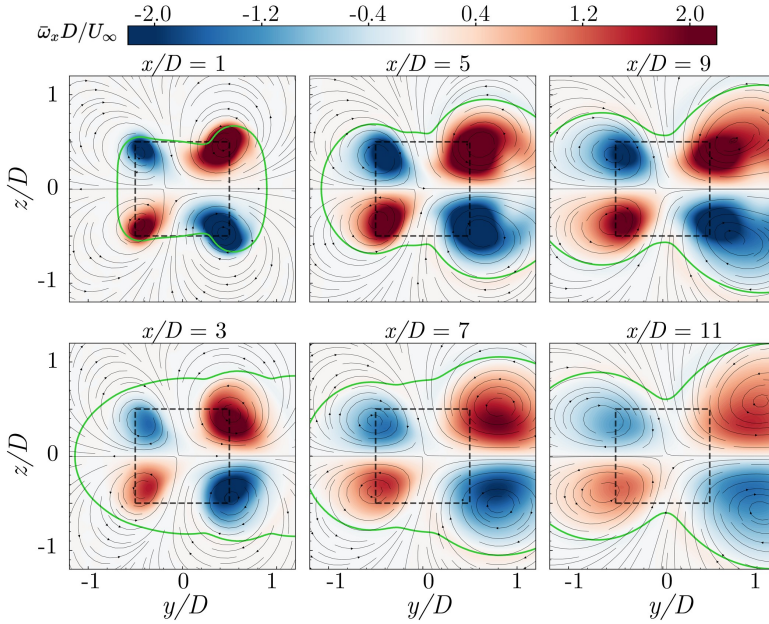
Figure 9.30: P10×3: Comparison of streamwise vorticity contours at $1D$ ($x/D = \{1,5,9\}$) and $3D$ ($x/D = \{3,7,11\}$) behind each turbine.
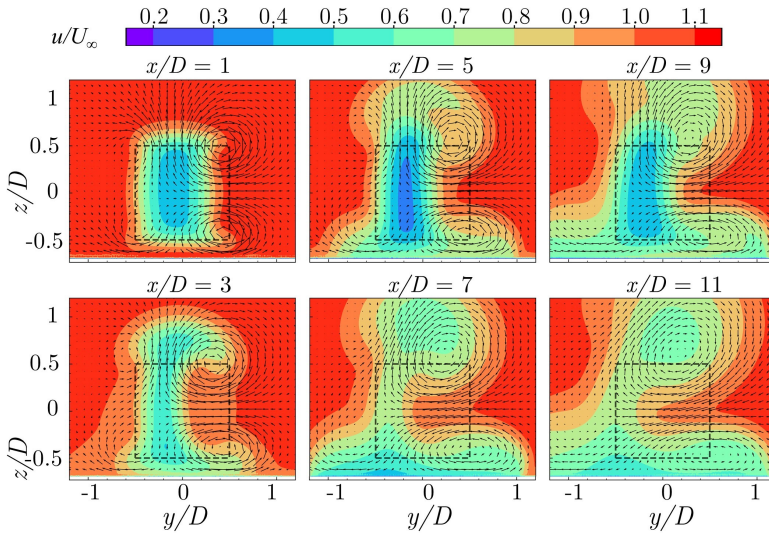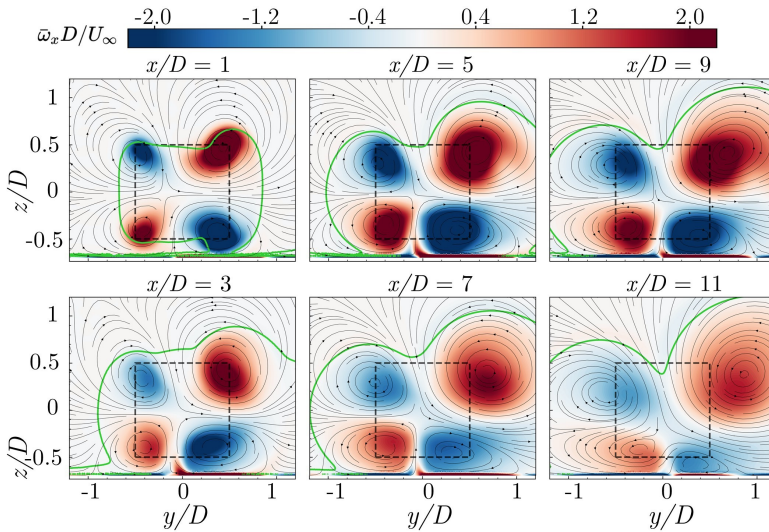

Figure 9.31: P10×3_F: Comparison of streamwise vorticity contours at $1D$ ($x/D = \{1,5,9\}$) and $3D$ ($x/D = \{3,7,11\}$) behind each turbine. Floor presents at $z/D = -0.7$.

(a)

(b)
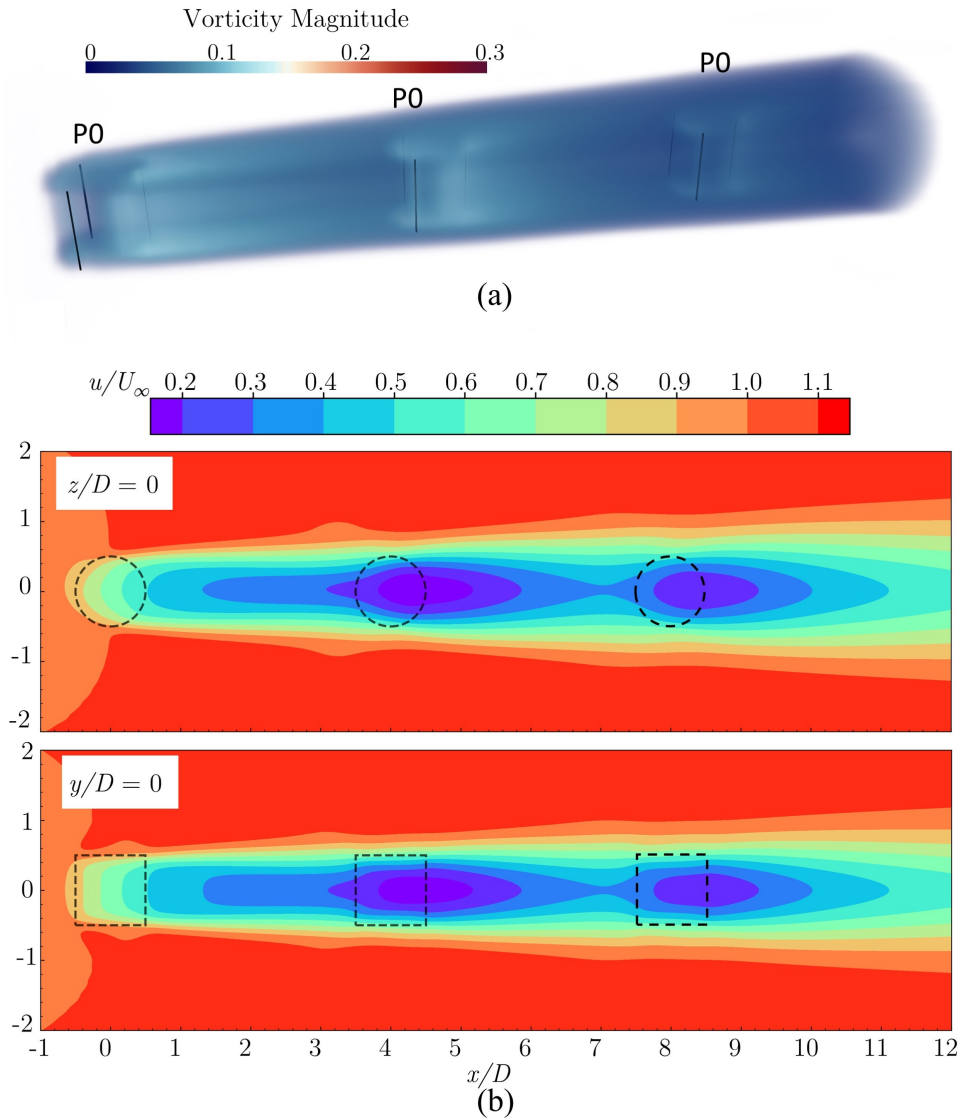
Figure 9.32: P0×3: (a): volume rendering of the instantaneous vorticity magnitude; (b): Streamwise velocity contours in different planes.
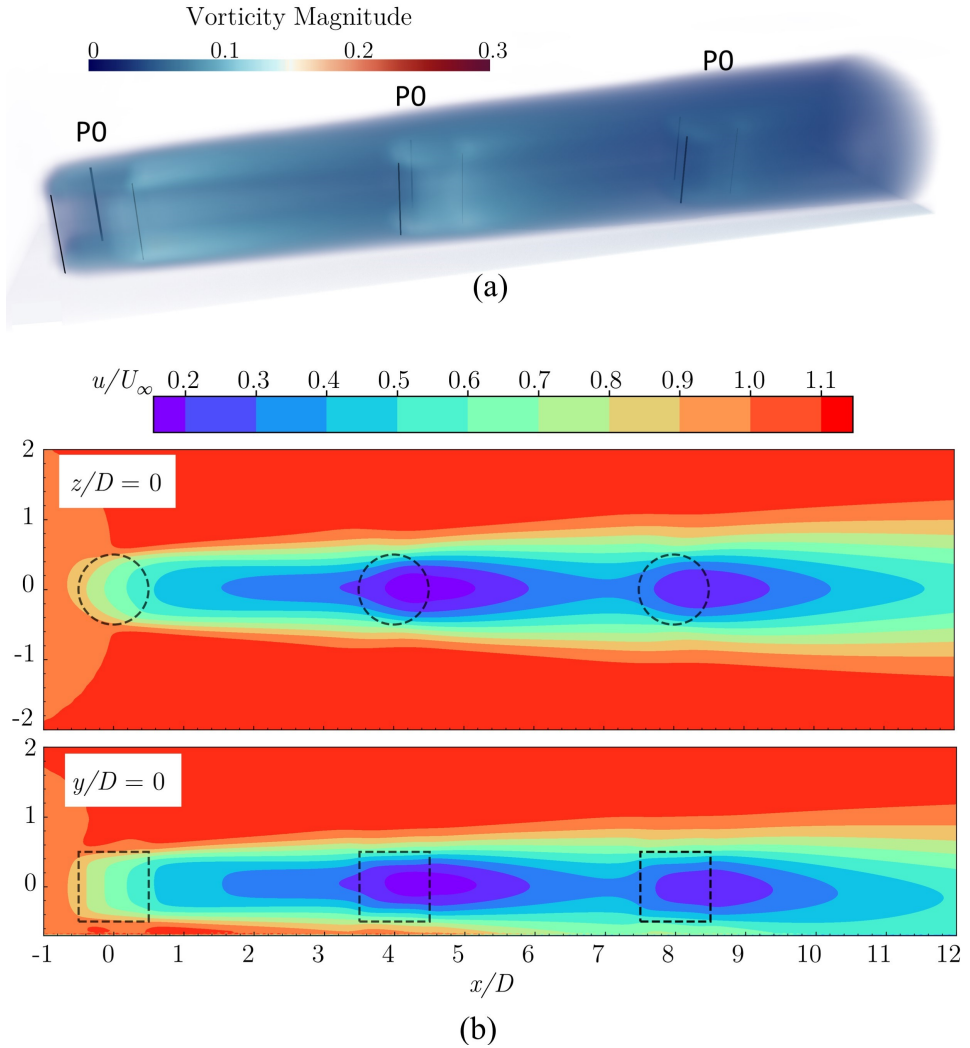
Figure 9.33: P0×3_F: (a): volume rendering of the instantaneous vorticity magnitude; (b): Streamwise velocity contours in different planes.
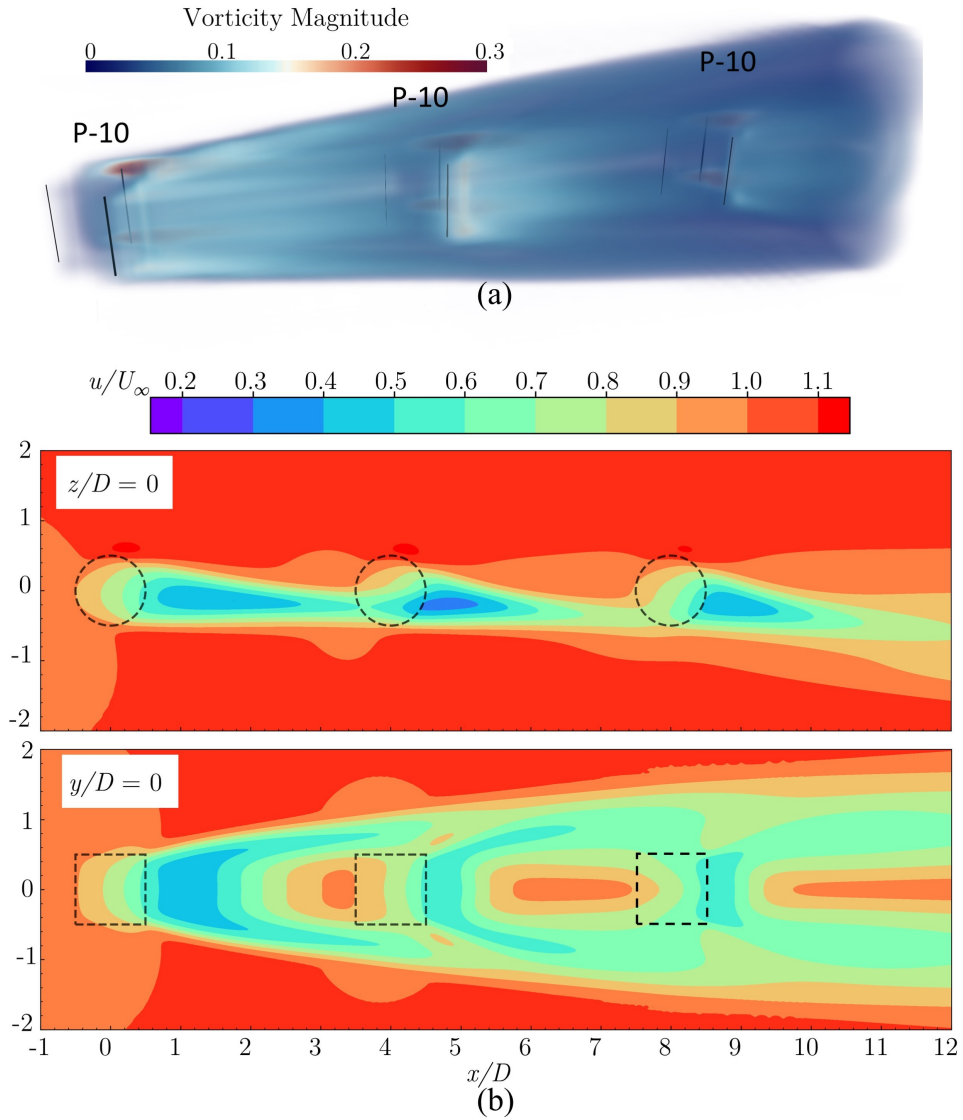
Figure 9.34: P-10×3: (a): volume rendering of the instantaneous vorticity magnitude; (b): Streamwise velocity contours in different planes.
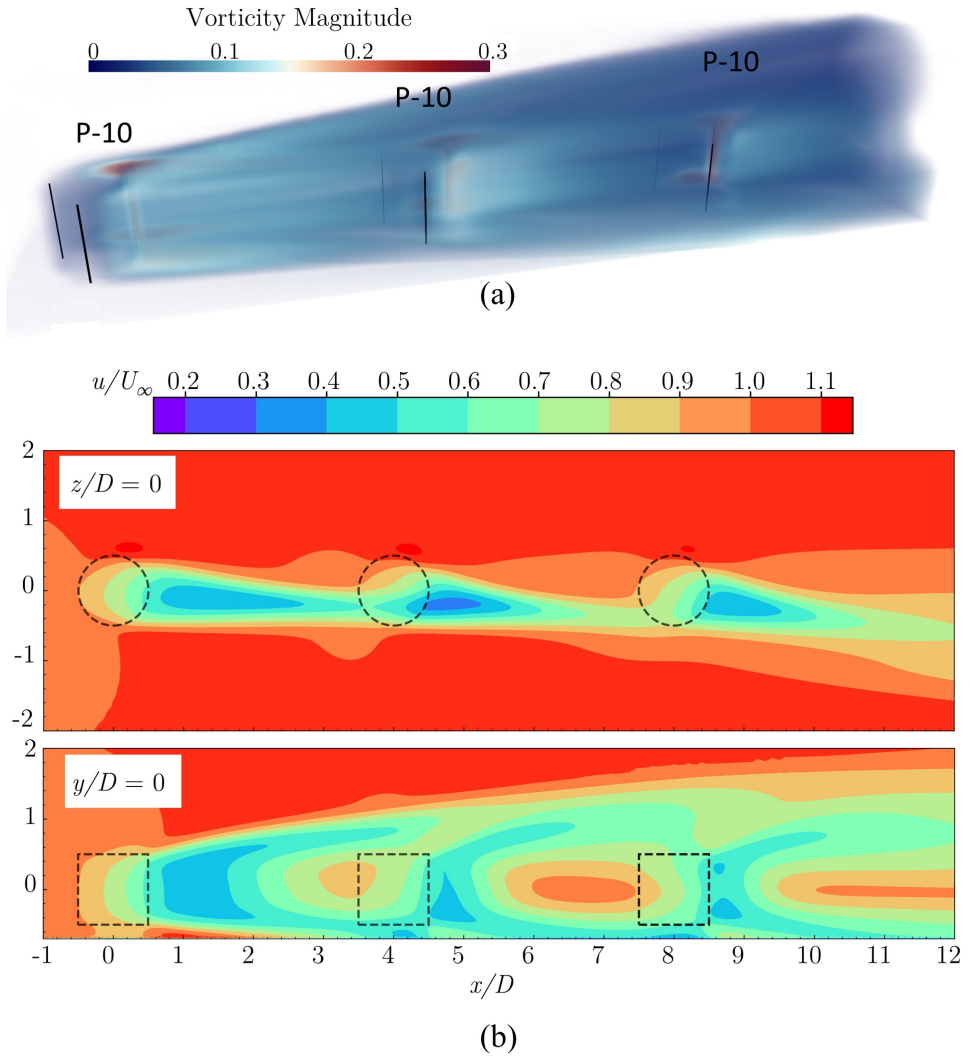
Figure 9.35: P-10×3_F: (a): volume rendering of the instantaneous vorticity magnitude; (b): Streamwise velocity contours in different planes.
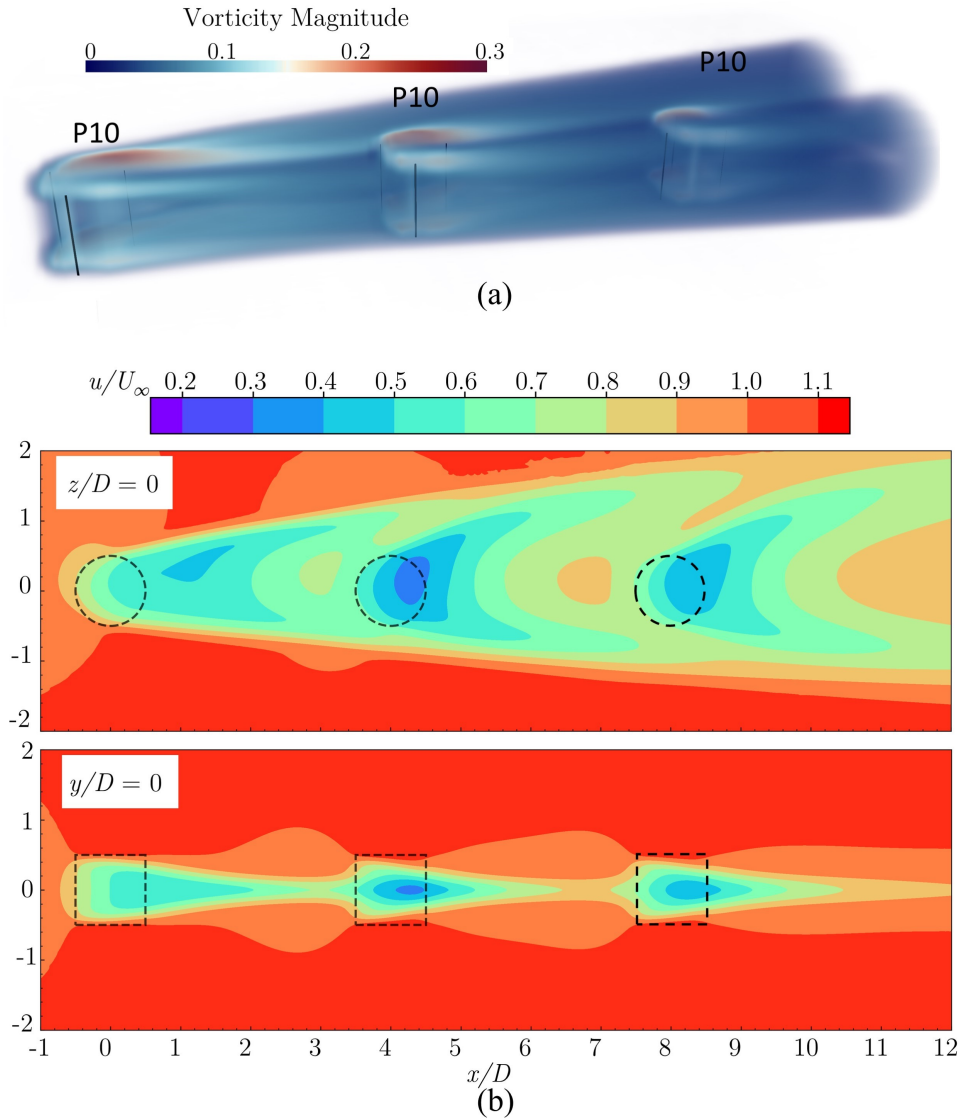
Figure 9.36: P10×3: (a): volume rendering of the instantaneous vorticity magnitude; (b): Streamwise velocity contours in different planes.
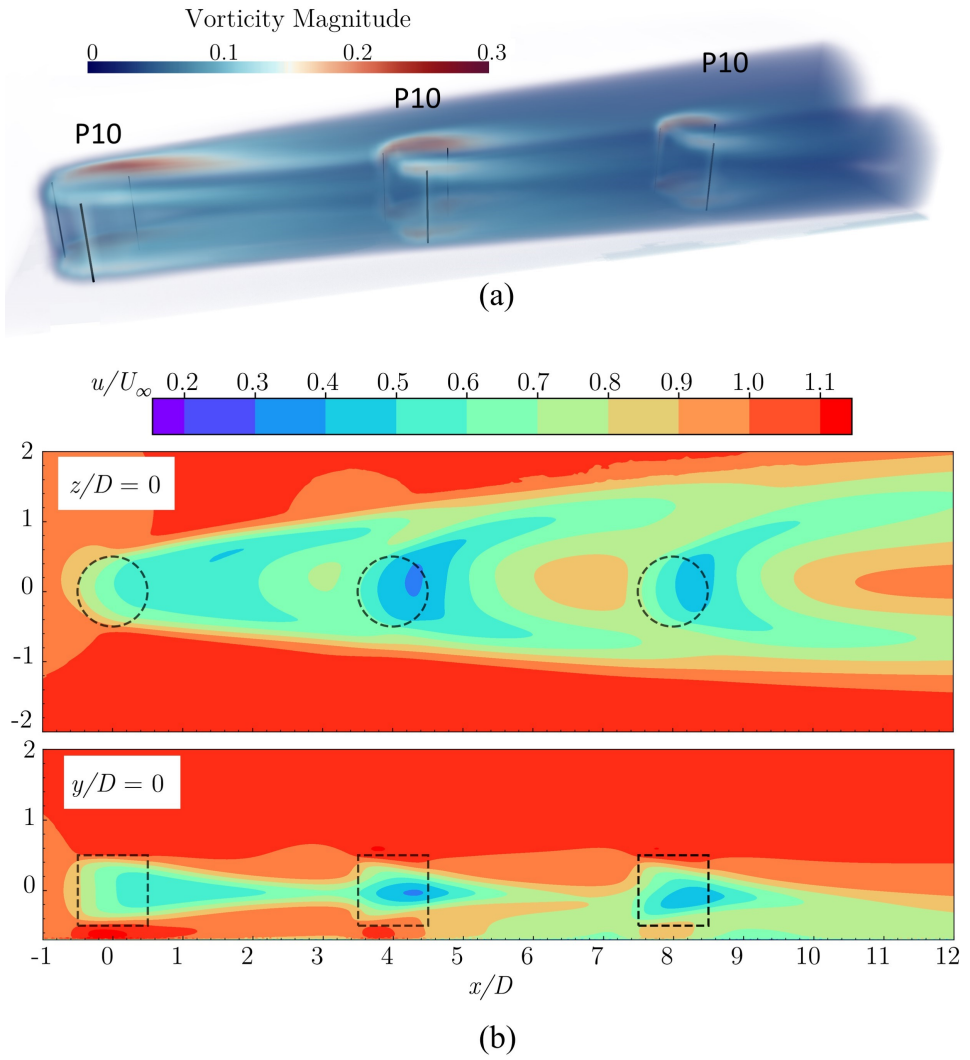
Figure 9.37: P10×3_F: (a): volume rendering of the instantaneous vorticity magnitude; (b): Streamwise velocity contours in different planes.

9.3.4. VELOCITY PRODUCTS

Some velocity products are presented in figures 9.38 and 9.39 to qualitatively understand the blade pitches effects on the momentum convection and further on the enhancement of power extraction. Figure 9.38 compares the products of vertical and streamwise velocities ($-wu$) at the upper tip of the rotors, where minus sign means that the vertical velocity w pointing into the turbine region is treated positive instead of that towards z-direction. It is obvious that the wake of pitched VAWTs generates more vigorous vertical momentum convection at this plane. A wind farm in the atmospheric boundary layer will benefit from such process significantly, where the vertical fluxes of momentum is vital to the energy replenishment (Stevens and Meneveau, 2017; Hezaveh and Bou-Zeid, 2018). P-10×3_F brings momentum into the field on windward side while brings out right behind the VAWTs; Whereas P10×3_F performs the opposite. Judging by the visual comparison, P10×3_F brings the most amount of momentum among the cases.
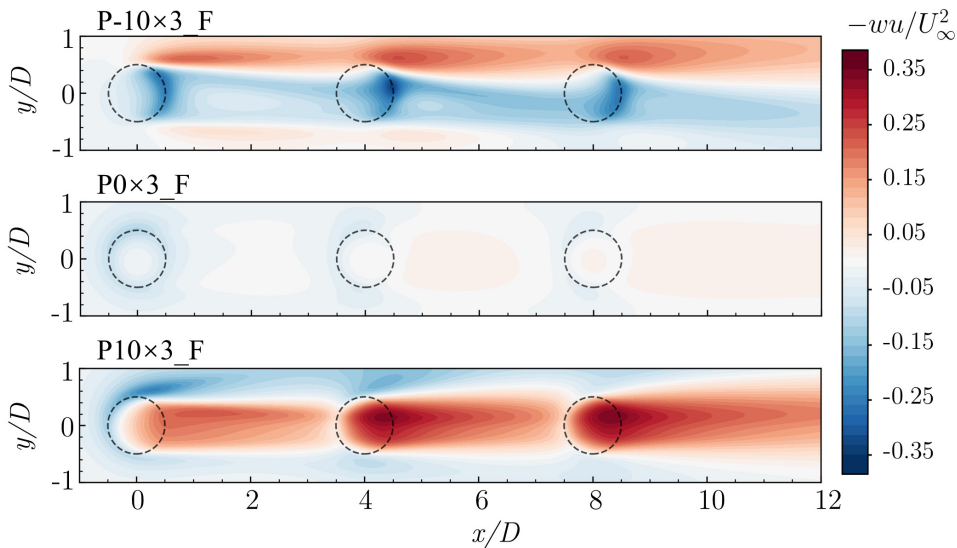
Figure 9.38: Products of vertical and streamwise velocities at upper-tip plane ($z/D = 0.5$, the origin is at the rotor center of VAWT1) for the cases with floor.

The advective influxes of momentum along the lateral surfaces are shown in figure 9.39, where the same procedure on the surface normal is taken, resulting in positive values for influxes and negative for out-fluxes. Again, P-10×3_F and P10×3_F feature stronger fluxes at these planes. Judging by the visual comparison, the former yields an overall influx of momentum through the sides, whereas the latter transfers momentum out of the turbine volume.

In all, for a control volume bounded by the planes $z/D = 0.5$, $y/D = -1$ and 1, the momentum entrainment are increased by the pitching VAWTs. The increased influxes mostly occur at the top lid of the CV crossing the upper tips of the blades. Such enhancement in momentum advection is essential for full-scale VAWTs operating in the atmospheric boundary layer, because the wind speed at upper tips usually is higher and

thus featuring higher momentum,
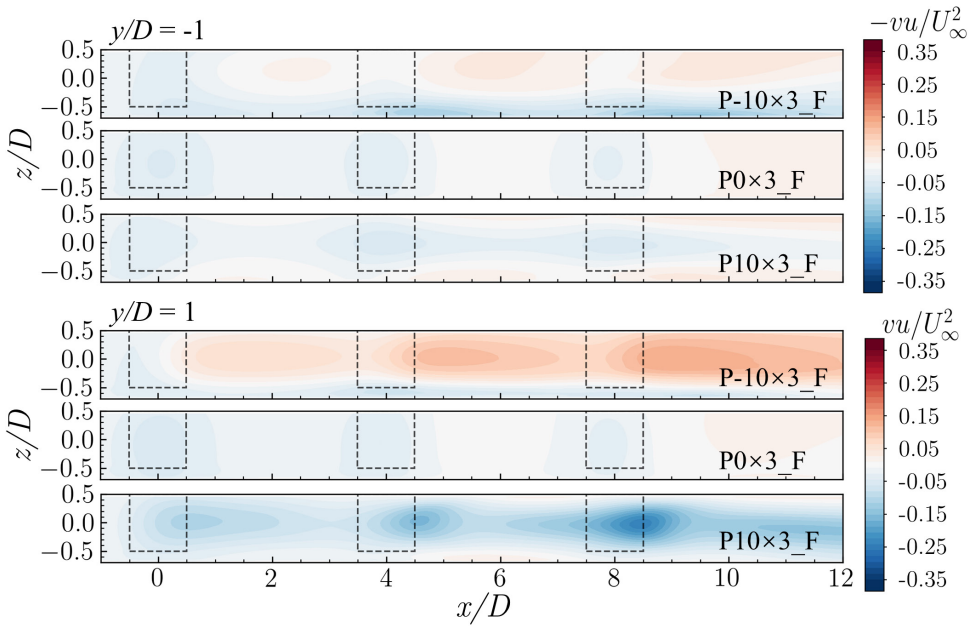
Figure 9.39: Products of lateral and streamwise velocities at $y/D = -1$ and 1.

9.4. CONCLUSIONS

The performance and wake aerodynamics of up-scaled VAWTs have been simulated and assessed. The simulation confirms the efficacy of wake deflection using blade pitches; the overall power coefficient is increased by 45% for a tested two-turbine-array compared to the one without deflection operation. The shift of normal force and torque coefficients are visualised following the simplified model proposed in chapter 6. These results match the model prediction, validating the simplified model for the control of VAWT wakes. Furthermore, the wakes are scrutinised for different array configurations, focusing on the wake topologies, interactions and momentum recovery. Other main findings in the chapter are as follows:

- The concept of VAWT wake deflection using fixed blade pitch at a high Reynolds number has been preliminarily proved. By blade pitching, the loading distribution and torque coefficients are effectively shifted along the swept area of the blades. Moreover, shifting of the loading results in significantly deflected and deformed wakes.

- Wake deflection of the upwind VAWT has a significant impact on the performances of downwind VAWTs. It increases the overall power output by 15-45% in the VAWT array simulated in this work.

- The wake interactions between two VAWTs placed in tandem cannot be represented simply by wake superposition, because the complex vorticity systems cannot be linearly superimposed.

- For an array of VAWTs deflecting the wake in the same direction, wakes of upwind VAWTs make downwind turbines more effective in wake deflection; Relatively, the downwind VAWT enhances the wake deflections in the upwind ones. This indicates a potential rule for VAWT farm deployments.

- The wake of pitched VAWT arrays in the present work feature quicker momentum recovery. The main source of momentum influxes is the vertical advection along the top boundary of the wind turbine region.

9

IV

EPILOGUE

10

CONCLUSIONS AND RECOMMENDATIONS

By experimentally measuring, numerically simulating and theoretically analysing the VAWT wake aerodynamics, the dissertation has revealed the mechanisms underlying the relationship between rotor loading and wake development. Using the high-fidelity experimental data acquired via PIV, a set of simulations and analytical models have been validated, and further adopted to demonstrate the efficacy of wake deflection on wind farm power output. This chapter concludes the dissertation by answering the research questions, summarising the contributions, reflecting on the limitations, and recommending future works.

10.1. ANSWERS TO THE RESEARCH QUESTIONS

HOW TO CHARACTERISE THE WAKE OF VAWTS?

On the one hand, the wake of VAWTs has attributes common to that of HAWTs. It features a streamwise velocity deficit governed by mass and momentum conservation; It exhibits self-similarity in the far wake region. Also, properties of bluff body wake, such as meandering, vortex street, etc., are observed in the wake of VAWTs (Araya et al., 2017).

On the other hand, VAWTs' wake is distinct in two aspects. First, it manifests more vigorous cross-wake motions induced by the unique vorticity system; The latter is imparted by the rotating blades on VAWTs that exert forces varying with the azimuth positions. The cross-wake motion has an essential impact on wake recovery via enhancing the advection of momentum. Second, VAWTs usually generate higher turbulence intensity in the wake. The orbital motion along the vertical axis causes frequent interactions between the blades and the rotor wake, stimulating more significant turbulence. The turbulence intensity is positively related to the Reynolds stress and the turbulent transport of mean kinetic energy (MKE), and thus the wake recovery rate.

HOW TO CONTROL THE TRAJECTORY AND RECOVERY OF A VAWT WAKE?

Pitched blades are effective in controlling the wake of VAWTs. The blade loading is varied along azimuth and thus the vortex system. The overall lateral force determines the crossflow deflection. The cross-section shape can be controlled by regulating the force distribution along the rotor swept area. The upwind half with higher loading will make the wake expands more horizontally; in contrast, when the downwind half is loaded more, the wake tends to stretch vertically.

To enhance the wake recovery, one can design the load distribution to increase the vorticity strength. In this way, more outer flow with higher momentum can be convected into the wake region, increasing the kinetic energy in the wake. Additionally, one can deform the wake to increase its perimeter and increase the interface with the freestream. This will improve the turbulent transport of MKE.

WHAT IS THE EFFECT OF WAKE-ROTOR/WAKE-WAKE INTERACTION OF VAWTS?

When VAWTs are placed in tandem and the downwind turbines are still in the wake of the upwind ones, the upwind VAWTs are found to play a leading role in the overall wake topology and power output. The vortex systems generated by the turbines interact with each other, increasing the turbulence intensity in the wake.

HOW TO MODEL WAKE-ROTOR AND WAKE-WAKE INTERACTION?

The existing analytical wake and wake superposition models for VAWTs are mostly extrapolated from those for HAWTs. However, the huge differences between the wakes of turbines in different kinds prelude the failure of those models in predicting the wake of VAWT, especially when complex phenomena like wake deflection and deformation exist. This thesis demonstrates the mechanisms of VAWT wake deflection, revealing that the 3D loading effect has to be taken into account when modelling the VAWT wake.

The thesis employs the actuator line model to investigate the wake interactions; Be-

10

cause the model together with RANS simulation manifest a great balance in the accuracy and the computational cost. With the validated simulation model, we investigated the enhancement of power extraction in an VAWT array where two up-scaled VAWTs are placed in tandem. The total power coefficient is increased up to 45% when the upwind turbine deflects the wake using fixed blade pitches.

10.2. CONTRIBUTIONS TO THE STATE-OF-THE-ART

In the present dissertation, the main contributions are as follows:

- We propose an effective mixing diameter D^* to scale the streamwise momentum recovery for actuators of arbitrary shape. Compared with existing scaling lengths, D^* not only accounts for the momentum deficit imparted within the actuator/turbine frontal area, but also the momentum exchange rate across the effective wake interfacial area (characterised by actuator perimeter). The latter is proven to be non-negligible using experiments and numerical simulations, especially for elongated actuators. (Chapter 4)

- We characterise the wake of VAWTs in considerable detail, stressing its essential differences in comparison with the wake of planar actuator discs; The latter is often referred to as effective representatives of HAWTs. The differences stem from the 3D distribution of loading in VAWTs. (Chapter 5)

- We demonstrate the relation between spatial load distributions on VAWT's rotor and streamwise vorticity patterns. In doing so, we propose a simplified trailing vortex model of VAWTs based on the concept of a three-dimensional actuator cylinder model, accounting for the VAWT wake deflection and deformation under various loading conditions. The proposed vortex system compares well with the PIV and force balance measurements. (Chapter 6)

- We show the efficacy of VAWT wake deflection in enhancing power output in array configurations, via experiments on wake interactions of VAWTs. (Chapter 7 & Chapter 8)

- We validate the actuator line model using the high-fidelity experiment data. The ALM is further implemented to investigate the VAWT performance and wind power output in array configurations. (Chapter 9)

- We demonstrate the significant enhancement in power extraction by wake deflection in an up-scaled VAWT array using the validated simulation model. At most an overall increment of 45% of the power coefficient is achieved by constant blade pitches of the upwind VAWT. For downwind turbines, the power coefficients are increased by 87%-145%.

- We compare the state-of-the-art analytical wake models with the numerical simulation and experiment results, showing the models' limitations in accounting for the wake deflection. A wake similarity analysis of the experiment data sheds light on possible improvements that can be incorporated into the models, for instance, using a double Gaussian shape function to match the deflections.

10

- We examine the wakes of a full-scale VAWT using the validated numerical simulation method. The VAWT performances and the wake aerodynamics in arrays with or without blade pitches and with or without floors are presented. For the arrays with pitched blades, the momentum influx is increased significantly. The vertical momentum advection is identified as the main source of momentum influxes along the top boundary of the wind turbine region. This mechanism is vital for sustaining the enhancement on wind power extraction, and will be more effective when the turbine is operating in ABL condition where the top boundary features higher momentum.

10.3. Outlook and recommendations

There remain numerous open questions to advance the wind farm aerodynamics of VAWTs. Hence, this section recommends a few interesting topics that the author identifies necessary, based on the conclusions and reflections on the current dissertation.

- **How to analytically model the VAWT wake to account for the wake control?**

  We have seen the limitations of the current analytical models on account of wake deflection and deformation. Based on the observation that the deflection is positively related to the overall lateral force, introducing mass and momentum balance for cross-flow is recommended to model the lateral force effect on deflections.

- **How to measure the instant blade loading along the azimuth accurately?**

  This dissertation has proposed four simplified load distributions of VAWTs, yielding wakes with different patterns of deflection and deformation. But this also raises the question of how to experimentally identify the instant blade loading. By answering this question, one would acquire high-fidelity data to validate the proposed model and, more importantly, to monitor the load variation and apply active pitch control accordingly; The latter is listed as another interesting topic below.

- **How to design an active pitch-control schedule?**

  We have shed light on how the 3D force field of VAWTs affects wake development and momentum recovery. Technically, one can design the force field based on the simplified model proposed in chapter 6. However, how to yield a specific force field using actively pitched blades remains unsolved. To do so, one has to consider the unsteady aerodynamics of airfoils, the inflow variation, blade-wake interaction, etc.

- **Is wake deflection observed in this dissertation valid in high Reynolds numbers?**

  Upscaling is a trend for the future offshore wind; Wind turbines with huge rotor sizes generally work in a high Reynolds number scheme. The faster wake recovery and higher power output in an array configuration as presented in the dissertation are beneficial to the offshore wind farm. Therefore, the wake response to the 3D load fields of VAWTs in high Reynolds numbers is worth investigating.

10

- **How to design the control strategy in VAWT arrays to achieve higher power density?**

  The thesis showed the immense potential of wake deflection employing blade pitch to increase total power extraction. However, the adopted configurations are simplified and just for concept demonstration. Exploring the potential of different VAWT wind farm layouts and wake control strategies for increasing power density could have a large impact on the future of wind energy.

10

BIBLIOGRAPHY

Abkar, M. Theoretical Modeling of Vertical-Axis Wind Turbine Wakes. *Energies*, 12(1):10, 2018.

Abkar, M. and Dabiri, J. O. Self-similarity and flow characteristics of vertical-axis wind turbine wakes: an LES study. *Journal of Turbulence*, 18(4):373–389, 2017.

Abkar, M. and Porté-Agel, F. Mean and turbulent kinetic energy budgets inside and above very large wind farms under conventionally-neutral condition. *Renewable Energy*, 70: 142–152, 2014.

Ackermann, T. and Söder, L. An overview of wind energy-status 2002. *Renewable and Sustainable Energy Reviews*, 6(1-2):67–127, 2002.

Aihara, A., Mendoza, V., Goude, A., and Bernhoff, H. Comparison of Three-Dimensional Numerical Methods for Modeling of Strut Effect on the Performance of a Vertical Axis Wind Turbine. *Energies*, 15(7), 2022.

Ainslie, J. F. Calculating the flowfield in the wake of wind turbines. *Journal of Wind Engineering and Industrial Aerodynamics*, 27(1-3):213–224, 1988.

Anderson Jr, J. *Fundamentals of Aerodynamics*. McGraw-Hill, New York, fifth edit edition, 1985.

Araya, D. B., Colonius, T., and Dabiri, J. O. Transition to bluff-body dynamics in the wake of vertical-axis wind turbines. *Journal of Fluid Mechanics*, 813:346–381, 2017.

Aubrun, S., Loyer, S., Hancock, P. E., and Hayden, P. Wind turbine wake properties: Comparison between a non-rotating simplified wind turbine model and a rotating model. *Journal of Wind Engineering and Industrial Aerodynamics*, 120:1–8, 2013.

Aubrun, S., Bastankhah, M., Cal, R., Conan, B., Hearst, R., Hoek, D., Hölling, M., Huang, M., Hur, C., Karlsen, B., Neunaber, I., Obligado, M., Peinke, J., Percin, M., Saetran, L., Schito, P., Schliffke, B., Sims-Williams, D., Uzol, O., Vinnes, M., and Zasso, A. Round-robin tests of porous disc models. In *Journal of Physics: Conference Series*, volume 1256. IOP Publishing, 2019.

Bachant, P. and Wosnik, M. Characterising the near-wake of a cross-flow turbine. *Journal of Turbulence*, 16(4):392–410, 2015.

Bachant, P. and Wosnik, M. Effects of reynolds number on the energy conversion and near-wake dynamics of a high solidity vertical-axis cross-flow turbine. *Energies*, 9(2): 1–18, 2016.

Bachant, P., Goude, A., and Wosnik, M. Actuator line modeling of vertical-axis turbines. *arXiv preprint*, pages 1–21, 2016.

Balaras, E. Modeling complex boundaries using an external force field on fixed Cartesian grids in large-eddy simulations. *Computers and Fluids*, 33(3):375–404, 2004.

Barthelmie, R. J. and Jensen, L. E. Evaluation of wind farm efficiency and wind turbine wakes at the Nysted offshore wind farm. *Wind Energy*, 13(6):573–586, 2010.

Barthelmie, R. J., Folkerts, L., Larsen, G. C., Rados, K., Pryor, S. C., Frandsen, S. T., Lange, B., and Schepers, G. Comparison of wake model simulations with offshore wind turbine wake profiles measured by sodar. *Journal of Atmospheric and Oceanic Technology*, 23(7):888–901, 2006.

Barthelmie, R. J., Frandsen, S. T., Nielsen, M. N., Pryor, S. C., Rethore, P. E., and Jørgensen, H. E. Modelling and measurements of power losses and turbulence intensity in wind turbine wakes at middelgrunden offshore wind farm. *Wind Energy*, 10(6):517–528, 2007.

Barthelmie, R. J., Hansen, K., Frandsen, S. T., Rathmann, O., Schepers, J. G., Schlez, W., Phillips, J., Rados, K., Zervos, A., Politis, E. S., and Chaviaropoulos, P. K. Modelling and measuring flow and wind turbine wakes in large wind farms offshore. *Wind Energy*, 12(5):431–444, 2009.

Bartl, J., Mühle, F., Schottler, J., Sætran, L., Peinke, J., Adaramola, M., and Hölling, M. Wind tunnel experiments on wind turbine wakes in yaw: Effects of inflow turbulence and shear. *Wind Energy Science*, 3(1):329–343, 2018.

Bastankhah, M. and Porté-Agel, F. A new analytical model for wind-turbine wakes. *Renewable Energy*, 70:116–123, 2014.

Bastankhah, M. and Porté-Agel, F. Experimental and theoretical study of wind turbine wakes in yawed conditions. *Journal of Fluid Mechanics*, 806:506–541, 2016.

Bastankhah, M. and Porté-Agel, F. Wind farm power optimization via yaw angle control: A wind tunnel study. *Journal of Renewable and Sustainable Energy*, 11(2):023301, 2019.

Bastankhah, M., Shapiro, C. R., Shamsoddin, S., Gayme, D. F., and Meneveau, C. A vortex sheet based analytical model of the curled wake behind yawed wind turbines. *Journal of Fluid Mechanics*, 933, 2021a.

Bastankhah, M., Shapiro, C. R., Shamsoddin, S., Gayme, D. F., and Meneveau, C., 2021b.

Betz, A. Schraubenpropeller mit geringstem Energieverlust. Mit einem Zusatz von l. Prandtl. *Nachrichten von der Gesellschaft der Wissenschaften zu Göttingen, Mathematisch-Physikalische Klasse*, 1919:193–217, 1919.

Boersma, S., Doekemeijer, B. M., Gebraad, P. M., Fleming, P. A., Annoni, J., Scholbrock, A. K., Frederik, J. A., and Van Wingerden, J. W. A tutorial on control-oriented modeling and control of wind farms. *Proceedings of the American Control Conference*, pages 1–18, 2017.

Bossuyt, J., Meneveau, C., and Meyers, J. Wind farm power fluctuations and spatial sampling of turbulent boundary layers. *Journal of Fluid Mechanics*, 823:329–344, 2017.

Bossuyt, J., Scott, R., Ali, N., and Cal, R. B. Quantification of wake shape modulation and deflection for tilt and yaw misaligned wind turbines. *Journal of Fluid Mechanics*, 917: A3, 2021.

Boudreau, M. and Dumas, G. Comparison of the wake recovery of the axial-flow and cross-flow turbine concepts. *Journal of Wind Engineering and Industrial Aerodynamics*, 165(March):137–152, 2017.

Boussinesq, J. Essai sur la theorie des eaux courantes. In *Memoires presentes par divers savants a l'Academie des Sciences de l'Institut National de France*, Paris, 1877. Imprimerie Nationale.

Brownstein, I. D., Wei, N. J., and Dabiri, J. O. Aerodynamically Interacting Vertical-Axis Wind Turbines: Performance Enhancement and Three-Dimensional Flow. *Energies*, 12(14):2724, 2019.

Campagnolo, F., Petrović, V., Bottasso, C. L., and Croce, A. Wind tunnel testing of wake control strategies. In *Proceedings of the American Control Conference*, volume 2016-July, pages 513–518. Institute of Electrical and Electronics Engineers Inc., 2016.

Castro, I. P. Wake characteristics of two-dimensional perforated plates normal to an airstream. *Journal of Fluid Mechanics*, 46(3):599–609, 1971.

Chatelain, P., Duponcheel, M., Zeoli, S., Buffin, S., Caprace, D. G., Winckelmans, G., and Bricteux, L. Investigation of the effect of inflow turbulence on vertical axis wind turbine wakes. In *Journal of Physics: Conference Series*, volume 854, page 012011. IOP Publishing, 2017.

Chaviaropoulos, P. K., Beurskens, H., and Voutsinas, S. Moving Towards Large(r) Rotors Is that a good idea? In *Proceedings of EWEA*, Vienna, Austria, 2013.

Chaviaropoulos, P. K., Natarajan, A., and Jensen, P. H. Key performance indicators and target values for multi-megawatt offshore turbines. *European Wind Energy Association Conference and Exhibition*, 2014.

Cleve, J., Greiner, M., Enevoldsen, P., Birkemose, B., and Jensen, L. Model-based analysis of wake-flow data in the Nysted offshore wind farm. *Wind Energy*, 12(2):125–135, 2009.

Coleman, R. P., Feingold, A. M., and Stempln, C. W. Evaluation of the induced-velocity field of an idealized helicopter rotor. Technical report, National Advisory Committee for Aeronautics, Washington, D.C, 1945.

Corke, T. C. and Thomas, F. O. Dynamic stall in pitching airfoils: Aerodynamic damping and compressibility effects. In *Annual Review of Fluid Mechanics*, volume 47, pages 479–505, 2015.

10

Craig, A. E., Dabiri, J. O., and Koseff, J. R. A Kinematic Description of the Key Flow Characteristics in an Array of Finite-Height Rotating Cylinders. *Journal of Fluids Engineering*, 138(7):070906, 2016a.

Craig, A. E., Dabiri, J. O., and Koseff, J. R. Flow Kinematics in Variable-Height Rotating Cylinder Arrays. *Journal of Fluids Engineering*, 138(11):111203, 2016b.

Craig, A. E., Dabiri, J. O., and Koseff, J. R. Low order physical models of vertical axis wind turbines. *Journal of Renewable and Sustainable Energy*, 9(1):1–17, 2017.

Dabiri, J. O. Potential order-of-magnitude enhancement of wind farm power density via counter-rotating vertical-axis wind turbine arrays. *Journal of Renewable and Sustainable Energy*, 3(4):043104, 2011.

Darcy, H. Recherches expérimentales relatives au mouvement de l'eau dans les tuyaux. In *Mallet-Bachelier*, page 268 pages and atlas, Paris, 1857.

De Tavernier, D., Ferreira, C., Paulsen, U., and Madsen, H. The 3D effects of a vertical-axis wind turbine: rotor and wake induction. *Journal of Physics: Conference Series*, 1618:52040, 2020.

De Tavernier, D. *Aerodynamic advances in vertical-axis wind turbines.* Phd thesis, Delft University of Technology, 2021.

Dessoky, A., Lutz, T., Bangga, G., and Krämer, E. Computational studies on Darrieus VAWT noise mechanisms employing a high order DDES model. *Renewable Energy*, pages 404–425, 2019.

Devenport, W. J., Rife, M. C., Liapis, S. I., and Follin, G. J. The structure and development of a wing-tip vortex. *Journal of Fluid Mechanics*, 312:67–106, 1996.

Dufresne, N. P. and Wosnik, M. Velocity deficit and swirl in the turbulent wake of a wind turbine. *Marine Technology Society Journal*, 47(4):193–205, 2013.

Dyachuk, E., Goude, A., and Bernhoff, H. Dynamic stall modeling for the conditions of vertical axis wind turbines. *AIAA Journal*, 52(1):72–81, 2014.

Ennis, B. L. and Griffith, D. T. System Levelized Cost of Energy Analysis for Floating Offshore Vertical-Axis Wind Turbines. 2018.

Esteban, M. D., Diez, J. J., López, J. S., and Negro, V. Why offshore wind energy?, 2011.

Fail, R., Lawford, J. A., and Eyre, R. C. W. -. *Aeronautical Research Council, reports and memoranda*, 3120(3120):1–21, 1957.

Faleiros, D. E., Tuinstra, M., Sciacchitano, A., and Scarano, F. Generation and control of helium-filled soap bubbles for PIV. *Experiments in Fluids*, 60(40), 2019.

Fei, Z., Tengyuan, W., Xiaoxia, G., Haiying, S., Hongxing, Y., Zhonghe, H., Yu, W., and Xiaoxun, Z. Experimental study on wake interactions and performance of the turbines with different rotor-diameters in adjacent area of large-scale wind farm. *Energy*, 199: 117416, 2020.

10

Ferreira, C. S. *The near wake of the VAWT 2D and 3D views of the VAWT aerodynamics.* PhD thesis, Delft University of Technology, 2009.

Fleming, P., Annoni, J., Shah, J. J., Wang, L., Ananthan, S., Zhang, Z., Hutchings, K., Wang, P., Chen, W., and Chen, L. Field test of wake steering at an offshore wind farm. *Wind Energy Science*, 2:229–239, 2017.

Fleming, P., King, J., Dykes, K., Simley, E., Roadman, J., Scholbrock, A., Murphy, P., Lundquist, J. K., Moriarty, P., Fleming, K., van Dam, J., Bay, C., Mudafort, R., Lopez, H., Skopek, J., Scott, M., Ryan, B., Guernsey, C., and Brake, D. Initial results from a field campaign of wake steering applied at a commercial wind farm – Part 1. *Wind Energy Science*, 4(2):273–285, 2019.

Fleming, P., King, J., Simley, E., Roadman, J., Scholbrock, A., Murphy, P., K. Lundquist, J., Moriarty, P., Fleming, K., Van Dam, J., Bay, C., Mudafort, R., Jager, D., Skopek, J., Scott, M., Ryan, B., Guernsey, C., and Brake, D. Continued results from a field campaign of wake steering applied at a commercial wind farm - Part 2. *Wind Energy Science*, 5(3): 945–958, 2020.

Fleming, P. A., Gebraad, P. M., Lee, S., van Wingerden, J. W., Johnson, K., Churchfield, M., Michalakes, J., Spalart, P., and Moriarty, P. Evaluating techniques for redirecting turbine wakes using SOWFA. *Renewable Energy*, 70:211–218, 2014.

Frandsen, S. On the wind speed reduction in the center of large clusters of wind turbines. *Journal of Wind Engineering and Industrial Aerodynamics*, 39(1-3):251–265, 1992.

Frandsen, S., Barthelmie, R., Pryor, S., Rathmann, O., Larsen, S., Højstrup, J., and Thøgersen, M. Analytical modelling of wind speed deficit in large offshore wind farms. *Wind Energy*, 9(1-2):39–53, 2006.

Froude, R. On the Part Played in Propulsion by Difference in Pressure. *Transaction of the Institute of Naval Architects*, 30:390–405, 1889.

Ghasemian, M., Ashrafi, Z. N., and Sedaghat, A. A review on computational fluid dynamic simulation techniques for Darrieus vertical axis wind turbines. *Energy Conversion and Management*, 149:87–100, 2017.

Glauert, H. *Airplane Propellers*, pages 169–360. Springer, Berlin, Heidelberg, 1935.

Göçmen, T., Laan, P. V. D., Réthoré, P. E., Diaz, A. P., Larsen, G. C., and Ott, S. Wind turbine wake models developed at the technical university of Denmark: A review. *Renewable and Sustainable Energy Reviews*, 60:752–769, 2016.

Gormont, R. E. A mathmatical model of unsteady aerodynamics and radial flow for application to helicopter rotors. Technical Report December, The Boeing Company, Philadelphia, Pennsylvania, 1973.

Goude, A. *Fluid Mechanics of Vertical Axis Turbines : Simulations and Model Development.* PhD thesis, Uppsala University, Electricity, 2012.

10

Guo, J. and Lei, L. Flow Characteristics of a Straight-Bladed Vertical Axis Wind Turbine with Inclined Pitch Axes. *Energies 2020, Vol. 13, Page 6281*, 13(23):6281, 2020.

GWEC. Global Offshore Wind Report 2021. Technical report, Global Wind Energy Council, 2021.

Hamilton, N., Kang, H. S., Meneveau, C., and Cal, R. B. Statistical analysis of kinetic energy entrainment in a model wind turbine array boundary layer. *Journal of Renewable and Sustainable Energy*, 4(6):063105, 2012.

Hansen, M. H., Gaunaa, M., and Madsen, H. A. A Beddoes-Leishman type dynamic stall model in state-space and indicial formulations. Technical Report Risø-R-1354(EN), Risø National Laboratory, Roskilde, Denmark, 2004.

Hasager, C. B., Nygaard, N. G., Volker, P. J., Karagali, I., Andersen, S. J., and Badger, J. Wind farm wake: The 2016 Horns Rev photo case. *Energies*, 10(3), 2017.

Helvig, S. d. J., Vinnes, M. K., Segalini, A., Worth, N. A., and Hearst, R. J. A comparison of lab-scale free rotating wind turbines and actuator disks. *Journal of Wind Engineering and Industrial Aerodynamics*, 209, 2021.

Hezaveh, S. H. and Bou-Zeid, E. Mean kinetic energy replenishment mechanisms in vertical-axis wind turbine farms. *Physical Review Fluids*, 3(9):094606, 2018.

Hezaveh, S. H., Bou-Zeid, E., Dabiri, J., Kinzel, M., Cortina, G., and Martinelli, L. Increasing the Power Production of Vertical-Axis Wind-Turbine Farms Using Synergistic Clustering. *Boundary-Layer Meteorology*, 169(2):1–22, 2018.

Howland, M. F., Bossuyt, J., Martínez-Tossas, L. A., Meyers, J., and Meneveau, C. Wake structure in actuator disk models of wind turbines in yaw under uniform inflow conditions. *J. Renewable Sustainable Energy*, 8:043301, 2016.

Howland, M. F., Lele, S. K., and Dabiri, J. O. Wind farm power optimization through wake steering. *Proceedings of the National Academy of Sciences of the United States of America*, 116(29):14495–14500, 2019.

Huang, M., Ferreira, C., Sciacchitano, A., and Scarano, F. Experimental Comparison of the Wake of a Vertical Axis Wind Turbine and Planar Actuator Surfaces. In *Journal of Physics: Conference Series*, volume 1618(5), 2020.

Huang, M., Sciacchitano, A., and Ferreira, C. On the wake deflection of vertical axis wind turbines by pitched blades. *Wind Energy*, n/a(n/a):1–23, 2023.

IRENA. Future of wind. Technical report, International Renewable Energy Agency, 2019.

IRENA. Renewable Power Generation Costs 2020. Technical report, International Renewable Energy Agency, 2021.

Jadeja, A. Wake Deflection Technique for Vertical Axis Wind Turbines using Actuator Line Model in OpenFOAM. Master's thesis, Delft University of Technology, 2018.

10

Jensen, N. A note on wind generator interaction. In *Risø-M*, volume No.2411, Roskilde, 1983. Risø National Laboratory, Risø National Laboratory.

Jiménez, Á., Crespo, A., and Migoya, E. Application of a LES technique to characterize the wake deflection of a wind turbine in yaw. *Wind Energy*, 13(6):559–572, 2010.

Johansson, P. B. V., George, W. K., and Gourlay, M. J. Equilibrium similarity, effects of initial conditions and local Reynolds number on the axisymmetric wake. *Physics of Fluids*, 15(3):603–617, 2003.

Joukowsky, J. Vortex theory of the screw Propeller I. *Trudy Avia Raschetno- Ispytatelnogo Byuro (in Russian) Also published in Gauthier-Villars et Cie. (eds). Th´eorie Tourbillonnaire de l'H´elice Propulsive, Quatri'eme M´emoire.*, 16(1):1–31, 1912.

Joukowsky, J. Vortex theory of the screw propeller IV. *Trudy Avia Raschetno- Ispytatelnogo Byuro (in Russian] Also published in Gauthier-Villars et Cie. (eds). Th´eorie Tourbillonnaire de l'H´elice Propulsive, Quatri'eme M´emoire. 1929*, 3:1–97, 1918.

Jux, C., Sciacchitano, A., Schneiders, J. F., and Scarano, F. Robotic volumetric PIV of a full-scale cyclist. *Experiments in Fluids*, 59(4):74, 2018.

Kaldellis, J. K., Triantafyllou, P., and Stinis, P. Critical evaluation of Wind Turbines' analytical wake models. *Renewable and Sustainable Energy Reviews*, 144:110991, 2021.

Katić, I., Højstrup, J., and Jensen, N. O. A Simple Model for Cluster Efficiency. In Palz, W. and Sesto, E., editors, *EWEC'86. Proceedings. Vol. 1*, pages 407–410. A. Raguzzi, 1987.

Keane, A., Aguirre, P. E. O., Ferchland, H., Clive, P., and Gallacher, D. An analytical model for a full wind turbine wake. *Journal of Physics: Conference Series*, 753:32039, 2016.

Kinzel, M., Mulligan, Q., and Dabiri, J. O. Energy exchange in an array of vertical-axis wind turbines. *Journal of Turbulence*, 14(6):38–39, 2013.

Kinzel, M., Araya, D. B., and Dabiri, J. O. Turbulence in vertical axis wind turbine canopies. *Physics of fluids*, 27:115102, 2015.

Lam, H. F. and Peng, H. Y. Development of a wake model for Darrieus-type straight-bladed vertical axis wind turbines and its application to micro-siting problems. *Renewable Energy*, 114:830–842, 2017.

Larsen, G. A Simple Wake Calculation Procedure. In *Risø-M*, volume No. 2760. Risø National Laboratory, 1988.

Larsen, G. C. A simple stationary semi-analytical wake model. *Denmark. Forskningscenter Risoe. Risoe-R*, 1713(August):1–21, 2009.

Larsen, J. W., Nielsen, S. R., and Krenk, S. Dynamic stall model for wind turbine airfoils. *Journal of Fluids and Structures*, 23(7):959–982, 2007.

LeBlanc, B. *Dynamics of the Pitch-able VAWT: a study of the dynamics of a vertical axis wind turbine with pitch control*. Phd thesis, Delft University of Technology, 2023.

10

Leblanc, B. and Ferreira, C. Experimental Demonstration of Thrust Vectoring with a Vertical Axis Wind Turbine using Normal Load Measurements. In *Journal of Physics: Conference Series*, volume 1618(5), page 52030. IOP Publishing Ltd, 2020.

LeBlanc, B. and Ferreira, C. Estimation of blade loads for a variable pitch vertical axis wind turbine from particle image velocimetry. *Wind Energy*, 2021.

Leblanc, B. P. and Ferreira, C. S. Experimental Determination of Thrust Loading of a 2-Bladed Vertical Axis Wind Turbine. *Journal of Physics: Conference Series*, 1037(2): 022043, 2018.

Lee, S., Churchfield, M., Moriarty, P., and Jonkman, J. Atmospheric and wake turbulence impacts on wind turbine fatigue loadings. In *Proc. of the 50th AIAA Aerospace Sciences Meeting*, number NREL/CP-5000-53567, pages 1–15, 2012.

Leishman, J. G. and Beddoes, T. S. A semi-empirical model for dynamic stall. *Journal of the American Helicopter Society*, 34(3):3–17, 1989.

Lignarolo, L. E. M., Ragni, D., Ferreira, C. J., and van Bussel, G. J. W. Experimental comparison of a wind-turbine and of an actuator-disc near wake. *Journal of Renewable and Sustainable Energy*, 8(2):023301, 2016.

Lignarolo, L. E., Ragni, D., Scarano, F., Simão Ferreira, C. J., and Van Bussel, G. J. Tip-vortex instability and turbulent mixing in wind-turbine wakes. *Journal of Fluid Mechanics*, 781:467–493, 2015.

Lignarolo, L. E. M., Ragni, D., Krishnaswami, C., Chen, Q., Simão Ferreira, C. J., Van Bussel, G. J. W., Ferreira, C. J. S., and Van Bussel, G. J. W. Experimental analysis of the wake of a horizontal-axis wind-turbine model. *Renewable Energy*, 70:31–46, 2014.

Lissaman, P. B. S. Energy Effectiveness of Arbitrary Arrays of Wind Turbines. *Journal of Energy*, 3(6):323–328, 1979.

Liu, Q., Miao, W., Li, C., Hao, W., Zhu, H., and Deng, Y. Effects of trailing-edge movable flap on aerodynamic performance and noise characteristics of VAWT. *Energy*, 189: 116271, 2019.

Madsen, H. A., Paulsen, U. S., and Vitae, L. Analysis of VAWT aerodynamics and design using the actuator cylinder flow model. *Journal of Physics: Conference Series*, 555(1), 2014.

Madsen, H. A. The Actuator Cylinder: A Flow Model for Vertical Axis Wind Turbines. Technical Report January 1982, The institute of Industrial Constructions and Energy Technology, Aalborg University Centre, Aalborg, Denmark, 1982.

Madsen, H. A. On the ideal and real energy conversion in a straight bladed vertical axis wind turbine. Technical Report September, 1983.

Massie, L., Ouro, P., Stoesser, T., and Luo, Q. An actuator surface model to simulate vertical axis turbines. *Energies*, 12(24):1–16, 2019.

10

McAlister, K., Lambert, O., and Petot, D. Application of the ONERA Model of Dynamic Stall. Technical report, National Aeronautics and Space Administration Moffett Field CA AMES Research Center, 1984.

Medici, D. and Alfredsson, P. H. Measurements on a wind turbine wake: 3D effects and bluff body vortex shedding. *Wind Energy*, 9(3):219–236, 2006.

Medici, D. and Alfredsson, P. H. Wind turbine near wakes and comparisons to the wake behind a disc. In *43rd AIAA Aerospace Sciences Meeting and Exhibit - Meeting Papers*, pages 15593–15604. American Institute of Aeronautics and Astronautics Inc., 2005.

Mendoza, V. and Goude, A. Improving farm efficiency of interacting vertical-axis wind turbines through wake deflection using pitched struts. *Wind Energy*, 22(4):538–546, 2019.

Mendoza, V., Bachant, P., Wosnik, M., and Goude, A. Validation of an Actuator Line Model Coupled to a Dynamic Stall Model for Pitching Motions Characteristic to Vertical Axis Turbines. In *Journal of Physics: Conference Series*, volume 753, 2016.

Mendoza, V., Bachant, P., Ferreira, C., and Goude, A. Near-wake flow simulation of a vertical axis turbine using an actuator line model. *Wind Energy*, 22(2):171–188, 2019.

Mereu, R., Federici, D., Ferrari, G., Schito, P., and Inzoli, F. Parametric numerical study of Savonius wind turbine interaction in a linear array. *Renewable Energy*, 113:1320–1332, 2017.

Meyers, J. and Meneveau, C. Optimal turbine spacing in fully developed wind farm boundary layers. *Wind Energy*, 15(2):305–317, 2012.

Migliore, P. G., Wolfe, W. P., and Fanucci, J. B. Flow Curvature Effects on Darrieus Turbine Blade Aerodynamics. *Journal of energy*, 4(2):49–55, 1980.

Möllerström, E., Gipe, P., Beurskens, J., and Ottermo, F. A historical review of vertical axis wind turbines rated 100 kW and above. *Renewable and Sustainable Energy Reviews*, 105:1–13, 2019.

Monni, D. Numerical simulating and analytical modelling the wake behind vertical axis wind turbines: a verification analysis. Master's thesis, Politecnico di Torino, 2021.

Mycek, P., Gaurier, B., Germain, G., Pinon, G., and Rivoalen, E. Experimental study of the turbulence intensity effects on marine current turbines behaviour. Part I: One single turbine. *Renewable Energy*, 66:729–746, 2014.

Nallasamy, M. Turbulence models and their applications to the prediction of internal flows: A review. *Computers & Fluids*, 15(2):151–194, 1987.

Nanos, E. M., Letizia, S., Clemente, D. J. B., Wang, C., Rotea, M., and Bottasso, C. L. Vertical wake deflection for offshore floating wind turbines by differential ballast control. In *Journal of Physics: Conference Series*, volume 1618, page 22047. IOP Publishing, 2020.

10

Nedić, J., Ganapathisubramani, B., and Vassilicos, J. C. Drag and near wake characteristics of flat plates normal to the flow with fractal edge geometries. *Fluid Dynamics Research*, 45(6):061406, 2013.

Nedić, J., Supponen, O., Ganapathisubramani, B., and Vassilicos, J. C. Geometrical influence on vortex shedding in turbulent axisymmetric wakes. *Physics of Fluids*, 27(3): 035103, 2015.

Niayifar, A. and Porté-Agel, F. A new analytical model for wind farm power prediction. *Journal of Physics: Conference Series*, 625(1), 2015.

Nikhilesh, K. V. Simulation and validation of wake deflection in vertical-axis wind turbines. Master's thesis, Delft University of Technology, 2021.

Novara, M. and Scarano, F. A particle-tracking approach for accurate material derivative measurements with tomographic PIV. *Experiments in Fluids*, 54(8):1–12, aug 2013.

Ouro, P. and Lazennec, M. Theoretical modelling of the three-dimensional wake of vertical axis turbines. *Flow*, 1, 2021.

Ouro, P., Runge, S., Luo, Q., and Stoesser, T. Three-dimensionality of the wake recovery behind a vertical axis turbine. *Renewable Energy*, 133:1066–1077, 2019.

Owens, B. N. *The Wind Power Story: A Century of Innovation that Reshaped the Global Energy Landscape.* 2019.

Paraschivoiu, I. Double-Multiple Streamtube Model for Darrieus Wind Turbines. In *Wind Turbine Dynamics*, volume 1, pages 19–25. NASA Lewis Research Center, 1981.

Park, J. and Law, K. H. Cooperative wind turbine control for maximizing wind farm power using sequential convex programming. *Energy Conversion and Management*, 101:295–316, 2015.

Parkin, P., Holm, R., and Medici, D. The application of piv to the wake of a wind turbine in yaw. In *DLR-Mitteilung*, number 3 in DLR-Mitteilung, pages 155–162, 2001.

Patil, Y. V. PIV Experimental Comparison of Vertical Axis Wind Turbine Wake with Theoretical Models. Master's thesis, Delft University of Technology, 2021.

Paulsen, U. S., Borg, M., Madsen, H. A., Pedersen, T. F., Hattel, J., Ritchie, E., Ferreira, C. S., Svendsen, H., Berthelsen, P. A., and Smadja, C. Outcomes of the DeepWind conceptual design. *Energy Procedia*, 80:329–341, 2015.

Penã, A., Réthoré, P. E., and Van Der Laan, M. P. On the application of the Jensen wake model using a turbulence-dependent wake decay coefficient: The Sexbierum case. *Wind Energy*, 19(4):763–776, 2016.

Peng, H. Y., Liu, H. J., and Yang, J. H. A review on the wake aerodynamics of H-rotor vertical axis wind turbines. *Energy*, 232:121003, 2021.

10

Pierella, F., Krogstad, P. Å., and Sætran, L. Blind Test 2 calculations for two in-line model wind turbines where the downstream turbine operates at various rotational speeds. *Renewable Energy*, 70:62–77, 2014.

Pierella, F., Saetran, L., and Sætran, L. Wind tunnel investigation on the effect of the turbine tower on wind turbines wake symmetry. *Wind Energy*, 20(10):1753–1769, 2017.

Pierik, J., Dekker, J. W. M., Braam, H., Bulder, B. H., Winkelaar, D., Larsen, G. C., Morfiadakis, E. E., Chaviaropoulos, P. K., Derrick, A., and P.Molly, J. European wind turbine standards II (EWTS-II). In *Wind energy for the next millennium.*, pages 568–571, London, 1999.

Pope, S. B. Turbulent Flows. *Measurement Science and Technology*, 12(11):2020–2021, 2001.

Porté-Agel, F., Bastankhah, M., and Shamsoddin, S. Wind-Turbine and Wind-Farm Flows: A Review. *Boundary-Layer Meteorology*, 174(1):1–59, 2020.

Posa, A. Wake characterization of coupled configurations of vertical axis wind turbines using Large Eddy Simulation. *International Journal of Heat and Fluid Flow*, 75:27–43, 2019.

Posa, A., Parker, C. M., Leftwich, M. C., and Balaras, E. Wake structure of a single vertical axis wind turbine. *International Journal of Heat and Fluid Flow*, 61:75–84, 2016.

Raffel, M., Willert, C. E., Scarano, F., Kähler, C. J., Wereley, S. T., and Kompenhans, J. *Particle Image Velocimetry: A Practical Guide*. Springer, 3rd edition, 2018.

Rankine, W. On the Mechanical Principles of the Action of Propellers. *Transaction of the Institute of Naval Architects*, 6:13–39, 1865.

Rezaeiha, A. and Micallef, D. Wake interactions of two tandem floating offshore wind turbines: CFD analysis using actuator disc model. *Renewable Energy*, 179:859–876, 2021.

Rezaeiha, A., Montazeri, H., and Blocken, B. Characterization of aerodynamic performance of vertical axis wind turbines: Impact of operational parameters. *Energy Conversion and Management*, 169:45–77, 2018a.

Rezaeiha, A., Montazeri, H., and Blocken, B. Towards optimal aerodynamic design of vertical axis wind turbines: Impact of solidity and number of blades. *Energy*, 165: 1129–1148, 2018b.

Rockel, S., Peinke, J., Hölling, M., and Cal, R. B. Wake to wake interaction of floating wind turbine models in free pitch motion: An eddy viscosity and mixing length approach. *Renewable Energy*, 85:666–676, 2016.

Rolin, V. F. and Porté-Agel, F. Experimental investigation of vertical-axis wind-turbine wakes in boundary layer flow. *Renewable Energy*, 118:1–13, 2018.

10

Ryan, K. J., Coletti, F., Elkins, C. J., Dabiri, J. O., and Eaton, J. K. Three-dimensional flow field around and downstream of a subscale model rotating vertical axis wind turbine. *Experiments in Fluids*, 57(3):38, 2016.

Sahebzadeh, S., Rezaeiha, A., and Montazeri, H. To cite this article: Sadra Sahebzadeh et al. *Journal of Physics: Conference Series*, 1618:42002, 2020.

Sarlak, H., Meneveau, C., and Sørensen, J. N. Role of subgrid-scale modeling in large eddy simulation of wind turbine wake interactions. *Renewable Energy*, 77:386–399, 2015.

Schanz, D., Gesemann, S., and Schröder, A. Shake-The-Box: Lagrangian particle tracking at high particle image densities. *Experiments in Fluids*, 57(5):70, 2016.

Schlichting, H. and Gersten, K. *Boundary-Layer Theory*. Springer Berlin Heidelberg, Berlin, Heidelberg, 6th edition, 2017.

Schmitz, S. and Maniaci, D. C. Methodology to determine a tip-loss factor for highly loaded wind turbines. *AIAA Journal*, 55(2):341–351, 2017.

Schneiders, J. F. G., Scarano, F., Jux, C., and Sciacchitano, A. Coaxial volumetric velocimetry. *Measurement Science and Technology*, 29(6):065201, 2018.

Schreiber, J., Balbaa, A., and Bottasso, C. L. Brief communication: A double-Gaussian wake model. *Wind Energy Science*, 5(1):237–244, 2020.

Sciacchitano, A. and Scarano, F. Elimination of PIV light reflections via a temporal high pass filter. *Measurement Science and Technology*, 25(8):084009, 2014.

Sciacchitano, A. and Wieneke, B. PIV uncertainty propagation. *Measurement Science and Technology*, 27(8):084006, jun 2016. ISSN 13616501.

Scott, R., Viggiano, B., Dib, T., Ali, N., Hölling, M., Peinke, J., and Cal, R. B. Wind turbine partial wake merging description and quantification. *Wind Energy*, 23(7):1610–1618, 2020.

Shamsoddin, S. and Porté-Age, F. A large-eddy simulation study of vertical axiswind turbine wakes in the atmospheric boundary layer. *Energies*, 9(5):1–23, 2016.

Shamsoddin, S. and Porté-Agel, F. Effect of aspect ratio on vertical-axis wind turbine wakes. *Journal of Fluid Mechanics*, 889(R1):R1 1–12, 2020.

Shapiro, C. R., Gayme, D. F., and Meneveau, C. Modelling yawed wind turbine wakes: A lifting line approach. *Journal of Fluid Mechanics*, 841:R11–R112, 2018.

Sheng, W., Galbraith, R. A. D., and Coton, F. N. A modified dynamic stall model for low mach numbers. *Journal of Solar Energy Engineering, Transactions of the ASME*, 130(3): 0310131–03101310, 2008.

10

Shi, L., Riziotis, V. A., Voutsinas, S. G., and Wang, J. A consistent vortex model for the aerodynamic analysis of vertical axis wind turbines. *Journal of Wind Engineering and Industrial Aerodynamics*, 135:57–69, 2014.

Silva, J. E. and Danao, L. A. M. Individual Rotor and Overall Cluster Performance. *Energies*, 14:1–22, 2021.

Snel H., Houwink R., and Bosschers J. Sectional prediction of lift coefficients on rotating wind turbine blades in stall. Technical report, Netherlands Energy Research Foundation (ECN), Petten (Netherlands), Netherlands, 1994.

Sørensen, J. N. and Shen, W. Z. Numerical modeling of wind turbine wakes. *Journal of Fluids Engineering, Transactions of the ASME*, 124(2):393–399, 2002.

Spalart, P. and Allmaras, S. *A one-equation turbulence model for aerodynamic flows.* 1992.

Steiros, K. and Hultmark, M. Drag on flat plates of arbitrary porosity. *Journal of Fluid Mechanics*, 853(R3):R3 1–11, 2018.

Stevens, R. J. A. M., Gayme, D. F., and Meneveau, C. Large eddy simulation studies of the effects of alignment and wind farm length. *Journal of Renewable and Sustainable Energy*, 6(2):023105, 2014.

Stevens, R. J. and Meneveau, C. Flow Structure and Turbulence in Wind Farms. *Annual Review of Fluid Mechanics*, 49:311–339, 2017.

Stevens, R. J., Gayme, D. F., and Meneveau, C. Effects of turbine spacing on the power output of extended wind-farms. *Wind Energy*, 19:359–370, 2016.

Strickland, J. H., Webster, B. T., and Nguyen, T. A vortex model of the darrieus turbine: An analytical and experimental study. *Journal of Fluids Engineering, Transactions of the ASME*, 101(4):500–505, 1979.

Strickland, J. H. The Darrieus Turbine: A Performance Prediction Model Using Multiple Streamtubes. Technical report, Sandia Laboratories, Albuquerque, N.Mex, 1975.

Sun, H., Gao, X., and Yang, H. A review of full-scale wind-field measurements of the wind-turbine wake effect and a measurement of the wake-interaction effect. *Renewable and Sustainable Energy Reviews*, 132(August 2019):110042, 2020.

Tennekes, H. and Lumley, J. L. *A First Course in Turbulence.* MIT Press, 1972.

Tescione, G., Ragni, D., He, C., Simão Ferreira, C. J., and van Bussel, G. J. Near wake flow analysis of a vertical axis wind turbine by stereoscopic particle image velocimetry. *Renewable Energy*, 70:47–61, 2014.

Tescione, G., Simão Ferreira, C. J., and van Bussel, G. J. Analysis of a free vortex wake model for the study of the rotor and near wake flow of a vertical axis wind turbine. *Renewable Energy*, 87:552–563, 2016.

10

Tescione, G. *On the aerodynamics of a vertical axis wind turbine wake An experimental and numerical study.* doctoral thesis, TU Delft University, 2016.

Tigelaar, L. Could Local Residents Living Close to Wind Turbines Be Compensated for Damage to Their Health and Loss of Value of Their Homes? *Journal for European Environmental and Planning Law*, 17(3):333 – 350, 2020.

Troldborg, N. *Actuator Line Modeling of Wind Turbine Wakes.* PhD thesis, Teechnical University of Denmark, 2008.

Troldborg, N., Larsen, G. C., Madsen, H. A., Hansen, K. S., Sørensen, J. N., and Mikkelsen, R. Numerical simulations of wake interaction between two wind turbines at various inflow conditions. *Wind Energy*, 14(7):859–876, 2011.

van der Hoek, D., Frederik, J., Huang, M., Scarano, F., Simao Ferreira, C., and van Wingerden, J.-W. Experimental analysis of the effect of dynamic induction control on a wind turbine wake. *Wind Energy Science*, 7(3):1305–1320, 2022.

Van Der Horst, S., Van De Wiel, J., Ferreira, C. S., and García, N. R. Flow curvature effects for VAWT: A review of virtual airfoil transformations and implementation in XFOIL. *34th Wind Energy Symposium*, pages 1–9, 2016.

van Kuik, G. A. M. *The Fluid Dynamic Basis for Actuator Disc and Rotor Theories.* IOS Press, Amsterdam, Netherlands, 2018.

VerHulst, C. and Meneveau, C. Large eddy simulation study of the kinetic energy entrainment by energetic turbulent flow structures in large wind farms. *Physics of Fluids*, 26 (2):25113, 2014.

Villeneuve, T., Winckelmans, G., and Dumas, G. Increasing the efficiency of vertical-axis turbines through improved blade support structures. *Renewable Energy*, 2021.

Vogel, C. R. and Willden, R. H. Investigation of wind turbine wake superposition models using Reynolds-averaged Navier-Stokes simulations. *Wind Energy*, 23(3):593–607, 2020a.

Vogel, C. R. and Willden, R. H. Investigation of wind turbine wake superposition models using Reynolds-averaged Navier-Stokes simulations. *Wind Energy*, 23(3):593–607, mar 2020b. ISSN 10991824.

Voutsinas, S., Rados, K., and Zervos, A. On the Analysis of Wake Effects in Wind Parks. *Wind Engineering*, 14(4):204–219, 1990.

Wang, J., Qin, S., Jin, S., and Wu, J. Estimation methods review and analysis of offshore extreme wind speeds and wind energy resources. *Renewable and Sustainable Energy Reviews*, 42:26–42, 2015.

Wei, N. J., Brownstein, I. D., Cardona, J. L., Howland, M. F., and Dabiri, J. O. Near-wake structure of full-scale vertical-axis wind turbines. *Journal of Fluid Mechanics*, 914:17, 2021.

Wen, B., Li, Z., Jiang, Z., Tian, X., Dong, X., and Peng, Z. Floating wind turbine power performance incorporating equivalent turbulence intensity induced by floater oscillations. *Wind Energy*, 25(2):260–280, 2022.

Wharton, S. and Lundquist, J. K. Atmospheric stability affects wind turbine power collection. *Environmental Research Letters*, 7(1), 2012.

White, F. M. *Viscous Fluid Flow*. McGraw-Hill, 2006.

Willert, C. Stereoscopic digital particle image velocimetry for application in wind tunnel flows. *Measurement Science and Technology*, 8(12):1465–1479, 1997.

WindEurope. Offshore wind in Europe – key trends and statistics 2020. Technical report, 2021.

Yu, W., Ferreira, C., and van Kuik, G. A. The dynamic wake of an actuator disc undergoing transient load: A numerical and experimental study. *Renewable Energy*, 132:1402–1414, 2019.

Zong, H. and Porté-Agel, F. A momentum-conserving wake superposition method for wind farm power prediction. *Journal of Fluid Mechanics*, 889, 2020a.

Zong, H. and Porté-Agel, F. A point vortex transportation model for yawed wind turbine wakes. *Journal of Fluid Mechanics*, 890, 2020b.

10

A

SPATIAL RESOLUTION EFFECT: A COMPARISON BETWEEN ROBOTIC PIV AND PLANAR PIV MEASUREMENTS

THIS appendix presents a comparison between robotic PIV and planar PIV measure-ments. A Quantel *Evergreen* double-pulsed Nd:YAG laser produces pulses with 200 mJ energy at a wavelength of 532 nm within a laser sheet of approximately 2 mm width. A SAFEX smoke generator releases water-glycol seeding particles of average 1 μm diam-eter. The seeding particles convected through the test section are imaged by a LaVision Imager LX 2MP camera (10-bit, image resolution of 1628 px × 1236 px, pixel pitch of 4.4 μm). The field of view extends from 0.5D upstream to 0.3D downstream. The experi-ments are conducted with the circular porous plate. The comparison of the robotic PIV and the planar PIV measurement parameters is listed in table A.1.

The velocity fields measured by the planar and robotic PIV, along with the win-dows/bins are compared in figure A.1. The results return excellent agreement upstream of the plate. For instance, at $y/D = 0$, and x/D from $-0.5D$ to $-0.1D$, the relative error of the velocity is approximately 1.3%. Differences can be observed immediately down-stream of the disc, where the alternate patterns of high velocity through the pore and separated flow after the solid portion of the mesh can be appreciated with the higher resolution of planar PIV. By contrast, the velocity field measured by robotic PIV returns a spatially averaged value in the close proximity of the plate.
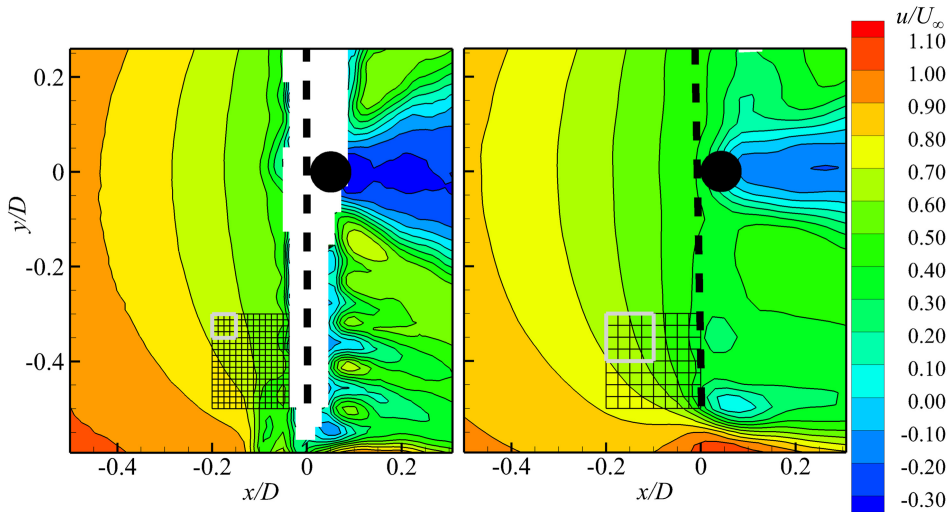

Figure A.1: Colour contours of the time-averaged and normalised streamwise velocity of the cir-cular actuator in the x-y plane at $z/D = 0$. Measurements by planar (left) and robotic PIV (right). The grid in the bottom-right corner indicates the vector data spacing in the measurement, the grey grids indicate the window/bin size.

Table A.1: Experimental parameters for robotic and planar PIV measurements.

		Robotic PIV	Planar PIV
Seeding	Tracer particle	Helium-filled soap bubbles	Water-glycol particles
	Particle size	400 μm	1 μm
	Particle density	1.2 $kg\,m^{-3}$	10^3 $kg\,m^{-3}$
Illumination	Pulse energy	50 mJ	2 × 200mJ
	Wavelength	527 nm	532 nm
	IFOV	A pyramid which extends from 8 × 13 cm^2 to 25 × 40 cm^2, with a height of 40 cm	2 mm thick sheet of 210(H) × 280(W) mm^2
Optics	Focal length	4 × 4mm	65 mm
	Numerical aperture	8	11.2
Imaging	Tomographic aperture	4° at 40 cm away from the camera plane	–
	Active sensor	512 × 500 px	1628 × 1236 px
	Pixel pitch	4.8 μm	4.4 μm
	Acquisition frequency	789 Hz	5 Hz
Post processing	Windowbin size	20 × 20 × 20 mm^3	64 × 64 px (11 × 11 mm^2)
	Overlap	75%	75%
	Vector pitch	5 mm	2.25 mm

B

A SHORT REVIEW OF THE EXAMINED KINEMATIC WAKE MODELS

T HIS appendix includes a short review of the examined kinematic wake models.

B.1. THE JENSEN MODEL

The Jensen model (Jensen, 1983) is one of the simplest wake models that is widespread through both academia and industry, and it is further developed by Katić et al. (1987) for multiple wakes. It assumes a top-hat shaped velocity deficit and a linear wake expansion along downstream distance x, which only depends on a turbulent wake decay constant k. The normalized velocity along the streamwise direction is computed based on the mass conservation that is applied in a control volume immediately downwind of the turbine. The normalized streamwise velocity deficit is calculated as:

$$\frac{\Delta u}{U_\infty} = \frac{1 - \sqrt{1 - C_T}}{(1 + 2kx/D)^2}, \tag{B.1}$$

where C_T is the thrust coefficient, ΔU the difference between the streamwise velocity at location x and the free-stream velocity U_∞, and D is the rotor diameter. Jensen proposes a decay constant $k = 0.1$, while 0.075 for on-shore cases (Barthelmie et al., 2006), 0.04 or 0.05 for offshore cases are suggested in the literature (Barthelmie et al., 2007; Barthelmie and Jensen, 2010; Cleve et al., 2009).

B.2. THE FRANDSEN MODEL

Frandsen et al. (2006) proposed an analytical wake model with top-hat wake deficit distributions expressed as follows:

$$\frac{\Delta u}{U_\infty} = \frac{1}{2}\left(1 - \sqrt{1 - 2\frac{A_0}{A_w}C_T}\right) \tag{B.2}$$

where $A_w(x = 0) = A_a$, and A_a is the cross-sectional area of the wake after initial expansion, the latter is assumed to occur right after the rotor disc. A_a is expressed as:

$$A_a = \beta A_0, \tag{B.3}$$

where β is a function of thrust coefficient:

$$\beta = \frac{1}{2}\frac{1 + \sqrt{1 - C_T}}{\sqrt{1 - C_T}}. \tag{B.4}$$

Compared to the Jensen model, Frandsen (1992) examined a control volume sufficiently large that bounds the wind turbine; Additionally, they also proposed an analytical formula for the calculation of the decay constant:

$$k = 0.5/\ln\left(\frac{z}{z_0}\right), \tag{B.5}$$

where z is the hub height of the wind turbine, and z0 is the surface roughness of the wind farm.

B.3. THE LARSEN MODEL

The Larsen model introduces the Prandtl mixing length theory as the turbulence closure, and the wake is assumed to be incompressible, stationary and axis-symmetric. In this model, the velocity deficit is calculated as the function of the wake expansion, and the deficit is distributed smoothly within the wake region (Pierik et al., 1999):

$$\frac{\Delta u}{U_\infty} = \frac{\Delta u_c}{U_\infty} \left[1 - \left(2 \frac{r}{\delta} \right)^{\frac{3}{2}} \right]^2, \text{ for } r \leq \frac{\delta}{2}, \tag{B.6}$$

where Δu_c is the velocity deficit at the center-line, expressed by:

$$\Delta u_c = \frac{35}{9} \frac{1}{2} \frac{C_T}{(\delta/D)^2} \tag{B.7}$$

δ/D is the wake width normalized by the rotor diameter, which is proportional to the downstream distance:

$$\frac{\delta}{D} = \sqrt[3]{\left(\frac{\delta_{\text{eff}}}{D} \right)^3 + \frac{k}{D^2} \cdot \frac{x}{D}} \tag{B.8}$$

where δ_{eff} is the effective rotor diameter, defined as the wake width right after pressure recovery, and k is the wake decay constant, which are given by:

$$\frac{\delta_{\text{eff}}}{D} = \sqrt{\frac{1 + \sqrt{1 - C_T}}{2\sqrt{1 - C_T}}}, \tag{B.9}$$

$$k = \frac{1}{9.5} \left(\left(\frac{\delta_{9.5}}{D} \right)^3 - \left(\frac{\delta_{\text{eff}}}{D} \right)^3 \right). \tag{B.10}$$

$\delta_{9.5}$ is the wake width at $9.5D$ downstream, which is related to the inflow turbulence intensity. When the ground effect is not presented:

$$\frac{\delta_{9.5}}{D} = \begin{cases} 2.16, \text{ for } I_\infty \leq 0.05 \\ 2.16 + 43.4 \left(I_\infty - 0.05 \right), \text{ for } I_\infty > 0.05 \end{cases}. \tag{B.11}$$

When considering the ground effect:

$$\frac{\delta_{9.5}}{D} = \begin{cases} \frac{\delta_{9.5}}{D} & \text{for } \delta_{9.5} \leq \frac{z_h}{2} \\ \frac{z_h}{D} + \frac{1}{2} \delta_{9.5} D & \text{for } \delta_{9.5} > \frac{z_h}{2} \end{cases} \tag{B.12}$$

B.4. THE BASTANKHAH AND PORTÉ-AGEL (BPA) MODEL

In classical shear flow theories, the wakes of bluff bodies feature a Gaussian profile of velocity deficit (see Johansson et al., 2003). The similar phenomenon has been found in the wakes of HAWTs as well (see Dufresne and Wosnik, 2013). Based on these observations, Bastankhah and Porté-Agel (2014) proposed an analytical HAWT wake model with Gaussian distribution for velocity deficit. The maximum velocity deficit at centre-line is calculated as follows:

$$\frac{\Delta u_c}{U_\infty} = 1 - \sqrt{1 - \frac{C_T}{8 \left(\sigma^2 / D \right)}}, \tag{B.13}$$

B

where d_0 is the rotor diameter and C_T is the thrust coefficient, σ denotes the standard deviation of a Gaussian velocity deficit profile. In comparison with the Jensen and the Larsen model, the wake expansion of the BPA model is not an explicit function of downstream distance, but a function of σ. And σ is a function of C_T and it expanses linearly with respect to downstream distance:

$$\frac{\sigma}{d_0} = k^* \frac{x}{D} + 0.2 \sqrt{\frac{1 + \sqrt{1 - C_T}}{2\sqrt{1 - C_T}}}, \tag{B.14}$$

where k^* and D stand for the growth rate and rotor diameter respectively. The velocity deficit is distributed in a Gaussian profile:

$$\frac{\Delta u}{U_\infty} = \frac{\Delta u_c}{U_\infty} \exp\left[-\frac{1}{2}\left(\frac{r}{\sigma}\right)^2\right], \tag{B.15}$$

where r is the axial coordinate.

An empirical expression relating the growth rate with the ambient turbulence I is implemented as suggested by Niayifar and Porté-Agel (2015):

$$k^* = 0.3837I + 0.003678 \tag{B.16}$$

B.5. THE EXPANDED JENSEN AND BPA MODELS FOR VAWTS

Abkar (2018) expanded the Jensen model and the BPA model to predict the velocity field of the wake of an H-shaped VAWT. The expended models assume that the turbine has a rectangular shape with dimensions of H and D, and consider the aspect ratio (H divided by D) effect by applying separate wake expansion and decay factors in radial and spanwise direction.

B.5.1. THE JENSEN MODEL FOR VAWTS

The wake expansions in two directions are calculated in the following equations:

$$H_w = H + 2k_z x, \quad D_w = D + 2k_y x, \tag{B.17}$$

and the velocity deficit:

$$\frac{\Delta u}{U_\infty} = \frac{1 - \sqrt{1 - C_T}}{(1 + 2k_z x/H)(1 + 2k_y x/D)}, \tag{B.18}$$

the velocity deficit profile is uniformly distributed in the wake.

B.5.2. THE BPA MODEL FOR VAWTS

Standard deviation of Gaussian shape velocity profiles in radial and spanwise directions are functions taking H and D into account respectively:

$$\sigma_z = k_z^* x + \varepsilon H, \quad \sigma_y = k_y^* x + \varepsilon D, \tag{B.19}$$

where

$$\varepsilon = 0.2 \sqrt{\frac{1 + \sqrt{1 - C_T}}{2\sqrt{1 - C_T}}}. \tag{B.20}$$

Centreline velocity deficit:

$$\frac{\Delta u_c}{U_\infty} = 1 - \sqrt{1 - \frac{C_T}{8\left(\sigma_y \sigma_z\right)/(HD)}}.$$

(B.21)

Velocity deficit profile:

$$\frac{\Delta u}{U_\infty} = \frac{\Delta u_C}{U_\infty} \exp\left[-\frac{1}{2}\left(\frac{r}{\sigma_y \sigma_z}\right)^2\right].$$

(B.22)

It is noted that the wake decay factors for radial and spanwise are assumed to be the same as recommended by Abkar (2018), and when aspect ratio equals to 1, these models are the same as the corresponding HAWT wake models.

B

C

THRUST QUANTIFICATION USING WAKE RAKE METHOD

THIS appendix introduces the wake rake method for calculating thrust forces using the velocity fields from both the URANS simulations and the PIV measurements. This procedure is adopted to verify the thrusts measured by an in-house designed balance.

C.1. WAKE RAKE MODEL FOR THRUST QUANTIFICATION

Take a streamtube that bounds the VAWT as the control volume. The CV consists of an inlet, an outlet, and a bunch of streamlines that close the streamtube. Assume the streamtube is sufficiently large, such that the pressure term and the shear stress along the side faces are negligible. Similar to the well accepted wake rake method for calculating the drag of a 2D airfoil, the drag of a VAWT is assumed to be calculated by:

$$D' = \rho \iint_S u_2 (u_1 - u_2) \, dy \tag{C.1}$$

where S represents the area of the outlet of the streamtube that bounds the VAWT; u_1 and u_2 are velocities at inlet and outlet, respectively. The inlet is selected far enough away from the turbine such that $u_1 = U_\infty$. The derivation is following the wake rake method introduced by Anderson Jr (1985).

FREE STREAM VELOCITY DETECTION

The key process that ensures the correctness of the wake rake method is the U_∞ detection. For numerical simulation, even though the U_∞ is predefined at the inlet as the initial boundary condition, it is not necessary that the exact value keeps constant when the simulation completed. The same happens to the wind tunnel experiment. Actually, due to the effect of blockage, uncertainty of the driving motor of the wind tunnel, etc., the U_∞ is not likely to be exact the same as predefined values. Thus, $U_i nf$ is detected based on the measured velocity fields, as the averaged velocity at a square region that is far enough from the turbine. The square region has a dimension of $0.1D * 0.1D$.

SHAPE EFFECT OF THE INTEGRATION WINDOW

Theoretically, circular streamtube is smoother compared with square, especially in terms of the shear stress; the latter is supposed to be negligible in the wake rake method. However, previous study shows that the shape has big effects on the wake of an actuator that creates a streamtube. Therefore, to check whether the shape of the integration window affects much of the estimated force, a square and a circular are compared. Both integration window are selected in a way that the edge of the window is sufficiently far away from the turbine. The side length of the square window is $7D$, while the radius of the circular window is $3.5D$.

The shape of the integration window has very small effect on the estimated C_T. Thus, square integration window is selected for sake of simplicity.

SIZE EFFECT OF THE INTEGRATION WINDOW

The size effect of the integration window is inspected in this section, with the side length ranging from 2 to $7D$. The centre of the VAWT's rotor is located in the centre of the integration window.
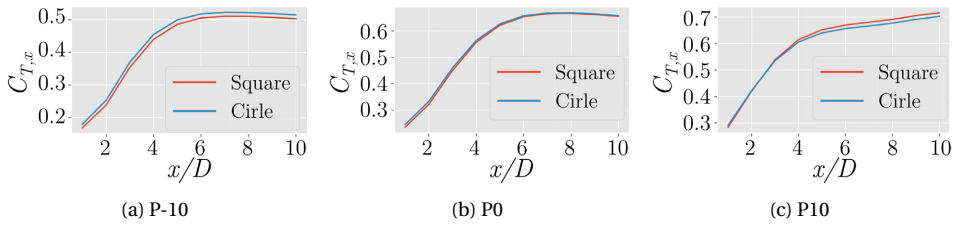
(a) P-10   (b) P0   (c) P10

Figure C.1: The shape effect of the integration window

(a) P-10   (b) P0   (c) P10
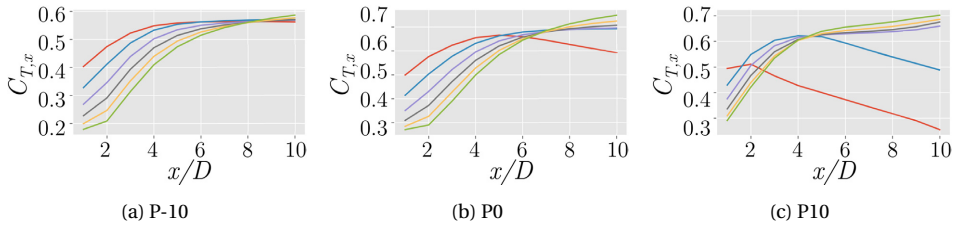
Figure C.2: The size effect of the integration window

The comparison presented in figure C.2 shows that when the side length of the integration window reaches 4 and 5D, the C_T calculation converges very well for all the cases. Smaller integration windows cannot capture the entire deficit area, leading to an underestimation of the C_T. Larger areas, on the contrary, are affected by the uncertainty from the domain boundary of the CFD simulation. That is because a Neumann boundary condition (zero gradient) that is usually used to avoid too large computational domain. However, this boundary condition allows for velocity propagation and slip at the boundary, and could lead to a velocity marginally lower than U_∞. This minor difference does not affect the macro behavior of the flow field, but will be accumulated when a large field is selected for integration. Figure C.3 depicts the boundary condition effect on the velocity field.
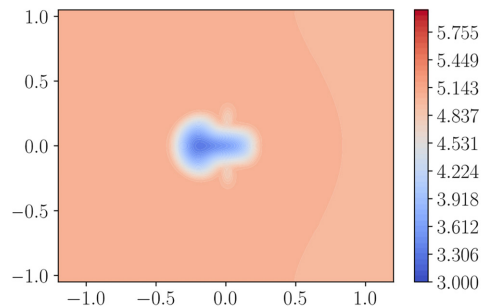
Figure C.3: The boundary effect on the velocity field. The presented streamwise velocity contour is of P0, at $x/D = 10$

COMPARISON OF THE $C_{T,x}$-x/D CURVE

Figure C.4 takes the converged curves of C_T-x/D for comparison; it is clear that after $x/D = 6$ P-10 and P0 almost converges; on the contrary, P10 keeps increasing. That is likely due to the fact that, for P-10 and P0, the pressure drop recovers after $6D$ downstream the turbine, while it is not recovered until $10D$ for P10 and thus not negligible.
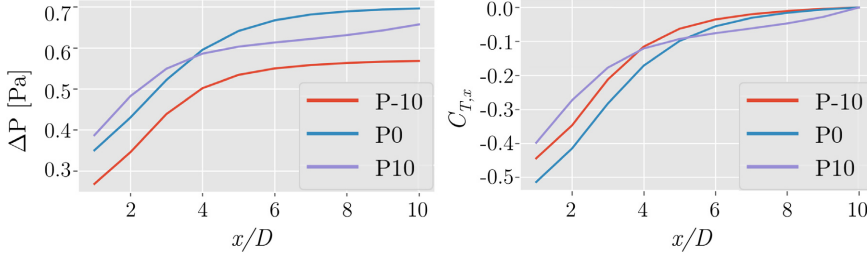

Figure C.4: Comparisons of the C_T-x/D and ΔP-x/D curve of different cases. Integration window is a square region with a size of $4D \times 4D$.

VALIDATION AGAINST THE ACTUATOR LINE MODEL

The calculated C_T based on the wake rake model is compared with that calculated from the actuator line. At $x/D = 6$, the wake rake method has already come to a good agreement with AL model, with differences of 3.7%, 2.5% and 7.4% for P-10, P0 and P10, respectively.

Table C.1: Comparison of the thrust coefficients calculated

	$C_{T,\text{AL}}$	$C_{T,\text{WR}}$		
		$x/D = 6$	$x/D = 8$	$x/D = 10$
P-10	0.571	0.550	0.563	0.568
P0	0.684	0.667	0.689	0.696
P10	0.662	0.613	0.631	0.657

D

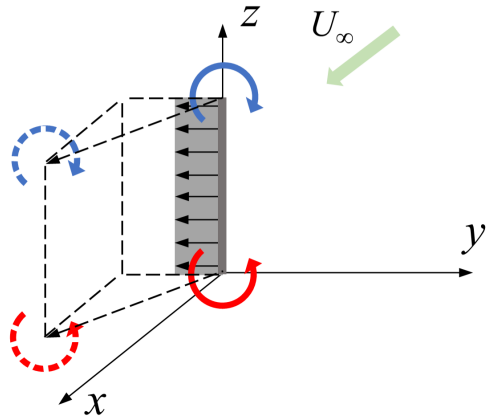## THE PRINCIPLE OF VORTEX GENERATION BY FORCE FIELDS

Figure D.1: A schematic of the vortex generated by an actuator line in the 3D space.

C ONSIDER the Navier-Stokes equation for the conservation of momentum:

$$\rho \frac{D\mathbf{u}}{Dt} = \mathbf{f} - \nabla p + \mu \nabla^2 \mathbf{u}, \tag{D.1}$$

where $\mathbf{f}$, p, $\mathbf{u}$, μ are the body force, pressure, velocity and dynamic viscosity, respectively. The bold letters represent vectors.

Taking the curl of equation 1, the vorticity transport equation is obtained:

$$\rho \frac{D\boldsymbol{\omega}}{Dt} = \nabla \times \mathbf{f} + (\boldsymbol{\omega} \cdot \nabla)\mathbf{u} - \boldsymbol{\omega}(\nabla \cdot \mathbf{u}) + \mu \nabla^2 \boldsymbol{\omega}, \tag{D.2}$$

where $\boldsymbol{\omega}$ is the vorticity vector: $\boldsymbol{\omega} = \nabla \times \mathbf{u}$. Because a flow field wherein a wind turbine is placed can be regarded as incompressible, the third term in the RHS is zero. The viscous term $\mu \nabla^2 \boldsymbol{\omega}$ can be neglected due to a sufficiently large Reynolds number. For a uniform inflow that is irrational originally, the term $(\boldsymbol{\omega} \cdot \nabla)\mathbf{u}$ will remain zero until vorticity is generated by the curl of a force field. Therefore, it is clear that the generation of vorticity is attributed to a specific force field. To demonstrate the vortex generation principle, assume a uniform force field $\mathbf{f}$ that is distributed on a line element placed along the z-axis in a 3D space, as depicted in figure D.1; The latter is usually referred to as an actuator line (AL). The AL applies a force to the flow towards the direction of negative y. The incoming flow U_∞ is directed towards the positive x. Applying equation D.2 to the AL, the material derivative of the vorticity vector is given by:

$$\rho \frac{D\boldsymbol{\omega}}{Dt} = \nabla \times \mathbf{f} = \left(\frac{\partial f_z}{\partial y} - \frac{\partial f_y}{\partial z}\right)\hat{i} + \left(\frac{\partial f_x}{\partial z} - \frac{\partial f_z}{\partial x}\right)\hat{j} + \left(\frac{\partial f_y}{\partial x} - \frac{\partial f_x}{\partial y}\right)\hat{k} = -\frac{\partial f_y}{\partial z}\hat{i}, \tag{D.3}$$

where $\hat{i}$, $\hat{j}$, and $\hat{k}$ are the unit vectors for the x-, y-, and z-axes, respectively. According to equation D.3, vorticity is generated only when the spatial gradient of a force field is not null, that is at the extremities of the actuator line. For a simple uniform AL as illustrated, a pair of counter-rotating vortices are thus generated, whose axis is perpendicular to the plane defined by the force vector and the actuator line. The counter-rotating vortices propagate along the free-stream direction (positive x), they are also deflected laterally (towards negative y) under the effect of the transverse velocity induced by the force field. It should be noted that in the above discussion the stretching and redirecting of the vortices are omitted for sake of simplicity, and this simplification is valid in the near wake of the AL. A similar phenomenon occurs in the wakes of airplanes, whereby the lift distribution over the wing generates a pair of counter-rotating tip vortices which move downwards under the effect of the downwash they induce (Devenport et al., 1996).

E

Wake of the isolated lab-scale VAWT with different fixed blade pitches

THE time-averaged stream-wise velocity contours and in-plane velocity vectors of the isolated lab-scale VAWT with different pitch angles are presented in figure E.1. The velocity contours at $x_1/D = 6, 8, 10$ are illustrated. The results are acquired by stereo-PIV measurements. The VAWT's frontal area is represented as grey lines.
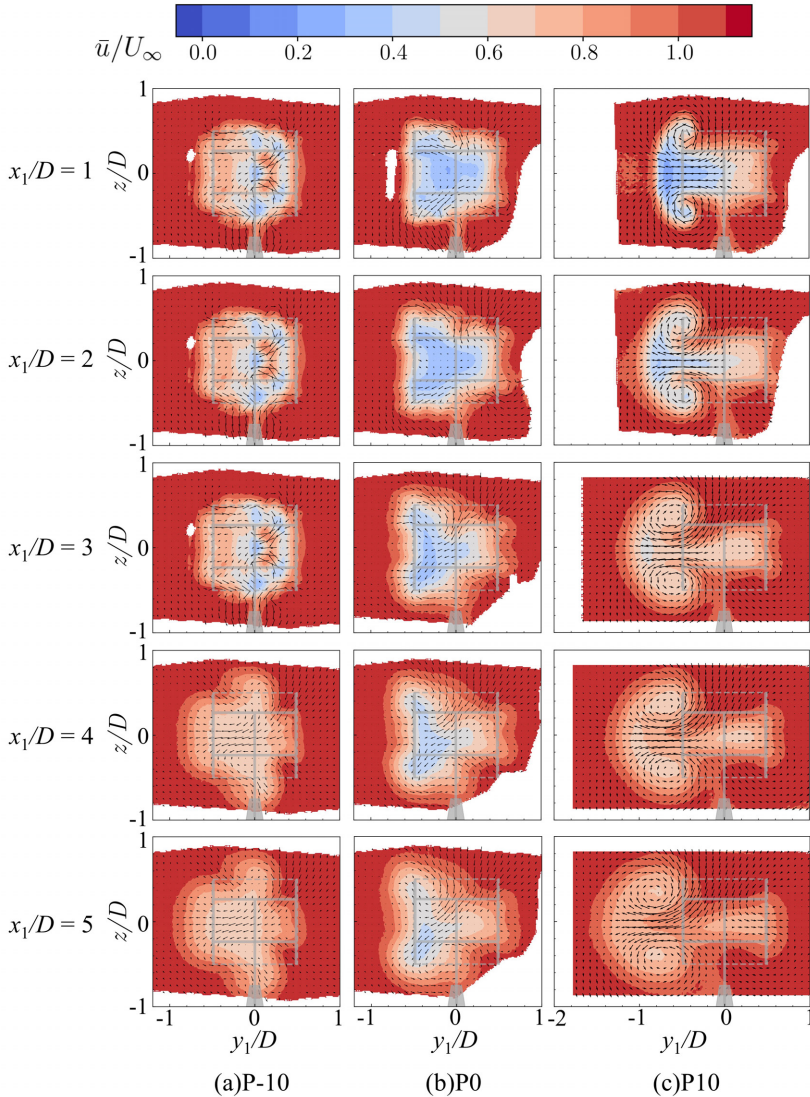
E

Figure E.1: Contours of streamwise velocity with in-plane velocity vectors for the isolated VAWT P-10, P0 and P10 at near wake ($x_1/D = 1, 2, 3, 4, 5$). Grey schematic of the VAWT denotes its transverse location and frontal area of the VAWT1.
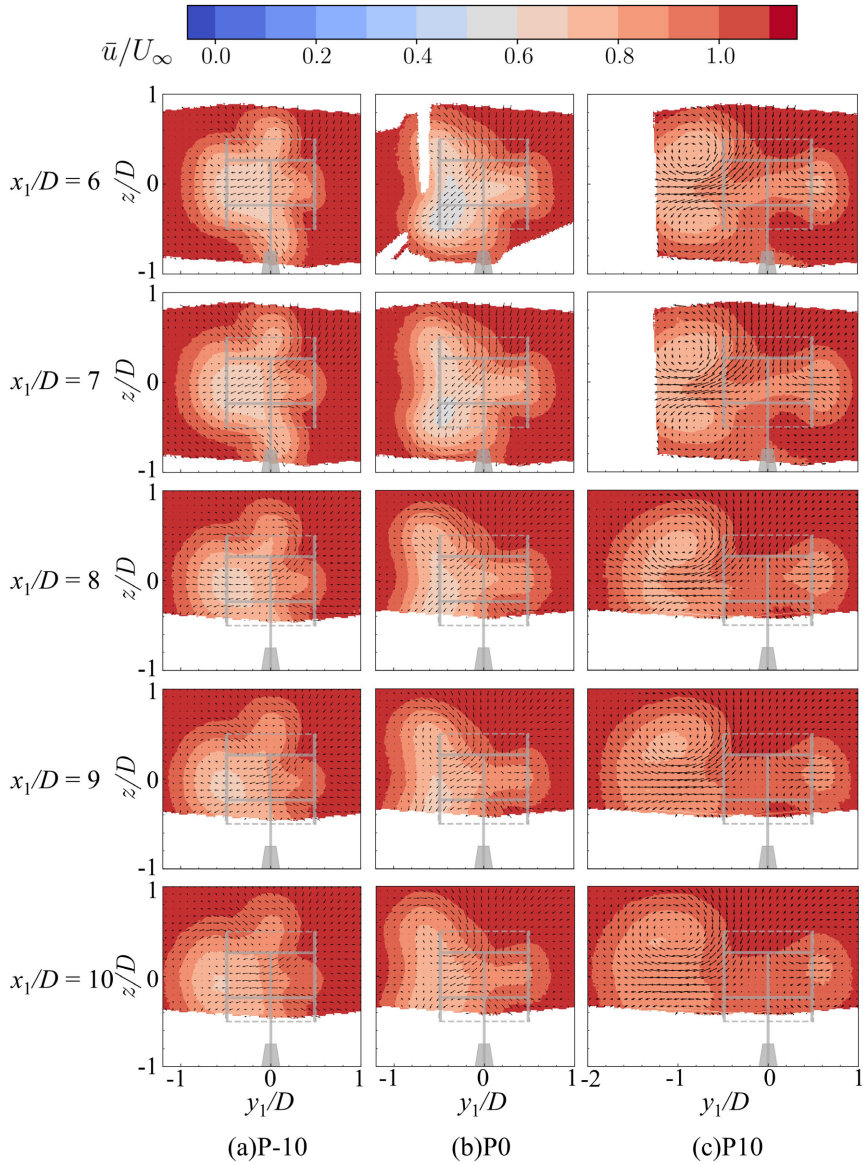
Figure E.2: Contours of streamwise velocity with in-plane velocity vectors for the isolated VAWT P-10, P0 and P10 at near wake ($x_1/D = 6, 7, 8, 9, 10$). Grey schematic of the VAWT denotes its transverse location and frontal area.

E.1. STREAMWISE VORTICITY

The streamwise vorticity of the control group P-10, P0, and P10 are illustrated in figure E.3 and E.4, where the in-plane streamlines are plotted to identify the location of streamwise vortices. The green contour line denotes the wake outline defined by $u/U_\infty = 1$.
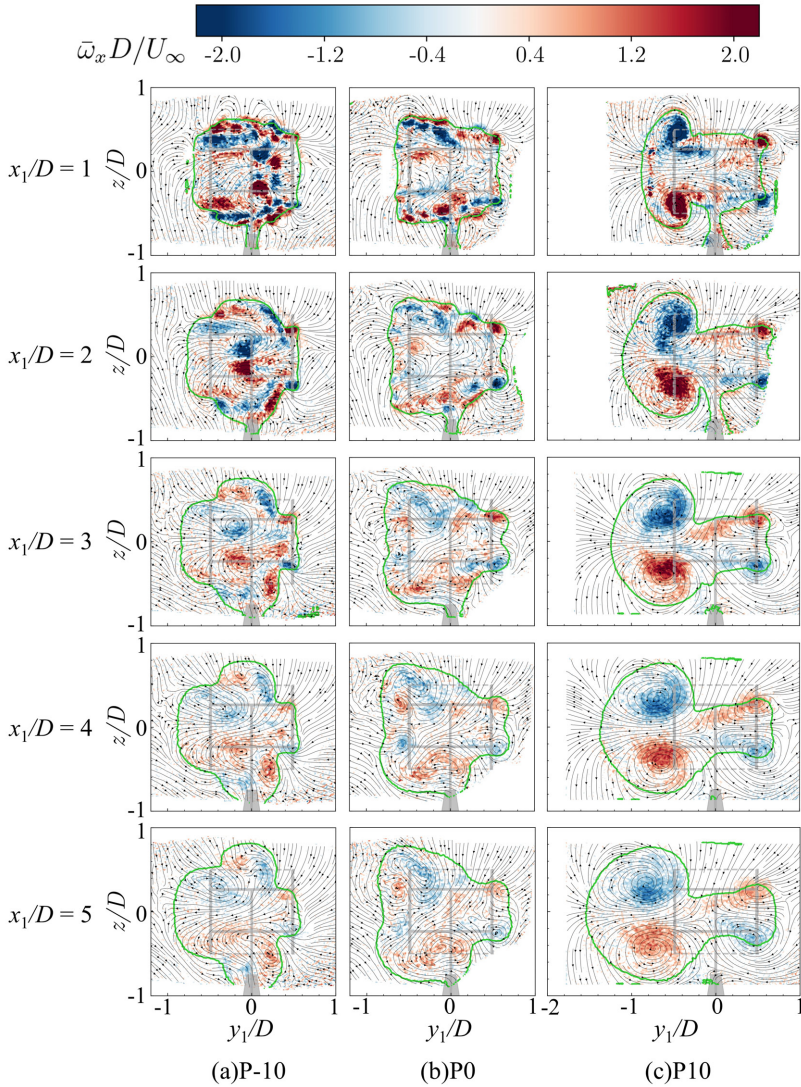

Figure E.3: Contours of streamwise vorticity with in-plane streamlines for P-10, P0 and P10 at near wake ($x_1/D = 1, 2, 3, 4, 5$). Grey schematic of the VAWT denotes its transverse location and frontal area of the VAWT1.
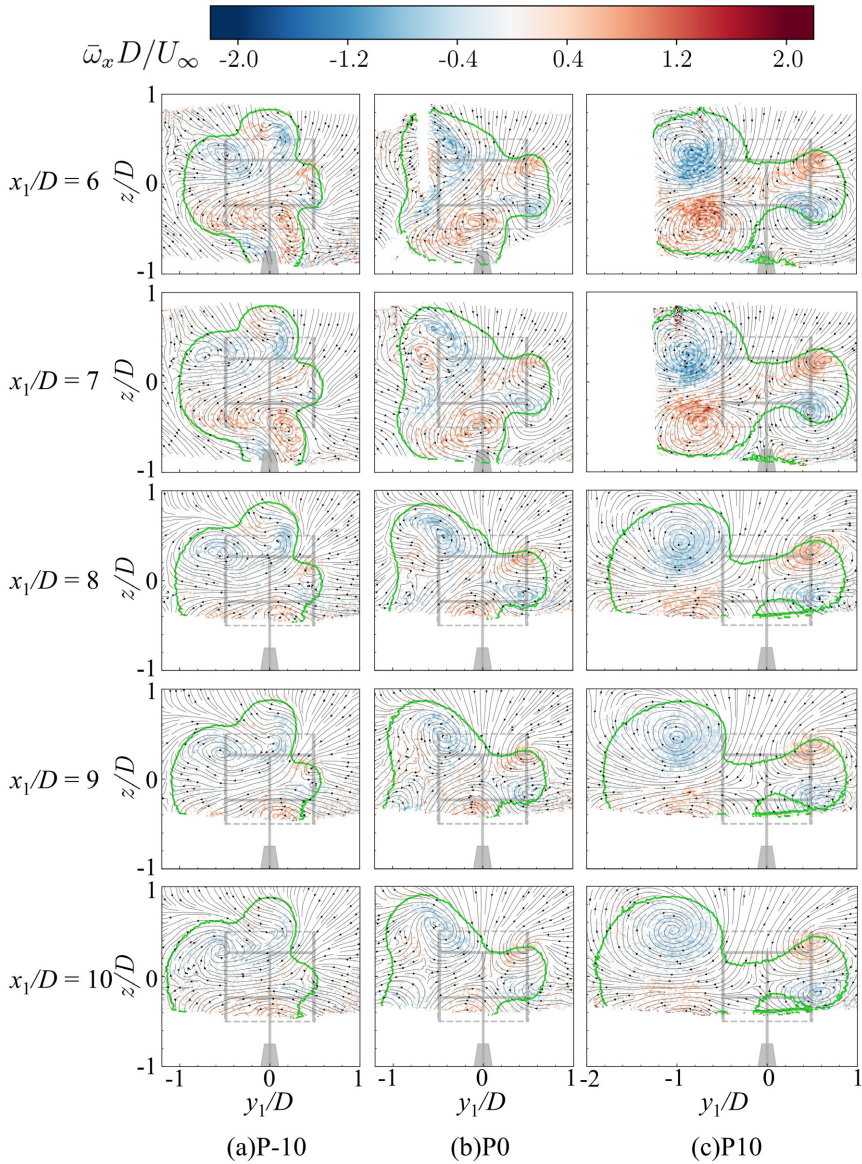
Figure E.4: Contours of streamwise vorticity with in-plane streamlines for P-10, P0 and P10 at near wake ($x_1/D = 6, 7, 8, 9, 10$). Grey schematic of the VAWT denotes its transverse location and frontal area of the VAWT1.

E.2. TURBULENCE INTENSITY

The turbulence intensity in the wake of the control group P-10, P0, and P10 are illustrated in figure E.5 and E.6,
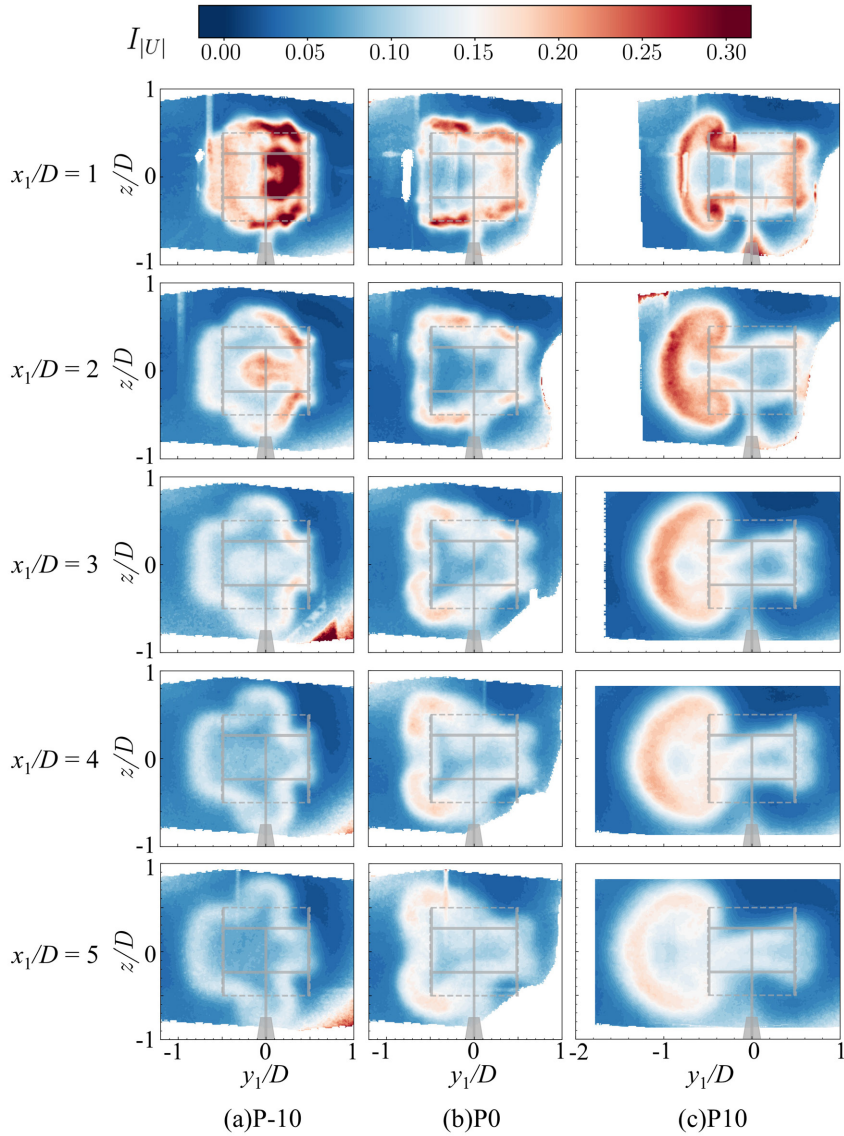

Figure E.5: Contours of turbulence intensity for P-10, P0 and P10 at near wake ($x_1/D = 1, 2, 3, 4, 5$). Grey schematic of the VAWT denotes its transverse location and frontal area of the VAWT1.
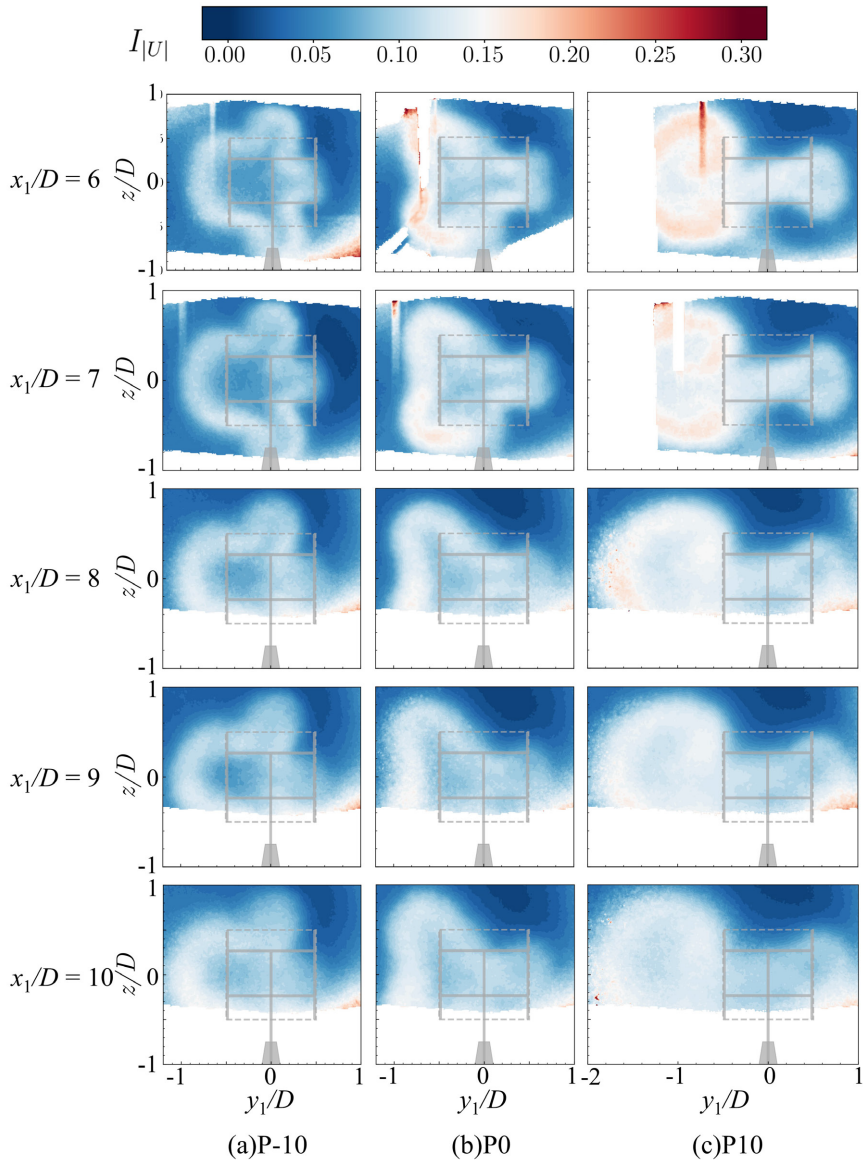
Figure E.6: Contours of turbulence intensity for P-10, P0 and P10 at far wake ($x_1/D = 6, 7, 8, 9, 10$). Grey schematic of the VAWT denotes its transverse location and frontal area of the VAWT1.

LIST OF PUBLICATIONS

JOURNAL PAPERS

4. **Huang, M.**, Sciacchitano, A., and Ferreira, C. On the wake deflection of vertical axis wind turbines by pitched blades. *Wind Energy*, 2023.

3. **Huang, M.**, Ferreira, C., Sciacchitano, A, and Scarano, F. Wake scaling of actuator discs in different aspect ratios. *Renewable Energy*, 183:866–876, 2022.

2. **Huang, M.**, Patil, Y. V., Sciacchitano, A., and Ferreira, C. Experimental study of the wake interaction between two vertical axis wind turbines. *Wind Energy*, (Under Review).

1. van der Hoek, D., Frederik, J., **Huang, M.**, Scarano, F., Simao Ferreira, C., and van Wingerden, J.-W. Experimental analysis of the effect of dynamic induction control on a wind turbine wake. *Wind Energy Science*, 7(3):1305–1320, jun 2022.

CONFERENCE PAPERS

2. **Huang, M**, Ferreira, C., Sciacchitano, A, and Scarano, F. Experimental Comparison of the Wake of a Vertical Axis Wind Turbine and Planar Actuator Surfaces. *Journal of Physics: Conference Series*, 1618(5), sep 2020.

1. Aubrun, S., Bastankhah, M., Cal, R., Conan, B., Hearst, R., Hoek, D., Hölling, M., **Huang, M.**, Hur, C., Karlsen, B., Neunaber, I., Obligado, M., Peinke, J., Percin, M., Saetran, L., Schito, P., Schliffke, B., Sims-Williams, D., Uzol, O., Vinnes, M., and Zasso, A. Round-robin tests of porous disc models. In *Journal of Physics: Conference Series* 1256, jul 2019.

DATA REPOSITORY

3. **Huang, M.**, Patil, Y. V., Sciacchitano, A., and Ferreira, C. Underlying data for article "Experimental study of the wake interaction between two vertical axis wind turbines". *4TU.ResearchData*, 2022. .

2. **Huang, M.**, Sciacchitano, A., and Ferreira, C. Underling data for "On the wake deflection of vertical axis wind turbines by fixed-pitched blades". *4TU.ResearchData*, 2022. .

1. **Huang, M.**, Ferreira, C., Sciacchitano, A., and Scarano, F. Underlying data, figures and scripts of the publication "Wake scaling of actuator discs in different aspect ratios". *4TU.ResearchData*, 2020. .

CURRICULUM VITÆ

Ming HUANG

24-01-1993   Born in Jiangxi, China.

EDUCATION

2018–2023   PhD researcher in Wind Energy
Delft University of Technology, Netherlands
Thesis: *Wake and Wind Farm Aerodynamics of Vertical Axis Wind Turbines*

2015–2018   Master of Science in Fluid Mechanics
Northwestern Polytechnical University, China
Thesis: *Efficient Multi-objective Aerodynamic Design Optimisation for
Airfoils of Rigid Co-axial Rotors Using Surrogate Models*

2011–2015   Bachelor of Engineering in Aerospace Safety Engineering
Northwestern Polytechnical University, China
Thesis: *Multi-objective Aerodynamic Design Optimisation Based on NSGA-II*

AWARDS

2023   2nd prize: TU Delft Wind Energy Institute Best Paper Award 2023
Huang, M., Sciacchitano, A., and Ferreira, C. (2022).
On the wake deflection of vertical axis wind turbines by pitched blades.
Wind Energy, 2023.

2022   1st prize: TU Delft Wind Energy Institute Best Paper Award 2022
Huang, M., Ferreira, C., Sciacchitano, A., and Scarano, F. (2022).
Wake scaling of actuator discs in different aspect ratios.
Renewable Energy, 2022, 183, 866-876.

TUDelft